On the Stability and Detection of Compact Objects in General Relativity

A Ph.D. thesis

submitted to

Tata Institute of Fundamental Research, Mumbai

for the degree of

Doctor of Philosophy

in

Physics

by

Prashant Kocherlakota

Department of Astronomy & Astrophysics

Tata Institute of Fundamental Research, Mumbai

Mumbai - 400005, India

***

Final Version Submitted October 2021
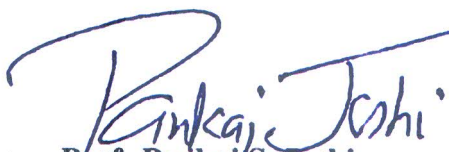
Declaration of Authorship

This thesis is a presentation of my original research work. Wherever contributions of others are involved, every effort is made to indicate this clearly, with due reference to the literature, and acknowledgement of collaborative research and discussions.

The work was done under the guidance of Prof. Pankaj S. Joshi and Prof. Sudip Bhattacharyya, at the Tata Institute of Fundamental Research, Mumbai.

Prashant Kocherlakota

In our capacity as supervisors of the candidate's thesis, we certify that the above statements are true to the best of our knowledge.

Prof. Pankaj S. Joshi
Date: 24 Sept 2019
Supervisor until 31ˢᵗ October, 2018

Prof. Sudip Bhattacharyya
Date: 24-09-2019
Supervisor from 1ˢᵗ November, 2018

The curvature of spacetime acts on matter to manifest itself as "gravity," and energy and momentum influence spacetime to create curvature.

Sean M. Carroll

Abstract

Tata Institute of Fundamental Research, Mumbai

Department of Astronomy & Astrophysics

Doctor of Philosophy

On the Stability and Detection of
Compact Objects in General Relativity

by Prashant Kocherlakota

This thesis has two broad themes: stability and detection of compact objects. However, we think it natural to divide further the material on detection presented here, due to their evident disparateness, into analyses of (a) the structures of their shadows and images, and (b) how gravitomagnetism affects the appearance of pulsars present in the vicinity of compact objects.

After a short prelude to the main body in Chapter 1, we begin with an extensive pedagogical introduction to the notions of stability in general relativity in Chapter 2. We then move to a discussion of the quasi-normal mode stability analysis of near-extremal Kerr superspinars. These are hypothetical non-singular compact objects whose exterior geometry is given by the overspinning Kerr metric ($M^2 \lesssim J$), and we will show that they are indeed stable, for a fairly large class of inner boundary conditions. A short description of our nascent results on the extent of non-linear stability of the Schwarzschild black hole formation process, via the Datt-Oppenheimer-Snyder collapse of dust, against fluid density perturbations is then presented. We end this chapter by presenting an attempt to study the stability of spacetimes within the framework of symplectic geometry; we also import some of the language of dynamical systems into general relativity.

In Chapter 3, we examine the behaviour of light in the presence of compact objects, and show in particular how some static naked singularity models cast shadows that are indistinguishable from those that are cast by static Schwarzschild black holes. Further, images of their accretion discs, as seen by an asymptotic observer, are also identical in these cases. On the other hand, we identify a class of naked singularity models whose images are distinctly different from those of the black holes.

In Chapter 4, we study the origin and properties of the so-called gravitomagnetic interaction that couples the intrinsic spin-angular momenta of a test object and a compact object. Specifically, this interaction causes the spin-axis of the test object to precess, and we proceed to outline local tests, based on this effect, that can be used to distinguish Kerr black holes from Kerr naked singularities. For example, if one considers the naturally appealing model of circular motion around the central compact object for the test object, it can be shown that the associated frequency of precession grows as the size of the orbit shrinks. Remarkably, in the approach to an event horizon, it becomes unbounded. We end with a comprehensive application of these results to pulsar-black hole systems, and comment on how it may be possible to obtain an independent accurate estimate for black hole parameters from pulsar timing measurements, by incorporating these effects, in the future.

We conclude with a summary and a discussion of future directions briefly in Chapter 5.

Acknowledgements

Contents

List of Publications

Papers and preprints that are presently relevant:

1. C. Chakraborty, **P. Kocherlakota**, and P. S. Joshi,
   "*Spin Precession in Black Hole and Naked Singularity Spacetimes*,"
   Phys. Rev. D **95**, 044006 (2017); arXiv:1605.00600 [gr-qc]. (Chapter 4)

2. C. Chakraborty, **P. Kocherlakota**, M. Patil, S. Bhattacharyya, P. S. Joshi, and A. Królak,
   "*Distinguishing Kerr Naked Singularities and Black Holes using the Spin Precession of a Test Gyro in Strong Gravitational Fields*,"
   Phys. Rev. D **95**, 084024 (2017); arXiv:1611.08808 [gr-qc]. (Chapter 4)

3. K.-I. Nakao, P. S. Joshi, J.-Q. Guo, **P. Kocherlakota**, H. Tagoshi, T. Harada, M. Patil, and A. Królak,
   "*On the Stability of a Superspinar*,"
   Phys. Lett. B **780**, 410 (2018); arXiv:1707.07242 [gr-qc]. (Chapter 2)

4. R. Shaikh, **P. Kocherlakota**, R. Narayan, and P. S. Joshi,
   "*Shadows of Spherically Symmetric Black Holes and Naked Singularities*,"
   Mon. Not. R. Astron. Soc. **482**, 52 (2018); arXiv:1802.08060 [astro-ph.HE]. (Chapter 3)

5. **P. Kocherlakota**, P. S. Joshi, S. Bhattacharyya, C. Chakraborty, A. Ray, and S. Biswas,
   "*Gravitomagnetism and Pulsar Beam Precession near a Kerr Black Hole*,"
   Mon. Not. R. Astron. Soc. **490**, 3262 (2019); arXiv:1711.04053 [astro-ph.HE]. (Chapter 4)

6. **P. Kocherlakota** and P. S. Joshi,
   "*An Approach to Stability Analyses in General Relativity via Symplectic Geometry*,"
   Arab. J. Math. (2019); arXiv:1902.08219 [gr-qc]. (Chapter 2)

Other Papers:

- D. Dey, **P. Kocherlakota** and P. S. Joshi
  "*A General Relativistic Approach to Small-Scale Structure Formation*,"
  arXiv:1907.12792 [gr-qc].

- R. Roy, **P. Kocherlakota** and P. S. Joshi
  "*Mode stability of a near-extremal Kerr superspinar*,"
  arXiv:1911.06169 [gr-qc].

The work that constitutes this thesis has been taken from material that has previously been published in peer refereed journals, and parts of the textual description have been quoted verbatim whenever the presentation in the original submission seemed hard to improve. Significant departures from the original material have only been made whenever an improvement in the pedagogy was deemed necessary. In particular, the introductory review material presented in §2.2–§2.4 does not appear in the papers listed above; however, it will be reported elsewhere in the form of proceedings of ST^4 2019, for lectures presented there by the author. In reporting this work here, we have drawn from figures previously prepared by the author or by collaborators for the corresponding journal.

Chapter 1

Introduction

General relativity is the theory of space, time, and gravitation developed by Einstein between 1907-1915. In this framework, spacetime is modelled by a four-dimensional Lorentzian manifold $\mathcal{M}$ equipped with a metric g, which is a smooth, non-degenerate, symmetric (0,2)-type tensor field. Remarkably, spacetime is a dynamical object and the associated dynamical equations are called the Einstein field equations. These relate the local spacetime curvature, characterized by the metric, to the matter distribution within that spacetime, described by an energy-momentum-stress tensor.

The focus of this thesis will mostly be on the exploration of various aspects of spacetimes containing compact objects like black holes and naked singularities. Several well known solutions of the field equations have been found that describe the geometries outside such objects [1–6], and the success of general relativity as the theory of classical gravity [7] supports, at this level, the possibility of their existence (see also [8–11]).

Since it is always useful to have a broad perspective of the aim and value of scientific studies, we think it useful to point out in brief, right at the get-go, why it is interesting to study compact objects, both from a theoretical and an astrophysical standpoint.

Theoretical studies of the existence, formation, stability and detection of black holes and naked singularities are of utmost importance towards a proof of the validity or invalidity of the cosmic censorship hypothesis [12–17]; we discuss these in some detail below. One could also systematically test the black hole "no-hair" theorems" [8, 18] by studying properties of gravitational waves emitted by binaries containing black holes [19] and also the spectra of accretion discs around black holes [20–23]. Since black holes are, quite uniquely, both extremely massive and extremely compact, they sit as novel objects of interest at the interface of the theories of general relativity and of quantum fields, and interesting notions like the black hole information paradox arise [24]. Analyzing departures from current theoretical expectations of gravitational wave observations could potentially lead us closer to the deeper UV-complete theory of gravity [25]. The AdS/CFT correspondence [26], for example, is another avenue of research that is of fundamental importance since it offers a new perspective on notoriously difficult problems, such as the aforementioned information loss paradox, the nature of singularities in black holes, and quantum gravity. Very nicely, it goes both ways, and studies of the characteristic vibrational quasi-normal modes of black holes in the context of the AdS/CFT correspondence have become a standard tool in considering the near-equilibrium behaviour of gauge theory plasmas with a dual gravity description [27].

On the other hand, old white dwarfs have been used to calibrate the age of the Milky Way galaxy [28] and of the universe [29]. The first indirect confirmation of gravitational radiation [30, 31], the discovery of the first extra-solar planetary system [32], and the first detection of gas in a globular cluster [33] are some of the successes of pulsar physics. The detection of a highly relativistic double neutron star binary system [34] played a crucial role in predicting the success of gravitational wave detectors by providing a reliable estimate of the merger rate of such systems. Currently, there is also compelling evidence for the presence of compact regions in the universe with very large mass, and this is interpreted as strong indirect evidence for the existence of black holes: the compact object Sagittarius A* at our Galactic center, with a mass of $4 \times 10^6 M_\odot$, is the best example of such an object [35, 36]. Moreover, there is substantial evidence that supermassive black holes exist at the cores of galaxies [35–41], and studying their properties could potentially yield crucial insight into how galaxies formed in the early universe. It is also thought that sources of extremely energetic processes like gamma-ray bursts could be merger events of neutron stars and black holes [42]. In the future, measuring the shape and size of the shadow and surrounding lensed photon ring could provide yet another test of the black hole no-hair theorems [43].

Now that we have said that these objects exist, in the sense that the metrics that describe their exterior geometries are solutions of the field equations, and that it is useful to study them, we are led to engage in a discussion of how such novel objects may form from gravitational collapse. Such a study is important because, although these metrics may be solutions of the Euler-Lagrangian field equations, it is important to check whether or not they can also be constructed within the initial value formulation of general relativity. We discuss these aspects schematically in Chapter 2.

Such objects may arise as end-states of the catastrophic continual gravitational collapse of massive stars, at the end of their life-cycles. Having exhausted their internal nuclear fuel, these stars end up as compact stellar-mass objects. Indeed various instances of black holes and naked singularities forming as a result of gravitational collapse have been reported [44–51]. It turns out that, in various scenarios, the formation or otherwise of an event horizon, as well as the actual epoch of horizon formation, are governed by the specific regular initial conditions from which the collapse evolves, and the final state could be either a black hole or a naked singularity. In Chapter 2, we review the formation of the Schwarzschild black hole, the Lemaître-Tolman-Bondi black holes, and of the Lemaître-Tolman-Bondi naked singularities[1] [44, 45, 47–50]. Alternatively, clustering of matter in the central region of a galaxy may generate a massive compact object, which may then grow further in mass by accretion [52].

From a practical (/conservative) viewpoint, it is useful to pay attention to these objects only if we are reasonably certain that they may be observed, which is only possible if they are stable (atleast on the relevant dynamical time-scale). Essentially, instability of an astrophysical object implies transience, and so one must ensure that the metrics corresponding to realistic astrophysical objects are stable as solutions to the dynamical equations.

Canonically, stability analyses are broadly divided into two categories: linear and non-linear. That is, when studying the stability of a particular spacetime that forms from some 'valid' initial data, one may deform the initial data by 'valid' infinitesimal (linear) or finite (non-linear) perturbations, and ask whether the new evolutions are 'close' to the original spacetime of interest. A precise discussion of these aspects, with illustrative examples, is the main goal of Chapter 2.

---

[1]We denote by Lemaître-Tolman-Bondi black holes those black holes that form from an inhomogeneous initial density configuration, as opposed to the Datt-Oppenheimer-Snyder black holes. This is a useful distinction to make since Lemaître-Tolman-Bondi black holes can contain *locally*-visible naked singularities [47].

As we shall see in Chapter 2, linear stability amounts to studying 'small disturbances' of the exterior geometry of a black hole or a naked singularity, and checking whether or not they oscillate around the background metric without causing significant deviations in it, in the same way a mechanical system oscillates around a local minimum configuration of its potential energy. One can also ask, in similar vein, whether more exotic objects like boson stars [53], preon stars [54] or superspinars [55] can be stable.

One may restrict to studying linear perturbations that have a harmonic time behaviour ($e^{-i\omega t}$, with ω a constant), akin to the normal modes of a conservative system, since such an analysis is far simpler. Recognizing the importance of stablity analyses of spacetimes in general relativity, a study of linear mode stability from the point of view of metric perturbations was initiated in two seminal papers [56, 57], where a Schrödinger-like equation for the radial dependence of axial-parity metric perturbations was arrived at, as we will see in considerable detail in Chapter 2. Since the Kruskal-Szekeres extension of the Schwarzschild spacetime [58, 59] had not yet been known at the time, the coordinate singularity at the Schwarzschild horizon made it difficult to ascertain whether or not divergences exhibited by these perturbations at this surface were real. This analysis was eventually completed in [60], where it was demonstrated that the Schwarzschild black hole spacetime was indeed mode stable. A Schrödinger-like equation for the radial dependence of polar metric perturbations was obtained in [61], and a unification of the of stability analyses of the axial-parity and polar-parity metric perturbations was achieved in [62] (see also [63]), via the discovery of a transformation that connected the seemingly disparate potentials of these two classes of perturbations. A gauge-invariant formulation of metric perturbations was later provided in [64], and an alternative approach via the Newman-Penrose [65] formalism was set up in [66] for the mode analysis of the Schwarzschild spacetime. This was later extended to the Kerr family of solutions in [67], and the celebrated result regarding the mode stability of Kerr black holes was obtained in the seminal paper of [68]. Various authors, including us, have since studied the stability of Kerr naked singularities [69], Kerr superspinars [70, 71] and other objects [27, 72–80].

Questions regarding the genericity of the occurrence of these compact objects which, as we argue in Chapter 2, are essentially concerned with the extent of their (*non-linear*) stability against finite changes in the initial data from which they evolve, have been explored extensively, with particular emphasis being laid on the study of the formation of trapped surfaces, apparent horizons, and event horizons. Powerful results like the Birkhoff theorem [81], along with various other analytical [82–90] and numerical studies [91–95] have bolstered our expectation that black holes can, in fact, occur frequently, or equivalently that they do form generically as endstates of continual gravitational collapse. However, despite significant effort [49, 50, 96–103], the genericity of evolutions of regular configurations of matter to naked singularities is less clear. That is, even if naked singularities do form for some particular choice of initial data of gravitational collapse d in the space of all allowed initial data $\mathcal{D}$, do they also form for other arbitrary initial data chosen within some open neighborhood of d in $\mathcal{D}$? Further, how is this space of all allowed initial data $\mathcal{D}$ partitioned into regions that produce black holes versus those that generate naked singularities? These are fundamental open questions in GR and are related to the cosmic censorship hypotheses [12–17], which roughly require a positive or negative statement regarding whether the set of initial data that eventually lead to naked singularities make up a 'sufficiently significant' portion of the space of all allowed initial data.

Therefore, it becomes clear that a study of the stability of these solutions against changes in initial data, both linear and non-linear, is of fundamental importance. In Chapter 2, we will discuss first our results on how near-extremal Kerr superpsinars are in fact (linear) mode stable [71], and also review some of our recent

(somewhat restrictive) findings on the non-linear stability of the formation process of the Schwarzschild black hole spacetime against changes in the fluid density initial data [104].

Statements regarding the various notions of stability in general relativity are typically made in its initial value formulation, and there are several excellent review articles in the literature on the same [105–110]. We propose in Chapter 2 that restating these notions using symplectic geometry earns us substantial insight since one can then draw formal analogies between the seemingly abstruse notions of stability of spacetimes in general relativity and the more familiar notions of stability in classical Galilei-Newton mechanics. There is also traction to be gained in numerical computations of stability analyses of spacetimes with the incorporation of symplectic integrators. Symplectic integrators possess, as a conserved quantity, a Hamiltonian which is slightly perturbed from the original one, which is advantageous when computing long-term symplectic structure-preserving evolutions of complex non-linear Hamiltonian systems (see for example [111]).

Having addressed to some degree the aspects of existence and stability of these compact objects, one must consider how they may be detected, as alluded to above. The spacetimes of interest here will be the Kerr family of black holes which, as we have mentioned above, are mode stable; in fact, the non-rotating Schwarzschild black hole is *linearly stable* [112]. Additionally, we will also consider the so-called Joshi-Malafarina-Narayan naked singularities [51, 113], which are expected to form from collapse, and are stable against perturbations of the fluid's initial density profile [114].

One may analyse, for example, how light behaves near such compact objects, which forms the central theme of Chapter 3. The direct evidence for the presence of a black hole requires an actual detection of the event horizon, the surface that encloses the compact interior of the black hole, and from where no material particles or light rays can escape. A number of tests have been proposed to confirm the presence of event horizons in black hole candidates [38–40]. The evidence is strong but, of necessity [41], not conclusive.

With the purpose of strengthening the evidence for the presence of a black hole in Sgr A*, as well as in the nucleus of the nearby galaxy M87, the event horizon telescope (EHT; [115, 116]), an Earth-spanning millimeter-wave interferometer, has recently been constructed. While nothing escapes from the interior of a black hole, the exterior spacetime has a photon sphere which is predicted to create a characteristic shadow-like image of the radiation emitted by an accretion flow around the black hole [117–119]. The goal of the EHT is to verify the presence of this shadow at mm wavelengths in the image of Sgr A*, which would add considerably to the evidence that Sgr A* is a black hole. Remarkably, EHT has already recorded the first ever image of a black hole (M87*) this year [120]. In a recent project [121], we showed that some static naked singularity spacetimes also possess photon spheres and therefore cast shadows, akin to static black holes. Strikingly, for the models we considered, the shadow and image structures are degenerate for the black hole and naked singularity case. We discuss these results in Chapter 3 below.

Another avenue with which to study massive compact objects is to study how test objects like stars and pulsars are influenced by a black hole or naked singularity. For example, it has been ascertained, from monitoring the motion of stars in the central region of our galaxy, that a large amount of mass, roughly about $4.2 \times 10^6 M_\odot$ [36, 122], is enclosed within a volume of radius smaller than 0.01 pc (see [123, 124]), supporting our belief that our Galaxy houses a supermassive black hole Sgr$A^\star$ at its centre [35, 36, 122]. In our recent work [125], we considered the effects that the intrinsic gravitomagnetism in the spacetime of a stationary black hole or naked singularity has on the appearance of a pulsar, and found that the evolution of its beam does in fact pick up clear tell-tale signatures of the compact object. We discuss our results in Chapter 4 and believe they are particularly

promising since locating pulsars in the vicinity of black holes has been an active pursuit in astronomy. Again, the interest in such systems is fuelled by the hope that by studying deviations in the observed frequency of pulses due to strong gravitational fields, one could study the properties of black holes and eventually even test general relativity in these strong-curvature regimes [126], which aligns with the theme of our investigations very nicely. Encouragingly, a magnetar (neutron star with large magnetic field and high rotation frequency) SGR J1745–2900 has recently been identified in the proximity of Sgr$A^\star$[127]. This detection is expected to yield rich dividends: it offers an unparalleled tool for probing the ionized interstellar medium toward the galactic center [128] and a possible avenue with which to test quantum gravity effects [129].

Furthermore, one of the desired objectives of X-ray and gamma-ray space telescopes like Fermi [130], and of large radio telescopes such as the upcoming Square Kilometre Array (SKA; [131, 132]) and the Five-hundred-meter Aperture Spherical radio Telescope (FAST; [133, 134]) has been to detect more such pulsar-black hole systems. This is true also of gravitational wave observatories like the Laser Interferometer Gravitational-Wave Observatory (LIGO; [135]) and the Virgo interferometer [136], and the next generation Laser Interferometric Space Antenna (LISA; see for example [137]). We discuss where one may find such systems in Chapter 4.

A pulsar, which can be treated effectively as a test spinning particle near a sufficiently massive black hole (for black hole masses of about $10^2 M_\odot$ or greater; see for example [138]), is affected in characteristically distinct ways depending on whether or not the black hole posseses angular momentum. For example, particle orbits precess due to geodetic precession around a non-spinning Schwarzschild black hole [139], and the rate of the advance of the periapsis depends only on the mass of the central black hole. The precession of particle orbits near a spinning Kerr black hole was studied in [117], and it was found there that an additional Lense-Thirring precession [140] piece arises due to the coupling of the orbital angular momentum of the particle with the angular momentum of the Kerr black hole. These orbit-precession effects would be experienced by both spinning and non-spinning test particles, and can be neatly thought of as causing the rotation of the associated Laplace-Runge-Lenz vector of the test object (see for example [141]). The Lense-Thirring or gravitomagnetic frame-dragging precession of orbits has been explored in a variety of astrophysically important contexts including for accretion disc matter [142–144] and for pulsars present in the vicinity of spinning black holes [145, 146].

In addition to these orbit-precession effects, the spin-axis of a test spinning object could precess, relative to a fixed observer at infinity. This is evident from the evolution of its intrinsic spin angular momentum, which is governed by the Fermi-Walker transport law ([147, 148]; see also [149]). The focus of our recent work [125] was on this particular curious effect of *spin*-precession on observations of pulsars on *circular* orbits in binaries with sufficiently massive black holes so the pulsars may effectively be treated as test objects. Spin-precession experienced by test spinning objects present near a Schwarzschild black hole was studied in [150], and it was found notably that when these objects remain at fixed spatial locations, they do not experience these effects. However, when pulsars move through the curved space (on geodesics) near a Schwarzschild black hole, they experience non-zero spin-precession. Therefore, spin-precession in a static spacetime is a kinetic effect, and this geodetic spin-precession depends only on the mass of the central non-spinning black hole [139] and the properties of motion of the pulsar. However, when in the vicinity of a (rotating) Kerr black hole, even pulsars that remain spatially-fixed experience non-zero spin-precession [151]. This is due to the intrinsic gravitomagnetic frame-dragging effects, characteristic of a spinning central mass, that are encoded into the metric of a stationary spacetime. Essentially, the intrinsic spin angular momentum of the pulsar couples to the

gravitomagnetic field associated with the non-zero spin of the central black hole [152–154]; for a discussion on gravitomagnetism, we direc tthe reader to see [155–157].

Searching for these characteristic general relativistic couplings by measuring the precession properties of a gyroscope in earth's gravitational field was first proposed in [158]. This search was successfully conducted by Gravity Probe B (GPB; [159]), and data from four gyroscopes of the GPB mission measured (one sigma results) both a geodetic and a gravitomagnetic frame-dragging frequency of 6601.8 ± 18.3 marc-s yr^{-1} and 37.2 ± 7.2 marc-s yr^{-1} respectively (1 marc-s = 4.848×10^{-9} radians). To compare, the general relativity-predicted values are 6606.1 marc-s yr^{-1} and 39.2 marc-s yr^{-1}. In recent decades, precession experienced by both isolated pulsars due to their internal structure [160], and those in binaries has been explored [161, 162]. However, the effect of gravitomagnetic spin-precession in pulsar-black hole systems on pulsar beam profiles has not been sufficiently well characterized, and this forms the focus of our work [125], which we discuss in Chapter 4. We note how this problem is complicated by difficulties in (a) evaluating the precession frequency experienced by pulsars on arbitrary time-like orbits, and in (b) relating statements made in the pulsar-frame to the frame of an asymptotic spatially-fixed observer. The spin-precession frequency, which is the rate at which the intrinsic spin-angular momentum or the spin-axis of a pulsar precesses, depends on the properties of motion of the pulsar, like its distance from the central collapsed object and its four-velocity, as well as on the characteristics of the central object, like its mass and angular momentum. Employing a completely covariant formalism, the spin-precession frequency experienced by gyroscopes moving on Killing orbits in arbitrary stationary spacetimes was calculated in [151], which will be the orbits of choice in the Chapter 4. It should be noted that major leaps in overcoming both of the hurdles mentioned above have come recently in two seminal papers [153, 163], where gyroscopic spin-precession along unbound equatorial plane orbits and along general timelike geodesics in the Kerr spacetime respectively was analysed. However, we will not attempt to go through this material here.

We live in exciting times to be studying compact objects, both theoretically and via observations, courtesy of various forward-looking large-scale astronomy missions such as LIGO, Virgo, LISA, EHT, SKA, FAST and Fermi that are actively looking to detect them and study their properties.

Part I: Stability of Spacetimes in General Relativity

Chapter 2

Stability in General Relativity

2.1 Outline

When describing gravity in the absence of matter, the only dynamical entity is the metric g of the spacetime, and the usual approach to treating general relativity (GR) as a field theory is based on the covariant Lagrangian formulation. The Einstein-Hilbert action for this system is given as,

$$S_{\text{EH}} = \frac{1}{2} \int \sqrt{-|g|} \mathrm{d}^4 x \, R, \tag{2.1.1}$$

where $|g| \equiv \det(g_{\mu\nu})$ is the determinant of the metric tensor, R is the associated Ricci scalar and we have used Geometrized units, $8\pi\mathscr{G} = c = 1$. Our convention for the metric signature will be $(-, +, +, +)$. With the introduction of the associated Christoffel connections $\Gamma^{\rho}_{\mu\nu} = \frac{1}{2} g^{\rho\alpha} \left(2g_{\alpha(\mu,\nu)} - g_{\mu\nu,\alpha} \right)$, the Riemann tensor $R^{\rho}_{\sigma\mu\nu} = 2 \left(\Gamma^{\rho}_{\alpha[\mu} \Gamma^{\alpha}_{\nu]\sigma} - \Gamma^{\rho}_{\sigma[\mu,\nu]} \right)$ and the Ricci tensor $R_{\mu\nu} = R^{\rho}_{\mu\rho\nu}$, the Ricci scalar is defined as $R = g^{\mu\nu} R_{\mu\nu}$. Then the governing Euler-Lagrange equations of motion can be derived as being,

$$G_{\mu\nu} = 0, \tag{2.1.2}$$

where in the above we have introduced the trace-reversed Ricci tensor G, which is more famously known as the Einstein tensor, as $G_{\mu\nu} = R_{\mu\nu} - \frac{1}{2} g_{\mu\nu} R$. The square brackets denote antisymmetrization in the outermost indices $A_{[\mu\cdots\nu]} = \frac{1}{2} \left(A_{\mu\cdots\nu} - A_{\nu\cdots\mu} \right)$ and round brackets mean symmetrization similarly defined, $S_{(\mu\cdots\nu)} = \frac{1}{2} \left(S_{\mu\cdots\nu} + S_{\nu\cdots\mu} \right)$. The above set of equations are called the vacuum Einstein field equations (EFEs) and metrics g that satisfy these equations are called the vacuum solutions of GR. The EFEs are a set of non-linear, partial differential equations that are essentially hyperbolic (wave-like) in nature (see [105] for details).

When matter is introduced into the mix, the full action of theory is given by the Einstein-Hilbert term plus a matter term L_{M} as,

$$S = \int \sqrt{-|g|} \mathrm{d}^4 x \left(\frac{R}{2} + L_{\text{M}} \right). \tag{2.1.3}$$

The corresponding Euler-Lagrange equations of motion are then given as,

$$G_{\mu\nu} = T_{\mu\nu}, \tag{2.1.4}$$

9

where in the above we have introduced the energy-momentum-stress tensor T of the matter fields as,

$$T_{\mu\nu} = g_{\mu\nu}L_{\mathrm{M}} - 2\frac{\delta L_{\mathrm{M}}}{\delta g_{\mu\nu}}. \tag{2.1.5}$$

See for example [106, 164] for the expressions of energy-momentum-stress tensors associated with different types of fields. As an example, the reader may also see §2.8 below, where dust (zero-pressure perfect fluid) is the matter model of choice. It will presently become evident why this is an interesting system to study.

Exact solutions of the EFEs (2.1.4) provide important insight into how this "new theory" of classical gravity modifies our description of nature. For example, the Schwarzschild metric [1] captures the geometry outside an isolated massive object, and it can be shown for example that the continual gravitational collapse of a homogeneous and isotropic cloud of dust terminates in the formation of a Schwarzschild black hole [44]. Now, whether or not it forms similarly as the end-state of collapse processes when the initial matter configuration is modified must be investigated. This is of vital importance since if the formation process is *not* stable under even infinitesimal perturbations, then intuition that is built based on these models is not useful. Futher, in the case that it is unstable under only finite perturbations, it would be immensely useful to characteristize the sizes and nature of these perturbations, for obvious reasons. Indeed these issues have been studied rigorously in this context over the years [45, 49, 50, 99–101], and such questions have also been of great interest in broader contexts to the general relativity and astrophysics community. Stability analyses have been canonically been organized into two categories, based on the size of the perturbation, into linear and non-linear stability analyses, for when the perturbing field is infinitesimal or finite respectively.

Roughly, the question of whether a stationary spacetime $(\mathcal{M}, g)$ is linearly stable can be summarized as follows. If one adds to the metric g, an infinitesimal perturbation h such that the perturbed metric $\bar{g} = (g + h)$ also satisfies the Einstein field equations, *then does h remaining bounded to its initial data, by some suitable norm*? If this statement holds true for arbitrary regular initial data for h, then g is linearly stable as an solution to the EFEs. One can also study the stronger statement of asymptotic linear stability, i.e. whether or not solutions h asymptotically decay.

In particular, if for some spacetime $(\mathcal{M}, g)$ one can find a time-coordinate t such that all metric components are independent of t, then such a solution of the EFEs is said to be stationary[1]. These sorts of time-invariant solutions of the EFEs correspond to equilibrium points (in the phase space of GR), in the usual sense, and one can study their stability against harmonic perturbations, i.e. linear perturbations with the time dependence of the form $e^{i\omega t}$, akin to a normal mode analysis. This brings us to a discussion of a far simpler, yet sufficiently powerful, linear mode stability analysis of a stationary spacetime: *do the linearized equations admit solutions with frequencies ω, all restricted to the upper half plane?*[2] This corresponds to all modes dying off as $t \to +\infty$. If yes, then g is mode-stable as an equilibrium solution to the EFEs. We think it relevant to mention here that the well known Kerr-Newman family of black hole metrics [1, 2, 4, 5] comprises of stationary solutions; therefore, setting up mode stability analyses of stationary solutions in general relativity is of immediate astrophysical interest. It is also clear that a mode stability analysis is superseded by a linear stability analysis, since one is only interested in a specific type of linear perturbations when studying mode stability.

---

[1]Equivalently, a spacetime $(\mathcal{M}, g)$ is defined to be stationary if it admits a time-like Killing vector [10]. That is, if $\pounds_{\xi} g = 0$ for ξ a time-like vector, then g is an equilibrium solution. Here, $\pounds$ represents the Lie derivative.

[2]Note that sometimes the following convention for defining the harmonic form is used, $e^{-i\omega t}$. In this case, the frequencies must lie naturally in the lower half plane.

Now, in order to study the linear stability of a solution, one must obtain the evolution equations for the metric perturbation h, and this is the program of §2.2 and §2.3. The strategy we will use to obtain the equations of motion for h is straightforward. We write down the EFEs for the full perturbed metric $\bar{g}$, and subtract from it the EFEs for the 'background metric' g. It will then become clear that the smallness of the perturbation h will ensure that it satisfies a linearized version of the field equations. At this point we must note here that we will not actually attempt to solve the linearized equations for arbitrary metric perturbations h. This is in general a difficult task as can be seen from the seminal works [165, 166] and [112] on the linear stability of the Minkowski and Schwarzschild spacetimes respectively. We will instead use the linearized equations reported in §2.2 and §2.3 to review the mode stability of the Schwarzschild black hole in §2.4 in some detail. After these pedagogical sections, we will finally discuss our results on the mode stability of near-extremal Kerr superspinars in §2.5. We will make some concise comments on the non-trivial difference between a mode stability analysis and a full linear stability analysis in GR, in §2.6.

We will suspend a discussion on the slightly more nuanced notions of a non-linear stability analysis of a spacetime until we reach §2.7, after we have briefly addressed the need for, and the framework of, the initial value formulation of GR. We end this chapter with a discussion on our partial results on the non-linear stability of the Schwarzschild black hole against fluid density perturbations, as a demonstrative example, in §2.8.

2.2   Perturbations of the Minkowski Spacetime[3]

Before we enter into a derivation of the dynamical equations that govern the time evolution of infinitesimal (linear) metric perturbations of arbitrary vacuum solutions to the Einstein field equations, it is pedagogically simpler to derive them for the Minkowski solution, which we review in this section.

We add to the Minkowski metric η an arbitrary "small" metric perturbation h,

$$\bar{g}_{\mu\nu} = \eta_{\mu\nu} + h_{\mu\nu}, \quad \|h_{\mu\nu}\| \ll 1, \tag{2.2.1}$$

such that $\bar{g}$ is also a solution of the EFEs and $\|h_{\mu\nu}\|$ denotes the magnitude of a typical non-zero component of h. Then the question of whether or not the Minkowski metric is linearly stable as a stationary solution of the vacuum EFEs, as mentioned above, reduces to a study of whether or not h remains bounded for all forward time, for arbitrary initial data. Indeed it turns out that this is the case, as was shown in the seminal work of [165], which we will not go into here.

It is to be noted that since Lorentzian metrics are not positive definite, there is no natural norm which captures the notion of "smallness" of a metric tensor. However an adequate definition of smallness in this context is that the components of h be much smaller than unity as we have indicated, which applies if we work in some global inertial coordinate system of η, in which it takes its canonical form $\eta_{\mu\nu} = \text{diag}(-1, +1, +1, +1)$. Note that this smallness-condition on the metric perturbation doesn't really make sense in coordinates that are not (approximately) Cartesian[4].

---

[3]This section follows [8, 10, 74, 167–169].

[4]One can see the related notions of Riemann normal or holonomic coordinates [170]. A local condition for a basis $\{e_0, e_1 \cdots e_n\}$ to be holonomic is that all mutual Lie derivatives vanish, $[e_i, e_j] = \pounds_{e_i} e_j = 0$.

Now, in such a weak-field situation, one can expand the field equations for $\bar{g}$ in powers of h, and retain terms that are at most linear in h; this is the framework of the linearized theory of gravity[5]. Since everything (Christoffels, Riemann, Ricci) vanishes for the present choice of the background stationary metric $g = \eta$, writing out the EFEs for the perturbed metric will evidently be equivalent to obtaining the linearized equations of motion that govern the evolution of h.

To obtain the Einstein tensor $\bar{G}$ for the perturbed metric $\bar{g}$, we require its inverse $\bar{g}^{\mu\nu}\bar{g}_{\nu\rho} = \delta^{\mu}_{\rho}$. That is,

$$\bar{g}^{-1} = (\eta + h)^{-1} = \eta^{-1}\left(1 + \eta^{-1}h\right)^{-1} = \eta^{-1}\left[1 - \eta^{-1}h + \left(\eta^{-1}h\right)^2 - \left(\eta^{-1}h\right)^3 + \cdots\right]. \tag{2.2.2}$$

In components, we may write,

$$\begin{aligned}
\bar{g}^{\mu\nu} &= \eta^{\mu\alpha}\left[\delta^{\nu}_{\alpha} - \left(\eta^{-1}h\right)^{\nu}_{\alpha} + \left(\eta^{-1}h\right)^{\beta}_{\alpha}\left(\eta^{-1}h\right)^{\nu}_{\beta} - \left(\eta^{-1}h\right)^{\beta}_{\alpha}\left(\eta^{-1}h\right)^{\gamma}_{\beta}\left(\eta^{-1}h\right)^{\nu}_{\gamma} + \cdots\right], \\
&= \eta^{\mu\alpha}\left[\delta^{\nu}_{\alpha} - h_{\alpha\beta}\eta^{\beta\nu} + h_{\alpha\gamma}\eta^{\gamma\beta}h_{\beta\delta}\eta^{\delta\nu} - h_{\alpha\gamma}\eta^{\gamma\beta}h_{\beta\delta}\eta^{\delta\gamma}h_{\gamma\epsilon}\eta^{\epsilon\nu} + \cdots\right], \\
&= \eta^{\mu\nu} - h^{\mu\nu} + h^{\mu\beta}h^{\nu}_{\beta} - h^{\mu\beta}h^{\gamma}_{\beta}h^{\nu}_{\gamma} + \cdots.
\end{aligned} \tag{2.2.3}$$

A point to note is that in writing the last equation above, we have raised h using the background Minkowski metric η as, $h^{\mu\nu} \equiv \eta^{\mu\alpha}h_{\alpha\beta}\eta^{\beta\nu}$. This is because in this linearized theory, as noted above, we can discard terms that are of higher order in h, without much loss of accuracy. We will in fact similarly raise and lower indices using η since the corrections would be of higher order in the perturbation otherwise[6]. Therefore, to leading order in h, the inverse of the perturbed metric is clearly just,

$$\bar{g}^{\mu\nu} \approx \eta^{\mu\nu} - h^{\mu\nu}. \tag{2.2.4}$$

The associated Christoffel symbols $\bar{\Gamma}$ for the perturbed metric $\bar{g}$ are then given as,

$$\bar{\Gamma}^{\rho}_{\mu\nu} = \frac{1}{2}\bar{g}^{\rho\sigma}\left(2\bar{g}_{\sigma(\mu,\nu)} - \bar{g}_{\mu\nu,\sigma}\right) \approx \frac{1}{2}\left(\eta^{\rho\sigma} - h^{\rho\sigma}\right)\left(2h_{\sigma(\mu,\nu)} - h_{\mu\nu,\sigma}\right) \approx \frac{1}{2}\eta^{\rho\sigma}\left(2h_{\sigma(\mu,\nu)} - h_{\mu\nu,\sigma}\right). \tag{2.2.5}$$

Since the connection coefficients are already first order in h, the only contribution to the Riemann tensor (which is structurally of the form $\Gamma\Gamma - \Gamma\Gamma + \partial\Gamma - \partial\Gamma$) will come from the derivatives of the Γ's and not the Γ^2 terms. Now, lowering an index for convenience, with

$$\bar{\Gamma}_{\rho\mu\nu} = \eta_{\rho\alpha}\bar{\Gamma}^{\alpha}_{\mu\nu} = h_{\rho(\mu,\nu)} - \frac{1}{2}h_{\mu\nu,\rho}, \tag{2.2.6}$$

we obtain the (all-lowered) Riemann tensor corresponding to the perturbed metric $\bar{g}$ as,

$$\bar{R}_{\rho\sigma\mu\nu} = \eta_{\rho\alpha}\bar{R}^{\alpha}_{\ \sigma\mu\nu} = -2\eta_{\rho\alpha}\bar{\Gamma}^{\alpha}_{\sigma[\mu,\nu]} = -2h_{[\mu[\rho,\sigma]\nu]}. \tag{2.2.7}$$

---

[5]Instead of studying the stability of the Minkowski spacetime, this theory is infact used as an important theory in its own right to describe astrophysical situations when the full spacetime metric $\bar{g}$ deviates only slightly from the flat one η, for example, to describe the gravitational field of the solar system, where $\|h_{\mu\nu}\| \sim 10^{-6}$ [8].

[6]It is to be noted that $\bar{g}^{\mu\nu} = \eta^{\mu\nu} - h^{\mu\nu}$ is the full perturbed inverse metric, as opposed to $\eta^{\mu\alpha}\bar{g}_{\alpha\beta}\eta^{\beta\nu}$, and this will be the only exception to the notational convention adopted in this section.

We prefer to write down the linearized Riemann tensor in this form (2.2.7) to make the symmetries in its indices obvious. The linearized Ricci tensor $\bar{R}_{\mu\nu} = \eta^{\rho\sigma}\bar{R}_{\rho\mu\sigma\nu}$ then becomes,

$$\bar{R}_{\mu\nu} = \frac{\eta^{\rho\sigma}}{2}\left(-h_{\rho\sigma,\nu\mu} + h_{\rho\nu,\sigma\mu} + h_{\mu\sigma,\nu\rho} - h_{\mu\nu,\sigma\rho}\right) = h^{\rho}_{(\mu,\nu)\rho} - \frac{1}{2}h_{,\mu\nu} - \frac{1}{2}\Box h_{\mu\nu}, \qquad (2.2.8)$$

where we have introduced $h \equiv \eta^{\rho\sigma}h_{\rho\sigma}$ and $\Box \equiv \partial^{\sigma}\partial_{\sigma} = -\partial_t^2 + \partial_x^2 + \partial_y^2 + \partial_z^2$, the flat-space d'Alembertian[7]. The linearized Ricci scalar $\bar{R} = \eta^{\mu\nu}\bar{R}_{\mu\nu}$ is of course,

$$\bar{R} = h^{\mu\nu}_{,\mu\nu} - \Box h, \qquad (2.2.9)$$

and the linearized Einstein tensor corresponding to the perturbed metric $\bar{g}$ is,

$$\bar{G}_{\mu\nu} = \bar{R}_{\mu\nu} - \frac{1}{2}\eta_{\mu\nu}\bar{R} = h^{\rho}_{(\mu,\nu)\rho} - \frac{1}{2}h_{,\mu\nu} - \frac{1}{2}\Box h_{\mu\nu} - \frac{1}{2}\eta_{\mu\nu}h^{\rho\sigma}_{,\rho\sigma} + \frac{1}{2}\eta_{\mu\nu}\Box h. \qquad (2.2.10)$$

Finally, the linearized Einstein's equations $\bar{G}_{\mu\nu} = \bar{T}_{\mu\nu}$ for the perturbed metric $\bar{g}$ are,

$$h^{\rho}_{\mu,\nu\rho} + h^{\rho}_{\nu,\mu\rho} - h_{,\mu\nu} - \Box h_{\mu\nu} - \eta_{\mu\nu}h^{\rho\sigma}_{,\rho\sigma} + \eta_{\mu\nu}\Box h = 2\bar{T}_{\mu\nu}, \qquad (2.2.11)$$

where $\bar{T}$ is the energy-momentum tensor that generates the perturbation h. In particular, the *vacuum* linearized EFEs (i.e., for $\bar{T} = 0$) are simply $\bar{R}_{\mu\nu} = 0$,

$$h^{\rho}_{(\mu,\nu)\rho} - \frac{1}{2}h_{,\mu\nu} - \frac{1}{2}\Box h_{\mu\nu} = 0. \qquad (2.2.12)$$

Further, it can generally (non-vacuum cases also) be seen by direct computation that the contracted Bianchi identity reduces to [172],

$$\bar{G}_{\mu\nu}{}^{;\nu} = 0, \qquad (2.2.13)$$

and so, with equation 2.2.11, it is evident that the conservation equations become,

$$\bar{T}_{\mu\nu}{}^{;\nu} = 0. \qquad (2.2.14)$$

The linearized equations (2.2.11) form a system of ten second-order, linear partial differential equations for ten variables h in terms of the sources $\bar{T}$. It is tempting to try to solve for h but this is not yet possible since a choice of coordinate system has not yet been made; It is not hard to see why this would be important. Deviations h in the background Minkowski metric η could arise because the spacetime is genuinely perturbed due, for example, to the propagation of a small amount matter or of a weak-electromagnetic or -gravitational wave in it. Alternatively, under a small coordinate transformation of the sort, $x \to x + \xi$ (with $\|\xi^{\mu}\| \ll 1$), the flat-space metric tensor would transform in general as, $\eta \to \eta + h$, causing the metric to appear to be perturbed. Furthermore, there may be other coordinate systems in which the metric can still be written as the Minkowski metric plus a small perturbation, but the perturbation will be different. Now, since the description of the equations of motion of gravity is independent of the choice of coordinate system, we recognise such coordinate transformations (or equivalently, infinitesimal diffeomorphisms) as being a gauge symmetry of the linearized theory [8, 10, 167, 172]. We will address this issue and demonstrate a popular gauge-fixing choice in the following subsection.

---

[7]Since we use η to raise and lower indices, remember that spatial indices can be written either in the 'up' position or the 'down' position without changing the value of a quantity: $f^x = f_x$. Raising or lowering a time index, by contrast, switches sign: $f^t = -f_t$.

2.2.1 Gauge Considerations

We have indicated already that there is a certain ambiguity in identifying the perturbed spacetime with the background spacetime, and this ambiguity may be expressed in terms of a gauge transformation. Now, since a gauge theory represents physically distinct states of a dynamical system as an equivalence class of detailed local field configurations, with any two such configurations in the same equivalence class being related by a gauge transformation, most of the quantitative physical predictions of a gauge theory can only be obtained under a coherent prescription for suppressing or ignoring these unphysical degrees of freedom. This prescription involves making a gauge choice, and a quick description of an example for the same follows.

Although the default notation in this thesis is the elegant one of Carroll [167] (and Schutz [171], except for the placement of the indices, which there is always north by south-east for two-tensors for example), where accents are placed on the indices, we depart from convention in this subsection[8]. Let us consider two coordinate systems x^μ and x'^μ, that differ from each other by a very small amount ξ^μ as,

$$x'^\mu = x^\mu + \xi^\mu(x), \quad \|\xi^\mu\| \ll 1. \tag{2.2.15}$$

Then, inverting the above to linear order in $\boldsymbol{\xi}$ as $x^\mu = x'^\mu - \xi^\mu(x')$, we have the inverse Jacobian,

$$\frac{\partial x^\alpha}{\partial x'^\mu} = \delta^\alpha_{\ \mu} - \xi^\alpha_{\ ,\mu}. \tag{2.2.16}$$

Armed with this Jacobian, we can now find the components of the metric $\bar{g} = \eta + h$ in these two systems to be related as,

$$\bar{g}'_{\mu\nu} = \frac{\partial x^\alpha}{\partial x'^\mu} \frac{\partial x^\beta}{\partial x'^\nu} \bar{g}_{\alpha\beta} = \left(\delta^\alpha_{\ \mu} - \xi^\alpha_{\ ,\mu}\right)\left(\delta^\beta_{\ \nu} - \xi^\beta_{\ ,\nu}\right)\left[\eta_{\alpha\beta} + h_{\alpha\beta}\right],$$
$$\approx \bar{g}_{\mu\nu} - 2\xi_{(\mu,\nu)}. \tag{2.2.17}$$

Subtracting an η from both sides above, we can find the change in the metric perturbation h due to the (small[9]) coordinate transformation given in equation 2.2.15 to be,

$$\Delta h_{\mu\nu} = h'_{\mu\nu} - h_{\mu\nu} = -2\xi_{(\mu,\nu)}, \tag{2.2.18}$$

where we have defined $h' = \bar{g}' - \eta$. It must be noted that to within the precision of the linearized theory, the functional forms of all other scalars, vectors and tensors undergo no changes (see for example Box 18.2 of [8]). Clearly, since perturbing *coordinate systems* should not affect physics or more concretely the spacetime geometry, we immediately recognize that a change of the form,

$$h_{\mu\nu} \rightarrow h_{\mu\nu} - 2\xi_{(\mu,\nu)} \tag{2.2.19}$$

is simply a gauge transformation. Note that this gauge transformation can be re-expressed in its more familiar form using a Lie-derivative as,

$$h_{\mu\nu} \rightarrow h_{\mu\nu} + \pounds_\xi \eta_{\mu\nu}. \tag{2.2.20}$$

---

[8]In particular, equation 2.2.17 looks ridiculous/incomprehensible in the Schutz-Carroll notation.
[9]Small enough to leave $\|h'_{\mu\nu}\| \ll 1$.

See for example [10, 167, 172] for nice geometric interpretations of this equation. Now, it can be checked explicitly that although the metric and the associated Christoffel symbols transform under a small coordinate transformation (2.2.15), the Riemann tensor is left unchanged. Therefore, as expected, the linearized Einstein tensor and hence the linearized equations of motion are indeed invariant under a gravitational gauge transformation (2.2.19).

One way to cope with the ambiguity introduced due to gauge degeneracy is to simply choose a gauge. This, in GR, is achieved by fixing the coordinate system. A popular choice is the harmonic coordinate system,

$$\Box x^\mu = 0, \tag{2.2.21}$$

which reduces to,

$$0 = \eta^{\rho\sigma}\partial_\rho\partial_\sigma x^\mu - \eta^{\rho\sigma}\Gamma^\lambda_{\rho\sigma}\partial_\lambda x^\mu = -\eta^{\rho\sigma}\Gamma^\lambda_{\rho\sigma} = -\eta^{\rho\sigma}\eta^{\lambda\delta}\left(h_{\delta(\rho,\sigma)} - \frac{1}{2}h_{\rho\sigma,\delta}\right); \tag{2.2.22}$$

that is,

$$h^{\lambda\rho}{}_{,\rho} - \frac{1}{2}h^{,\lambda} = 0. \tag{2.2.23}$$

This condition is known as the Lorentz gauge, and goes by many other names including the Einstein gauge, Hilbert gauge, de Donder gauge, and Fock gauge.

It is worth noting that in flat space, Cartesian coordinates, in which $\Gamma^\rho_{\mu\nu} = 0$ (and therefore trivially satisfy equation 2.2.22), are harmonic coordinates.

Now, in this gauge, the linearized Einstein field equations 2.2.11 simplify to,

$$\Box h_{\mu\nu} - \frac{1}{2}\eta_{\mu\nu}\Box h = -2\bar{T}_{\mu\nu}. \tag{2.2.24}$$

The linearized equations of motion (2.2.24) along with the gauge condition (2.2.23) uniquely determine the evolution of a perturbation of the Minkowski spacetime. Also, the vacuum $(\bar{T}_{\mu\nu} = 0)$ linearized equations $\bar{R}_{\mu\nu} = 0$ in particular, in this choice of gauge, become simply,

$$\Box h_{\mu\nu} = 0. \tag{2.2.25}$$

2.2.2 An Alternative Viewpoint of this Linearized Theory

This linearized theory can be thought of as describing the theory of a symmetric two-tensor field h propagating[10] in vacuum i.e., on a flat background spacetime [10, 167]. This theory is Lorentz invariant in the sense of special relativity i.e., h transforms as a tensor under Lorentz transformations, $x^{\mu'} = \Lambda^{\mu'}_\mu x^\mu$, as[11],

$$h_{\mu'\nu'} = \Lambda^\mu_{\mu'}h_{\mu\nu}\Lambda^\nu_{\nu'}. \tag{2.2.26}$$

---

[10]It is to be noted that the metric perturbation h encapsulates gravitational waves, but contains additional, non-radiative degrees of freedom as well.

[11]However, under careful scrutiny, one finds that h does not actually transform as a tensor under general coordinate transformations [168], and things are as they should be.

Furthermore, the Einstein tensor $\bar{G}$ corresponding to the perturbed metric (2.2.10) can be obtained by varying the Fierz-Pauli Lagrangian given below w.r.t. $h_{\mu\nu}$ [167, 172, 173],

$$L = \frac{1}{4}h_{\mu\nu,\sigma}h^{\mu\nu,\sigma} - \frac{1}{2}h_{\mu\nu,\sigma}h^{\sigma\nu,\mu} - \frac{1}{4}h_{\sigma}h^{,\sigma} + \frac{1}{2}h_{,\sigma}h^{\nu\sigma}{}_{,\nu}, \tag{2.2.27}$$

lending credibility to this viewpoint.

2.2.3 The Trace-Reversed Perturbation Variable

As is now standard, we can introduce the trace-reversed perturbation variable $\bar{h}$ as,

$$\bar{h}_{\mu\nu} = h_{\mu\nu} - \frac{1}{2}\eta_{\mu\nu}h. \tag{2.2.28}$$

This simplifies considerably the form of the linearized EFEs (2.2.11), which contains six terms on the left. That is, by substituting [12] $h_{\mu\nu} = \bar{h}_{\mu\nu} - \frac{1}{2}\eta_{\mu\nu}\bar{h}$ in equation 2.2.11, we obtain,

$$\bar{h}^{\rho}{}_{\mu,\nu\rho} + \bar{h}^{\rho}{}_{\nu,\mu\rho} - \Box\bar{h}_{\mu\nu} - \eta_{\mu\nu}\bar{h}^{\rho\sigma}{}_{,\rho\sigma} = 2\bar{T}_{\mu\nu}. \tag{2.2.29}$$

Further, we see that the gauge transformation (2.2.18) in terms of this variable is,

$$\begin{aligned} \bar{h}'_{\mu\nu} &= h'_{\mu\nu} - \frac{1}{2}\eta_{\mu\nu}h', \\ &= h_{\mu\nu} - 2\xi_{(\mu,\nu)} - \frac{1}{2}\eta_{\mu\nu}h + \eta_{\mu\nu}\xi^{\rho}{}_{,\rho}. \end{aligned} \tag{2.2.30}$$

This is just,

$$\Delta\bar{h}_{\mu\nu} = \bar{h}'_{\mu\nu} - \bar{h}_{\mu\nu} = -2\xi_{(\mu,\nu)} + \eta_{\mu\nu}\xi^{\rho}{}_{,\rho}, \tag{2.2.31}$$

and the connection to the Lorentz gauge of electromagnetism also looks much more suggestive when equation 2.2.23 is rewritten in terms of $\bar{h}$ as [13],

$$\bar{h}^{\mu\alpha}{}_{,\alpha} = 0. \tag{2.2.32}$$

Now, in this gauge, the full linearized field equations (2.2.29) become,

$$\Box\bar{h}_{\mu\nu} = -2\bar{T}_{\mu\nu}, \tag{2.2.33}$$

from which the vacuum equations are seen to be,

$$\Box\bar{h}_{\mu\nu} = 0. \tag{2.2.34}$$

For completeness, let us also suppose we have on our hands a metric perturbation $\bar{h}$ does not satisfy the Lorentz gauge (2.2.32), then we can always rewrite it as $\bar{h}'$ so that now it does,

$$0 = \bar{h}'^{\mu\alpha}{}_{,\alpha} = \bar{h}^{\mu\alpha}{}_{,\alpha} - \Box\xi^{\mu} - \xi^{\alpha,\mu}{}_{,\alpha} + \xi^{\rho,\alpha}{}_{,\rho}. \tag{2.2.35}$$

---

[12] From equation 2.2.28, it is clear that $\bar{h} = \eta^{\mu\nu}\bar{h}_{\mu\nu} = -h$ since $\eta^{\mu\nu}\eta_{\mu\nu} = 4$ in four-dimensions.

[13] Remember that in electromagnetism the field strength $F_{\mu\nu} = -2A_{(\mu,\nu)}$ is left unchanged under the gauge transformation $A_{\mu} \to A_{\mu} + \partial_{\mu}\lambda$, and a popular gauge choice is the Lorentz gauge, $A^{\alpha}{}_{,\alpha} = 0$.

That is, we can put any metric perturbation into the Lorentz gauge by performing an infinitesimal coordinate transformation using $\boldsymbol{\xi}$ which satisfies,

$$\Box \xi^\mu = \bar{h}^{\mu\alpha}{}_{,\alpha}. \tag{2.2.36}$$

The amount of gauge freedom has now been reduced from four freely-specifiable functions of four variables to four functions of four variables that satisfy the homogeneous wave equation $\Box \xi^\mu = 0$, or equivalently, to eight freely-specifiable functions of three variables on a Cauchy hypersurface[14][168].

We have now derived the linearized equations of motion for an arbitrary metric perturbation of the Minkowski solution, and have also discussed associated gauge-related aspects. We will however not use these equations to find explicit solutions here. One can look at any standard treatment [8, 167, 168] to obtain gravitational waves propagating on the Minkowski background from these equations, for example. However, our primary aim here was to set up the framework in which to study the linear stability of the Minkowski spacetime, which we have now done, and we direct the reader to the see the works of [165, 166] for a proof of the same; as mentioned earlier, a description of this analysis is beyond the scope of this thesis. We will now develop quickly the linearized theory on a curved background spacetime following [10, 168, 172], and see that many of the results from this section carry over with slight modifications. We will again not study the most general solutions to the linearized equations, instead choosing to restrict to those that are harmonic in nature, i.e. we will consider in particular linear-mode stability. A mode stability analysis of a stationary solution of the vacuum EFEs is typically sufficient for most astrophysical purposes. Of course, a full linear stability analysis is far more powerful and equally important, but the inherent difficulty involved dissuades one from attempting to study these aspects in full generality for most spacetimes.

2.3 Perturbation Theory of Curved Vacuum Spacetimes[15]

Having set up the perturbation theory of the Minkowski spacetime, we will consider now small metric perturbations $\boldsymbol{h}$ around arbitrary stationary solutions $\boldsymbol{g}$ such that,

$$\bar{g}_{\mu\nu} = g_{\mu\nu} + h_{\mu\nu}, \quad \|h_{\mu\nu}\| \ll \|g_{\mu\nu}\|, \tag{2.3.1}$$

is also a solution of the field equations. It should be noted that this analysis inherently uses a coordinate system that allows the metric coefficients to be split as above. Now, due to the smallness of typical components of $\boldsymbol{h}$ relative to the components of the background $\boldsymbol{g}$, and since we want to set up the framework of a linearized theory, we can raise and lower indices with $\boldsymbol{g}$. Therefore, we can write immediately the inverse of the perturbed metric to leading order in the perturbation $\boldsymbol{h}$ as,

$$\bar{g}^{\mu\nu} = g^{\mu\nu} - h^{\mu\nu}, \tag{2.3.2}$$

---

[14]One can choose initial data for $\boldsymbol{\xi}$ and its normal derivative on any Cauchy hypersurface, and solve the corresponding initial value problem.

[15]This section is based on [10, 168].

where now $h^{\mu\nu} = g^{\mu\alpha}h_{\alpha\beta}g^{\beta\nu}$. Let us now look at the Christoffel symbols associated with the full metric $\bar{g}$,

$$
\begin{aligned}
\bar{\Gamma}^{\rho}_{\mu\nu} &= \frac{1}{2}\bar{g}^{\rho\alpha}\left(2\bar{g}_{\alpha(\mu,\nu)} - \bar{g}_{\mu\nu,\alpha}\right) = \frac{1}{2}\left(g^{\rho\alpha} - h^{\rho\alpha}\right)\left(2g_{\alpha(\mu,\nu)} + 2h_{\alpha(\mu,\nu)} - g_{\mu\nu,\alpha} - h_{\mu\nu,\alpha}\right), \\
&= \Gamma^{\rho}_{\mu\nu} + \frac{1}{2}g^{\rho\alpha}\left(2h_{\alpha(\mu,\nu)} - h_{\mu\nu,\alpha}\right) - \frac{1}{2}h^{\rho\alpha}\left(2g_{\alpha(\mu,\nu)} - g_{\mu\nu,\alpha}\right) + O(h^2), \\
&\approx \Gamma^{\rho}_{\mu\nu} + \frac{1}{2}g^{\rho\alpha}\left(2h_{\alpha(\mu,\nu)} - h_{\mu\nu,\alpha}\right) - \frac{1}{2}g^{\rho\beta}h_{\beta\sigma}g^{\sigma\alpha}\left(2g_{\alpha(\mu,\nu)} - g_{\mu\nu,\alpha}\right), \\
&\approx \Gamma^{\rho}_{\mu\nu} + \frac{1}{2}g^{\rho\alpha}\left(2h_{\alpha(\mu,\nu)} - h_{\mu\nu,\alpha}\right) - \frac{1}{2}g^{\rho\alpha}h_{\alpha\sigma}g^{\sigma\beta}\left(2g_{\beta(\mu,\nu)} - g_{\mu\nu,\beta}\right), \\
&\approx \Gamma^{\rho}_{\mu\nu} + \frac{1}{2}g^{\rho\alpha}\left(2h_{\alpha(\mu,\nu)} - h_{\mu\nu,\alpha}\right) - g^{\rho\alpha}h_{\alpha\sigma}\Gamma^{\sigma}_{\mu\nu}. \quad (2.3.3)
\end{aligned}
$$

Now, with the introduction of "$\nabla = {}_|$" to denote the covariant derivative relative to the background g following [8], we note that,

$$
\begin{aligned}
h_{\alpha\mu,\nu} &= h_{\alpha\mu|\nu} + \Gamma^{\sigma}_{\alpha\nu}h_{\sigma\mu} + \Gamma^{\sigma}_{\mu\nu}h_{\alpha\sigma}, \\
h_{\alpha\nu,\mu} &= h_{\alpha\nu|\mu} + \Gamma^{\sigma}_{\alpha\mu}h_{\sigma\nu} + \Gamma^{\sigma}_{\nu\mu}h_{\alpha\sigma}, \\
-h_{\mu\nu,\alpha} &= -h_{\mu\nu|\alpha} - \Gamma^{\sigma}_{\mu\alpha}h_{\sigma\nu} - \Gamma^{\sigma}_{\nu\alpha}h_{\mu\sigma},
\end{aligned} \quad (2.3.4)
$$

and so, we can write,

$$
2h_{\alpha(\mu,\nu)} - h_{\mu\nu,\alpha} = 2h_{\alpha(\mu|\nu)} - h_{\mu\nu|\alpha} + 2h_{\alpha\sigma}\Gamma^{\sigma}_{\mu\nu}. \quad (2.3.5)
$$

Therefore, the first-order correction $\boldsymbol{\delta\Gamma}$ to the Christoffel symbols due to the metric perturbation can be expressed elegantly from equation 2.3.3 as,

$$
\delta\Gamma_{\rho\mu\nu} \equiv \bar{\Gamma}_{\rho\mu\nu} - \Gamma_{\rho\mu\nu} = h_{\rho(\mu|\nu)} - \frac{1}{2}h_{\mu\nu|\rho}. \quad (2.3.6)
$$

It is to be noted that (as the bold-faced notation used above already suggests) $\boldsymbol{\delta\Gamma}$ is a genuine tensor.

Now, the derivation of the the linearized EFEs for $\boldsymbol{h}$ proceeds as before. Most equations from §2.2 continue to apply with the old background $\boldsymbol{\eta}$ being replaced by the new background $\boldsymbol{g}$, and with partial derivatives being replaced by covariant derivatives w.r.t. the background, as has been demonstrated in writing equation 2.3.6.

We can obtain the linearized Riemann tensor $\delta R_{\rho\sigma\mu\nu}$ by simply evaluating the perturbed Riemann tensor $\bar{R}_{\rho\sigma\mu\nu}$ (corresponding to the perturbed metric $\bar{g}$) in a coordinate system in which the background connections vanish $\Gamma^{\rho}_{\mu\nu} = 0$, so that $\nabla_a = \partial_a$, and[16],

$$
\bar{R}_{\rho\sigma\mu\nu} = R_{\rho\sigma\mu\nu} - \delta\Gamma_{\rho\sigma[\mu,\nu]} + \mathcal{O}(h^2). \quad (2.3.7)
$$

Then, keeping terms that are only linear in the perturbation, equation 2.3.7 for general coordinate systems, from the principle of general covariance, can be written as,

$$
\delta R_{\rho\sigma\mu\nu} \equiv \bar{R}_{\rho\sigma\mu\nu} - R_{\rho\sigma\mu\nu} = -2\delta\Gamma_{\rho\sigma[\mu|\nu]} = -2h_{[\mu[\rho|\sigma]\nu]} - h_{\rho\sigma|[\mu\nu]}. \quad (2.3.8)
$$

---

[16]The mileage that this approach gives can be seen simply as follows. The type of terms to be found in the perturbed Riemann (to linear order in the perturbation variable) are, $\bar{R} \sim \partial\bar{\Gamma} + \bar{\Gamma}\bar{\Gamma} \sim \partial\Gamma + \partial\boldsymbol{\delta\Gamma} + \Gamma\Gamma + (\boldsymbol{\delta\Gamma})\Gamma + \Gamma(\boldsymbol{\delta\Gamma}) \sim R + \partial\boldsymbol{\delta\Gamma} + (\boldsymbol{\delta\Gamma})\Gamma + \Gamma(\boldsymbol{\delta\Gamma})$. If we work in a coordinate system in which $\Gamma = 0$, then the last two terms simply drop out and we see immediately what the structure of the linearized Riemann $\boldsymbol{\delta R} \equiv \bar{\boldsymbol{R}} - \boldsymbol{R}$ must be. Also, one can see heuristically from equation 2.3.4 how $\partial\boldsymbol{\delta\Gamma} \to \boldsymbol{\nabla}\boldsymbol{\delta\Gamma}$ in general coordinate systems (see for example [74]).

Note that this last term on the R.H.S. above did not arise previously when we were writing the linearized EFEs around a flat backgrounds (i.e., for $g = \eta$) since partial derivatives commute. Now, we can find the linearized Ricci tensor $\delta R_{\mu\nu} = g^{\rho\sigma}\delta R_{\rho\mu\sigma\nu}$ and the linearised Ricci scalar $\delta R = g^{\mu\nu}\delta R_{\mu\nu}$ respectively to be,

$$\delta R_{\mu\nu} = h^{\rho}_{(\mu|\nu)\rho} - \frac{1}{2}h_{|\mu\nu} - \frac{1}{2}\Box_g h_{\mu\nu}, \text{ and } \delta R = h^{\mu\nu}_{|\mu\nu} - \Box_g h, \tag{2.3.9}$$

where in the above we have introduced $h \equiv g^{\rho\sigma}h_{\rho\sigma}$ and $\Box_g \equiv \nabla^{\sigma}\nabla_{\sigma}$. The *vacuum* linearized Einstein's equations, $\delta R_{\mu\nu} = 0$, are then given as (cf. equation 2.2.12),

$$h^{\rho}_{(\mu|\nu)\rho} - \frac{1}{2}h_{|\mu\nu} - \frac{1}{2}\Box_g h_{\mu\nu} = 0. \tag{2.3.10}$$

Now, as above (2.2.28), if we introduce the trace-reversed perturbation variable as,

$$\bar{h}_{\mu\nu} = h_{\mu\nu} - \frac{1}{2}g_{\mu\nu}h, \tag{2.3.11}$$

we can rewrite the vacuum linearized EFEs (2.3.10) as,

$$0 = 2\delta G_{\mu\nu} = \bar{h}^{\rho}_{\mu|\nu\rho} + \bar{h}^{\rho}_{\nu|\mu\rho} - \Box_g \bar{h}_{\mu\nu} - g_{\mu\nu}\bar{h}^{\rho\sigma}_{|\rho\sigma} + 2R_{\rho\nu\mu\sigma}\bar{h}^{\rho\sigma}. \tag{2.3.12}$$

On comparision with equation 2.2.29, we see the last term on the R.H.S. as arising due to the curvature of the background spacetime.

If we specialise the gauge-choice from the Lorentz gauge (which is also called transverse condition; compare with equation 2.2.32) and require further that the trace of the perturbation also vanish $\bar{h} = 0$, i.e. if we work in the transverse-traceless gauge,

$$\bar{h}^{\mu\alpha}_{|\alpha} = \bar{h} = 0, \tag{2.3.13}$$

the linearized vacuum EFEs (2.3.12) reduce to,

$$\Box_g \bar{h}_{\mu\nu} - 2R_{\rho\nu\mu\sigma}\bar{h}^{\rho\sigma} = 0. \tag{2.3.14}$$

2.3.1 Existence of the Transverse-Traceless Gauge

Under a small coordinate transformation (cf. equation 2.2.15),

$$x'^{\mu} = x^{\mu} + \xi^{\mu}(x), \quad \|\xi^{\mu}\| \ll 1, \tag{2.3.15}$$

the metric perturbation h and its trace h transform as,

$$h_{\mu\nu} \to h'_{\mu\nu} = h_{\mu\nu} - 2\xi_{(\mu|\nu)}, \tag{2.3.16}$$
$$h \to h' = h - 2\xi^{\mu}_{|\mu}.$$

Under this gauge transformation, the divergence of the trace-reversed perturbation variable transforms as [168],

$$\bar{h}'^{\mu\nu}_{|\mu} = \bar{h}^{\mu\nu}_{|\mu} - \Box_g \xi^{\nu}. \tag{2.3.17}$$

The condition that the gauge vector $\boldsymbol{\xi}$ must satisfy so a perturbation $\bar{h}$ that does not satisfy the transverse condition can be (gauge) transformed to another $\bar{h}'$ which does, i.e., $\bar{h}'^{\mu\nu}_{|\nu} = 0$, can be obtained from the equation above to be (cf. equation 2.2.36),

$$\Box_g \xi^\nu = \bar{h}^{\mu\nu}_{|\mu}. \tag{2.3.18}$$

Therefore, one must find a vector field $\boldsymbol{\xi}$ that satisfies equation 2.3.18 and (for tracelessness),

$$\xi^\mu_{|\mu} + \frac{\bar{h}}{2} = 0. \tag{2.3.19}$$

Again, one can choose initial data for $\boldsymbol{\xi}$ on any Cauchy hypersurface for which the quantity in equation 2.3.19 and also its normal derivative vanish.

2.3.2   Complications in Linear Stability Analyses

What we have shown thus far in this chapter can be summarized as follows[17] . Given a solution to the vacuum Einstein field equations $\boldsymbol{g}$, we can look for solutions $\bar{\boldsymbol{g}}$ that are 'close' to $\boldsymbol{g}$ in the space of solutions such that we may write $\bar{\boldsymbol{g}} = \boldsymbol{g} + \boldsymbol{h}$, with $\|\boldsymbol{h}\|/\|\boldsymbol{g}\| \ll 1$. To obtain such solutions $\bar{\boldsymbol{g}}$, which we can think of as being a one-parameter (or multi-parameter) family of exact solutions $\bar{\boldsymbol{g}}(\lambda)$, instead of solving the full non-linear vacuum EFEs,

$$\bar{G}[\bar{\boldsymbol{g}}(\lambda)] = 0, \tag{2.3.20}$$

we can solve a set of *linear* partial differential equations (cf. equation 2.3.14)

$$\mathscr{L}_{\boldsymbol{g}}(\boldsymbol{h}) = 0, \tag{2.3.21}$$

for the perturbation,

$$\boldsymbol{h} = \left.\frac{\mathrm{d}\bar{\boldsymbol{g}}}{\mathrm{d}\lambda}\right|_{\lambda=0}, \tag{2.3.22}$$

which may be obtained by linearizing the vacuum EFEs (2.3.20) around the 'background solution' $\boldsymbol{g}$ as [10],

$$\left.\frac{\mathrm{d}}{\mathrm{d}\lambda}\bar{G}[\bar{\boldsymbol{g}}(\lambda)]\right|_{\lambda=0} = \boldsymbol{0}. \tag{2.3.23}$$

Here λ is a parameter (or set of parameters) that measures the size of the perturbation in the sense that $\bar{\boldsymbol{g}}(\lambda)$ depends differentiably on λ and $\bar{\boldsymbol{g}}(0) = \boldsymbol{g}$. For further (geometric) intuition on what this linear operator $\mathscr{L}_{\boldsymbol{g}}$ is, it might be useful to see §2.9 below.

As derived in this setup, the existence of a one or many parameter family of solutions $\bar{\boldsymbol{g}}(\lambda)$ implies the existence of a solution of the linearized equation (2.3.21). However, the converse is not necessarily true always: the existence of a solution of the linearized equation does not necessarily imply the existence of a corresponding family of solutions, i.e., there may be spurious solutions of (2.3.21); this is a property of non-linear theories. Therefore, one needs to show the existence of exact solutions corresponding to a solution of (2.3.21) before a perturbation analysis can be applied reliably [10], and this is the crux of the issue of linear stability of a solution. More precisely, the system of non-linear vacuum EFEs (2.3.20) is said to be linearly stable at a

---

[17]We use different "language" here to summarize the material presented in the chapter previously, but the connection between the two should be evident; one can see for example [10] for a more careful description of the material presented in the current section.

solution g if every solution h of the linearized equation (2.3.21) is tangent to a curve of solutions to the original non-linear equations (see for example the discussion in [174, 175]).

Now, the existence of spurious solutions depends on the particular theory at hand and the background solution (with its symmetries and topology) about which linearization is carried out. If such so called "non-integrable" solutions exist, perturbation theory in some directions of solution space fails and we say that the theory is not linearly stable at that exact solution. Essentially, such spurious solutions cannot be obtained from the linearization of exact solutions. To be clear, the process of linearizing first the EFEs and then finding solutions to the linearized equations can yield results that are different from linearizing exact solutions that already solve the non-linear EFEs. This basically signals a breakdown of the first order perturbation theory, and can be precisely defined (see [174]). This happens because the linearized equations of the theory are not sufficient to constrain the linearized solutions: quadratic constraints on the linearized solutions, in the form of integrals (of 'Taub conserved quantities' for each Killing fields) arise [174]. In fact, the set of solutions to the EFEs form a smooth manifold except at solutions with infinitesimal symmetries and spacetimes with compact Cauchy hypersurfaces at which points there are conical singularities. If we introduce the second derivative k of the λ-parametrized metric family $\bar{g}$, a covariant two-tensor, as,

$$k = \frac{\mathrm{d}^2 \bar{g}}{\mathrm{d}\lambda^2}\bigg|_{\lambda=0}, \tag{2.3.24}$$

then it can be shown that, for the consistency of the perturbation theory, the linearized and second-order linearized forms of the EFEs relate h and k.

In fact, if the second-order linearized form of the EFEs has a solution k such that it does not impose a constraint on h, then the non-linear version of the field equations are linearly stable at g [174]; of course, one is required to ensure that higher-order linearized EFEs do not impose constraints on h either. In GR atleast, it is known that the constraint equations are related to the zeroes of the moment map and hence no additional constraints would arise from higher-order considerations beyond the second-order [176].

Now, since the vacuum linearized equations around a vacuum curved background (2.3.14) form a very complicated system of coupled partial differential equations, for the reasons discussed in this section, perturbation analyses have been successful only in restricted settings e.g., when the background metric has a great deal of symmetry or possesses other simplifying properties. Even in these cases, a direct assault on equation 2.3.14 has not typically yielded great dividends. However, after a tremendous amount of effort, the linear stability of the Minkowski spacetime [165] and, very recently, the Schwarzschild spacetime [112] have been shown. Further, it is believed that all asymptotically-flat background spacetimes are linearly stable against asymptotically-flat perturbations. We will not go into a description of these analyses since these are beyond the scope of this thesis. For a detailed account on linearization stability in general relativity, one may see [177].

Instead now we will enter into a discussion of linear mode stability of *stationary* spacetimes, which has the implication that we will only be interested in the class of solutions to the linearized EFEs (2.3.10) that have a harmonic time dependence, i.e. we can write,

$$\boldsymbol{h}(t, r, \theta, \phi) = \mathrm{e}^{\mathrm{i}\omega t}\tilde{\boldsymbol{h}}(r, \theta, \phi). \tag{2.3.25}$$

Here ω is a fixed number, and as we shall see below, takes complex values. A mode stability analysis, although far less powerful that a full linear stability analysis, is very useful since (a) it is typically not as intractable, and (b) it is reasonably indicative of the linear stability of the solution: for example, if even a single solution of the form given in equation 2.3.25 with $\mathrm{Im}(\omega) < 0$ is found (a 'diverging' mode), then one can conclude immediately that the background solution is not linearly stable. Therefore, a mode stability analysis suffices to prove linear *instability*. We will discuss the differences between a mode stability analysis and a full linear stability analysis in §2.6 in brief.

We will start now with a detailed discussion of the linear mode stability of the Schwarzschild black hole solution to give the reader a flavour of what it entails, before we set up the same for the Kerr spacetime. Eventually, we will discuss our results, reported in [71], on the mode stability of a Kerr superspinar in §2.5.

2.4 Mode Stability of the Schwarzschild Solution[18]

The Schwarzschild metric g_{M} is a one-parameter family of solutions of the vacuum EFEs (2.1.2), and is given in Schwarzschild coordinates (t, r, θ, ϕ) as [1],

$$\mathrm{d}s^2 = -\left(1 - \frac{2M}{r}\right)\mathrm{d}t^2 + \left(1 - \frac{2M}{r}\right)^{-1}\mathrm{d}r^2 + r^2\left(\mathrm{d}\theta^2 + \sin^2\theta\,\mathrm{d}\phi^2\right).$$

This metric contains a genuine curvature singularity at $r = 0$, which can be seen from the divergence at this location of curvature invariants (under diffeomorphisms) like the Kretschmann scalar $\mathscr{K} = R^{\rho\mu\nu\sigma}R_{\rho\mu\nu\sigma}$ which, in Geometrized units $8\pi\mathscr{G} = c = 1$, for the current context yields [178],

$$\mathscr{K} = \frac{3M^2}{4\pi^2 r^6}. \tag{2.4.1}$$

This metric also possesses an event horizon, whose location is obtained from the condition of vanishing null expansion, i.e., at the zero of g_{rr}^{-1}, which occurs at $r = 2M$. Therefore, this metric describes the geometry of a static black hole.

Because of the spherical symmetry of the Schwarzschild background, the linearized field equations (2.3.21) for the perturbation $\boldsymbol{h}$ are, schematically, in the form of a rotationally-invariant differential operator $\mathscr{L}_{\mathrm{Schw}}$ acting on $\boldsymbol{h}$ equals to zero (more generally, it is set equal to the source terms $\bar{\boldsymbol{T}}$ [179]). We can therefore separate out the angular variables of the linearized equations (2.3.12) for this background spacetime. However, a naïve deomposition into a θ, ϕ-dependent function and a t, r-dependent function for each of the ten metric components $h_{\mu\nu}$ does not work [56, 74, 179], as we will see below, since the metric perturbation $\boldsymbol{h}$ transforms as a tensor under rotations of the two-sphere spanned by $\left(\partial_\theta, \partial_\phi\right)$.

In particular, the metric perturbation components h_{tt}, h_{tr}, and h_{rr} transform as independent scalars under rotations, and can each therefore be expanded as a sum of scalar spherical harmonics $Y_{lm}(\theta, \phi)$. For example, we could write h_{tt} as (see for example [180]),

$$h_{tt}(t, r, \theta, \phi) = \sum_{l,m} H_{0lm}(t, r)Y_{lm}(\theta, \phi). \tag{2.4.2}$$

---

[18]We have drawn from the seminal papers of [56, 57, 61, 179] and from the excellent modern review articles of [27, 73, 74].

Next, $\left(h_{t\theta}, h_{t\phi}\right)$ and $\left(h_{r\theta}, h_{r\phi}\right)$ transform as components of two-vectors, and can be expanded in terms of the fundamental vector spherical harmonics $\boldsymbol{V^1}$ and $\boldsymbol{V^2}$, which are defined as [56],

$$\left(V^1_{lm}\right)_a = (Y_{lm})_{;a} = \frac{\partial Y_{lm}}{\partial x^a}, \quad \left(V^2_{lm}\right)_a = \epsilon_a^{\ b} (Y_{lm})_{;b} = \epsilon_{ac}\gamma^{cb}\frac{\partial Y_{lm}}{\partial x^b}. \tag{2.4.3}$$

In the above, the space-time indices a, b, and c take values 2 or 3 (corresponding to the angular variables $x^2 = \theta$ and $x^3 = \phi$ respectively), γ is the metric on the two-sphere of unit-radius, ϵ is the totally antisymmetric tensor (Levi-Civita tensor or volume form) in two dimensions [167], i.e. $\epsilon_{ab} = \sin\theta \begin{bmatrix} 0 & -1 \\ 1 & 0 \end{bmatrix}$, and the covariant derivatives are to be taken on the two-sphere.

Finally, $h_{\theta\theta}, h_{\theta\phi}$ and $h_{\phi\phi}$ transform as components of a 2×2 tensor, and can be expanded in terms of the three fundamental two-tensor spherical harmonics $\boldsymbol{T^1}, \boldsymbol{T^2}$, and $\boldsymbol{T^3}$, which are [56],

$$\left(T^1_{lm}\right)_{ab} = (Y_{lm})_{;ab}, \quad \left(T^2_{lm}\right)_{ab} = Y_{lm}\gamma_{ab}, \quad \left(T^3_{lm}\right)_{ab} = \frac{1}{2}\left(\epsilon_a^{\ c}(Y_{lm})_{;cb} + \epsilon_b^{\ c}(Y_{lm})_{;ca}\right). \tag{2.4.4}$$

Further, since the background metric is also invariant against space inversions i.e., under the transformation $(\theta, \phi) \rightarrow (\pi - \theta, \pi + \phi)$, we expect naturally that the perturbation equations do not mix modes that transform differently under space inversions, i.e. modes of different parity. Therefore, an examination of the parity of the tensor spherical harmonics listed above becomes necessary. From the definition of the scalar spherical harmonics, evidently under such an inversion, we obtain $Y_{lm} \rightarrow (-1)^l Y_{lm}$. Since the covariant derivative of a function preserves parity, and a multiplication with ϵ inverts it [74], we can see that $\boldsymbol{V^1}, \boldsymbol{T^1}$, and $\boldsymbol{T^2}$ transform with a factor of $(-1)^l$ under space inversions, similar to the Y, and $\boldsymbol{V^2}$ and $\boldsymbol{T^3}$ transform with a factor of $(-1)^{l+1}$. It is useful therefore to categorize these perturbations along lines of parity, following [63], as being polar $\left[(-1)^l\right]$ and axial $\left[(-1)^{l+1}\right]$ perturbations. An important (physical) distinction between these two types of perturbations is also pointed out there: axial perturbations impart a differential rotation to the black hole, while polar perturbations do not. Of course, any of these tensor spherical harmonics $Y, \boldsymbol{V}, \boldsymbol{T}$ can be multiplied by arbitrary functions of t and r, without changing its transformation properties under a rotation.

To summarize, $\boldsymbol{h}$ can be expanded in tensor spherical harmonics as [56],

$$\boldsymbol{h} = \sum_{l,m}\left\{H_0 Y_{lm} + H_1 Y_{lm} + H_2 Y_{lm} + h_0\left(V^1_{lm} + V^2_{lm}\right) + h_1\left(V^1_{lm} + V^2_{lm}\right) + GT^1_{lm} + KT^2_{lm} + h_2 T^3_{lm}\right\}. \tag{2.4.5}$$

In the above we have, following the Regge-Wheeler (RW) naming convention [56], introduced eight coefficient functions $H_0, H_1, H_2, h_0, h_1, h_2, G, K$, each of which are functions only of t and r. However, there will be a set of coefficient functions for each (l, m)-pair, and we have simply omitted these subscripts for brevity.

Pictorially, when split along parity-lines into a polar and an axial piece, we can write,

$$
h = h^{\mathrm{P}} + h^{\mathrm{A}} =
\begin{bmatrix}
\boxed{H_0 Y} & \boxed{H_1 Y} & \boxed{h_0 V^1} \\
\boxed{*} & \boxed{H_2 Y} & \boxed{h_1 V^1} \\
\boxed{*} & \boxed{*} & \boxed{GT^1 + KT^2}
\end{bmatrix}
+
\begin{bmatrix}
\boxed{0} & \boxed{0} & \boxed{h_0 V^2} \\
\boxed{*} & \boxed{0} & \boxed{h_1 V^2} \\
\boxed{*} & \boxed{*} & \boxed{h_2 T^3}
\end{bmatrix},
$$

and in the above, asterisks denote components that are determined by symmetry.

Putting everything in, the general form of a polar metric perturbation h^{P}, of angular momentum l and its projection on the z-axis m, is [56],

$$
h^{\mathrm{P}}_{\mu\nu} =
\begin{bmatrix}
\left(1 - \frac{2M}{r}\right) H_0 Y & H_1 Y & h_0 \frac{\partial}{\partial \theta} Y & h_0 \frac{\partial}{\partial \phi} Y \\
* & \left(1 - \frac{2M}{r}\right)^{-1} H_2 Y & h_1 \frac{\partial}{\partial \theta} Y & h_1 \frac{\partial}{\partial \phi} Y \\
* & * & r^2 \left[K + G \frac{\partial^2}{\partial \theta^2} \right] Y & r^2 G \left[\frac{\partial^2}{\partial\theta\partial\phi} - \cot\theta \frac{\partial}{\partial\phi} \right] Y \\
* & * & * & r^2 \sin^2\theta \left[K + G \left(\cot\theta \frac{\partial}{\partial\theta} + \frac{1}{\sin^2\theta} \frac{\partial^2}{\partial\phi^2} \right) \right] Y
\end{bmatrix},
$$
$$(2.4.6)$$

and we have suppressed in the above the l, m subscripts of the scalar spherical harmonics Y as well, for simplicity. Similarly, for an axial metric perturbation h^{A}, we can write [56],

$$
h^{\mathrm{A}}_{\mu\nu} =
\begin{bmatrix}
0 & 0 & -h_0 \frac{1}{\sin\theta} \frac{\partial}{\partial\phi} Y & h_0 \sin\theta \frac{\partial}{\partial\theta} Y \\
* & 0 & -h_1 \frac{1}{\sin\theta} \frac{\partial}{\partial\phi} Y & h_1 \sin\theta \frac{\partial}{\partial\theta} Y \\
* & * & h_2 \frac{1}{\sin\theta} \left[\frac{\partial^2}{\partial\theta\partial\phi} - \cot\theta \frac{\partial}{\partial\phi} \right] Y & \frac{1}{2} h_2 \sin\theta \left[-\frac{\partial^2}{\partial^2\theta} + \left(\cot\theta \frac{\partial}{\partial\theta} + \frac{1}{\sin^2\theta} \frac{\partial^2}{\partial^2\phi} \right) \right] Y \\
* & * & * & -h_2 \sin\theta \left[\frac{\partial^2}{\partial\theta\partial\phi} - \cot\theta \frac{\partial}{\partial\phi} \right] Y
\end{bmatrix}.
$$
$$(2.4.7)$$

We are again at the point where a gauge choice must be made before we attempt to solve the linearized EFEs for the metric perturbations, or equivalently for the RW coefficient functions. It must be noted that the gauge of the background spacetime is essentially fixed, since we have decided to use the Schwarzschild metric *in Schwarzschild coordinates*. However, once the background metric is perturbed, the gauge choice can be modified to first order in the perturbation, thereby affecting only the first-order metric perturbations, but not the background metric. In particular, we want this infinitesimal gauge transformation to have the property that it conserves (a) the decomposition into tensor spherical harmonics, and (b) the separation into axial and polar metric perturbations. Since the gauge transformation given in equation 2.2.15 can be performed on any individual partial wave, one gauge vector (cf. equation 2.2.15) must be constructed so that it is axial under rotations, and another that transforms as a polar vector must be found. The Regge-Wheeler (RW) gauge [56] is a particularly convenient choice (for both axial and polar perturbations) here since it allows one to eliminate

terms that have the highest derivatives in the angles (θ, ϕ), and is imposed by requiring (see also [74]),

$$\frac{\partial}{\partial \theta}(\sin \theta h_{t\theta}) = -\frac{\partial}{\partial \phi}\left(\frac{1}{\sin \theta}h_{t\phi}\right), \quad h_{\theta\phi} = 0,$$

$$\frac{\partial}{\partial \theta}(\sin \theta h_{r\theta}) = -\frac{\partial}{\partial \phi}\left(\frac{1}{\sin \theta}h_{r\phi}\right), \quad h_{\phi\phi} = \sin^2 \theta h_{\theta\theta}. \qquad (2.4.8)$$

For axial perturbations (2.4.7), this means choosing the coefficient function $h_2(t, r)$ to be vanishing. For the polar perturbations, we can set $h_0(t, r) = h_1(t, r) = G(t, r) = 0$ (see [56] for details and also the excellent table I of [179]).

The equations of motion for the coefficient functions can be derived for the different parity perturbations separately, and we now quickly discuss the result of inserting the the axial perturbations (2.4.15) in the linearized EFEs derived earlier,

$$\delta R_{\mu\nu} = 2\delta\Gamma^{\beta}_{\mu[\nu\,|\beta]} = 0. \qquad (2.4.9)$$

For the axial case, of the ten linearized EFEs, some are satisfied trivially, and only three non-trivial ones remain: the $\delta R_{23}, \delta R_{13}, \delta R_{03}$ equations, in two variables h_0 and h_1 [74]. However, there is some redundancy in this system of equations and it turns out that the last of these three equations may be derived from the other two. We can therefore combine the remaining two equations to eliminate h_0 and obtain a single second-order equation for h_1 as [74],

$$\frac{\partial^2 \Psi^{\mathrm{A}}}{\partial t^2} - \frac{\partial^2 \Psi^{\mathrm{A}}}{\partial r_*^2} + \left(1 - \frac{2M}{r}\right)\left[\frac{l(l+1)}{r^2} - \frac{6M}{r^3}\right]\Psi^{\mathrm{A}} = 0, \qquad (2.4.10)$$

where we have introduced the axial perturbation variable Ψ^{A} as,

$$\Psi^{\mathrm{A}}(t, r) = \left(1 - \frac{2M}{r}\right)\frac{h_1(t, r)}{r}, \qquad (2.4.11)$$

and r_* is the "tortoise" radial coordinate, which ranges from $-\infty$ to $+\infty$, corresponding to the range of r from $2M$ to ∞, and is defined as,

$$\frac{r_*}{2M} = \frac{r}{2M} + \log\left(\frac{r}{2M} - 1\right). \qquad (2.4.12)$$

This radial coordinate is useful since it sends the coordinate singularity of the Schwarzschild metric in the Schwarzschild coordinates, which is at $r = 2M$ to $r_* = -\infty$. Also, we note that the eliminated coefficient function h_0 can be recovered from [180],

$$\frac{\partial h_0}{\partial t} = \frac{\partial}{\partial r_*}\left(r_* \Psi^{\mathrm{A}}\right). \qquad (2.4.13)$$

The time-dependent linearized EFEs for the polar perturbations in this gauge (2.4.6) can also be recast into a form akin to equation 2.4.10, and we will leave the reader to see for example [180] for further details.

We have now successfully separated out the angular dependence of the perturbations from the functional part that depends on the other coordinates, and the perturbation equations (2.4.10) now evidently only involve partial derivatives t and r.

2.4.1   Time-Independent Linearized Perturbation Equations and Quasi-Normal Modes

The general linearized equations given in equation 2.4.10 and its equivalent for the polar metric perturbations (see equation 94 of [180]) describe the response of the Schwarzschild black hole to external metric perturbations, and the time evolution of any initial perturbation can be determined by simply integrating them numerically. However, since we would like to study properties intrinsic to the black hole spacetime itself, rather than the effect of a specific perturbation, we are immediately inclined to look for and study 'fundamental vibrational modes' of the black hole. Indeed since in addition to the background spacetime being spherically symmetric and invariant under spatial reflections, it is also time independent, we can therefore look for solutions to the perturbation equations of fixed frequency ω; i.e., we can restrict in particular to metric perturbations that exhibit a harmonic time behaviour, $\boldsymbol{h}(t, r, \theta, \phi) = e^{i\omega t} \tilde{\boldsymbol{h}}(r, \theta, \phi)$. This means that we can variable-separate each of coefficient functions introduced above as, $h_i(t, r) = e^{i\omega t} \tilde{h}_i(r)$. Now, if the linearized equations for the Schwarzschild metric perturbations obtained above admit harmonic solutions whose amplitudes grow in time, then the black hole is unstable against these harmonic perturbations; otherwise, it is stable.

In the RW gauge, the following form for the harmonic polar perturbations results [27, 56],

$$
h_{\mu\nu}^{P} = e^{i\omega t} \begin{bmatrix} \left(1 - \frac{2M}{r}\right) \tilde{H}_0(r) & \tilde{H}_1(r) & 0 & 0 \\ * & \left(1 - \frac{2M}{r}\right)^{-1} \tilde{H}_2(r) & 0 & 0 \\ * & * & r^2 \tilde{K}(r) & 0 \\ * & * & * & r^2 \sin^2\theta \tilde{K}(r). \end{bmatrix} Y_{l0}. \tag{2.4.14}
$$

On the other hand, for harmonic axial metric perturbations, we obtain,

$$
h_{\mu\nu}^{A} = e^{i\omega t} \begin{bmatrix} 0 & 0 & 0 & \tilde{h}_0(r) \\ * & 0 & 0 & \tilde{h}_1(r) \\ * & * & 0 & 0 \\ * & * & * & 0 \end{bmatrix} \sin\theta \frac{\partial}{\partial\theta} Y_{l0}. \tag{2.4.15}
$$

Since we are dealing with a spherically symmetric background spacetime, one can intuitively expect that the angular dependence of the perturbations will not involve m (for details see [179, 181, 182]).

Now since we have set $h_1(t, r) = e^{i\omega t} \tilde{h}_1(r)$, we can define

$$
\psi^{A}(r) \equiv e^{-i\omega t} \Psi^{A} = \left(1 - \frac{2M}{r}\right) \frac{\tilde{h}_1(r)}{r}, \tag{2.4.16}
$$

and insert it into the time-dependent linearized perturbation equations displayed above (2.4.10), to obtain a single second-order time-independent equation as,

$$
\frac{d^2}{dr_*^2} \psi^{A} + \left(\omega^2 - V_l^{A}(r)\right) \psi^{A} = 0, \tag{2.4.17}
$$

with the RW potential V_l^{A} for harmonic axial perturbations being given as [57],

$$
V_l^{A} = \left(1 - \frac{2M}{r}\right) \left[\frac{l(l+1)}{r^2} - \frac{6M}{r^3}\right]. \tag{2.4.18}
$$

It is to be noted that ψ^{A} is invariant under first-order gauge transformations. Strikingly, even though we have reduced the problem to this simple Schrödinger-like equation (2.4.17), we can still reconstruct fully arbitrary harmonic axial perturbations (in the RW gauge) from it. Besides $\tilde{h}_1$, we only need $\tilde{h}_0$, which can be obtained from the other equations as [27],

$$\tilde{h}_0(r) = \frac{\mathrm{i}}{\omega} \frac{\mathrm{d}}{\mathrm{d}r_*}\left(r\psi^{\mathrm{A}}\right). \tag{2.4.19}$$

It was shown in [61] that the harmonic polar perturbation equations can also be put into a Schrödinger-like form similar to equation 2.4.17. In particular, if one inserts the general form of the harmonic polar perturbations given in equation 2.4.14 into the linearized equations, it can be shown that $H_0 = H_2 \equiv H$ [56]. Furthermore, it turns out that H can be given in terms of H_1 and K. Therefore, after accounting for all the redundancy, one is left with only two coefficient functions, H_1 and K, which must be solved for from a set of two coupled first-order linear differential equations [61]. Similar to the axial case, we can rewrite these as a single second-order Schrödinger-like equation in terms of an auxiliary function ψ^{P},

$$\frac{\mathrm{d}^2}{\mathrm{d}r_*^2}\psi^{\mathrm{P}} + \left(\omega^2 - V_l^{\mathrm{P}}(r)\right)\psi^{\mathrm{P}} = 0, \tag{2.4.20}$$

with the Zerilli potential V_l^{P} being given as [61],

$$V_l^{\mathrm{P}}(r) = \left(1 - \frac{2M}{r}\right)\left[\frac{2\lambda^2(\lambda+1)r^3 + 6\lambda^2 Mr^2 + 18\lambda M^2 r + 18M^3}{r^3(\lambda r + 3M)^2}\right]. \tag{2.4.21}$$

Here, we have introduced λ as, $2\lambda = (l-1)(l+2)$. The polar perturbation coefficient functions K and H_1 can be recovered from ψ^{P} via [27],

$$K = \frac{\mathrm{d}\psi^{\mathrm{P}}}{\mathrm{d}r_*} + \frac{\lambda(\lambda+1)r^2 + 3\lambda Mr + 6M^2}{r^2(\lambda r + 3M)^2}\psi^{\mathrm{P}}, \tag{2.4.22}$$

$$H_1 = -\mathrm{i}\omega\left(1 - \frac{2M}{r}\right)^{-1}\left[\frac{\mathrm{d}\psi^{\mathrm{P}}}{\mathrm{d}r_*} + \frac{\lambda r^2 - 3\lambda Mr - 6M^2}{r(\lambda r + 3M)}\psi^{\mathrm{P}}\right].$$

Also, for completeness, we display below the algebraic equation that can be used to obtain H [27],

$$\left[2\lambda + \frac{6M}{r}\right]H = \left[2\lambda - \left(1 - \frac{2M}{r}\right)^{-1}\left(\frac{2\omega^2 r^4 - 2Mr + 6M^2}{r^2}\right)\right]K + \mathrm{i}\left[2\omega r - \frac{l(l+1)M}{\omega r^2}\right]H_1. \tag{2.4.23}$$

What we have arrived is this: arbitrary small metric perturbations of the Schwarzschild spacetime are governed by two scalar functions ψ^{A} and ψ^{P}, which satisfy the ordinary second-order differential equations given in equations 2.4.17 and 2.4.20 respectively, which look like the Schrödinger equation (see Appendix A of [73]). These two seemingly different potentials V_l^{A} and V_l^{P} have the remarkable property of being isospectral, i.e. they possess the same frequency spectrum; see figure 2.1. On closer inspection, it was shown in [62] that one can in fact transform the perturbation equation for the harmonic axial perturbations into the one corresponding to the harmonic polar perturbations via a transformation involving differential operations, thereby uniting them under the same banner. It can also be shown that these perturbations equations are connected to the Bardeen-Press perturbation equation [66], which is derived via the Newman-Penrose formalism [65].

Equations 2.4.17 and 2.4.20 are wave equations with scattering potential barriers V_l^{A} and V_l^{P} respectively, and metric perturbations reaching the black hole from spatial infinity can be regarded as wave packets that will scatter under their influence. Therefore, they share all of the well-known properties of a wave equation in
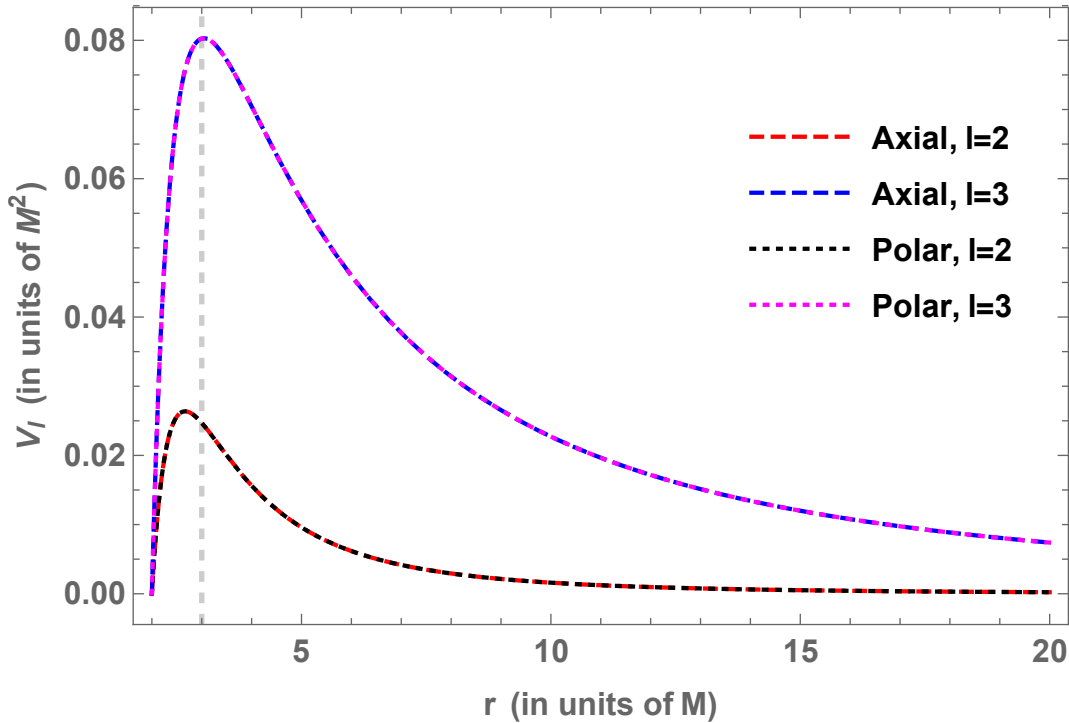
FIGURE 2.1: Here we show the effective potentials for the harmonic axial and polar perturbations V_l^A and V_l^P respectively for $l = 2, 3$, outside the Schwarzschild black hole horizon, which is at $r = 2M$. The first thing to note is that although the RW (2.4.18) and the Zerilli (2.4.21) potentials look markedly different, they are isospectral. Also, the maxima of these functions is approximately near the Schwarzschild photon sphere, which is located at $r = 3M$ (see for example Ch. 3 below).

a scattering potential. As in quantum mechanics, all of the wave packet will not in general be transmitted through the potential, and some of it, depending on the properties of the packet itself, will be reflected and reach spatial infinity again. It is important that both of these potentials are positive definite, have a single peak in the black hole exterior $r \geq 2M$ [183], and fall off to 0 exponentially as $r_* \to -\infty$ and as r_*^{-2} as $r_* \to \infty$. This implies that they do not allow bound states, and so we cannot impose as boundary conditions that solutions should vanish towards the boundaries [184].

Instead, we can look for harmonic perturbations that satisfy a pure outgoing-wave boundary condition at spatial infinity ($r \to \infty$ or $r_* \to \infty$) and a pure ingoing-wave boundary condition[19] at the horizon of the black hole ($r \to 2M^+$ or $r_* \to -\infty$). This choice of boundary conditions makes perfect sense since it essentially allows us to study the response of the metric outside the black hole to initial perturbations, with no interference from gravitational radiation sources present at spatial infinity, with the additional condition the black holes do not radiate classically. Now, as a result of the choice of boundary conditions for $|r_*| \to \infty$, we require that the solutions of equations 2.4.17 and 2.4.20 behave as,

$$\psi \sim \begin{cases} e^{i\omega r_*}, & \text{as } r_* \to -\infty, \\ e^{-i\omega r_*}, & \text{as } r_* \to -\infty. \end{cases} \tag{2.4.24}$$

In the above we have used ψ to denote both the axial ψ^A and polar ψ^P harmonic metric perturbation variables.

---

[19]At the horizon, the term ingoing denotes that the metric perturbation 'falls into the black hole.' However, it is more useful (and unifying) as is pointed out by [185] and also in [74] to call this set of boundary conditions to be outgoing at both boundaries since the wave leaves the domain we are studying.

The set of complex frequencies which allow solutions of equations 2.4.17 and 2.4.20, together with boundary conditions given in equation 2.4.24, are called quasi-normal frequencies (QNFs); the solutions constructed from them are the quasi-normal modes (QNMs). The 'quasi' in their names expresses the fact that they are not quite the same as normal modes: in general, they are not really stationary in time due to possible damping.

Now, numerous results that have been found for these types of (Schrödinger-like) equation can also be applied to the propagation of perturbations in the spacetime of Schwarzschild black hole (see [63] for a detailed discussion) to obtain its QNMs and QNFs. However, here we will simply show an approximation for the complex QN frequency, based on the standard WKB treatment of wave scattering on the peak of the potential barrier, which was given in [73, 185],

$$(M\omega_n)^2 = V_l(r_0) - i\left(n + \frac{1}{2}\right)\left[-2\frac{d^2 V_l(r_0)}{dr_*^2}\right]^{1/2}, \tag{2.4.25}$$

where r_0 is the peak of the potential barrier, which is close to $r = 3M$; see figure 2.1. See [186] for a list of these frequencies.

It is now well established that only a discrete set of QNFs satisfy these boundary conditions for the Schwarzschild black hole. Further, all of them have positive imaginary parts [60], and represent therefore damped modes; therefore a Schwarzschild black hole is mode stable. The damping time depends linearly on the mass of the black hole ($\omega \propto M^{-1}$), and is shorter for higher order modes ($\omega_n < \omega_{n+1}$). The QNMs in black holes are isospectral, i.e. axial and polar perturbations have the same complex QNFs.

Finally, it is useful to note that scalar ($s = 0$), electromagnetic ($s = 1$) and axial gravitational ($s = 2$) perturbations can in fact all be described by the equation 2.4.17 with the generalized effective potential $\mathscr{V}_l$ given as,

$$\mathscr{V}_l(r) = \left(1 - \frac{2M}{r}\right)\left[\frac{l(l+1)}{r^2} + \frac{2(1-s^2)M}{r^3}\right]. \tag{2.4.26}$$

In the above, we have introduced s to denote the spin of the perturbing field. Evidently, this potential reduces to the potential for the harmonic axial metric perturbations (2.4.18) for $s = 2$. This effective potential $\mathscr{V}_l$ is real and positive everywhere and vanishes near the horizon, $r_* \to -\infty$, where it decays exponentially, and at asymptotic infinity, $r_* \to \infty$, where it decays as r_*^{-2}. One may see §2 of [73] for insight on these perturbation equations; also see §3.1 therein for references to more detailed analyses. The potentials half-integer spin perturbations take a form different from equation 2.4.26 and we direct the reader to see [187] for details on the same.

2.5   Mode Stability of the Kerr Solution

The Kerr metric $g_{M,a}$ is a two-parameter family of solutions to the vacuum Einstein field equations and is given in Boyer-Lindquist coordinates (t, r, θ, ϕ) as [4, 188],

$$ds^2 = -\left(1 - \frac{2Mr}{\rho^2}\right)dt^2 - \frac{4Mar\sin^2\theta}{\rho^2}dtd\phi + \frac{A\sin^2\theta}{\rho^2}d\phi^2 + \frac{\rho^2}{\Delta}dr^2 + \rho^2 d\theta^2,$$

and we have employed Geometrized units $\mathscr{G} = c = 1$. In the above, we have introduced the specific angular momentum $a = J/M$, with $\Delta = r^2 - 2Mr + a^2$, $\rho^2 = r^2 + a^2\cos^2\theta$ and $A = (r^2 + a^2)^2 - a^2\Delta\sin^2\theta$.

This solution possesses a curvature singularity, which is located at $\rho = 0$, i.e., at $r = 0, \theta = \pi/2$, as can be seen from the associated Kretschmann scalar [189],

$$\mathcal{K} = \frac{3M^2}{4\pi^2\rho^6} \left(r^2 - a^2 \cos^2\theta \right) \left(\rho^4 - 16r^2a^2\cos^2\theta \right), \tag{2.5.1}$$

and event horizons, which are located at the zeroes of the null expansion scalar i.e. at $g_{rr}^{-1} = 0$,

$$r_\pm = M \pm \sqrt{M^2 - a^2}, \tag{2.5.2}$$

where r_+ and r_- correspond to the outer event horizon and the inner Cauchy horizon respectively. It is clear then that the metric (4.3.1) describes a black hole for $a \leq M$ or $J \leq M^2$, since $r_\pm$ are real valued. In the extremal case, $a = M$, there is only one degenerate event horizon. In the parameter regime $a > M$ or $J > M^2$, this metric continues to be a valid solution of the vacuum EFEs; however, it now describes the geometry of a spacetime containing a rotating naked singularity.

It turns out that the derivation of the linearized EFEs about the Kerr background is considerably more complicated than it was for the Schwarzschild case: a direct derivation for metric perturbations via the method adopted in the chapter thus far fails. It leads to gauge-dependent, and rather messy, formulations in which one cannot readily separate the variables as before. We note here that this method still works in the Kerr case for scalar perturbations [190, 191]. A theoretically attractive alternative for the general case is to examine curvature perturbations, the approach followed in the seminal papers [67], which we outline below.

If we introduce the complex Kinnersley null tetrad as [192],

$$l^\mu = \frac{1}{\Delta} \left(r^2 + a^2, \Delta, 0, a \right), \;\; n^\mu = \frac{1}{2\rho^2} \left(r^2 + a^2, -\Delta, 0, a \right), \;\; m^\mu = \frac{1}{\sqrt{2}(r + \mathrm{i}a\cos\theta)} \left(\mathrm{i}a\sin\theta, 0, 1, \frac{\mathrm{i}}{\sin\theta} \right),$$

then the electromagnetic field is characterized by the Newman-Penrose components [65],

$$\phi_0 = F_{\mu\nu} l^\mu m^\nu, \;\; \phi_1 = \frac{1}{2} F_{\mu\nu} \left(l^\mu n^\nu + \bar{m}^\mu m^\nu \right), \;\; \phi_2 = F_{\mu\nu} \bar{m}^\mu n^\nu, \tag{2.5.3}$$

where F is the electromagnetic field tensor, and $\bar{m}$ is the complex conjugate of m. In particular, ϕ_0 and ϕ_2 correspond to the ingoing and outgoing radiative parts of the field [67]. Similarly, gravitational radiation is described by perturbations in the Weyl tensor $C_{\alpha\beta\gamma\delta}$, which is the traceless part of the Riemann tensor, and has ingoing and outgoing radiative parts given by $\tilde{\Psi}_0$ and $\tilde{\Psi}_4$ given as [67],

$$\tilde{\Psi}_0 = -C_{\alpha\beta\gamma\delta} l^\alpha m^\beta l^\gamma m^\delta, \;\; \tilde{\Psi}_4 = -C_{\alpha\beta\gamma\delta} n^\alpha \bar{m}^\beta n^\gamma \bar{m}^\delta, \tag{2.5.4}$$

It can be demonstrated that these components are invariant under gauge transformations and infinitesimal tetrad rotations. Now, if we introduce a perturbation variable Ψ similar to the Schwarzschild case to describe these different fields as [67],

$$\phi_0 = \Psi, \;\; \phi_2 = \rho^2\Psi, \;\; \tilde{\Psi}_0 = \Psi, \;\; \tilde{\Psi}_4 = \rho^4\Psi. \tag{2.5.5}$$

it was shown in [67] that the Newman-Penrose version of the vacuum linearized EFEs for the Kerr metric are given in a unified manner as,

$$\left[\frac{(r^2+a^2)^2}{\Delta}-a^2\sin^2\theta\right]\frac{\partial^2\Psi}{\partial t^2}+\frac{4Mar}{\Delta}\frac{\partial^2\Psi}{\partial t\partial\phi}+\left[\frac{a^2}{\Delta}-\frac{1}{\sin^2\theta}\right]-\Delta^{-s}\frac{\partial}{\partial r}\left(\Delta^{s+1}\frac{\partial\Psi}{\partial r}\right)-\frac{1}{\sin\theta}\frac{\partial}{\partial\theta}\left(\sin\theta\frac{\partial\Psi}{\partial\theta}\right)$$
$$-2s\left[\frac{a(r-M)}{\Delta}+\frac{i\cos\theta}{\sin\theta}\right]\frac{\partial\Psi}{\partial\phi}-2s\left[\frac{M(r^2-a^2)}{\Delta}-r-ia\cos\theta\right]\frac{\partial\Psi}{\partial t}+(s^2\cot^2\theta-s)\Psi=0,\qquad(2.5.6)$$

where we have introduced the spin-weight $s=0,\pm1,\pm2$ for scalar, electromagnetic and gravitational perturbations respectively.

Note that in the Schwarzschild case, the background metric is *static*[20] and spherically symmetric, so the time and angular dependence can easily be separated out of the equations. Moreover, the replacement of spherical symmetry by axial symmetry means that a separation into spherical harmonics is no longer possible; one expects to end up with partial differential equations in r and θ instead of ordinary differential equations in r.

If we now introduce a harmonic perturbation variable ψ that respects the Killing symmetries of the background spacetime (see for example the discussions in Chapter 4),

$$\psi=e^{-i\omega t+im\phi}R_{lm}(r)S_{lm}(\theta),\qquad(2.5.7)$$

the linearized equations (2.5.6) separate into the radial and angular Teukolsky equations as [67],

$$\Delta^{-s}\frac{d}{dr}\left(\Delta^{s+1}\frac{dR_{lm}}{dr}\right)+\left(\frac{K^2-2is(r-M)K}{\Delta}+4is\omega r-\lambda\right)R_{lm}=0,\qquad(2.5.8)$$

$$\frac{1}{\sin\theta}\frac{d}{d\theta}\left(\sin\theta\frac{dS_{lm}}{d\theta}\right)+\left[(a\omega\cos\theta+s)^2-\left(\frac{m+s\cos\theta}{\sin\theta}\right)^2-s(s-1)+F\right]S_{lm}=0.\qquad(2.5.9)$$

In the above, we have have introduced $K\equiv(r^2+a^2)\omega-am$ and $\lambda\equiv F+a^2\omega^2-2am\omega$. We now make some comments on the angular equation. For each complex $a^2\omega^2$ and positive integer m, equation 2.5.9 together with the boundary conditions of regularity on the axis (i.e., at $\theta=0$ and $\theta=\pi$), determines a Sturm-Liouville eigenvalue problem. It has solutions for eigenvalues $F={}_sF^l_{m,\omega}$[21] when the integer l is larger than or equal to $\max(|m|,|s|)$, and the corresponding eigenfunctions $S_{lm}(\theta)$ are the spheroidal (oblate) harmonics. These eigenfunctions exist for all complex ω^2. For real ω^2, the spheroidal harmonics are complete in the sense that any function of $z=\cos\theta$, absolutely integrable over the interval over $[-1,1]$, can be expanded into spheroidal harmonics of fixed m. Since the angular equation is well understood, one is required to solve now only the radial differential equation (2.5.8).

The asymptotic behaviour of the solutions to the radial equation (2.5.8) at $r=\infty$ can be shown to be $e^{i\omega r}/r^{(2s+1)}$ for outgoing waves and $e^{-i\omega r}/r$ for ingoing waves. Before we enter into a treatment of QNMs, it is convenient to introduce $\tilde{R}_{lm}$ as,

$$R_{lm}=\Delta^{-s}\tilde{R}\exp\left(-i\int\frac{dr}{\Delta}K\right).\qquad(2.5.10)$$

---

[20]It admits a global, non-vanishing, timelike Killing vector field $\boldsymbol{\xi}$ which is irrotational, i.e., whose orthogonal distribution is involutive.
[21]This F is not to be confused with the electromagnetic field tensor previously introduced.

This is roughly the statement that we're moving to the Kerr-equivalent of the tortoise coordinates[22]. Then, in terms of $\tilde{R}$, the radial Teukolsky equation (2.5.8) becomes,

$$\Delta \frac{d^2\tilde{R}}{dr^2} - \left[2i\omega(r^2 + a^2) - 2(\tilde{s}+1)(r-M) - 2iam\right]\frac{d\tilde{R}}{dr} - \left[2(2\tilde{s}+1)i\omega r + \tilde{\lambda}\right]\tilde{R} = 0, \qquad (2.5.11)$$

where, using $F = E - s(s+1)$, we have introduced $\tilde{s} := -s$ and $\tilde{\lambda} := \lambda + 2s = E + a^2\omega^2 - 2am\omega - \tilde{s}(\tilde{s}+1)$.

Finally, we note that ω will acquire the interpretation of being the characteristic QNF, when the appropriate boundary conditions are imposed. The boundary condition at spatial infinity for a QNM analysis is independent of the spacetime under considerations, and we will again impose purely outgoing boundary conditions there. Now, black holes have a natural inner boundary condition corresponding to purely absorbing ones at $r = r_+$. In this case, the corresonding QNFs have been shown to have a negative imaginary part, implying stability [68]. Kerr naked singularities, on the other hand, admit QNMs with a purely positive imaginary part, and are therefore unstable [193]. This already suggests the reliability of the weak version of the cosmic censorship hypothesis whose statement is, roughly speaking, that spacetime singularities formed from generic initial conditions are enclosed by event horizons.

However, if we adopt the more generous spirit of [55], that "the Kerr bound is a consequence of the detailed prejudice about the regions of very strong curvature (for example, if one assumes the exact validity of classical GR); it should thus be viewed as an approximate bound and expected to receive substantial corrections in string theory. $\cdots$ In this sense, the cosmic censorship conjecture would be invalid in its most naïve GR form: Some 'naked singularities' of GR would be legitimate not because they hide behind horizons, but because they are resolved due to high-energy effects of the deeper theory. It is indeed important to apply to astrophysical objects lessons learned in effective field theory: Observations at a given energy scale (or spacetime curvature) should not require detailed knowledge of the physics at a much higher energy scale (or curvature). Imposing standard cosmic censorship of GR on astrophysical objects violates this 'decoupling principle,' by extrapolating GR into the high-curvature regime," then one must study the properties of hypothetical, exotic objects such as Kerr superspinars, the geometry in whose exterior is given by the overspinning Kerr solution.

Furthermore, since string theory has proven to be exceptionally good at resolving spacetimes containing various timelike singularities [194–197], following [55, 69, 70, 77], here we take the view that the Kerr naked singularity metric could possibly be 'cured' to represent new classes of legitimate compact objects in the string-theoretic completion of GR (or, more broadly speaking, in the ultimate theory of quantum gravity). In fact, the tension between the two notions of extremality for the presently relevant Kerr-Newman black hole family, namely, the notion from supersymmetry ($Q^2 \leq M^2$; the BPS bound) vs. the more restrictive GR one ($J^2 + Q^2 \leq M^2$; the Kerr-Newman bound) suggests that a more pragmatic view when considering such exotic objects could prove to be fruitful[23].

We now make a few comments on the scale of the stringy effects that would eventually determine the size of the superspinar. If we consider, for clarity, the case of the pathological supersymmetric BMPV naked singularity spacetimes in 4+1 spacetime dimensions [198], then we know that a stringy resolution of the central singularity, which uses a domain wall of size R, relaxes the Kerr bound [199]. While in this case there is not really a bound on J anymore, for large enough J, the domain wall becomes so large $\left(\text{since } J^2 \leq (Q+R)^3\right)$ that the object is not inside its Schwarzschild radius, and is therefore, no longer compact. Therefore, in this case, one could

---

[22]Obviously, this is not rigorous when considering non-black hole spacetimes.
[23]M, Q, and J are the mass, electric charge, and angular momentum of the spacetime respectively

say that the 5-d superspinar surface scales with its angular momentum. In another scenario, if one assumes a benign (from the point of view of an asymptotic observer) string-length scale modification ($\alpha \sim 10^{-35}$m) of the near-singular region, the eventual string-corrected object is a torus of cross-section $\sim \alpha^2$ but of radius J, since this is the physical size (Kerr-Schild coordinates; see Figure 4.1 for clarity on the relation between the Kerr-Schild and Boyer-Lindquist coordinates. Also see [200]) of the rotating singularity. Therefore, our analysis automatically sets the inner boundary of the spacetime, at which we impose conditions for the reflection/transmission of metric perturbations, at a radius of $\sim J$ in Kerr-Schild coordinates, and it would appear that this would be the length scale at which one would be required to match an interior solution for the superspinar with the overspinning Kerr metric.

Of course, before one can actually deem such exotic objects to be astrophysically relevant, one must a) find an interior metric that matches smoothly with the overspinning Kerr metric at the superspinar surface, b) establish that they form fairly generically as endstates of gravitational collapse from regular initial data, and c) that they are stable. While each of these problems is *prima facie* highly non-trivial, we consider the most tractable of the aforementioned analyses: mode stability.

Furthermore, since one of the greatest hopes for gaining insights into the quantum nature of compact objects has been to obtain associated signatures in gravitational wave detections from strong gravity regions [201, 202], it could be worthwhile, from such a perspective, to study the QNF-spectrum of Kerr superspinars. Since an interior solution is thus far unavailable, here we adopt an agnostic approach w.r.t. the inner boundary condition for metric perturbations, and parameterize the reflection coefficient at the inner boundary; then one can study the QNF-spectrum of this object by varying the reflection coefficient there. This goes with the understanding that if a legitimate interior metric is found, it would automatically correspond to a unique boundary condition at the surface of the superspinar.

It is important to note that since finding a valid interior solution can be difficult, and if one fails to match the first and second fundamentals of interior and exterior patches of a spacetime smoothly, a mode stability analysis based on simply parametrizing the reflectivity at the matching surface would be illegal. Here we *assume* that it might be possible to find an interior solution to the nearly-extremal overspinning Kerr spacetime that admits a smooth matching at the boundary, and ask whether Kerr superspinars could be stable then. The advantage of studying first their mode stability is in the following: If it turned out that Kerr superspinars were mode unstable, we could immediately disregard these classical solutions, at minimal cost.

With this view, a few studies on the stability of the over-spinning Kerr geometry [69, 70, 77] were conducted and it was suggested that superspinars would generically be unstable under various boundary conditions imposed at the surface of the superspinar, with the variety of boundary conditions being maximal in [70]. However, the most interesting case of *near-extremal* superspinars was not explored in sufficient detail, and this forms the focus of the following section. We show that under a variety of boundary conditions QNMs decay in time and these near-extremal superspinars are in fact mode stable. This result may have intriguing implications on the existence and physics of very rapidly rotating compact objects in the universe. It therefore follows from our results in [71] that, at the very least, a detailed study of physically allowed boundary conditions is necessary, in order to decide on the stability of superspinars or similar objects.

2.5.1   Mode Stability of Near-Extremal Kerr Superspinars[24]

Since we are interested in near-extremal superspinars, we can introduce ϵ to denote the departure from extremality $a = M$ as,

$$a = M(1 - \epsilon), \tag{2.5.12}$$

where $0 < |\epsilon| \ll 1$. The spacetime contains a near-extremal superspinar in the case of $\epsilon < 0$, and a black hole when $\epsilon > 0$.

For the Kerr black hole, it is known that the QNFs ω approach $m/2M$ for $m = l$ in the limit of approach to extremality, $\epsilon \to 0_+$ [203]. Results of the numerical study [70] indicate that even for Kerr superspinars, for these modes, one can expect the QNFs ω to approach $m/2M$, in the limit $\epsilon \to 0_-$. Hence, hereafter we focus on the modes of $m = l$ and _assume_ that ω differs from $m/2M$ only by an infinitesimal amount, which we parametrize by a positive constant p as,

$$M\omega - \frac{m}{2} = \mathcal{O}\left(|\epsilon|^p\right). \tag{2.5.13}$$

Now, If we introduce the dimensionless radial and frequency variables respectively as,

$$y = \frac{r}{M} - 1, \text{ and } \tilde{\omega} = M\omega, \tag{2.5.14}$$

we can rewrite equation 2.5.11 as,

$$(y^2 - 2\epsilon + \epsilon^2)\frac{d^2\tilde{R}}{dy^2} - \left[2i\tilde{\omega}y^2 + 2(2i\tilde{\omega} - \tilde{s} - 1)y + 2i(2\tilde{\omega} - m)(1 - \epsilon) + 2i\tilde{\omega}\epsilon^2\right]\frac{d\tilde{R}}{dy} \tag{2.5.15}$$
$$- \left[2(2\tilde{s} + 1)i\tilde{\omega}(y + 1) + \tilde{\lambda}\right]\tilde{R} = 0.$$

Our strategy to obtain the QNM frequency for the black hole case is as follows. First, we obtain the approximate solutions of equation 2.5.15 in the 'far' and 'near' zones, defined respectively as $\max\left[\sqrt{|\epsilon|}, |\epsilon|^p\right] \ll y$ and $y \ll 1$ separately. Then, we choose appropriate integration constants so that these solutions agree with each other in the overlapping region, $\max\left[\sqrt{|\epsilon|}, |\epsilon|^p\right] \ll y \ll 1$. Finally, we impose (a) the condition that there be no incoming waves at spatial infinity on the far-zone solution, and (b) a regularity condition on the near-zone solution at the event horizon, for black holes. A similar procedure is followed for the superspinar in order to make clear the analogy with the black hole case, and to enable a study of the contrast between the two.

In the far-zone, equation 2.5.15 approximates to,

$$y^2\frac{d^2\tilde{R}}{dy^2} - \left[2i\tilde{\omega}y^2 + 2(2i\tilde{\omega} - \tilde{s} - 1)y\right]\frac{d\tilde{R}}{dy} - \left[2(2\tilde{s} + 1)i\tilde{\omega}(y + 1) + \tilde{\lambda}\right]\tilde{R} = 0, \tag{2.5.16}$$

the solution of which can be written in terms of the confluent hypergeometric functions $_1F_1(\alpha; \gamma; z)$ as,

$$\tilde{R}^{\text{far}} = Ay^{-1/2 + 2i\tilde{\omega} + i\delta - \tilde{s}}\,_1F_1\left(\frac{1}{2} + 2i\tilde{\omega} + i\delta + \tilde{s}; 1 + 2i\delta; 2i\tilde{\omega}y\right) + B|_{\delta \to -\delta}, \tag{2.5.17}$$

where A and B are integration constants, and we have introduced,

$$\delta^2 \equiv 4\tilde{\omega}^2 - \frac{1}{4} - \tilde{\lambda} - \tilde{s}(\tilde{s}+1) \simeq \frac{1}{4}(7m^2 - 1) - E, \qquad (2.5.18)$$

a constant. It is to be noted that this definition for δ^2 differs from equation 9 of [204] due to a typo there.

For the near-zone analysis, we keep terms only of leading order in ϵ, and it is useful to introduce a new radial variable, $x \equiv y - \sqrt{2\epsilon}$. Then, equation 2.5.15 approximates to,

$$x(x+\sigma)\frac{d^2\tilde{R}}{dx^2} - \left[2\left(2i\tilde{\omega} - \tilde{s} - 1\right)x - (\tilde{s}+1)\sigma + 4i\tau\right]\frac{d\tilde{R}}{dx} - \left[2(2\tilde{s}+1)i\tilde{\omega} + \tilde{\lambda}\right]\tilde{R} = 0, \qquad (2.5.19)$$

where $\sigma \equiv 2\sqrt{2\epsilon}$, and $\tau \equiv (1+\sqrt{2\epsilon})\tilde{\omega} - \frac{m}{2}$. The solution of the equation above may expressed in terms of the Gauss hypergeometric function $_2F_1(\alpha, \beta; \gamma; z)$ in the form,

$$\tilde{R}^{\text{near}} = C\, x^{-\tilde{s}+4i\tau/\sigma} {}_2F_1(1/2 - 2i\tilde{\omega} + i\delta + 4i\tau/\sigma, 1/2 - 2i\tilde{\omega} - i\delta + 4i\tau/\sigma; 1 - \tilde{s} + 4i\tau/\sigma; -x/\sigma) \qquad (2.5.20)$$

$$+ D\, {}_2F_1(1/2 - 2i\tilde{\omega} + i\delta + \tilde{s}, 1/2 - 2i\tilde{\omega} - i\delta + \tilde{s}; 1 + \tilde{s} - 4i\tau/\sigma; -x/\sigma),$$

where C and D are integration constants.

As noted above, both the far- and near-zone solutions, given in equations 2.5.17 and 2.5.20 respectively, are valid in the over-lapping region, $\max\left[\sqrt{|\epsilon|}, |\epsilon|^p\right] \ll y \ll 1$. In the limit $y \to 0$, the far-zone solution (2.5.17) behaves as,

$$\lim_{y\to 0} \tilde{R}^{\text{far}} \to A y^{-1/2 + 2i\tilde{\omega} + i\delta - \tilde{s}} + B y^{-1/2 + 2i\tilde{\omega} - i\delta - \tilde{s}}. \qquad (2.5.21)$$

This is essentially the behaviour of the far-zone solution (2.5.17) at the inner edge of the overlapping region, i.e. at $y \approx \max\left[\sqrt{|\epsilon|}, |\epsilon|^p\right]$. Further, in the limit $y \to \infty$, the near-zone solution (2.5.20) behaves as,

$$\lim_{y\to\infty} \tilde{R}^{\text{near}} \to \mathcal{A} y^{-1/2 + 2i\tilde{\omega} + i\delta - \tilde{s}} + \mathcal{B} y^{-1/2 + 2i\tilde{\omega} - i\delta - \tilde{s}}, \qquad (2.5.22)$$

where $\mathcal{A}$ and $\mathcal{B}$ may be written in terms of the near-zone integration constants as,

$$\mathcal{A} = \sigma^{1/2 - 2i\tilde{\omega} - i\delta}\Gamma(2i\delta) \qquad (2.5.23)$$

$$\times \left[\frac{C\sigma^{4i\tau/\sigma}\Gamma(1 - \tilde{s} + 4i\tau/\sigma)}{\Gamma(1/2 + 2i\tilde{\omega} + i\delta - \tilde{s})\Gamma(1/2 - 2i\tilde{\omega} + i\delta + 4i\tau/\sigma)} + \frac{D\sigma^{\tilde{s}}\Gamma(1 - 4i\tau/\sigma + \tilde{s})}{\Gamma(1/2 - 2i\tilde{\omega} + i\delta + \tilde{s})\Gamma(1/2 + 2i\tilde{\omega} + i\delta - 4i\tau/\sigma)}\right],$$

$$\mathcal{B} = \mathcal{A}|_{\delta\to-\delta}. \qquad (2.5.24)$$

We have introduced $\mathcal{A}$ and $\mathcal{B}$ so that the matching condition can simply be immediately read off by glancing at equations 2.5.21 and 2.5.22 to be,

$$A = \mathcal{A} \quad \text{and} \quad B = \mathcal{B}. \qquad (2.5.25)$$

Now, to set the condition that there be no incoming radiation from spatial infinity, we must consider the other limit, $y \to \infty$, of the far-zone solution (2.5.17). This gives,

$$\lim_{y\to\infty} \tilde{R}^{\text{far}} \simeq Z_{\text{out}}\, y^{-(1-4i\tilde{\omega})} e^{2i\tilde{\omega}y} + Z_{\text{in}}\, y^{-(2\tilde{s}+1)},$$

where Z_{out} and Z_{in} are identified as the outgoing and ingoing solutions at spatial infinity, and are given as,

$$Z_{\text{in}} = A \frac{(-2i\tilde{\omega})^{-1/2-2i\tilde{\omega}-i\delta-\tilde{s}}\Gamma(1+2i\delta)}{\Gamma(1/2-2i\tilde{\omega}+i\delta-\tilde{s})} + B \frac{(-2i\tilde{\omega})^{-1/2-2i\tilde{\omega}+i\delta-\tilde{s}}\Gamma(1-2i\delta)}{\Gamma(1/2-2i\tilde{\omega}-i\delta-\tilde{s})}, \qquad (2.5.26)$$

$$Z_{\text{out}} = Z_{\text{in}}|_{\tilde{s}\to-\tilde{s},\tilde{\omega}\to-\tilde{\omega}}.$$

Thus, together with the matching condition, given in equation 2.5.25, and the condition that there be no incoming waves at spatial infinity, $Z_{\text{in}} = 0$, we obtain,

$$\mathcal{A} \frac{(-2i\tilde{\omega})^{-i\delta}\Gamma(1+2i\delta)}{\Gamma(1/2-2i\tilde{\omega}+i\delta-\tilde{s})} + (\delta \to -\delta) = 0 \qquad (2.5.27)$$

Now we must address the boundary condition on the inner edge of the domain of interest, $r \to M$. Here it is worthwhile to notice that, in the black hole case ($\epsilon > 0$), the regular singular point $x = 0$ of the near-zone equation (2.5.19) corresponds to the location of the event horizon. Since we impose the regularity of the solution at the event horizon, the integration constant C must vanish (note $\tilde{s} = 2$). By contrast, in the superspinar case ($\epsilon < 0$), the regular singular points $x = 0$ and $x = -\sigma$ of the same equation are equivalent to $y = \pm i\sqrt{2|\epsilon|}$. Hence, in the superspinar case, there is no regular singular point of the near-zone equation (2.5.19) on the real axis of y, or equivalently, on the real axis of r. It is important to note that the implication of this distinct feature (pole structure) is that the regularity requirement of the solution on the real axis of y does not lead to any condition on the integration constants C and D in the superspinar case. However, in order to obtain the QNFs in the superspinar case, we still need to fix C and D. For this purpose, we impose identical conditions for both the black hole ($\epsilon > 0$) and the superspinar ($\epsilon < 0$) on the inner boundary as,

$$C = 0 \quad \text{and} \quad D = 1. \qquad (2.5.28)$$

Substituting equations 2.5.23 and 2.5.24 along with the inner boundary condition given in equation 2.5.28 into the quasi-normal mode condition given in equation 2.5.27, we have,

$$-\frac{\Gamma(2i\delta)\Gamma(1+2i\delta)}{\Gamma(-2i\delta)\Gamma(1-2i\delta)} \frac{\Gamma(1/2-2i\tilde{\omega}-i\delta+\tilde{s})\Gamma(1/2-2i\tilde{\omega}-i\delta-\tilde{s})}{\Gamma(1/2-2i\tilde{\omega}+i\delta+\tilde{s})\Gamma(1/2-2i\tilde{\omega}+i\delta-\tilde{s})} = (-2i\tilde{\omega}\sigma)^{2i\delta} \frac{\Gamma(1/2+2i\tilde{\omega}+i\delta-4i\tau/\sigma)}{\Gamma(1/2+2i\tilde{\omega}-i\delta-4i\tau/\sigma)}. \qquad (2.5.29)$$

The above equation determines the quasi-normal mode frequency $\tilde{\omega}$ of a near-extremal Kerr superspinar under the inner boundary conditions given in equation 2.5.28, and the (informed) assumption that the QNF spectrum satisfies equation 2.5.13.

We now discuss the consequence of using the QNF ansatz (2.5.13), $\tilde{\omega} \to m/2$ as $a \to M$, or equivalently $\epsilon \to 0_\pm$. It is known that δ is real and positive in this limit, i.e., for the extremal black hole case $a = M$, for $|\tilde{s}| = 2$ and $l = |m| \geq 2$ [205, 206], and we restrict ourselves to a study of these modes of the superspinar. Then, the left hand side of equation 2.5.29 will have a finite limit for $\epsilon \to 0_\pm$, which we express in the form, L. H. S. $= q e^{i\chi}$. In order for the R. H. S. of the same equation to also have a finite limit, the equation $\tilde{\omega} \propto \sigma^{-1}$ or $\tau/\sigma \to \infty$ must hold in this limit. Here note that $\sigma \to 0$, in the limit of $\epsilon \to 0_\pm$. This fact implies that the former is inconsistent with our assumption, and τ/σ should diverge in the limit of $\epsilon \to 0_\pm$, i.e., p in equation 2.5.13) should satisfy $p < 1/2$.

Then, following the arguments given in [204], we have

$$\tilde{\omega}_{\mathrm{R}} \simeq \frac{m}{2} - \frac{1}{4m} \mathrm{e}^{(\chi - 2k\pi)/2\delta} \cos \zeta$$

$$\tilde{\omega}_{\mathrm{I}} \simeq -\frac{1}{4m} \mathrm{e}^{(\chi - 2k\pi)/2\delta} \sin \zeta,$$

for both the black hole and the superspinar, where k is an integer number consistent with $|\epsilon|^{1/2} \ll \mathrm{e}^{(\chi - 2k\pi)/2\delta} = \mathcal{O}(|\epsilon|^p)$ because of $0 < p < 1/2$. Since χ and δ will be of the order $|\epsilon|^0$, we have $k \ll -\ln|\epsilon|$ which corresponds to equation 28 of [204]. An estimate of ζ is available for Kerr black holes and superspinars, in case of $\tilde{\omega} \simeq m/2$; $0 < \zeta < 2$ [82].

Thus the imaginary part of the QNF $\tilde{\omega}_{\mathrm{I}}$ is negative. This result implies that, for the choice of boundary condition we have used at on the inner edge of the spacetime (2.5.28), both near-extremal Kerr black holes and superspinars are stable against gravitational wave mode perturbations with $m = l$. That is, the existence of at least one boundary condition under which the superspinar is stable against the gravitational perturbations of $m = l$ has been obtained. However, it must be noted that the physical meaning of the boundary condition is still unclear and needs to be further investigated.

2.6 Comments on Mode vs. Linear Stability

As we have seen, a mode stability analysis consists of studying the boundedness of linear perturbations that possess a harmonic time behaviour, i.e. they can be expressed in the form $h(t, r, \theta, \phi) = \mathrm{e}^{\mathrm{i}\omega t} \tilde{h}(r, \theta, \phi)$. Given appropriate boundary conditions, for such perturbations, a linear stability analysis essentially reduces to an eigenvalue problem. Now, since ω is complex, the linear differential operator $\mathscr{L}_g$ is not of the Sturm-Liouville variety. Most importantly, this implies that one must now check whether the quasi-normal modes form a complete basis.

To answer such a question, we must start by analysing the time-dependent linearized equation (like equation 2.4.10). A standard technique for identifying important contributions to the solution of such a differential equation consists of closing the contour of integration of the linearized equation. This relates analyticity properties of the Laplace-transformed solution to the asymptotic behaviour of the time-dependent solution [74]. The absence of essential singularities inside the contour implies that the integral evaluates to a sum over the residues inside the contour.

Typically, one closes the contour with a half circle at infinity in either the right or left half-plane. In fact, such a closure at $|s| = \infty$ should be regarded as the limit of a sequence of closures at finite values of $|s|$. Here, s is the Laplace transform variable and is not to be confused with a spin weight. If we are fortunate enough to be studying a problem where this sequence has a limit, the integral over the half circle at infinity vanishes in this limit, and there are no essential singularities inside the contour, then roughly any solution of the time-dependent wave equation can be represented completely by a sum over quasi-normal-mode solutions; i.e. these quasi-normal modes form a complete set in the space of solutions.

However, this definition of completeness does not generally apply to dissipative systems since the domain of the operator typically extends to infinity, where the quasi-normal-mode solutions diverge. Solutions of the time-dependent problem, on the other hand, have to be bounded everywhere. In particular, for perturbations of

black holes, essential singularities arise. If one tries to remove them (typically they are at $s = 0$), the piece of the integral corresponding to the closing of the contour at $|s| = \infty$ produces a non-vanishing contribution. This implies, it turns out, that the quasi-normal modes of the Regge-Wheeler or the Zerilli potential, for example, do not in fact form a complete set. Therefore, a result of mode stability cannot, by definition, in such systems suffice to make a statement about full linear stability.

2.7   Non-linear Stability in General Relativity[25]

We begin with a brief review of the initial value formulation of general relativity, which is the typical setting of stability analyses in general relativity [109, 110]. For this a discussion on the Cauchy problem of the Einstein field equations [105–108] becomes absolutely necessary, as shall become obvious. In our discussion here, we shall concern ourselves primarily with spacetimes devoid of matter i.e., the only degrees of freedom of such a system are purely gravitational and the sole dynamical entity is the metric tensor g. At the end of this section, we will mention how one could carry this analogy through to include matter.

The Einstein field equations are partial differential equations, and are essentially hyperbolic in nature. This means that the general properties of solutions to these equations are similar to those found for the wave equation, and we have seen this explicitly for the linearized version above. In general, they are coupled to other partial differential equations describing the matter content of spacetime. It follows that it is reasonable to try to determine a solution by setting initial data on a spacelike hypersurface. Thus the Cauchy problem of the field equations must naturally be studied. Also, since the Einstein field equations are also non-linear, there is a big difference between the local and global Cauchy problems. In particular, a solution evolving from regular data may develop singularities.

Furthermore, as we have seen already, a special feature of the Einstein field equations is that they are diffeomorphism invariant. If the equations are written down in an arbitrary coordinate system, then the solutions of these coordinate equations are not uniquely determined by initial data. Diffeomorphisms map solutions into each other. However, if the chosen diffeomorphism is the identity on the chosen Cauchy surface up to first order, then the data are left unchanged by this transformation. In order to obtain a system for which uniqueness in the Cauchy problem holds in the straightforward sense that it does for the wave equation, some coordinate or gauge fixing must be carried out. We will not attempt to demonstrate here a gauge fixing for the full non-linear field equations.

Now, a triple (Σ, q, K) with Σ a smooth orientable 3-manifold, q a Riemannian metric and K a symmetric 2-tensor field, both on Σ, forms a valid initial data set for the vacuum Einstein field equations (2.1.2) if the geometry initial data fields $d_{\mathrm{g}} \equiv (q, K)$ satisfy certain constraint equations. Given such an initial data set, one expects to generate a 4-dimensional spacetime $(\mathcal{M}, g)$ and a one-parameter family of embeddings $\theta : \Sigma \times \mathbb{R} \to \mathcal{M}$ such that g satisfies the EFEs (2.1.2), $\theta(\Sigma)$ forms a Cauchy hypersurface in $\mathcal{M}$, and the fields q and K are the first and second fundamentals respectively of Σ in $(\mathcal{M}, g)$ (see for example p. 226 of [9]). The constraint equations mentioned above are simply the mathematical consequences of the desire that Σ 'fit properly' into $\mathcal{M}$, i.e. d_{g} satisfies what are called the Gauss and Codazzi-Mainardi equations, which govern the embeddings of hypersurfaces into manifolds. In the context of GR, these are usually called the Einstein

---

[25]Reprinted excerpt with permission from [**P. Kocherlakota** and P. S. Joshi, Arab. J. Math. (2019)]. Copyright (2019) by Springer; We refer the reader to see also [9, 105–110, 164] for a more detailed discussion on these aspects.

Hamiltonian and momentum constraint equations and are given respectively as (see for example [164]),

$$^{(3)}R - K_{ij}K^{ij} + \left(K^i_{\ i}\right)^2 = 0, \tag{2.7.1}$$

$$\nabla^j K_{ij} - \nabla_i K^j_{\ j} = 0, \tag{2.7.2}$$

where $^{(3)}R$ is the Ricci scalar and ∇ the covariant derivative associated with q. For insight into the structure of the constraint differential equations we direct the reader towards [105–107]. This property that initial data fields cannot be freely specified but must satisfy certain constraint equations is not characteristic to GR and, for example, is also a feature of Maxwell's equations for electromagnetism, where the constraint equation is the Gauss law [207].

Technically, $(\mathcal{M}, \theta, g)$ is called a development of (Σ, d_g) and the evolution or Cauchy problem in GR refers to the construction of the former from the latter. The Cauchy problem of a given field theory is well-posed if for any valid choice of initial data, there exists a solution which is consistent with that data, and the map from the space of initial data to solutions is continuous [106]. It was shown in the seminal papers of [208, 209] that the Cauchy problem in GR is indeed well-posed (see also Chapter 6 of [10]). Further, in [210], it was established that each such initial data set has a unique maximal future development $(\mathcal{M}, g)$, namely a development which extends every other development of the same initial data set[26]. It was subsequently pointed out in [211] that for any such development $(\mathcal{M}, g)$, the manifold $\mathcal{M}$ is diffeomorphic to $\Sigma \times \mathbb{R}$, and such spacetimes are called globally hyperbolic spacetimes. These fundamental results are critical to argue the existence of solutions in GR and to set up the Hamiltonian formulation of GR.

In this context, the stability of a spacetime $(\mathcal{M}, g)$ is understood as follows. First one finds the initial data d_g whose evolution under the Einstein field equations yields $(\mathcal{M}, g)$. Then, in the space of all allowed initial data, one considers neighbourhoods around d_g and checks whether their future developments yield metrics g' such that "$g' \approx g$," in some sense. Depending on whether or not the neighbourhoods under consideration are infinitesimal or not, one is conducting then either a linear or non-linear stability analysis respectively. For example, the Kerr family of spacetimes $(\mathcal{M}, g_{M,a})$ is a 2-parameter family of solutions of the Einstein field equations and contains the 1-parameter family of Schwarzschild solutions denoted by $g_{M,0}$. Within this family is also the Minkowski metric for which the metric can be represented as $g_{0,0}$. Therefore, if a particular member $g_{M,a}$ were generated by some initial data $d_{M,a}$ and one considers another initial data within an infinitesimal neighbourhood of $d_{M,a}$, which let us denote by $d_{M+\delta M,a+\delta a}$, then if the future development of the latter $g_{M+\delta M,a+\delta a}$ is such that $|g_{M+\delta M,a+\delta a} - g_{M,a}| \ll 1$, then one can say that the spacetime $g_{M,a}$ is linearly stable. If such a statement holds for all M, a, then one can argue that the family of Kerr spacetimes is linearly stable. To find the full extent of stability of a particular solution $g_{M,a}$, one must conduct a non-linear stability analysis which requires one examine to the future developments of initial data chosen within arbitrary, non-infinitesimal neighbourhoods of $d_{M,a}$. These issues of stability are extremely important, both from theoretical and astrophysical standpoints, and difficult to examine and thus far, significant progress has been made and the non-linear stability of the Minkowski spacetime [166] and the linear stability of the Schwarzschild spacetime [112] has been established, and it has also been shown that the Kerr family of spacetimes are mode stable [68]. For more detailed and excellent discussions on stability see [110].

In the following section, we demonstrate a typical non-linear stability analysis in general relativity, in the setting of a simplistic spherically symmetric collapse model. We will take our matter model to be that of a

---

[26]Another development $(\mathcal{M}', \theta', g')$ of (Σ, d_g) is called an extension of $\mathcal{M}$ if there is a diffeomorphism α of $\mathcal{M}$ into $\mathcal{M}'$ such that $\theta'(\Sigma) = (\alpha \circ \theta)(\Sigma)$ and $\alpha_* g' = g$. In particular, a maximal extension is an extension of any development of (Σ, d_g) [9].

fluid with vanishing pressure since for such systems, the mass contained within a shell of arbitrary comoving radius is conserved throughout the collapse, leading to substantial simplifications in the dynamical equations, making a purely analytical approach tractable.

2.8   Extent of Non-Linear Stability of the Schwarzschild Black Hole[27]

The Datt-Oppenheimer-Snyder (DOS, [44]) solution of the Einstein field equations evolves a regular, homogeneous, spherically symmetric ball of dust (pressureless fluid) to a Schwarzschild black hole. We will see that the prescription of initial data for this process corresponds to specifying the initial density to be homogeneous throughout the matter cloud,

$$\rho(t = 0, r) = \rho_0 = \text{const.,} \tag{2.8.1}$$

and the initial binding energy profile of the dust cloud, characterised by $f(r)$. We review here our findings, reported in [104], relating to a partial non-linear stability analysis of the marginally bound ($f = 0$) DOS collapse processes against a *specific* class of deformations of allowed initial data, and matter models: we will only consider departures of the initial density profile from homogeneity. What we mean by this is that we will consider initial density profiles $\rho(0, r)$ of the form,

$$\rho(0, r) = \rho_0 - \rho_2 r^2, \ \ \rho_2 \geq 0, \tag{2.8.2}$$

(for $\rho_2 = 0$, we recover the DOS collapse process) and study the local and global visibility of the eventual singularity that forms as a result of continual collapse. This will give us the size of the region in the (restricted) space of initial data (i.e., the ρ_0-ρ_2 parameter space), around $(\rho_0, 0)$, whose evolutions under Einstein field equations result in black holes. If the size of this region is an infinitesimal open set around $(\rho_0, 0)$, we will conclude that the DOS collapse process is linearly stable against changes in initial data. However, if this region is larger, then this will provide us with a measure of the extent to which the DOS collapse process is non-linearly stable against changes in initial data.

Now, since it is known that the marginally bound DOS collapse processes sit as a one-parameter (ρ_0) subclass of the marginally-bound Lemaître-Tolman-Bondi (LTB [45]) solutions, which have an entire square integrable-function's worth of freedom (corresponding to the initial density profile of the matter $\rho(0, r)$) that can be freely prescribed, the evolutions of the initial data corresponding to the inhomogeneous initial density profiles given in equation 2.8.2 are already known. We avoid the term proportional to r to avoid density cusps at the centre of the collapsing cloud (see §2.8.2 below). Now, following [50], we analyse the structure of the singularity that forms in the class of marginally bound LTB collapse models with initial density profiles given above (2.8.2). A more exhaustive non-linear stability analysis of the formation of a Schwarzschild black hole as an end-state of the Datt-Oppenheimer-Snyder (DOS) collapse process incorporating recent results [212–215] will be reported elsewhere.

2.8.1   Dynamics of Dust Collapse

The spacetime geometry associated with a spherically symmetric collapsing cloud of matter is described by the (interior) metric,

$$\mathrm{d}s^2 = -\mathrm{e}^{2\nu(t,r)}\,\mathrm{d}t^2 + \frac{R'^2(t,r)}{1+f(t,r)}\,\mathrm{d}r^2 + R(t,r)^2\,\mathrm{d}\Omega^2, \tag{2.8.3}$$

where in the above (t, r, θ, ϕ) are Langrangian coordinates, comoving with the matter field, i.e. in these coordinates the matter four-velocity is given as $u^\alpha = \mathrm{e}^{-\nu}\delta^\alpha_t$. The range of the radial coordinate is $0 \le r \le r_\mathrm{B}$, where r_B is the boundary of the matter cloud and we have written g_{rr} in this form, anticipating convenience. The $'$ denotes a derivative w.r.t. r and

$$\mathrm{d}\Omega^2 = \mathrm{d}\theta^2 + \sin^2\theta\,\mathrm{d}\phi^2 \tag{2.8.4}$$

is the standard metric on a unit two-sphere. The metric function ν is related to the redshift, R is the proper radius of a shell of collapsing matter present at a comoving radius r and time t, and f characterizes the binding energy profile of the collapsing cloud [11]. In anticipation of its immediate use, we now introduce the Misner-Sharp mass function $F(t, r)$ which measures the amount of mass contained within a shell of comoving radius r at a time t is given as [216, 217],

$$F(t,r) \equiv R\left(1 - g^{\alpha\beta}\partial_\alpha R\,\partial_\beta R\right) = R\left(\mathrm{e}^{-2\nu}\dot{R}^2 - f(t,r)\right), \tag{2.8.5}$$

where g is the metric tensor obtained from equation 2.8.3. Since this metric only describes a portion of the spacetime ($0 \le r \le r_\mathrm{B}$), if one wants to consider the collapse of matter that has compact support on the initial spacelike hypersurface $t = 0$, to complete the spacetime one must match this interior collapsing metric at the boundary with an appropriate exterior metric, which via Birkhoff's theorem [81], must necessarily be the Schwarzschild metric.

The interior collapsing metric g contains an apparent horizon, which is the marginally trapped surface, if the radial null expansion scalar, defined as [218]

$$\theta(t,r) \equiv g^{\alpha\beta}\partial_\alpha R\,\partial_\beta R \tag{2.8.6}$$

vanishes. Therefore, it is seen from equation 2.8.5 that the apparent horizon curve $t_\mathrm{AH}(r)$, which tracks the location of the apparent horizon during the evolution of the collapse can be found from,

$$F(t_\mathrm{AH}(r), r) = R(t_\mathrm{AH}(r), r). \tag{2.8.7}$$

Now, if we consider the spherically symmetric collapse of a fluid with vanishing pressure in this choice of comoving coordinates, we can write the associated matter stress-energy tensor as,

$$T^\mu_\nu = \mathrm{diag}(-\rho, 0, 0, 0). \tag{2.8.8}$$

The choice to consider fluids with vanishing pressure $p_r = p_\theta = 0$ greatly simplifies the collapse evolution (see for example §4.2 of [212]). Firstly, $F = F(r)$ and $f = f(r)$ become time independent and are therefore completely set by their initial values; F, f are no longer dynamical functions. Further, ν does not depend on r and $\nu = \nu(t)$ i.e., by rescaling time for the interior metric, we can set $\nu = 0$. Then the governing EFEs,

$\mathbb{G}^{\mu}_{\ \nu} = T^{\mu}_{\ \nu}$, for the evolution of such a fluid are given as,

$$\rho = \frac{F'}{R^2 R'}, \tag{2.8.9}$$

$$\dot{R} = -\sqrt{\frac{F}{R} + f}, \tag{2.8.10}$$

where in the above we have rewritten equation 2.8.5) as equation 2.8.10 and have chosen the negative root since we are interested here in collapsing solutions.

Also, throughout the collapse process we shall require that the weak energy condition is satisfied everywhere i.e. $T_{\mu\nu}v^{\mu}v^{\nu} \geq 0$ for all non-spacelike vectors v^{μ}. This implies that the energy density is everywhere positive $\rho \geq 0$, including near $r = 0$. Singularities are points of spacetime where the usual differentiability and manifold structures break down. They are characterized by divergences in the matter energy density or curvature invariants constructed from the Riemann curvature tensor, like the Kretschmann scalar $\mathscr{K} \equiv R_{\mu\nu\rho\sigma}R^{\mu\nu\rho\sigma}$. As can be seen from equation 2.8.9, the energy density diverges when $R = 0$ or when $R' = 0$. The latter condition corresponds to the collision of different radial shells of matter, which cause what are known as 'shell-crossing singularities.' These types of singularities are weak singularities and are removable by a suitable change of coordinates (see for example §6.8 of [11] for further discussion; also see [212]). Therefore, we shall also require that R satisfy $R' \neq 0$. Further, for the weak energy condition to hold on the initial epoch $\rho(0, r) \geq 0$ from which the collapse begins, we require that $F' \geq 0$ from equation 2.8.11. Now, for collapse processes of interest here we have $F = F(r)$ which means that for the energy condition to hold at all times $\rho(t, r) \geq 0$, we require specifically from equation 2.8.9 that $R' > 0$. Finally, $R(t_{\rm s}(r), r) = 0$ are genuine spacetime singularities, also called shell-focussing singularities, and $t_{\rm s}(r)$ is called the singularity curve i.e. it is the time at which the shell at comoving radius r reaches the singularity. Therefore the coordinate time runs from $-\infty < t < t_{\rm s}(r)$.

2.8.2   Initial Data

We now discuss how one sets valid initial data, $d = \{R(0, r), f(r), \dot{R}(0, r), \rho(0, r), F(r), \dot{\rho}(0, r)\}$. We can partition this set of initial data heuristically into geometry $d_{\rm g} = \{R(0, r), f(r), \dot{R}(0, r)\}$ and matter $d_{\rm m} = \{\rho(0, r), F(r), \dot{\rho}(0, r)\}$ initial data. By valid initial data, we mean that the set of functions listed in d must be chosen such that they respect the Hamiltonian and momentum constraints, are smooth and are such that no singularity or apparent horizon is present on the Cauchy surface, $t = 0$.

First we shall inquire after the number of independent initial data functions in this collapse model. If, without loss of generality, we choose the initial scaling as $R(0, r) = r$, then prescribing the initial density profile $\rho(0, r)$ at the initial epoch fixes the matter profile of the cloud $F(r)$ from equation 2.8.9 as,

$$F(r) = \int_0^r d\tilde{r}\rho(0, \tilde{r})\tilde{r}^2. \tag{2.8.11}$$

Further, picking $f(r)$ fixes $\dot{R}(0, r)$ from equation 2.8.5 and $\dot{\rho}(0, r)$ is set then from equation 2.8.9. In summary, one is free only to pick three functions independently on the Cauchy surface $t = 0$, which here will be $R(0, r), f(r), \rho(0, r)$. The remaining initial data $\{\dot{R}(0, r), F(r), \dot{\rho}(0, r)\}$ are then fixed from the constraint equations.

Now we move to a discussion on the smoothness of initial data. The requirement that $\rho(0, r)$ be smooth implies that F is atleast $\mathcal{O}(r^3)$ near $r = 0$. Also, since realistically the centre of the collapsing cloud has non-zero density, i.e. $\rho(0, 0) > 0$, we have also $F'''(0) > 0$. Moreover, for $\dot{R}(0, r)$ to be regular, we shall require that

$$\pi(r) \equiv -\frac{rf(r)}{F(r)} \tag{2.8.12}$$

also be regular throughout the dust cloud. Specifically, for $\pi(r)$ to be regular at $r = 0$, we require f to be $\mathcal{O}(r^2)$ near $r = 0$. If we choose the usual scaling $R(0, r) = r$, then the remaining freely specifiable initial data $(f(r), \rho(0, r))$ will be assumed to be atleast square integrable. We will also require that there be no cusps at the centre of the cloud and so, we will impose the restriction that $f(r), \rho(0, r)$ not have terms that are odd powers of r near $r = 0$ [219]. Further, for no trapped surfaces to exist on the Cauchy surface $t = 0$, we require $F(r)/R(0, r) < 1$. Finally, the requirement that there also be no singularity on the Cauchy surface $t = 0$ must be discussed on a case by case basis.

2.8.3   Non-linear Stability of the Datt-Oppenheimer-Snyder Collapse Process

Since the governing equations of motion (2.8.9, 2.8.10) are closed, they evolve valid initial data uniquely and depending on the specific choice of initial data, the singularity may or may not be covered entirely from an asymptotic observer by a horizon, corresponding to the formation of a black hole or a globally naked singularity respectively. Here, for simplicity, we shall restrict ourselves to the class of marginally bound LTB models ($f = 0$). For this class of collapse models, we can immediately integrate equation 2.8.10 to obtain the scale factor R analytically as,

$$R(t, r) = r\left(1 - \frac{3}{2}\sqrt{\frac{F}{r^3}}t\right)^{2/3}. \tag{2.8.13}$$

The energy density $\rho(t, r)$ is then given as,

$$\rho(t, r) = \frac{F'}{r^2\left(1 - \frac{3}{2}\sqrt{\frac{F}{r^3}}t\right)\left(1 - \frac{rF'}{2F}\sqrt{\frac{F}{r^3}}t\right)}. \tag{2.8.14}$$

The above two equations completely specify the marginally bound LTB collapse models. The singularity $t_s(r)$ and the apparent horizon $t_{AH}(r)$ curves are obtained from the conditions $R(t_s(r), r) = 0$ and $R(t_{AH}(r), r) = F(r)$ respectively as,

$$t_s(r) = \frac{2}{3}\sqrt{\frac{r^3}{F}}, \quad t_{AH}(r) = t_s(r)\left[1 - \left(\frac{F}{r}\right)^{3/2}\right]. \tag{2.8.15}$$

Since we have already seen that F is atleast $O(r^3)$ and always non-negative, it is clear from the above equation that $t_{AH}(r) < t_s(r)$ for all $0 < r$. Therefore, outgoing null geodesics emitted from events $(t_s(r), r)$ for $r \neq 0$ are all trapped. Now, to determine the causal structure of a particular model, namely whether it represents a black hole or a globally visible naked singularity, it is necessary to examine families of radial null geodesics emerging from the event $(t_s(0), 0)$. Our analysis closely follows the procedure outlined in [50]. It is evident from equation 2.8.3 that along future-directed radial null geodesics, we have,

$$\frac{dt}{dr} = R'. \tag{2.8.16}$$

More importantly, since we are concerned with outgoing null geodesics that are emitted from $(t_s(0), 0)$, we should check whether there exist null geodesics along which $dR/dr > 0$ at $(t_s(0), 0)$, corresponding to a positive future null expansion. Further, since R vanishes as $t \to t_s(0), r \to 0$, if there exists such a geodesic, then one can find a positive constant α such that along it, near $(t_s(0), 0)$, we can write $R \sim r^\alpha$. α is initial data dependent and, if it exists, can be found via the procedure outlined below.

Now, to analyse dR/dr it is useful to change variables from r to $u = r^\alpha$ so that along null geodesics we can write,

$$\frac{dR}{du} = \frac{1}{\alpha r^{\alpha-1}} \left[R' + \dot{R}\frac{dt}{dr} \right] = \left[1 - \sqrt{\frac{\Lambda}{X}} \right] \frac{R'}{\alpha r^{\alpha-1}} \equiv \left[1 - \sqrt{\frac{\Lambda}{X}} \right] \frac{H(X, u)}{\alpha}, \qquad (2.8.17)$$

where we have introduced $\Lambda(u) = F(u)/u$ and $X(R, u) = R/u$. Further, $H(X, u)$ defined as above can be written out as,

$$H(X, u) = \frac{u^{\frac{3-3\alpha}{2\alpha}}}{\sqrt{X}} \left(1 - \frac{\eta}{3} \right) + \frac{\eta X}{3}, \qquad (2.8.18)$$

where $\eta(u) = u^{1/\alpha} F'/F$. Note that the event $(t, r) = (t_s(0), 0)$ is now at $(R, u) = (0, 0)$. The above differential equation (2.8.17) has a singular point at $(X, u) = (0, 0)$ and if there exist null geodesics that meet this singularity, we can write along them,

$$\lim_{R \to 0, r \to 0} \frac{R}{u} = \lim_{R \to 0, r \to 0} \frac{dR}{du} = X_0. \qquad (2.8.19)$$

and we are assured that they are outgoing if $X_0 > 0$. Therefore, the necessary and sufficient condition for the singularity to be visible in dust collapse is that X_0, which can be found as the root of the algebraic equation,

$$X = \left[1 - \sqrt{\frac{\Lambda_0}{X}} \right] \frac{H(X, 0)}{\alpha}, \qquad (2.8.20)$$

exists and is positive. Here we have introduced $\Lambda_0 = \lim_{u \to 0} \Lambda(u)$. The parameter α is chosen, when possible, such that dR/du is well defined along such null geodesics, i.e. $H(X, 0)$ is well defined.

The existence of a real positive root of equation 2.8.20 ensures that a family of outgoing null geodesics terminates at the singularity in the past and guarantees that the singularity is naked; when no real positive roots exist, the singularity is space-like and the spacetime contains an DOS-like black hole. Even when a real positive root X_0 of equation 2.8.20 exists, whether or not the singularity is globally visible (visible to asymptotic observers) depends on the initial density profile (or equivalently the mass function F), as we discuss below. A singularity is globally visible *if and only if* there exist families of outgoing null geodesics that emanate from the singularity and have a positive future null expansion. This condition is given as (see §III.C of [50]),

$$\eta \Lambda < \alpha X_0. \qquad (2.8.21)$$

The above condition must be satisfied along null geodesics that are outgoing from the the singularity throughout the matter cloud i.e., for $0 \le r \le r_b$. Outgoing null geodesics emanating from the singularity that satisfy this condition continue to remain outside the apparent horizon as they move into the future till they reach the boundary of the dust cloud. These trajectories then reach future null infinity in the exterior Schwarzschild region.
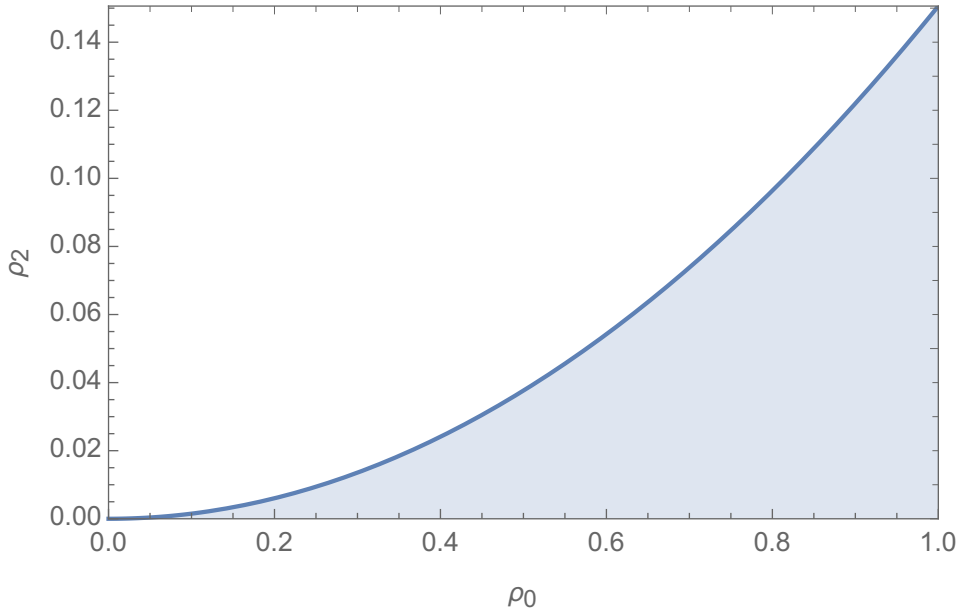
FIGURE 2.2: The space of initial data of the marginally bound Lemaître-Tolman-Bondi dust collapse models with a quadratic initial density profile $\rho(0,r) = \rho_0 - \rho_2 r^2$ ($\rho_2 \geq 0$) is parametrized by (ρ_0, ρ_2). Here we indicate by the shaded region the set of initial data that develop black holes. The complementary region, in white, corresponds to the set of initial data for which the spacetime contains a globally visible naked singularity. Although here we have only displayed the region $0 \leq \rho_0 \leq 1$ of the parameter space, it is evident from equation 2.8.27 that this partitioning is representative of the entire parameter space ρ_0–ρ_2. Also, since we require that the energy condition $\rho \geq 0$ be satisfied throughout the cloud, its maximum radius cannot exceed $r_{b,\,max} = \sqrt{\rho_0/\rho_2}$.

Now, for the choice of initial data we are interested in, the initial density profile is given as,

$$\rho(0,r) = \rho_0 - \rho_2 r^2, \quad \text{with} \ \rho_2 \geq 0. \tag{2.8.22}$$

Then we can expand $H(X,u)$ around $u = 0$ to leading order for each term in equation 2.8.18 to obtain,

$$H(X,0) = \frac{1}{\sqrt{X}} \frac{2\rho_2}{5\rho_0} u^{\frac{7-3\alpha}{2\alpha}} + X. \tag{2.8.23}$$

It is evident that for $H(X,0)$ to be well defined, we must set $\alpha \leq 7/3$. However, we obtain a real root X_0 of the 'root equation' (2.8.20) only for $\alpha = 7/3$, which is now given as,

$$\frac{7}{3}X = \frac{1}{\sqrt{X}} \frac{2\rho_2}{5\rho_0} + X. \tag{2.8.24}$$

That is, $X_0^{3/2} = 3\rho_2/10\rho_0$. Therefore, with the slightest deviation from homogeneity ($\rho_2 > 0$), the LTB singularity becomes locally naked. Further, the condition for global visibility (2.8.21) can be written as,

$$\left(\rho_0 - \rho_2 r^2\right) r^{2/3} < \frac{7}{3}\left(\frac{3}{10}\frac{\rho_2}{\rho_0}\right)^{2/3}. \tag{2.8.25}$$

This inequality must hold for the largest value of the expression on the left, which is attained at $r = \sqrt{\rho_0/4\rho_2}$. Then we can write,

$$\left(\rho_0 - \rho_2 \frac{\rho_0}{4\rho_2}\right)\left(\frac{\rho_0}{4\rho_2}\right)^{1/3} < \frac{7}{3}\left(\frac{3}{10}\frac{\rho_2}{\rho_0}\right)^{2/3}, \tag{2.8.26}$$

to get,

$$\frac{\rho_0^2}{\rho_2} < \left(\frac{7^3 \cdot 4^4}{3 \cdot 10^2}\right)^{1/3} \approx 6.6395. \tag{2.8.27}$$

Using the above inequality, in figure 2.2, we partition the $\rho_0 - \rho_2$ parameter space into regions that develop black holes and globally visible naked singularities at the end of gravitational collapse in blue and white respectively, to obtain insight into the extent of the stability of the formation process of a Schwarzschild black hole from the gravitational collapse of a marginally bound, spherically symmetric ball of dust.

Equivalently, if we impose the condition that the initial density of the dust cloud vanishes at its boundary i.e., $\rho(0, r_b) = 0$, then we obtain $r_b = \sqrt{\rho_0/\rho_2}$ for such a cloud. We can now equivalently parametrize the space of allowed initial data using the ADM mass M of the cloud and its initial radial size r_b. In terms of what we call the initial compactness parameter χ for this cloud,

$$\chi \equiv \frac{M}{r_b} = \frac{1}{15}\frac{\rho_0^2}{\rho_2}, \tag{2.8.28}$$

the above global visibility condition (2.8.27) can be rewritten as,

$$\chi \lesssim 0.4426. \tag{2.8.29}$$

Thus, for a marginally bound collapsing dust cloud with the density profile $\rho(0, r) = \rho_0 - \rho_2 r^2$, the cloud must start off sufficiently extended i.e., it must have a small enough mass to radius ratio (or low compactness) in order to form a global naked singularity. If the cloud is more compact than the above limit, the collapse still leads to a naked singularity, but it is of the local variety. However, when the cloud is perfectly homogeneous at the initial epoch ($\rho_2 = 0$), then the eventual singularity is not visible even locally. If we introduce the Schwarzschild (or gravitational) radius of a cloud of total mass M as $r_{\text{Schw}} = 2M$, then the above equation can also be written as,

$$1.1297\, r_{\text{Schw}} \lesssim r_b. \tag{2.8.30}$$

That is, for these models, if initial radius of the dust cloud is larger than about 1.1297 times its Schwarzschild radius, it ends up forming a globally visible naked singularity. Figure 2.2 indicates the sensitivity of the nature of the eventual singularity, that forms in marginally bound dust collapse, on initial data, i.e. it is demonstrative of the size of the basin of attraction of the Schwarzschild family of spacetime metrics.

2.9   A Geometric Approach to Stability in Classical Mechanics and the attempt to jump to GR[28]

Statements regarding the various notions of stability in GR are typically made in the initial value formulation of GR and there are several excellent review articles in the literature on the same [105–110]. We propose here that restating these notions using symplectic geometry earns us substantial insight since one can then draw formal analogies between the seemingly abstruse notions of stability of spacetimes in general relativity and the more familiar notions of stability in classical Galelei-Newton mechanics.

---

[28]Reprinted excerpt with permission from [**P. Kocherlakota** and P. S. Joshi, Arab. J. Math. (2019)]. Copyright (2019) by Springer.

Therefore, in this section, we review the formal statements of non-linear, linear and mode stability of dynamical systems in classical Galelei-Newton mechanics. We begin with a quick summary of Hamilton's equations and in §2.9.1, we restate their dynamical content in the language of symplectic geometry. In specific, Hamilton's equations can equivalently be thought of as being the flow equations of an appropriately defined symplectic Hamiltonian vector field, with trajectories in phase space corresponding to flows of this vector field. We present the construction of the phase space of a classical mechanical system, which is a symplectic manifold, discuss what constitutes a Hamiltonian system and introduce the concept of the flow of the aforementioned Hamiltonian vector field. Since our eventual aim is to discuss the various formulations of stability analyses of such dynamical systems, we will also define 'tangent (to the Hamiltonian vector field) flows.' In §2.9.2, we discuss the various notions of stability and it will become apparent that this geometric approach supplies valuable insight.

Our discussions here will be limited to autonomous or time-independent Hamiltonian dynamical systems, whose descriptions on symplectic manifolds is well established [220–227]. We take the view that a discussion of non-autonomous Hamiltonian systems does not add substantial additional insight towards our primary goal of highlighting the analogy between the notions of stability in CM and GR. Further, noting that non-autonomous Hamiltonian dynamical systems can, in various settings, be replaced by autonomous Hamiltonian dynamical systems defined on 'extended phase space' (see for example [228, 229]), we shall conveniently omit a review of such systems.

Now, in the canonical Hamiltonian formulation of CM, an arbitrary instantaneous state of a dynamical system with n-degrees of freedom is characterized by specifying its generalised coordinates $(q^1, q^2, \cdots, q^n)$ and momenta $(p_1, p_2, \cdots, p_n)$. The collection of all such possible states is called its phase space. Then, given a Hamiltonian function $H(q^1, q^2, \cdots, q^n, p_1, p_2, \cdots, p_n)$ defined over phase space, the governing dynamical equations are the Hamilton equations given as,

$$\frac{\mathrm{d}q^i}{\mathrm{d}t} = \frac{\partial H}{\partial p_i}, \quad \frac{\mathrm{d}p_i}{\mathrm{d}t} = -\frac{\partial H}{\partial q^i}. \tag{2.9.1}$$

That is, given a specific initial state $(q^1(0), q^2(0), \cdots, q^n(0), p_1(0), p_2(0), \cdots, p_n(0))$ of the system, its unique future time evoution is obtained by solving the initial value problem of Hamilton's equations.

2.9.1 Dynamics using Symplectic Geometry in Classical Mechanics

The instantaneous configuration of an autonomous dynamical system, in classical mechanics, is described by the values of the n-generalized coordinates $(q^1, q^2, \cdots, q^n)$ and corresponds to a particular point q in configuration space Q. An element in the cotangent bundle T^*Q of configuration space consists of a 1-form defined in the cotangent space T_q^*Q at every point $q \in Q$, and such a form is given by its n-components $(p_1, p_2, \cdots, p_n)$, which characterize the instantaneous generalized momentum of the system of interest (see for example Ch. 8 of [221]). These $2n$ numbers, denoted succinctly by $z^a \equiv (q^1, q^2, \cdots, q^n, p_1, p_2, \cdots, p_n)$, with the index a running from 1 to $2n$, form a collection of local coordinates for points in T^*Q, which can then immediately be identified as the momentum phase space (henceforth, just phase space) of the dynamical system under consideration.

Further, since phase space is the cotangent bundle of a smooth manifold, it comes naturally equipped with a symplectic structure and is therefore a symplectic manifold; i.e., there exists a closed, non-degenerate

differential 2-form ω on T^*Q. In the current context, this symplectic 2-form is simply given as,

$$\omega = \sum_{i=1}^{n} dp_i \wedge dq^i. \tag{2.9.2}$$

Since ω is non-degenerate, it sets up an isomorphism from the tangent bundle to the cotangent bundle of phase space, $\omega : T\Pi \to T^*\Pi$, where we have introduced $\Pi \equiv T^*Q$ to denote phase space. Then for every smooth, real-valued function $H : \Pi \to \mathbb{R}$, one can associate a unique vector field X_H via $\omega(X_H, \bullet) = -dH$. Introducing the inverse isomorphism, $\Omega : T^*\Pi \to T\Pi$, $\Omega = \omega^{-1}$, which in local coordinates is given as,

$$\Omega^{ab} = \begin{bmatrix} 0_n & I_n \\ -I_n & 0_n \end{bmatrix}, \tag{2.9.3}$$

where O_n and I_n are the n-dimensional zero and identity matrices, we find $X_H \equiv \Omega\, dH$. And in local coordinates we can write,

$$X_H^a = \Omega^{ab} \partial_b H = \Omega^{ab} \frac{\partial H}{\partial z^b} = \left(\frac{\partial H}{\partial p_1}, \frac{\partial H}{\partial p_2}, \cdots, \frac{\partial H}{\partial p_n}, -\frac{\partial H}{dq^1}, -\frac{\partial H}{dq^2}, \cdots, -\frac{\partial H}{dq^n} \right). \tag{2.9.4}$$

X_H is a symplectic vector field since it leaves the symplectic structure invariant, i.e. it satisfies $\mathscr{L}_{X_H} \omega = 0$, where $\mathscr{L}_{X_H}$ is the Lie-derivative w.r.t. X_H. Any such function H is called a Hamiltonian function and X_H is the associated symplectic Hamiltonian vector field.

The flow of X_H is a 1-parameter Lie group of symplectomorphisms $\phi_H^t : \mathbb{R} \times \Pi \to \Pi$ such that for some $z_0 \in \Pi$, $\phi_H^t(z_0) : \mathbb{R} \to \Pi$ is an orbit or integral curve of X_H, which passes through z_0 at $t = 0$. Let us denote such an orbit in local coordinates as $z^a(t) \equiv z^a(\phi_H^t(z_0))$. Then we can write,

$$\dot{z}^a(t) = X_H^a(z(t)), \; z^a(0) = z_0^a, \tag{2.9.5}$$

where the overdot represents differentiation w.r.t. t. It is apparent now that Hamilton's equations (2.9.1) are just the local flow equations of the symplectic Hamiltonian vector field X_H and $\phi_H^t(z_0)$ is the unique trajectory or future development in phase space of the Hamiltonian system with initial data z_0. Finally, we define a Hamiltonian system itself as being given by the triple (Π, ω, X_H). We also note that while we have used local coordinates here, all of the above can be stated in a coordinate-independent manner, making it explicitly symplectomorphism-invariant.

2.9.2   Stability of Hamiltonian Systems in Classical Mechanics

In classical mechanics, given a particular Hamiltonian system (Π, ω, X_H), equilibrium corresponds to a stationary state for variables describing such a system. This means that if a system has initial data $z_0 = z_\star$, and under Hamiltonian evolution one finds a stationary solution $z^a(t) = z_\star^a$, then $z_\star \in \Pi$ is an equilibrium point of the dynamical system. It is clear from the flow equations (2.9.5) that the Hamiltonian vector field must have a critical point there, i.e. we have $X_H(z_\star) = 0$. One can now inquire after the nature of the stability of $z_\star$. Such questions are typically concerned with the nature of future developments of initial data 'close' to it; i.e. under a 'moderate' change in initial data near a critical point, does the trajectory change drastically?

Alternate notions of stability of mechanical systems exist (see for example [230]). For example, the Kolmogorov-Arnold-Moser theory [231–234] is an example of a framework within which stability of flows against moderate changes in the Hamiltonian function H itself are dealt with. This sort of a *structural* stability analysis is important in various scenarios [235–237]. Here however we shall purely concern ourselves with stability of future time evolutions against changes in initial data. To qualify the nature of the stability of equilibrium points, we provide below the formal definitions of the notions of non-linear (or Lyapunov), linear and mode (or spectral) stability. There exist other closely related notions of stability, namely of asymptotic or of exponential stability, but we will not go into these here (see §1 of [112] for a description of these ideas, in the context of general relativity).

Definition: A critical point $z_\star \in \Pi$ of a Hamiltonian system (Π, ω, X_H) is non-linearly stable (Lyapunov stable) if for every neighborhood $U \subset \Pi$ of $z_\star$ there is a neighborhood $V \subset U$ of $z_\star$ such that for every $z \in V$ the corresponding orbit of the Hamiltonian vector field $\phi_H^t(z)$ remains in U for all $t \geq 0$. Further, if $z_\star$ is not stable, it is unstable.

A non-linear stability analysis of a critical point of a dynamical system is, in general, highly non-trivial since for arbitrary Hamiltonian functions, the associated vector field could define a non-linear flow and one is forced to look for solutions to complicated non-linear differential equations. Therefore, the extent of the stability (the size of the region of attraction and the behaviour of transients as they approach the equilibrium, for instance) is typically determined by the non-linearities of the system. However, due to the complexities involved in a non-linear stability analysis, as a preliminary measure, one considers the relatively simpler notions of linear stability.

A linear stability analysis is concerned with studying the behaviour of the future developments of initial data chosen within an *infinitesimal* neighbourhood $\delta U_\star \subset \Pi$ of the equilibrium point $z_\star$, and whether or not they converge to $z_\star$ at late times $t \rightarrow \infty$. For $z \in \delta U_\star$, we now introduce $\xi^a(t) \equiv z^a(t) - z_\star^a$. Then since $|\xi^a(0)| \ll 1$, the Hamiltonian flow equations (2.9.5) can be rewritten as,

$$\dot{z}_\star^a + \dot{\xi}^a = X_H^a\,(z_\star + \xi) = X_H^a(z_\star) + (\mathscr{L}_{H\star})^a{}_b\,\xi^b + \mathcal{O}(|\xi^a|^2), \tag{2.9.6}$$

where $\mathscr{L}_{H\star}$ is the Jacobian of the symplectic Hamiltonian vector field X_H at $z_\star$ and given as,

$$(\mathscr{L}_{H\star})^a{}_b \equiv \partial_b X_H^a(z_\star) = \partial_b \Omega^{ac} \partial_c H(z_\star) = \Omega^{ac} \partial_c \partial_b H(z_\star). \tag{2.9.7}$$

From the above, it can be seen that $\mathscr{L}_{H\star}$ can also be thought of as being the symplectic Hessian of the Hamiltonian function H. $\mathscr{L}_{H\star}$ is a constant Hamiltonian matrix, i.e. it satisfies $\mathscr{L}_{H\star}^T \Omega + \Omega \mathscr{L}_{H\star} = 0$. Then, the equation of motions near a critical point, to leading order in $|\xi^a|$, are given as,

$$\dot{\xi}^a = (\mathscr{L}_{H\star})^a{}_b\,\xi^b, \tag{2.9.8}$$

The above set of equations (2.9.8) are called the linearized equations of motion (about a fixed point of the Hamiltonian vector field), and are simply the flow equations of $L_{H\star}$, which is therefore called the linearization of the symplectic Hamiltonian vector field at the equilibrium point (see for example [238]). A solution $\xi(t)$ to these flow equations is called the tangent flow and we are now in a position to describe the statement of linear stability of a critical point of a Hamiltonian system.

Definition: A critical point $z_\star \in \Pi$ of a Hamiltonian system (Π, ω, X_H) is linearly stable if all orbits of the tangent flow are bounded for all forward time.

That is, to gauge the linear stability of a dynamical system against perturbations in initial data, we want to know whether the size of arbitrary solutions ξ grows, stays constant, or shrinks as $t \to \infty$. At simple critical points of the symplectic Hamiltonian vector field $z_\star$, the linearization $\mathscr{L}_{H\star}$ is non-singular, and under the assumption of distinct eigenvalues, we can write,

$$\xi(t) = \sum_{a=1}^{2n} c_a \mathrm{e}^{\mathrm{i}\sigma_a t} v_a, \tag{2.9.9}$$

where $\mathrm{i}\sigma_a$ and v_a are the eigenvalues and eigenvectors of $\mathscr{L}_{H\star}$ respectively. We have introduced the additional factor of i to match the usual convention in physics, and our discussion henceforth will be in terms of σ. It is not difficult to show that the eigenvalues of a Hamiltonian matrix come in $\pm$ pairs [221]. Consequently, equation 2.9.9 has exponentially growing or decaying terms unless all σ lie on the real axis. When $\mathscr{L}_{H\star}$ is singular, to perform a linear stability analysis, one must naturally look at flows of the first non-singular higher-order symplectic derivative of the Hamiltonian function at the critical point $\partial_{c_1}\partial_{c_2}\cdots\partial_{c_n}\Omega^{ab}\partial_b H(z_\star)$.

However, studying the forward time boundedness of *every* solution $\xi(t)$ of the linearized equations of motion is a demanding prospect, and a more tractable endeavour is to carefully examine the distribution of the eigenvalues of the Hamiltonian matrix $\mathscr{L}_{H\star}$, to find which eigenvectors represent stable and unstable directions in phase space. Now, the weakest statement (though still extremely useful) that can be made regarding the stability of a dynamical system is then as follows.

Definition: A critical point $z_\star \in \Pi$ of a Hamiltonian system (Π, ω, X_H) is mode stable (spectrally stable) if all eigenvalues of its corresponding linearization $\mathscr{L}_{H\star}$ lie in the left-half plane (or equivalently when all σ lie in the upper-half plane).

Then, eigenvectors corresponding to real σ are called normal modes and the eigenvalues σ themselves are called normal frequencies. Normal modes are the fundamental oscillatory modes of any conservative system. Similarly, eigenvectors corresponding to σ with non-zero imaginary parts are called quasi-normal modes (QNMs) and the corresponding eigenvalues σ are called quasi-normal frequencies (QNFs). These are the fundamental oscillatory modes of every dissipative system and the QNF is a complex number with two pieces of information: its real part corresponds to the temporal oscillation and its imaginary part captures the temporal rate of growth or decay. Therefore, from the properties of the linearization $\mathscr{L}_{H\star}$, one can identify the local stable and unstable manifolds of the critical point, denoted by $E_{\star s}$ and $E_{\star u}$, which are linear subspaces of $T_{z_\star}\Pi$, of dimensions given by the number of stable ($\mathrm{Im}(\sigma) \geq 0$) and unstable eigenvalues respectively, and spanned by the relevant eigenvectors and (in the degenerate case) generalised eigenvectors [239].

We note here a well-known comment regarding the relation between mode and linear stability. Mode stability excludes a particular type of exponentially growing solution; it does not rule out exponential growth in general let alone show that solutions are bounded or decay. The latter would correspond to full linear stability. The precise relation between the two, for autonomous Hamiltonian systems, is that an equilibrium is linearly

stable if and only if it is mode stable and all the Jordan blocks of the associated linearization matrix $L_{H\star}$ are one-dimensional [220, 221].

In summary, when examining the stability of a critical point, the first useful thing to do is to work in the linear approximation. However, for real applications, sometimes just a linear stability analysis can be very misleading and one must therefore pursue a study of the full non-linear stability of equilibria. Thus, nonlinear stability $\Rightarrow$ linear stability $\Rightarrow$ mode stability. Hamiltonian systems that exhibit resonance are classic examples of dynamical systems whose equilibrium configurations are mode stable but linearly unstable (see for example p. 33 of [224]). An example of a Hamiltonian system that has a critical point that is linearly stable but non-linearly unstable is the famous Cherry Hamiltonian [240].

Following [241], we now introduce the notions of a dynamical attractor and its basin of attraction; their use will become apparent in §2.9.3 when we discuss the stability of spacetimes in GR, and families of spacetimes. A critical point $z_\star$ of a dynamical system is called an attractor if points in some strictly positive measure neighbourhood $\rho(z_\star) \subset \Pi$, called its realm of attraction, flow to $z_\star$ in forward asymptotic time, i.e. for every $z \in \rho(z_\star)$, $\lim_{t\to\infty} \phi_H^t(z) \to z_\star$. If additionally the realm of attraction of such an attractor has the topology of an open set in Π, then it is typically called a basin of attraction, which we shall denote by $B(z_\star)$. Now, clearly, such an attractor corresponds to a linearly stable critical point, since $B(z_\star)$ contains within it an infinitesimal open neighbourhood of the attractor $\delta U_\star$. Further, the size of the basin of attraction of such an attractor is indicative of the extent of its non-linear (or Lyapunov) stability. If instead $\rho(z_\star)$ is a lower dimensional smooth manifold, then it is generally called the stable manifold of the attractor, akin to $E_{\star s}$ introduced above (note however that $E_{\star s}$ has been defined to be a *local* stable manifold). Such types of attractors were first discussed in [242–244].

Further, when a dynamical system admits a compact set of critical points in phase space, one can introduce the notion of a compact invariant set $C \subset \Pi$. Such sets C may be regarded as being generalizations of critical points [242]. If points in some strictly positive definite measure neighbourhood of C, which we will denote by $\rho(C)$ and call the realm of attraction of C, flow to C, i.e. $C = \bigcup \phi_H^t(z)$ for $z \in \rho(C)$, then C is called a dynamical attractor. Completely analogous criterion for when a compact invariant set is an attractor with a basis of attraction are discussed in [241], and the size of its basis of attraction determines the extent of its non-linear stability.

2.9.3   Symplectic Geometry and General Relativity

Now, to restate all of the notions of mode, linear and non-linear stability of spacetimes discussed earlier into the language of symplectic geometry, we need to define the conjugate momentum to q and identify the phase space of GR [245]. For this, one requires an explicit notion of time, which has the implication that one can only consider spacetimes that are topologically of the form $\Sigma \times \mathbb{R}$, where Σ is a 3-dimensional manifold of arbitrary, fixed topology and $\mathbb{R}$ is time. Due to the discussion presented above, this restriction is typically not considered a strong limitation. However, it is useful to remember that not all solutions of the Einstein field equations are globally hyperbolic. For example, the maximally extended Reissner-Nordstrom solution, representing the spacetime for a spherically symmetric charged particle, has a Cauchy horizon i.e., there is a region from which there exist past directed causal curves that do not pass through any candidate Cauchy surface. Generally such solutions are discarded as being physically unrealistic since a desirable quality of physical theories is that they be deterministic and that there exist a one-to-one map between the initial state

of motion and its trajectory ('a continuous dependence of the evolution on initial data'). However, it is still unclear whether only globally hyperbolic spacetimes should be considered in GR [246]. Here however we will restrict ourselves to a discussion of the stability of only globally hyperbolic spacetimes.

Further, one also requires the the symplectic structure [247] and the Hamiltonian [248] of GR, thus forming the Hamiltonian system of interest (Π, ω, X_H). Then, by analogy with the analysis for classical mechanics presented earlier, it will become clear how one can think about the usual notions of stability of a given spacetime. In our discussion here, we shall concern ourselves primarily with spacetimes devoid of matter i.e., the only degrees of freedom of such a system are purely gravitational and the sole dynamical entity is the metric tensor g. At the end of this section, we will mention how one could carry this analogy through to include matter.

Given a particular initial data set (q, K) that belongs to the space of valid initial data, one can define the corresponding element (q, p) of the phase space of general relativity Π via (see for example §20 of [164]),

$$p^{ij} = \sqrt{|q|}(K^{ij} - q^{ij}K^k_{\ k}), \tag{2.9.10}$$

where $|q| \equiv \det(q_{ij})$ and p, the momentum conjugate to q, is a symmetric 2-tensor. Then, we can write the Hamiltonian density function as [164],

$$\mathcal{H}_{\text{ADM}} = \alpha \left[-\sqrt{|q|} \ {}^{(3)}R + \frac{1}{\sqrt{|q|}} \left(p^{ij}p_{ij} - \frac{1}{2}|p|^2 \right) \right] - 2\beta_j \nabla_i p^{ij}, \tag{2.9.11}$$

where α and β are the lapse function and the shift vector respectively, as usual, and $|p| = \det(p^{ij})$. The ADM Hamiltonian is given as $H_{\text{ADM}} = \int_\Sigma \mathcal{H}_{\text{ADM}}$. With little effort, it is evident that the variation of H_{ADM} w.r.t α, β simply gives the constraint equations (2.7.1), rewritten in terms of q, p. The variation w.r.t the dynamical degrees of freedom[29] q, p now gives the Hamilton equations for GR,

$$\dot{q}_{ij} = \frac{2\alpha}{\sqrt{|q|}} \left(p_{ij} - \frac{1}{2}q_{ij}|p| \right) + \nabla_{(i}\beta_{j)}, \tag{2.9.12}$$

$$\dot{p}^{ij} = -\alpha\sqrt{|q|} \left({}^{(3)}R^{ij} - \frac{1}{2} \ {}^{(3)}Rq^{ij} \right) + \frac{\alpha q^{ij}}{2\sqrt{|q|}} \left(p_{mn}p^{mn} - \frac{1}{2}|p|^2 \right) - \frac{2\alpha}{\sqrt{|q|}} \left(p^{ik}p_k^{\ j} - \frac{1}{2}|p|p^{ij} \right) \tag{2.9.13}$$

$$+ \sqrt{|q|}(\nabla^i\nabla^j\alpha - q^{ij}\nabla^i\nabla_i\alpha) + \sqrt{|q|}\nabla_k \left(\frac{\beta^k p^{ij}}{\sqrt{|q|}} \right) - 2p^{k(i}\nabla_k\beta^{j)}.$$

The above equations are just the flow equations of the symplectic Hamiltonian vector field obtained from the ADM Hamiltonian function H_{ADM}. However, before one can study the stability of its critical points, one must worry about gauge degeneracies and the construction of the reduced phase space by forming the quotient space of the constrained phase space with the gauge orbits. Then on reduced phase space, one would be able to successfully draw a formal analogy between the notions of stability in classical mechanics to those in general relativity. This will be attempted elsewhere and here we only present partial results as motivation for the extended, deeper study.

It is clear that the Minkowski metric $g_{0,0}$, a stationary solution of the Einstein field equations, is a critical point in the phase space of the ADM Hamiltonian dynamical system. Similarly, it can be seen then that

---

[29]Note that the lapse function α and shift vector β are not dynamical because they describe how coordinates move in time from one hypersurface to the next and have to be fixed by four gauge conditions (see for example [172]). One simple choice corresponds to the Gaussian normal coordinates, for example, where one sets $\alpha = 1, \beta = 0$.

the Schwarzschild one-parameter family of solutions $g_{M,0}$ is a compact invariant set and the Kerr two-parameter family of metrics $g_{M,a}$ forms an even larger compact invariant set in phase space. Now, the results of Christodoulou and Klainerman [166] imply that the Minkowski solution is a dynamical (critical point) attractor in phase space and the results of Dafermos, Holzegel and Rodnianski [112] indicate that the Schwarzschild family of solutions is also an (compact invariant set) attractor in phase space. The basin of attraction of the Schwarzschild attractor remains to be completely characterized, and we make a restricted attempt to address this in §2.8.3. Now, we can express one of the most important aims of stability studies in general relativity, with significant implications for observational astrophysics, as being to show that the full Kerr family of solutions is an attractor, and a complete characterization of its basin of attraction will conclude a non-linear stability analysis of the Kerr family of spacetimes.

When matter is present, the full classical action of this system is given by the Einstein–Hilbert Lagrangian plus a piece describing the matter fields ϕ_i appearing in the theory, and extremizing this action with respect to the metric tensor $g_{\mu\nu}$ yields,

$$G_{\alpha\beta} \equiv R_{\alpha\beta}(g) - \frac{1}{2}g_{\alpha\beta}R(g) = T_{\alpha\beta}, \tag{2.9.14}$$

as we have seen above. Naturally, one needs to include the coupled matter equations of motion arising from the extremization of the action w.r.t. the matter fields ϕ_i to obtain the full set of equations that govern the dynamics of this system. In general, this set of Einstein plus matter equations of motion do not form a closed set of partial differential equations and one is required to introduce a constitutive relation determining the energy-momentum tensor $T_{\mu\nu}$ from the metric and the matter fields g and ϕ_i. These equations and relations can be constructed from the appropriate classical field theory describing the matter model of interest, scalar or electromagnetic fields or hydrodynamic fluids etc. (see for example [9, 106]). The initial data then for the associated Cauchy problem will is given by $d = d_g \cup d_m$, where d_m denotes the initial data for the matter sector.

2.10 Conclusions[30]

In this chapter we have reviewed some basic material pertaining to stability of spacetimes, and have discussed in detail the findings of our works [71, 104]. We end this chapter with a quick summary.

Reviewing [71], we have shown that there if one imposes a specific condition (2.5.28) as the inner boundary condition for the quasi-normal modes of a near-extremal superspinar, it mode stable. However, as discussed above, since equation 2.5.19 does not possess a singular point on the real axis of r in the superspinar case, a natural choice for inner boundary conditions does not exist, such that when imposed, they uniquely determine C and D, as was the situation when computing the QNF spectrum for Kerr black holes (purely ingoing waves at the horizon). Essentially, there is no *physical* requirement that determines $\tilde{\omega}$ for superspinars. We must, in this situation, rephrase the question of mode stability from usual one, i.e., "Which sign does $\tilde{\omega}_I$ have?", to

> *Does there exist a class of interior boundary conditions under which near-extremal Kerr super-spinars are mode stable?*

If such boundary conditions exist, then one could find such stable superspinars to understand their physical nature, leading to new insights.

Since we must check whether a near-extremal Kerr superspinar is stable against arbitrary boundary conditions at the inner edge of the spacetime, we now substitute equatoneions 2.5.23 and 2.5.24 into the outer boundary condition equation for QNMs (2.5.27). This yields,

$$D\sigma^{\tilde{s}}\left[\mathcal{F}(-\tilde{s}, \delta, -\tau/\sigma, -\tilde{\omega}) + \mathcal{F}(-\tilde{s}, -\delta, -\tau/\sigma, -\tilde{\omega})\right] = -C\sigma^{\frac{4i\tau}{\sigma}}\left[\mathcal{F}(\tilde{s}, \delta, \tau/\sigma, \tilde{\omega}) + \mathcal{F}(\tilde{s}, -\delta, \tau/\sigma, \tilde{\omega})\right],$$
(2.10.1)

where we have introduced $\mathcal{F}$ as,

$$\mathcal{F}(\tilde{s}, \delta, \tau/\sigma, \tilde{\omega}) = (-2i\tilde{\omega})^{-i\delta} \frac{\Gamma(2i\delta)\Gamma(1 + 2i\delta)\Gamma(1 + 4i\tau/\sigma - \tilde{s})}{\Gamma(1/2 - 2i\tilde{\omega} + i\delta - \tilde{s})\Gamma(1/2 + 2i\tilde{\omega} + i\delta - \tilde{s})\Gamma(1/2 - 2i\tilde{\omega} + i\delta + 4i\tau/\sigma)}.$$
(2.10.2)

The answer to this new question is then "*Yes*," since we may regard $\tilde{\omega}$ as an input parameter and equation 2.10.1 simply determines the ratio between the integration constants C and D.

Now, suppose we assume $\tilde{\omega} = m/2 + i\tilde{\omega}_I$ with $\tilde{\omega}_I = \mathcal{O}(|\epsilon|^p) < 0$. Since $\tilde{\omega}_I$ may be left to arbitrary as long as it is negative and is of size $\mathcal{O}(|\epsilon|^p)$, we obtain essentially an infinite number of boundary conditions under which near-extremal Kerr superspinars are stable. Once the ratio between C and D is determined through 2.10.1, we also obtain the ratio between A and B since the matching condition (2.5.25) must be satisfied. As a result, we have a damping solution for quasi-normal modes and can find the boundary condition at, for example, $y = 0$ from such a solution.

It is useful to remember that the present analysis is restricted to the modes of $m = l$ for the near-extremal case. However, situations for the fundamental and overtone modes of general l and m are qualitatively similar to the case when $m = l$. Since the radial Teukolsky equation (2.5.8) for superspinars has no singular point on the real axis, solutions with any frequencies can be regular in the domain $r > r_0$ (with r_0 an arbitrary constant) under the usual outer boundary condition for quasi-normal modes. That is, we do not have to explicitly solve the Teukolsky equation as an eigenvalue problem even to ensure the regularity of the solution. After solving the Teukolsky equation under the no-incoming wave condition at infinity, we will find inner boundary conditions at $r = r_0$; the set of such inner boundary conditions for all complex frequencies is denoted by $\mathcal{U}_{BC}$. This fact implies that we may assume any spectrum of the QNM for each l and m, which is a discrete set of complex numbers with negative imaginary parts (e.g., the QNM spectrum of the Kerr black hole). This assumption is equivalent to that on boundary conditions at $r = r_0$, which are elements of $\mathcal{U}_{BC}$ if and only if the frequencies are equal to those of assumed QNM spectrum. It is however a very non-trivial issue how to find out the physical information about the superspinar from the obtained boundary conditions at $r = r_0$, and hence it should be a future work. Although this is the "inverse problem" to the linear stability analysis, it is worthwhile to notice that the spectrum of the QNM frequencies cannot completely determine the physical nature of the superspinar since it does not uniquely fix the inner boundary condition.

Finally, it is to be noted that our findings are consistent with the numerical results reported in [70]. There, the Teukolsky equation was solved under two kinds of interior boundary conditions (i.e. at $r = r_0$): those corresponding to perfect reflection and perfect absorption. Figure 3 therewith shows that the imaginary part of the QNM frequency is negative for sufficiently large or small r_0 under the reflection boundary condition, or equivalently, that near-extremal superspinars are stable in these situations. Further, when $r_0 = 2M$, the

superspinar is stable against the perturbations with $l = 2$, $m = 0, 1, 2$. It appears that a mode with a larger m-value requires a larger r_0-value for it to correspond to a dying perturbation. This tendency seems to be reasonable from the point of view of the ergoregion instability [249, 250]: if there is an ergoregion around an axisymmetric stationary object, it is unstable against large m modes. If we regard r_0 as the surface of the superspinar, then naturally there is no ergoregion around the superspinar when $r_0 > 2M$. Therefore, it seems to be reasonable to conjecture that sufficiently large superspinars do not suffer from an ergoregion instability.

However, it should be noted that r_0 does not have to be a surface of the superspinar. A smooth extension of the solution to the domain, $r < r_0$ could be possible, due to the absence of a singular point in the radial Teukolsky equation. Therefore, the reflection boundary condition at $r = r_0 > 2M$ is equivalent to some other regular boundary condition imposed at, for example, $r = M$. Hence, figure 3 of [70] is also consistent with our statement that there exist infinitely many boundary conditions under which a near-extremal Kerr superspinar is mode stable.

<center>***</center>

Following [125], we have also discussed the stability analyses of equilibria of dynamical systems, in both classical mechanics and general relativity, in the framework of symplectic geometry, and have attempted to set up a neat analogy to enable a simple pedagogical discussion of the notions of the stability of a spacetime. We reviewed the Hamiltonian formulation of GR to remember how the governing equations of motion of a Hamiltonian dynamical system are simply the flow equations of the associated symplectic Hamiltonian vector field, defined on phase space. However, since here we have not accounted for gauge degeneracies in the ADM phase space, and the construction of the reduced phase space by forming the quotient space of the constrained phase space with the gauge orbits is not addressed, our results presented here are incomplete. The eventual goal will be to draw a formal analogy between the notions of stability in classical mechanics to those in general relativity, using its reduced phase space; the non-linear stability analysis of its critical points would simply have to do with the divergence of its flow on reduced phase space. Further, the linear stability of a critical point is concerned with the divergence of the flow of the linearization of the Hamiltonian vector field, otherwise called the tangent flow, at the critical point.

Also, as was pointed out here, only the set of globally hyperbolic spacetimes can be studied within the Hamiltonian formulation of GR [251], and for such spacetimes one can apply methods of symplectic geometry. Further, there is an isomorphism from the space of all globally hyperbolic solutions of the vacuum Einstein field equations to the space of allowed initial data. This is clear heuristically if one thinks of the solutions or 4-dimensional metrics g as being given equivalently by a one-parameter family of 3-dimensional Riemannian metrics $q(t)$ that satisfy the flow equations of the ADM+matter symplectic Hamiltonian vector field (along with the lapse function and the shift vector, of course). Then, if one quotients out the gauge orbits, roughly a collection of all allowed $q(t)$ would correspond to the space of solutions of the Einstein field equations. Since within the class of globally hyperbolic spacetimes, a particular evolution from a particular initial data set depends continuously on it, and trajectories in phase space don't intersect, it is possible to characterize a solution uniquely by its initial data $q(0)$. Typically, both these spaces (of solutions $q(t)$ and of initial data $q(0)$) are equivalent characterisations of the phase space of a physical theory and this is a feature of most typical (deterministic) physical theories like classical mechanics, quantum mechanics etc. Therefore, studying the stability of a given spacetime g (orbital stability) is equivalent to studying the stability (divergence) of the Hamiltonian flow near the initial data $q(0)$ that it evolves from. Further, if one shows that a particular critical

point $q_\star$, corresponding to a stationary solution $q(t) = q_\star$, is an attractor with a basin of attraction in phase space, then $q_\star$ corresponds to the metric of a linearly stable stationary spacetime. Additionally, the extent of its basin of attraction determines how non-linearly stable it is.

Since this is a nascent study, we have not analysed the potential benefits, from a numerical standpoint, of conducting a stability analysis using symplectic geometry here. One can numerically find the critical points of a Hamiltonian system by flowing along and minimising the (normal) gradient of its Hamiltonian function. Once such critical points are identified, one could study the properties of the local flow equations of the symplectic gradient of the Hamiltonian function numerically to gain insight into the nature of the stability of these critical points. Already in other contexts, for example, in applications of the theory of chaotic kinematics to oceanographic and atmospheric sciences, condensed matter, particle, accelerator and plasma physics, and also in string theory, symplectic geometry has proven to be a useful tool [252–257].

It is worth emphasising here that in general relativity, given an exact solution, obtaining the initial data set that it evolves from is generally a task of great difficulty and the branch of gravitational collapse, for example, is concerned with these issues. One of the few well characterized solutions $q(t)$ is the collapse process to a Schwarzschild black hole, which allowed us to demonstrate a non-linear stability analysis in the context of GR in §2.8.3. As mentioned before, some (non-globally hyperbolic) solutions of the Einstein field equations cannot even be found to depend continuously on initial data. Taking advantage of the fact that the evolution of a spherically symmetric, regular cloud of pressureless matter to a Schwarzschild black hole is known to be given by the Datt-Oppenheimer-Snyder collapse ([44]), it's initial data is well characterised, and the evolutions of nearby initial data are also well understood (determined by the Lemaître-Tolman-Bondi collapse models), we discussed the visibility of the eventual spacetime singularity that forms in these collapse evolutions. In specific, the DOS collapse to a Schwarzschild black hole evolves from homogeneous initial data ($\rho(0, r) = \rho_0$) and we considered a 2-parameter open subset of initial data $\rho(0, r) = \rho_0 - \rho_2 r^2 (\rho_2 \geq 0)$ around it. We showed that the initial compactness $\chi = M/r_b$ of collapsing cloud (where M is the total ADM mass of the cloud and r_b is its initial radius) governed the nature of the singularity in these models, i.e. when $\chi \lesssim .44$, the cloud formed a globally visible naked singularity and a black hole otherwise.

Part II: Detection of Black Holes and Naked Singularities

Chapter 3

Shadows and Images of Spherically Symmetric Black Holes and Naked Singularities[1]

3.1 Introduction

The study of shadows and images of compact objects has been a subject of great interest. The optical appearance of a star collapsing through its gravitational radius was first studied in [258], and of a star orbiting an extreme Kerr black hole in [259]. Many authors have studied the characteristics of shadows cast by various black holes [260–268]. Structures of shadows and images of black holes have been discussed in the context of determining their spins and masses, and in testing general relativity [43, 269, 270]. Implications of black hole shadows on the distribution of dark matter have been explored in [271]. The time-dependence of the angular radius of the shadow in the course of formation of a black hole from gravitational collapse has also been calculated in [272].

One of the early explorations of images and shadows cast by naked singularities was given in [273]. They studied how the central naked singularity that formed during the collapse of a self-similar dust cloud, was observed by distant observers. By investigating radial and non-radial null geodesics emanating from the singularity, they were able to show that the angular diameter of the image is time dependent; it grows monotonically and approaches the value $3\sqrt{3}M/R_o$ for an observer at $R = R_o \gg M$. The asymptotic value of the angular diameter comes from the geometry of the exterior Schwarzschild region. Later, in [274] the radiation emitted by collapsing spherically symmetric dust clouds evolving from different initial data, leading to both black holes and naked singularities as end states, was studied. They found that within their simplified model, both these objects had very similar observational features and that it was difficult to differentiate between them based on their light curves. That the redshift of photons travelling from past to future null infinity through a ball of collapsing dust could provide an observational signature capable of differentiating between the formation of a globally naked singularity from the formation of an event horizon was pointed out

in [275]. In a folllow up [276], it was shown that although at late times the image of the source perceived by the observer looks the same in both cases, the dynamical formation of the shadow and the redshift images have distinct features and time scales. Effects of gravitational lensing around naked singularities have also been investigated [277, 278]. Shadows cast by the overspinning Kerr geometry with its central singularity excised (akin to the superspinars above §2.5) were considered in [279].

The shadows and images cast by a compact object with a thermally emitting surface were studied in [280] and compared against those of a black hole. They showed that, in some cases, the images could be nearly identical. The geometry outside compact objects modeled using a static spherical polytropic perfect fluid was examined in [281] and it was found that they admit no photon spheres and therefore cast no shadows, allowing them to be distinguishable from black holes. The subject of whether there are supercompact objects, that are not black holes, which possess unstable circular orbits of photons, and how one can distinguish them from black holes based on their shadows was explored in [282]. Considering the spherical thin-shell model of a gravastar, it was found in [283] that unstable circular orbits of photons can appear around the gravastar, and that one could tell the difference between a black hole and a gravastar with high-resolution very-long-baseline-interferometry observations in the near future. Shadows cast by horizonless exotic compact objects such as wormholes have also been a subject of great interest [284–287].

Recently, physically reasonable spherically-symmetric gravitational collapse scenarios that end up as naked singularities were investigated in [51, 113], and various properties of these spacetimes were computed, such as the nature of stable circular orbits and the spectra of accretion discs. It was noted there that spectra, in particular, may be helpful to discriminate between black holes and naked singularities. The purpose of the present chapter, reported in [121], is to examine shadows and images of these naked singularity models, and to compare them with the images we expect from black holes. The goal is to check whether the images corresponding to the two kinds of model are clearly distinguishable. Our interesting conclusion is that, while black holes always cast a shadow, naked singularities may or may not, depending on the specific structure of the singularity. Therefore, while black holes imply shadows, the converse is not true. A shadow could be produced by certain naked singularities as well.

The plan of the current chapter is as follows. In §3.2, we briefly review the collapse models we use here, and outline some of their properties. In §3.3, we investigate geodesic motion, unstable photon orbits and the resulting shadows. In §3.4, we study gravitational lensing and relativistic images in the various spacetimes. In §3.5, we consider a simple accretion model and compute images, which we use to examine how black holes and naked singularities could be distinguished. We then repeat the analysis in §3.6 using a more realistic accretion flow model and show that the results are largely unchanged. We conclude in §3.7 with a summary of the key results.

3.2   The Black Hole and Naked Singularity Spacetimes

We compare images and shadows produced by a Schwarzschild black hole [1] with those produced by two different naked singularity spacetimes [51, 113]. The latter two solutions describe the geometry around compact objects formed from the spherically-symmetric gravitational collapse of two different types of fluids.

The first naked singularity solution, which we call JMN-1, is formed from the collapse of matter with zero radial pressure, and is described by the following metric [51],

$$ds_1^2 = -(1 - M_0) \left(\frac{r}{R_b}\right)^{M_0/(1-M_0)} dt^2 + \frac{dr^2}{1 - M_0} + r^2 \left(d\theta^2 + \sin^2\theta d\phi^2\right), \tag{3.2.1}$$

where the parameter M_0 is limited to the range $0 \leq M_0 \leq 4/5$ (the upper limit corresponds to the requirement that the sound speed should not exceed unity). The matter content of this spacetime has the following energy density ρ, radial pressure p_r, and tangential pressure p_θ:

$$\rho = \frac{M_0}{r^2}, \quad p_r = 0, \quad p_\theta = \frac{M_0}{4(1 - M_0)}\rho = \frac{M_0^2}{4(1 - M_0)}\frac{1}{r^2}. \tag{3.2.2}$$

This fluid has non-zero tangential pressure, but its radial pressure is assumed to vanish.

The second naked singularity solution, which we call JMN-2, is the end state of collapse of a spherical cloud with non-zero radial pressure. It describes, for example, the collapse of a perfect fluid cloud with a locally varying equation of state $k(r) = p/\rho$ (not strictly isothermal) that approaches a constant value in the neighborhood of the center of the cloud. This spacetime is described by the metric [113],

$$ds_2^2 = -\frac{1}{16\lambda^2(2 - \lambda^2)} \left[(1 + \lambda)^2 \left(\frac{r}{R_b}\right)^{1-\lambda} - (1 - \lambda)^2 \left(\frac{r}{R_b}\right)^{1+\lambda}\right]^2 dt^2 + (2 - \lambda^2)dr^2 + r^2 \left(d\theta^2 + \sin^2\theta d\phi^2\right), \tag{3.2.3}$$

where $0 \leq \lambda < 1$. The expressions for the energy density and pressure can be found in [113]. For easier comparison with the JMN-1 model, we define a parameter M_0,

$$M_0 = \frac{1 - \lambda^2}{2 - \lambda^2}, \tag{3.2.4}$$

which represents an alternative way (instead of λ) of parametrizing JMN-2.

Both JMN-1 and JMN-2 contain a time-like naked singularity at $r = 0$ and no trapped surface forms in these spacetime. Both solutions are matched at their boundary radius $r = R_b$ to the Schwarzschild geometry,

$$ds_0^2 = -\left(1 - \frac{2M}{r}\right) dt^2 + \frac{dr^2}{1 - \frac{2M}{r}} + r^2 \left(d\theta^2 + \sin^2\theta d\phi^2\right). \tag{3.2.5}$$

In both cases, the total mass M is given by

$$M = \frac{1}{2}M_0 R_b. \tag{3.2.6}$$

The three static spherically symmetric spacetimes we consider here can be written in the general form,

$$ds_i^2 = -f_i(r)dt^2 + \frac{d^2}{g_i(r)} + r^2 \left(d\theta^2 + \sin^2\theta d\phi^2\right), \tag{3.2.7}$$

with the index $i = 0, 1, 2$ corresponding to the Schwarzschild black hole, the JMN-1 and the JMN-2 naked singularity metric functions respectively, which are given as,

$$f_0(r) = g_0(r) = \left(1 - \frac{2M}{r}\right), \tag{3.2.8}$$

$$f_1(r) = (1 - M_0)\left(\frac{r}{R_b}\right)^{M_0/(1-M_0)}, \quad g_1(r) = (1 - M_0),$$

$$f_2(r) = \frac{1}{16\lambda^2(2 - \lambda^2)}\left[(1 + \lambda)^2\left(\frac{r}{R_b}\right)^{1-\lambda} - (1 - \lambda)^2\left(\frac{r}{R_b}\right)^{1+\lambda}\right]^2, \quad g_2(r) = \frac{1}{2 - \lambda^2}.$$

We now briefly discuss a few technical issues that are relevant for our study of images and shadows. First, we address the issues of whether the JMN spacetimes satisfy the Tolman-Oppenheimer-Volkoff equation (TOV, [288, 289]), which is derived by solving the Einstein field equations together with the conservation equations for a general time-independent, spherically symmetric metric (canonically for perfect fluids). Since the gravitational collapse process that leads to the the above JMN spacetimes is studied by solving the Einstein field equations together with the conservation equations (see [51, 113]), when a time-invariant configuration (equilibrium) is attained, the TOV equation must automatically be satisfied. For the JMN-2 class of spacetimes, the TOV equation at equilibrium is discussed and shown to be satisfied (see equation 27 of [113]). Here, we point out that the JMN-1 spacetime, containing an imperfect fluid, also obeys the anisotropic TOV equation. For a spacetime with metric given by 3.2.7 and supported by the energy-momentum tensor of the form $T^\mu_\nu = \text{diag}[-\rho, p_r, p_\theta, p_\theta]$, the anisotropic TOV equation is given by (see equation 21 of [290]),

$$p'_r = -(\rho + p_r)\frac{m(r) + r^3 p_r/2}{r(r - 2m(r))} + \frac{2}{r}(p_\theta - p_r), \tag{3.2.9}$$

where we have set $8\pi G = 1$ and $c = 1$, and

$$g_i(r) = 1 - \frac{2m(r)}{r}, \quad 2m(r) = \int_0^r dr\, \rho r^2. \tag{3.2.10}$$

For the JMN-1 spacetime, the energy density and pressures are given in equation 3.2.2 and $m(r) = \frac{1}{2}M_0 r$. It can immediately be checked that the TOV equation is satisfied by this spacetime.

The JMN-1 spacetime may not be physically realistic since the radial pressure is assumed to vanish (but this assumption simplifies the analysis considerably and allows simple analytical expressions). JMN-2 is more realistic since it is supported by a fluid with isotropic pressure. The matter for the JMN-2 can have an equation of state of the form $p = k\rho$, where k may not necessarily be a constant. Since the pressure must vanish at the surface $r = R_b$ whereas the density may not, we must have $k|_{r=R_b} = 0$. Other examples of stable configurations, where the matter has a constant density and isotropic pressure with a variable equation of state, exist in the literature (see §6.2 of [10] or equation 1 of [291]).

Next, we show that the JMN spacetimes can be smoothly matched across the $r = R_b$ hypersurface Σ, i.e., the metric tensor $g_{\mu\nu}$ and the extrinsic curvature K_{ab} are continuous across Σ. By construction $g_{\mu\nu}$ is continuous across Σ (see equation 3.2.8). To show that K_{ab} is also continuous, we first note that the coordinates in both the interior and the exterior are $x^\mu = (t, r, \theta, \phi)$, and those on Σ are $y^a = (t, \theta, \phi)$. Therefore, as seen from the Schwarzschild exterior, the induced metric on Σ is

$$ds^2_\Sigma = -(1 - M_0)dt^2 + R_b^2(d\theta^2 + \sin^2\theta d\phi^2), \tag{3.2.11}$$

where we have used equation 3.2.6. Also, as seen from the interior JMN spacetimes, the induced metric on Σ is the same as in equation 3.2.11. This is reminiscent of the fact that the metric tensor $g_{\mu\nu}$ is continuous across Σ. The non-zero components of the tangent $e^\mu_a = \partial x^\mu / \partial y^a$ on Σ are $e^t_t = 1$, $e^\theta_\theta = 1$ and $e^\phi_\phi = 1$. The extrinsic curvature of Σ is given by $K_{ab} = e^\mu_a e^\nu_b \nabla_\nu n_\mu$, where n^μ is a unit normal to Σ. Now, as seen either from the exterior Schwarzschild or from the interior JMN spacetimes (3.2.7), the unit normal is given by $n^\mu = (0, \sqrt{g_i(r)}, 0, 0)$. Therefore, as seen either from the exterior Schwarzschild or from the interior JMN spacetimes, the non-zero components of the extrinsic curvature are given by

$$K^t_t = \frac{f'_i(r)}{2f_i(r)}\sqrt{g_i(r)}\bigg|_{r=R_b}, \quad K^\theta_\theta = K^\phi_\phi = \frac{1}{r}\sqrt{g_i(r)}\bigg|_{r=R_b}. \tag{3.2.12}$$

Note that $f_{1,2}(R_b) = f_0(R_b) = (1 - M_0)$ and $g_{1,2}(R_b) = g_0(R_b) = (1 - M_0)$. Also, it is straighforward to show that $f'_{1,2}(R_b) = f'_0(R_b) = M_0/R_b$, implying that the extrinsic curvature is also continuous across Σ. Therefore, the JMN spacetimes are smoothly matched to the exterior Schwarzschild spacetime at $r = R_b$.

The JMN spacetimes do not contain any trapping region since $(1 - 2m(r)/r) = 1 - M_0 > 0$ always. However, to show that the singularities are actually naked, we have to show that photons emitted from the singularity, or from its vicinity, reach faraway observers in a finite time. To this end, we calculate both the affine time and the time measured by a faraway static observer. Taking $E = 1$ (see §3.3), as measured by a faraway static observer, the time taken by a radially outgoing photon ($L = 0$) to travel from r to the surface is given by

$$\Delta t = t(R_b) - t(r) = \int_r^{R_b} dr \frac{\dot{t}}{\dot{r}} = \int_r^{R_b} \frac{dr}{\sqrt{f_i(r)g_i(r)}}. \tag{3.2.13}$$

For JMN-1, this gives

$$\Delta t = t(R_b) - t(r) = \frac{2R_b}{2 - 3M_0}\left[1 - \left(\frac{r}{R_b}\right)^{\frac{2-3M_0}{2(1-M_0)}}\right]. \tag{3.2.14}$$

Note that, for $M_0 < 2/3$, Δt is finite for a photon escaping from the singularity $r = 0$ to reach the surface R_b. However, for $M_0 > 2/3$, Δt diverges as $r \to 0$, implying that, as measured by a faraway static observer, a photon escaping from the singularity takes infinite time to reach the observer. For JMN-2, we have

$$\Delta t = \frac{2(2 - \lambda^2)R_b}{1 - \lambda^2}\left[\log\frac{2(1 + \lambda)}{\lambda} - \log\frac{(1 + \lambda)R_b + (1 - \lambda)r}{(1 + \lambda)R_b - (1 - \lambda)r}\right]. \tag{3.2.15}$$

We see that Δt is finite as $r \to 0$, implying that a photon escaping from the singularity always takes finite time to reach a faraway observer. We next calculate the affine time τ. From equation 3.3.5, for radial null geodesics, we obtain

$$\Delta\tau = \tau(R_b) - \tau(r) = \int_r^{R_b} dr\sqrt{\frac{f_i(r)}{g_i(r)}}. \tag{3.2.16}$$

For JMN-1 spacetime, this becomes

$$\Delta\tau = \frac{2R_b(1 - M_0)}{2 - M_0}\left[1 - \left(\frac{r}{R_b}\right)^{\frac{2-M_0}{2(1-M_0)}}\right], \tag{3.2.17}$$

which is finite always as $r \to 0$, implying that a photon escaping from the JMN-1 singularity always reaches a faraway observer in a finite affine time. For JMN-2, we have

$$\Delta\tau = \frac{R_{\rm b}(1+\lambda)^2}{4\lambda(2-\lambda)}\left[1-\left(\frac{r}{R_{\rm b}}\right)^{2-\lambda}\right] - \frac{R_{\rm b}(1-\lambda)^2}{4\lambda(2+\lambda)}\left[1-\left(\frac{r}{R_{\rm b}}\right)^{2+\lambda}\right], \tag{3.2.18}$$

which is again finite as $r \to 0$, implying that a photon escaping from the JMN-2 singularity always reaches a faraway observer in a finite affine time.

Thus, except for the JMN-1 spacetime with $M_0 > 2/3$, both the coordinate time t and the affine time τ are finite for a photon escaping from the singularities and reaching a faraway observer. In the case of JMN-1 spacetime with $M_0 > 2/3$ however, even though the coordinate time t is infinite, the affine time τ is finite for photons emitted from an infinitesimally close vicinity of the singularity ($r \simeq 0$). In this case, the behaviour of null geodesics escaping from the singularity is very similar to that of null geodesics escaping from the event horizon of a Schwarzschild black hole. However, photons emitted from a finitely close vicinity ($r \sim 0$) of the singularity will take large but finite coordinate times t to reach a faraway observer.

Finally, it is worth emphasizing that the spacetimes we study here are merely toy models that we use to explore potential observational signatures of naked singularities. At this stage of our study, we do not view astrophysical realism as an important requirement. The main virtue of these models is that, they are not merely exact solutions of the steady state (time-independent) Einstein field equations (of which there are many), but we have shown that these solutions develop via time evolution of regular spherically-symmetric initial data [51, 113]. The latter is a rather stringent requirement. As is well-known, the Schwarzschild black hole metric forms via evolution from non-singular initial conditions, e.g., the famous Datt-Oppenheimer-Snyder model. However, none of the other black hole solutions (Reissner-Nordstrom, Kerr) has been shown to form in their entirety, i.e., both outside and inside the horizon, from regular initial conditions. Similarly, we do not believe that many of the naked singularity models in the literature, e.g., Kerr with $a > M$, Reissner-Nördstrom with $Q > M$ and the Janis-Newman-Winicour naked singularity have been shown to form from physically well-behaved initial conditions. In contrast, our naked singularity solutions do form from perfectly regular initial conditions, as we have demonstrated in our previous work. We view this as a major advantage of these models, and in this sense we consider our models to be "physically realistic".

3.3   Shadows of JMN Naked Singularities and Schwarzschild Black Hole

The shadow structures for the different spacetimes are determined by the properties of null geodesics in these spacetimes. We therefore begin with a discussion on this topic. We consider an extended source of radiation on the far side of the compact object. Photons from the source traverse the spacetime of the black hole or naked singularity, get deflected, and reach the observer. As viewed by the observer, we are interested in those directions for which no (or very little) radiation is received. The union of these directions constitutes the shadow of the gravitating object.

3.3.1 Geodesic Motion and Unstable Photon Orbits

The Lagrangian describing the motion of a photon in the spacetime geometry (3.2.7) is given by

$$2\mathcal{L} = -f_i(r)\dot{t}^2 + \frac{\dot{r}^2}{g_i(r)} + r^2\dot{\theta}^2 + r^2\sin^2\theta\dot{\phi}^2, \tag{3.3.1}$$

where a dot represents a derivative with respect to the affine parameter. Since the Lagrangian is independent of t and ϕ, we have two constants of motion:

$$p_t = \frac{\partial\mathcal{L}}{\partial\dot{t}} = -f_i(r)\dot{t} = -E, \tag{3.3.2}$$

$$p_\phi = \frac{\partial\mathcal{L}}{\partial\dot{\phi}} = r^2\sin^2\theta\dot{\phi} = L, \tag{3.3.3}$$

where E and L are, respectively, the energy and angular momentum of the photon. Using the null geodesic condition $g_{\mu\nu}\dot{x}^\mu\dot{x}^\nu = 0$, we obtain

$$\frac{1}{g_i}\dot{r}^2 + r^2\dot{\theta}^2 = \frac{r^2\sin^2\theta E^2 - f_i L^2}{f_i r^2\sin^2\theta}. \tag{3.3.4}$$

Since our spacetimes are spherically symmetric, the shadows and images will be circularly symmetric in the observer sky. Thus the intensity will be a function only of the impact parameter $b = L/E$ with respect to the center of the spacetime, and will be independent of the azimuthal angle θ. Therefore, we can simply choose $\theta = \pi/2$, $\dot{\theta} = 0$, and obtain all our results for this case. The same results can then be applied to all θ. Setting $\theta = \pi/2$ and $\dot{\theta} = 0$, we obtain

$$\frac{f_i}{g_i}\dot{r}^2 + V_{\text{eff}} = 0, \quad V_{\text{eff}} = L^2\frac{f_i(r)}{r^2} - E^2. \tag{3.3.5}$$

The impact parameter b can be related to the turning point r_{tp} of a photon, where $\dot{r} = 0$ and $V_{\text{eff}}(r_{\text{tp}}) = 0$:

$$b = \frac{r_{\text{tp}}}{\sqrt{f_i(r_{\text{tp}})}}. \tag{3.3.6}$$

This expression will be useful in our subsequent analysis. Circular photon orbits satisfy $V_{\text{eff}} = 0$ and $\mathrm{d}V_{\text{eff}}/\mathrm{d}r = 0$, and we have,

$$x f_{i,x} - 2f_i = 0, \tag{3.3.7}$$

$$\frac{b^2}{R_{\text{b}}^2} = \frac{x^2}{f_i}, \tag{3.3.8}$$

where $x = r/R_{\text{b}}$, and $f_{i,x}$ represents differentiation of f_i with respect to x. Note that the matching surface between the interior naked singularity spacetime and the exterior Schwarzschild spaceime is now at $x = x_b = 1$. The photon sphere comprises of circular unstable photon orbits, i.e., circular orbits that satisfy additionally $d^2V_{\text{eff}}/dr^2 < 0$.

Equation (3.3.7) does not have any non-trivial solution for the two interior JMN spacetimes we are considering. Therefore, there is no photon sphere for either interior JMN spacetime. However, the JMN spacetimes are matched on the exterior to the Schwarzschild geometry, and the latter spacetime does have unstable photon

orbits on a photon sphere located at

$$r_{\text{ph}} = 3M, \qquad x_{\text{ph}} \equiv \frac{r_{\text{ph}}}{R_{\text{b}}} = \frac{3}{2}M_0. \tag{3.3.9}$$

Therefore, the existence or not of a photon sphere in the naked singularity models depends on the relative sizes of x_{ph} and the matching radius x_b. A photon sphere exists whenever the following conditions, which are all equivalent, are satisfied

$$R_{\text{b}} \leq 3M, \qquad x_{\text{ph}} \geq x_b, \qquad M_0 \geq \frac{2}{3}. \tag{3.3.10}$$

There is no photon sphere when $M_0 < 2/3$, or equivalently, when $R_{\text{b}} > 3M$.

The JMN-1 spacetime satisfies reasonable physical conditions (e.g., sound speed less than unity) for the parameter range $0 < M_0 < 4/5$. The subset of these models with $2/3 \leq M_0 < 4/5$ have photon spheres, while the rest do not. The JMN-2 spacetime is parametrised by $0 \leq \lambda = \sqrt{(1 - 2M_0)/(1 - M_0)} \leq 1$, which means that the allowed range of M_0 is $0 \leq M_0 \leq 1/2$. Thus, JMN-2 is devoid of a photon sphere for the entire allowed range of parameter values. It should be noted that for the cases for which photon spheres exist, they are always located in the exterior Schwarzschild geometry. Setting $x = x_{\text{ph}} = 3M_0/2$ in equation 3.3.8, we obtain

$$b_{\text{ph}}^2 = \frac{27}{4}M_0^2 R_{\text{b}}^2 = 27M^2, \tag{3.3.11}$$

which is the same equation as that obtained for the Schwarzschild black hole. The only difference in the case of the JMN spacetimes is that we have the additional requirement, $M_0 \geq 2/3$ (or $R_{\text{b}} \leq 3M$), in order to have a photon sphere. In the above discussion, b_{ph} is the critical impact parameter of a photon on an unstable photon orbit.

3.3.2   Shadows

The unstable photon orbits constitute the photon sphere, and they define the boundary of the shadow cast by a compact object. Photons from a distant source with impact parameter b larger than the critical impact parameter b_{ph}, i.e.,

$$b^2 > 27M^2, \tag{3.3.12}$$

remain outside the photon sphere and reach the observer. However, photons with impact parameters smaller than the critical impact parameter are captured within the photon sphere and do not reach the observer, thereby creating dark spots in the observer's sky. The union of these dark spots constitutes the shadow. Therefore, the apparent shape of the shadow projected in the observer's sky is a circular disc whose radius is given by the critical impact parameter $b_{\text{ph}} = 3\sqrt{3}M$.

Figure 3.1 shows the shapes of shadows cast by the JMN-1 naked singularity and the Schwarzschild black hole. The circles represent the outer boundaries of the shadows. In the case of the black hole, shadows exist for all M. However, in the case of the JMN-1 naked singularity, depending on the value of M_0, a shadow may either form ($M_0 \geq 2/3$), or not form ($M_0 < 2/3$). As we noted earlier, in the case of the JMN-2 naked singularity there is no photon sphere, and therefore this spacetime does not cast any shadow.

(a) JMN-1 naked singularity   (b) Schwarzschild black hole
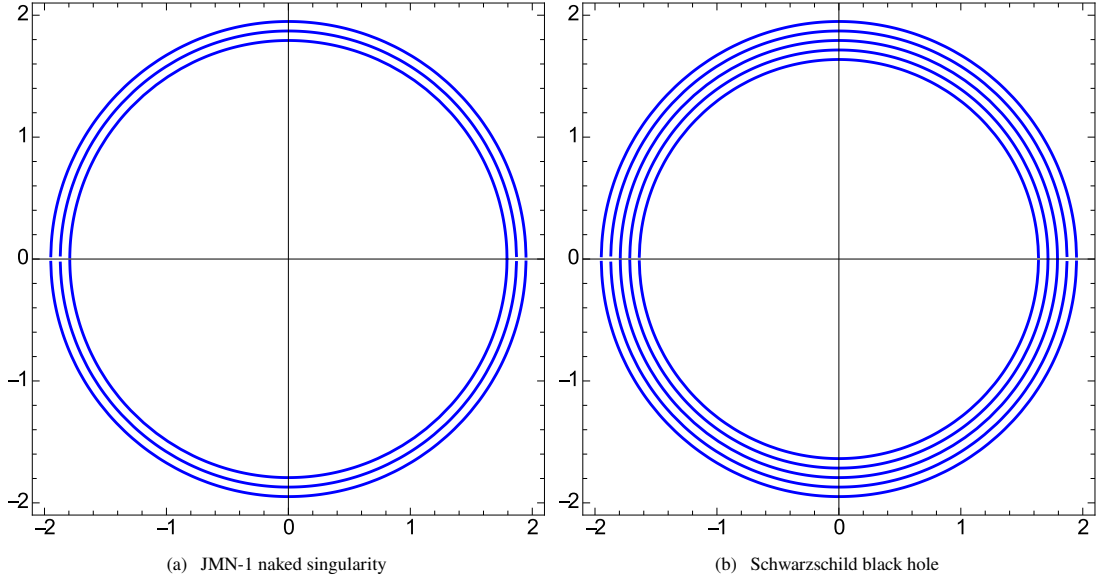
FIGURE 3.1: Shadows cast by (a) the JMN-1 naked singularity, matched to the exterior Schwarzschild spacetime at $x = x_{\text{b}} = 1$, for $M_0 = 0.75, 0.72, 0.69, 0.66, 0.63$ (from outer to inner), in the units of R_{b}, and (b) the Schwarzschild black hole with mass M equal to the same set of values (from outer to inner). For $M_0 < 2/3$, the JMN-1 naked singularity does not cast any shadow.

3.4 Gravitational Lensing and Relativistic Images

Since the shadows and images are the result of strong gravitational lensing, we now study lensing by the JMN naked singularities. From §3.3, we obtain

$$\frac{\text{d}\phi}{\text{d}r} = \frac{1}{r^2\sqrt{g_i(r)}} \frac{1}{\sqrt{\frac{1}{b^2 f_i(r)} - \frac{1}{r^2}}}, \qquad (3.4.1)$$

where b is the impact parameter. Defining $u = R_{\text{b}}/r$, we obtain the deflection angle

$$\alpha = 2 \int_0^{u_{\text{tp}}} \frac{\text{d}u}{\sqrt{g_i}} \frac{1}{\sqrt{\frac{1}{\bar{b}^2 f_i(u)} - u^2}} - \pi, \qquad (3.4.2)$$

where

$$\bar{b} = \frac{b}{R_{\text{b}}}, \qquad u_{\text{tp}} = \frac{R_{\text{b}}}{r_{\text{tp}}}, \qquad (3.4.3)$$

and r_{tp} is the turning point given by $\text{d}r/\text{d}\phi = 0$. For the spacetimes under consideration, the dimensionless impact parameter $\bar{b}$ is given by (see equation 3.3.6)

$$\bar{b} = \frac{1}{u_{\text{tp}}\sqrt{f_i(u_{\text{tp}})}}. \qquad (3.4.4)$$

Note that when $r_{\text{tp}} = R_{\text{b}}$, $u_{\text{tp}} = 1$. Therefore, if $u_{\text{tp}} < 1$, then the photon does not enter the interior of the JMN metric. In that case, the deflection is given by equations 3.4.2 and 3.4.4, with $f_i(r)$ and $g_i(r)$ given by the exterior Schwarzschild metric. However, if the photon does enter the JMN metric and has its turning point in

the interior ($r_{tp} < R_b$, i.e., $u_{tp} > 1$), then the deflection angle can be written as [292]

$$\alpha = 2 \int_0^1 \frac{\mathrm{d}u}{\sqrt{g_0}} \frac{1}{\sqrt{\frac{1}{\bar{b}^2 f_0(u)} - u^2}} + 2 \int_1^{u_{tp}} \frac{\mathrm{d}u}{\sqrt{g_{1,2}}} \frac{1}{\sqrt{\frac{1}{\bar{b}^2 f_{1,2}(u)} - u^2}} - \pi, \tag{3.4.5}$$

where $f_{1,2}$ refer to the JMN-1 or JMN-2 models, respectively, and the impact parameter $\bar{b}$ is given by equation 3.4.4. The first term in equation 3.4.5 is the contribution from the exterior Schwarzschild geometry and the second term is that from the interior JMN metric, α_{JMN1} or α_{JMN2}.

Because of its simple form, here we focus on the JMN-1 naked singularity. As discussed in §3.3, a photon sphere exists for $M_0 \geq 2/3$ and the photon sphere lies in the exterior Schwarzschild geometry. As a result, all the photons which participate in the image formation have their turning points outside of the photon sphere. Therefore, in this case, there is no difference in lensing behaviour between the JMN-1 naked singularity and the Schwarzschild black hole. On the other hand, since there is no photon sphere for $M_0 < 2/3$, photons may enter the interior of the JMN-1 spacetime and experience a turning point because of the infinite potential barrier at the singularity. Therefore, for this range of M_0, there is a clear distinction between the lensing behaviour of the JMN-1 naked singularity and that of the Schwarzchild black hole.

For $M_0 < 2/3$, the contribution of the JMN-1 spacetime to the deflection angle, α_{JMN1}, can be obtained analytically by a change of variables to $z = u^{(2-3M_0)/2(1-M_0)}$. We then obtain

$$\begin{aligned}
\alpha_{JMN1} &= 2 \int_1^{u_{tp}} \frac{\mathrm{d}u}{\sqrt{g_1}} \frac{1}{\sqrt{\frac{1}{\bar{b}^2 f_1(u)} - u^2}} = \frac{4\sqrt{1-M_0}}{2-3M_0} \int_1^{z_{tp}} \frac{\mathrm{d}z}{\sqrt{\frac{1}{\bar{b}^2(1-M_0)} - z^2}} \\
&= \frac{2\sqrt{1-M_0}}{2-3M_0} \left[\pi - 2\sin^{-1}\left(\frac{r_{tp}}{R_b}\right)^{\frac{2-3M_0}{2(1-M_0)}} \right], \tag{3.4.6}
\end{aligned}$$

where $r_{tp} \leq R_b$.

The analytical expression of the contribution due to the Schwarzschild geometry in the exterior of the JMN-1 model is the same as that of a Schwarzschild black hole and can be found in [293]. Figure 3.2 shows a plot of the deflection angle as a function of u_{tp}. Since a photon sphere exists for $M_0 \geq 2/3$, the deflection angle diverges as the turning point approaches the photon sphere. This divergence is logarithmic [294]. Therefore, theoretically, there will be an infinite number of images just outside the photon sphere.

For the JMN-1 naked singularity model with $M_0 < 2/3$, although there is no photon sphere, the deflection angle can still be large because, depending on the impact parameter, light rays may wind around the singularity several times. Due to this large bending, there can be many relativistic rings even for $M_0 < 2/3$.

In the following, for simplicity, we assume that the observer, the lens, and the distant point light source are all aligned. We also consider that the observer and the light source are far away from the lens. Therefore, in the observer's sky, the relativistic images will be concentric rings (known as relativistic Einstein rings) of radii given by the corresponding impact parameters $b(r_{tp})$. These impact parameter values $b(r_{tp})$ can be obtained by solving $\alpha \simeq 2\pi n$, where n is the ring number [294].

Figure 3.3 shows the relativistic Einstein rings in the observer's sky. In the case of the JMN-1 naked singularity with $M_0 \geq 2/3$ and the Schwarzschild black hole, all the relativistic images are clumped together outside the photon sphere, which forms the outer boundary of the shadow. The radius of the innermost image in the
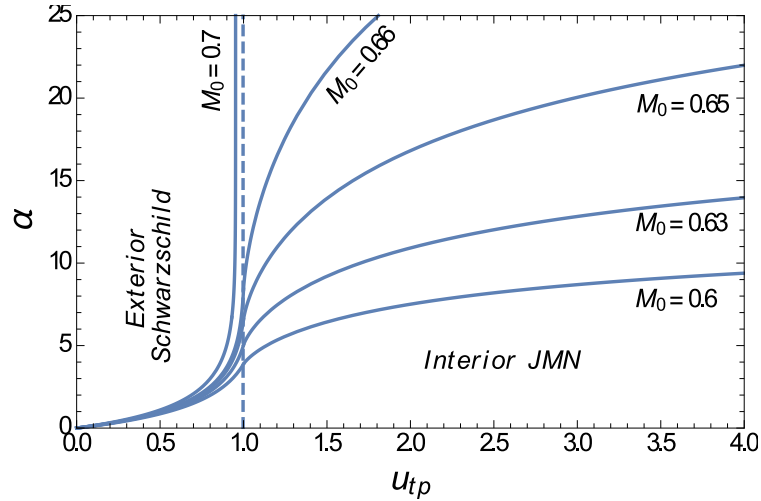
FIGURE 3.2: Deflection angle α as a function of u_{tp} of light rays for the JMN-1 naked singularity matched with an exterior Schwarzschild geometry. The vertical dashed line shows the boundary between the two geometries.

observer's sky is given by the minimum critical impact parameter b_{ph}. Photons with impact parameter less than b_{ph} are absorbed by the photon sphere. Hence, in this case, there is a shadow and many relativistic images clumped together just outside the edge of the shadow.

As an aside we note that, besides the relativistic Einstein rings discussed here, there is a standard Einstein ring formed as a result of weak deflection of light (weak deflection occurs when $M/r_{\text{tp}} \ll 1$). For all physically reasonable M_0 values, weak deflection and the traditional Einstein ring occur in the exterior Schwarzschild geometry. Therefore, the traditional Einstein ring of the JMN-1 naked singularity will be the same as that due to the Schwarzschild black hole (differences may arise when M_0 is uninterestingly small).

In the case of the JMN-1 naked singularity with $M_0 < 2/3$, there is no photon sphere and hence there is no capture of photons. As a result, we have many distinct rings corresponding to different relativistic images. The density of relativistic images increases as M_0 approaches 2/3. This is illustrated in figure 3.3.

The discussion so far is for a single point source aligned perfectly behind the lens. However, in realistic situations, we may have many light sources in different directions and at different distances around the lens. The angular positions of the relativistic images formed due to each source will be different. Therefore, in the observer's sky, there will be numerous relativistic images, which might fill the gaps between the relativistic images shown in figure 3.3. Hence, we may have a smooth continuous image. A similar situation occurs when the black hole or the JMN naked singularity is surrounded by an optically thin emission region, as we discuss in the next section.

3.5   Shadows and Images of Optically Thin Emission Regions surrounding Black Holes and Naked Singularities

The previous two sections dealt with distant sources of radiation, far behind the lensing compact object. Here we consider an optically thin, radiating, accretion flow surrounding the compact object and compute the

(a) $M_0 = 0.6$, JMN-1 naked singularity

(b) $M_0 = 0.63$, JMN-1 naked singularity

(c) $M_0 = 0.65$, JMN-1 naked singularity

(d) $M_0 = 0.66$, JMN-1 naked singularity

(e) $M_0 = 0.7$, JMN-1 naked singularity
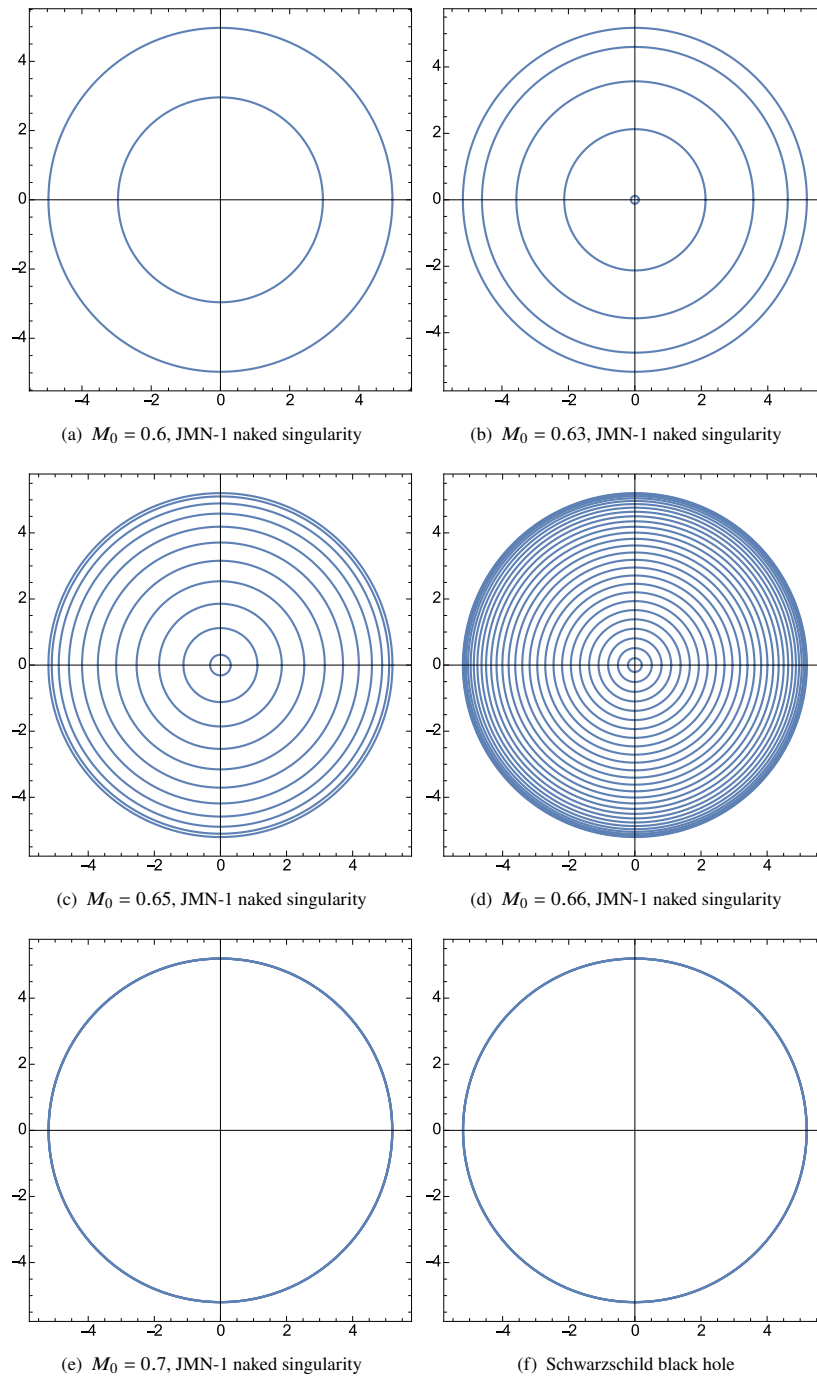
(f) Schwarzschild black hole

FIGURE 3.3: Relativistic Einstein ring images due to gravitational lensing by (a-e) the JMN-1 naked singularity with different values of M_0, and (f) the Schwarzschild black hole. The axes are in units of M.

observed image. The difference is that radiation is now emitted over an extended volume near the compact object, including regions inside the photon sphere.

The observed specific intensity I_{ν_o} (usually measured in erg s^{-1} cm^{-2} str^{-1} Hz^{-1}) at the observed photon frequency ν_o at the point (X, Y) in the observer's sky is given by [284, 295],

$$I_{\nu_o}(X, Y) = \int_\gamma \mathrm{d}l_{\mathrm{prop}}\, g^3\, j(\nu_e), \tag{3.5.1}$$

where ν_e is the emitted frequency, $g = \nu_o/\nu_e$ is the redshift factor, $j(\nu_e)$ is the emitter's rest-frame emissivity per unit volume, $\mathrm{d}l_{\mathrm{prop}} = -k_\alpha u_e^\alpha \mathrm{d}\lambda$ is the infinitesimal proper length in the rest frame of the emitter, k^μ is the four-velocity of the photons, u_e^μ is the four-velocity of the emitter, and λ is the affine parameter along the photon path γ. The subscript γ on the integral means that the integration is evaluated along an observed photon path γ. The redshift factor $g = \nu_o/\nu_e$ is given by,

$$g = \frac{k_\alpha u_o^\alpha}{k_\beta u_e^\beta}, \tag{3.5.2}$$

where $u_o^\mu = (1, 0, 0, 0)$ is the four-velocity of the distant observer (who is at infinity).

In the spirit of the simple spherically-symmetric spacetimes we are investigating, we consider a correspondingly simple model for the accreting gas. We assume that the gas is in radial free fall [284], with its four-velocity given by,

$$u_e^t = \frac{1}{f_i(r)}, \quad u_e^r = -\sqrt{\frac{g_i(r)}{f_i(r)}\left[1 - f_i(r)\right]}, \quad u_e^\theta = u_e^\phi = 0. \tag{3.5.3}$$

The four-velocity k^μ ($= \dot{x}^\mu$) of the photons was already obtained previously. In the subsequent calculations, we will need the following expression,

$$\frac{k^r}{k^t} = \pm f_i(r)\sqrt{g_i(r)\left[\frac{1}{f_i(r)} - \frac{b^2}{r^2}\right]}, \tag{3.5.4}$$

where the sign $+(-)$ is when the photon moves away from (approaches towards) the massive object. The redshift function g is thus given by,

$$g = \frac{1}{\frac{1}{f_i(r)} - \frac{k_r}{k_t}\sqrt{\frac{g_i(r)}{f_i(r)}(1 - f_i(r))}}. \tag{3.5.5}$$

For the specific emissivity, we assume the following simple model [284] in which the emission is monochromatic with emitter's rest-frame frequency $\nu_\star$, and the emission has a $1/r^2$ radial profile:

$$j(\nu_e) \propto \frac{\delta(\nu_e - \nu_\star)}{r^2}, \tag{3.5.6}$$

where δ is the Dirac delta function. Finally, the proper length in the emitter frame is given by

$$\mathrm{d}l_{\mathrm{prop}} = -k_\alpha u_e^\alpha \mathrm{d}\lambda = -\frac{k_t}{g k^r} \mathrm{d}r. \tag{3.5.7}$$

Integrating equation equation 3.5.1 over all the observed frequencies, we obtain the observed photon intensity [284]

$$I_{\text{obs}}(X, Y) \propto - \int_{\gamma} \mathrm{d}r \frac{g^3 k_t}{r^2 k^r}. \tag{3.5.8}$$

Note that the intensity map in the observer's sky will be circularly symmetric, with the impact parameter b of any equi-intensity circle given by $X^2 + Y^2 = b^2$. Figures 3.4 and 3.5 show intensity maps of the image of the above model accretion flow for the Schwarzschild black hole and the two JMN naked singularities.

We now note the qualitative differences in the shadows and images produced by the different models. As expected, the Schwarzschild black hole always casts a shadow (figure 3.4 a), though we should point out that the intensity inside the shadow does not quite go to zero as in the previous sections but has a small finite value (figure 3.4 d). This difference is because the accretion flow emits radiation inside the photon sphere and a small fraction of this radiation is able to escape to infinity.

In the case of the JMN-1 naked singularity, if the model has a photon sphere ($M_0 \geq 2/3$, $R_b \leq 3M$), then its shadow and image (figure 3.4 b) mimic those of the Schwarzschild black hole. However, if the JMN-1 naked singularity does not have a photon sphere, then it casts a "full-moon" image (figure 3.4 c), which is remarkably different from the images in figures 3.4 a and 3.4 b. Such a difference, if observationally detected, could greatly help distinguish a naked singularity from a black hole.

The JMN-2 naked singularity model does not have a photon sphere for any allowed value of the parameter λ. Therefore, the image in this case is always a full-moon, as illustrated in figures 3.5 b and 3.5 c.

Our results suggest that, though a naked singularity that has a photon sphere cannot be distinguished from a black hole through observations of the shadow or image, a naked singularity that does not have any photon sphere can be. Note that naked singularities without photon spheres arise when physically realistic collapse models are considered, such as the JMN-2 model [113].

Photons emitted from the close vicinity of either JMN naked singularity are highly redshifted. However, this is compensated by the fact that the rate of emission of photons from the accretion flow in the vicinity of the singularity is large. The redshift of photons emitted in the forward direction of the accretion flow is smaller than those emitted in the backward direction. Therefore, although the contribution of "backward photons" may be highly suppressed, "forward photons" turn and escape (in the absence of a photon sphere), contributing to the intensity profile. The center of the image in the observer's sky corresponds to photons with zero impact parameter. Such photons originate from the close vicinity of the singularity as well as from the accreting matter in between the singularity and the observer, along the line joining them. We note also that the redshift is irrelevant when considering the formation of shadows and full-moon images due to distant extended sources of light, as discussed in §3.3 and §3.4, since the blueshift suffered by a photon in going from the source to the turning point nearly cancels out the redshift suffered by it in going from the turning point to a faraway observer. In that case, the total redshift suffered by the photon is simply determined by the relative redshift between the source and observer's positions. When both the light source and the observer are at large distances, this redshift is negligible.

(a) $M = 1.0$, Schwarzschild black hole

(b) $M = 1.0$, Schwarzschild black hole

(c) $M_0 = 0.7$, JMN-1 naked singularity

(d) $M_0 = 0.7$, JMN-1 naked singularity

(e) $M_0 = 0.6$, JMN-1 naked singularity

(f) $M_0 = 0.6$, JMN-1 naked singularity

FIGURE 3.4: The images in the left column shows how an optically thin emission region looks like when surrounding a Schwarzschild black hole (a) or a JMN-1 naked singularity, with $M_0 = 0.7$ (b) and $M_0 = 0.6$ (c). The corresponding intensity distributions as a function of the impact parameter are shown in the right column. All spatial coordinates are in units of M.

(a) $M = 1.0$, Schwarzschild black hole

(b) $M = 1.0$, Schwarzschild black hole

(c) $\lambda = 0.8$, JMN-2 naked singularity

(d) $\lambda = 0.8$, JMN-2 naked singularity

(e) $\lambda = 0.4$, JMN-2 naked singularity

(f) $\lambda = 0.4$, JMN-2 naked singularity
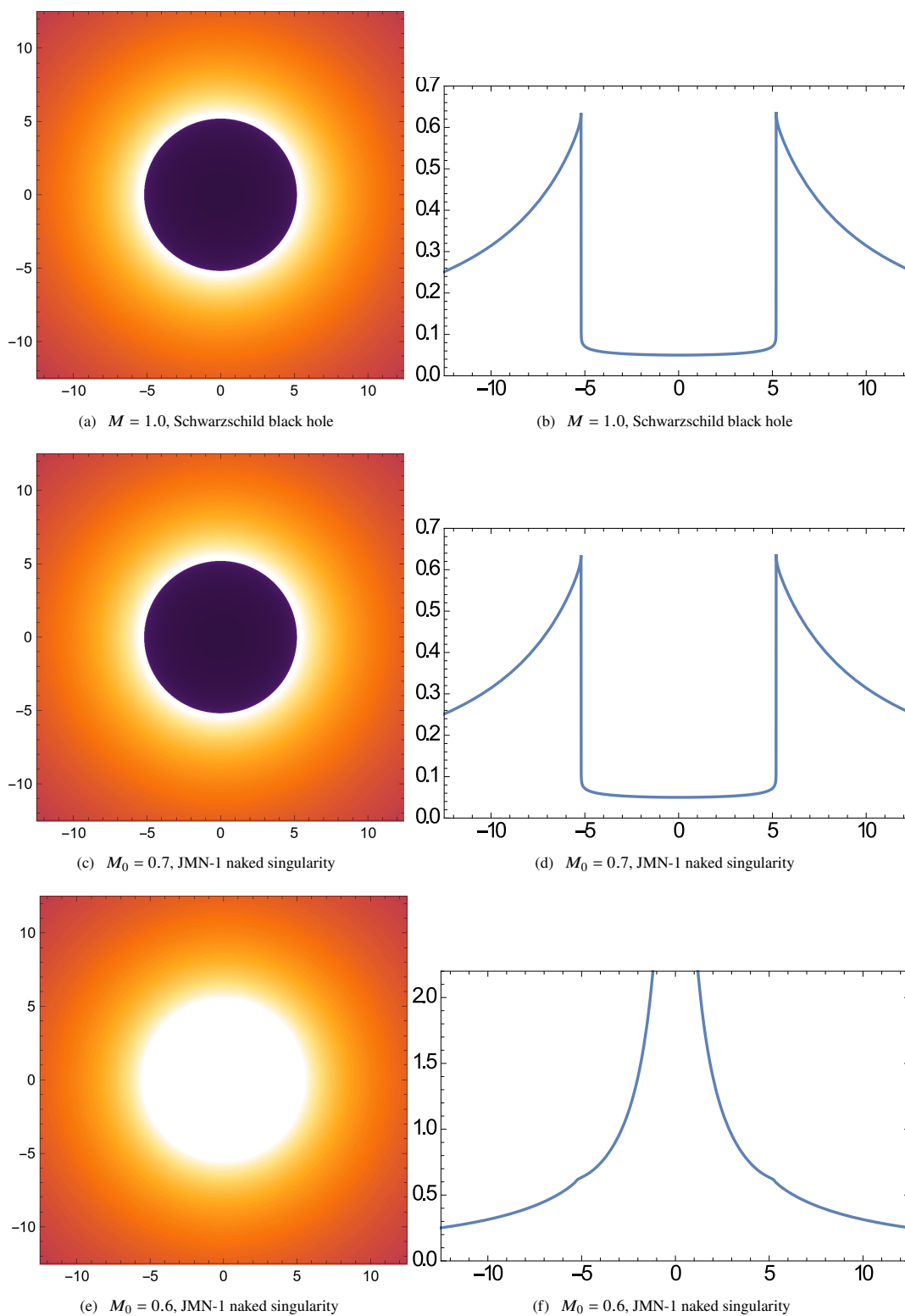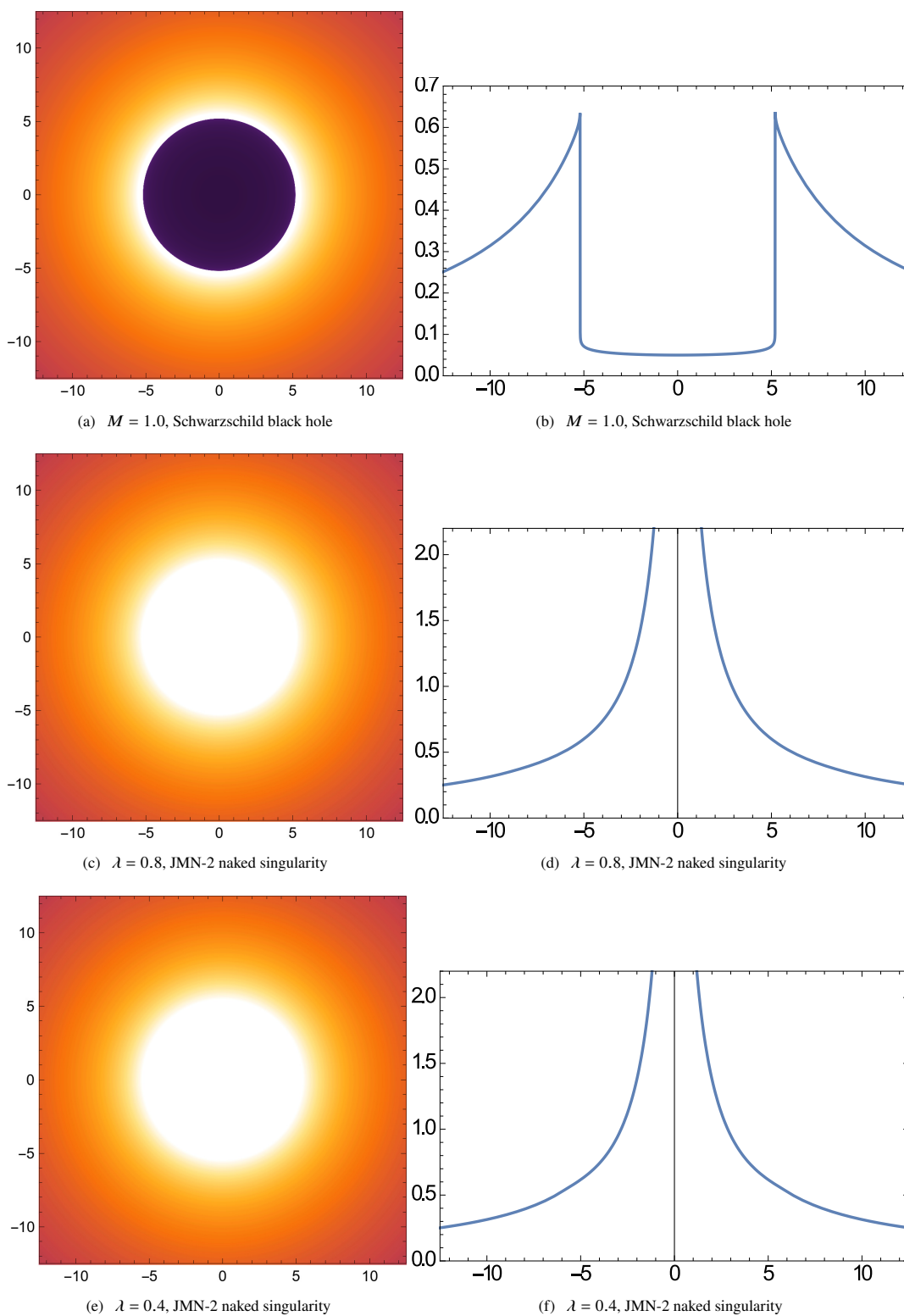
FIGURE 3.5: The images in the left column shows how an optically thin emission region looks like when surrounding a Schwarzschild black hole (a) and the JMN-2 naked singularity, with $\lambda = 0.8$ (b) and $\lambda = 0.4$ (c). The corresponding intensity distributions as a function of the impact parameter are shown in the right column. All spatial coordinates are in units of M.

3.6 Shadows and Images of more realistic Accretion Flows around Black Holes and Naked Singularities

We now describe a more realistic model of the accretion flow with several improvements: (i) we consider a physically motivated emissivity prescription, (ii) we analyze the spectrum of the radiation, and (iii) we avoid the assumption of optically thin emission. As we show, the results are similar to those obtained in §3.5.

3.6.1 The Model

With a view to specializing to the case of the Galactic Center compact object Sagittarius A* (Sgr A⋆), we consider a specific value for the mass of the central object: $M = 4 \times 10^6 M_\odot$. As in §3.5, we assume a spherically symmetric accretion flow, except that we set up the dynamics as in the Bondi accretion model [296]. Thus, we assume that the compact object is embedded in a uniform external medium with a temperature T_∞ and density ρ_∞. We choose $T_\infty = 10^7$ K, as appropriate for Sgr A⋆. For this choice, the Bondi radius, i.e., the transition radius where the flow changes in character from a uniform external medium to a freely-falling inner accretion flow, is $r_B \approx 10^6 M$. We keep ρ_∞ as a free parameter which we adjust (thereby tuning the mass accretion rate) such that the luminosity of the resulting accretion flow in the sub-millimeter band matches the observed flux of Sgr A⋆. Finally, in the spirit of the Bondi model, and in keeping with §3.5, we take the velocity profile of the accreting gas to be given by equation equation 3.5.3, using the appropriate $f_i(r)$ and $g_i(r)$ for each model. However, we modify the radial velocity profile at large radii so that the velocity transitions from the standard free-fall scaling, $v_r \propto r^{-1/2}$, at radii inside the Bondi radius to $v_r \propto r^{-2}$ outside the Bondi radius (as required for a constant mass accretion rate with a uniform gas density at large radii).

We assume that the accreting gas radiates thermal synchrotron and bremsstrahlung, and that the emitted radiation is Compton-scattered as it propagates out of the system. The radiation is treated via a complete radiative transfer model using the transfer code HEROIC [297, 298], with the relativistic enhancements described in [299]. In this code, a large number of ray directions is considered at each point in the accretion flow and the relativistic radiative transfer equation, which considers both emission and absorption, is solved for each ray over a grid of frequencies extending from $\nu = 10^8$ Hz to 10^{24} Hz. HEROIC was originally written for the Kerr spacetime, and all previous applications were restricted to that spacetime. For the present application, the code was generalized to handle the JMN-1 and JMN-2 spacetimes as well.

The radiative transfer computations enable us to compute the luminosity and radiative spectrum of the emerging radiation for each model. In addition, they also provide the net cooling (if emission dominates) or heating (if absorption dominates) of the accreting gas. We include this cooling/heating information in the energy equation of the accreting gas to solve for the temperature profile $T(r)$ of the flow[2]. In other words, the only temperature information we input to the model is the boundary condition at infinity ($T_\infty = 10^7$ K), which sets the location of the Bondi radius. The temperature everywhere else is obtained self-consistently as part of the solution.

The numerical computations are done on a uniform grid in $\log r$, with 20 points per decade. The grid extends from an outer radius $r_{\max} = 10^{6.5} M$ (a factor of a few larger than the Bondi radius) down to an inner radius

---

[2]For simplicity, we assume that the gas is a single-temperature plasma, although it is likely that the accreting gas in Sgr A⋆ is a two-temperature plasma [300]

r_{min}. In the case of the Schwarzschild black hole, we choose r_{min} to be just outside the horizon, specifically, $\log r_{min} = 0.35$. We assume absorbing boundary conditions at the inner edge of the grid, i.e., any radiation that crosses the horizon is lost from the system. For the two naked singularity models, we would ideally like to set $r_{min} = 0$, but this is not possible because of our use of a logarithmic grid. Hence, we use a small non-zero value, $r_{min} = 10^{-4}M$, again assuming absorbing boundary conditions.

3.6.2   Spectra and Temperature Profiles

Figure 3.6a shows spectra corresponding to five different models: Schwarzschild black hole (red curve), JMN-1 naked singularity with $M_0 = 0.7$ (green) and $M_0 = 0.6$ (blue), and JMN-2 naked singularity with $\lambda = 0.8$ (magenta) and $\lambda = 0.4$ (cyan). In each model, the mass accretion rate has been adjusted (by varying the density ρ_∞ of the external medium) so as to give the same luminosity, $\nu L_\nu = 10^{34.6} \, \text{erg s}^{-1}$ at $\nu = 200 \, \text{GHz}$ (indicated by the black dot), as seen by an observer at infinity. This is approximately the luminosity of Sgr A*.

As explained in previous sections, of the five spacetime models under consideration, only two have photon spheres, viz., the Schwarzschild black hole and the JMN-1 spacetime with $M_0 = 0.7$. Not surprisingly, these two models have nearly identical spectra. The primary peak at 10^{11} Hz is due to thermal synchrotron radiation from hot electrons at radii near the photon sphere. The other peaks are the result of Compton scattering, with a small contribution from bremsstrahlung in the last peak.

The Schwarzschild model and the JMN-1 model with $M_0 = 0.7$ are much less luminous than the other three models (JMN-1 $M_0 = 0.6$, JMN-2 $\lambda = 0.8$, JMN-2 $\lambda = 0.4$). The latter three spaceimes lack photon spheres and therefore allow radiation to escape more easily from the interior. As a result, they appear to be substantially more luminous, by orders of magnitude, for an observer at infinity.

Figure 3.6b shows the temperature as a function of radius for the same five models. All have essentially the same profile at radii larger than a few M, where the primary physical effect is compressive heating ($\rho \propto r^{-3/2}$ implies $T \propto r^{-1}$ at nonrelativistic temperatures) as gas flows in from the Bondi radius towards the center. At smaller radii ($r < M$), the gas in the four naked singularity models cools to much lower temperatures. Here the gas density is large enough that radiative cooling becomes important. Although much of the radiation is beamed towards small radii, nevertheless enough escapes to cause an enhanced luminosity at infinity. The only exception is the JMN-1 $M_0 = 0.7$ model where, because of the presence of a photon sphere, the amount of radiation that escapes to infinity is highly suppressed.

3.6.3   Images and Shadows

Figure 3.7 shows images corresponding to the accretion models under discussion. Only radiation with frequencies between 200 and 250 GHz is considered (initial EHT results will be at 230 GHz). The results are qualitatively similar to those shown in figures 3.4 and 3.5. Specifically, the Schwarzschild black hole and the JMN-1 naked singularity with $M_0 = 0.7$ have well-defined dark shadows, consistent with the existence of photon spheres in these two models. The other three models, JMN-1 with $M_0 = 0.6$, JMN-2 with $\lambda = 0.8$ and JMN-2 with $\lambda = 0.4$, all have filled centers, i.e., they have "full-moon" images, consistent with the lack of photon spheres.
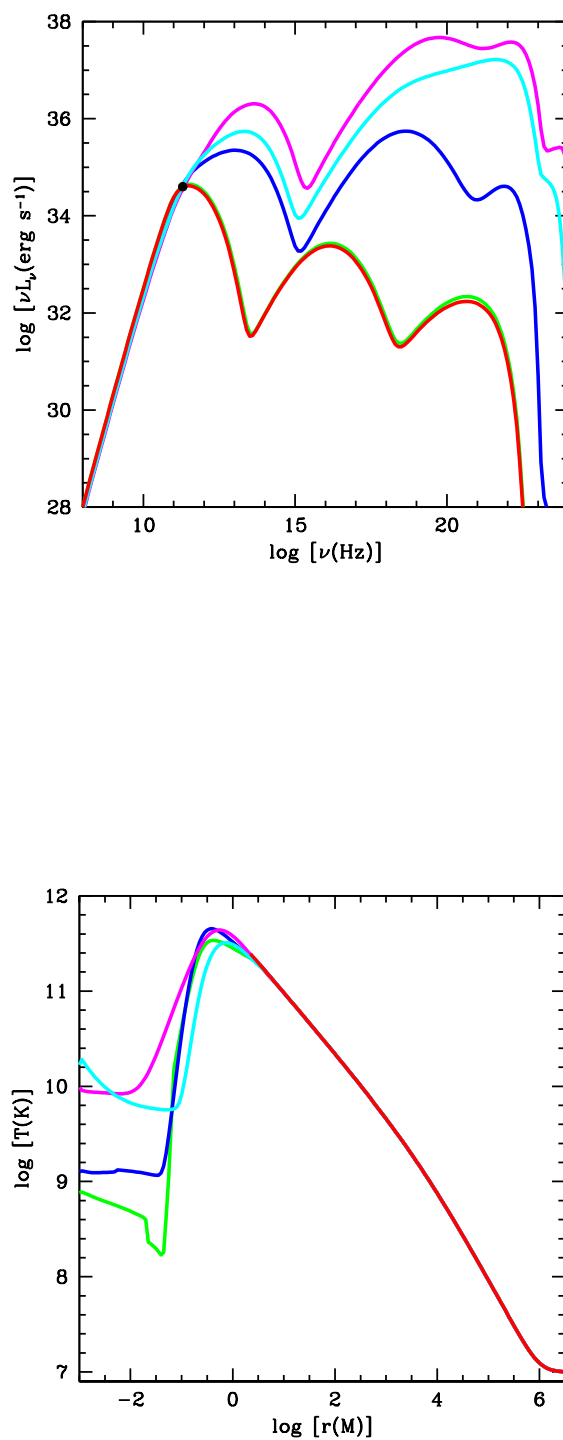
FIGURE 3.6: We show in panel (a) the spectra of models with a Schwarzschild black hole (red), JMN-1 naked singularity with $M_0 = 0.7$ (green, under red) and $M_0 = 0.6$ (blue), and JMN-2 naked singularity with $\lambda = 0.8$ (magenta) and $\lambda = 0.4$ (cyan). In panel (b), we show the radial temperature profiles of models with a Schwarzschild black hole (red), JMN-1 naked singularity with $M_0 = 0.7$ (green) and $M_0 = 0.6$ (blue), and JMN-2 naked singularity with $\lambda = 0.8$ (magenta) and $\lambda = 0.4$ (cyan).
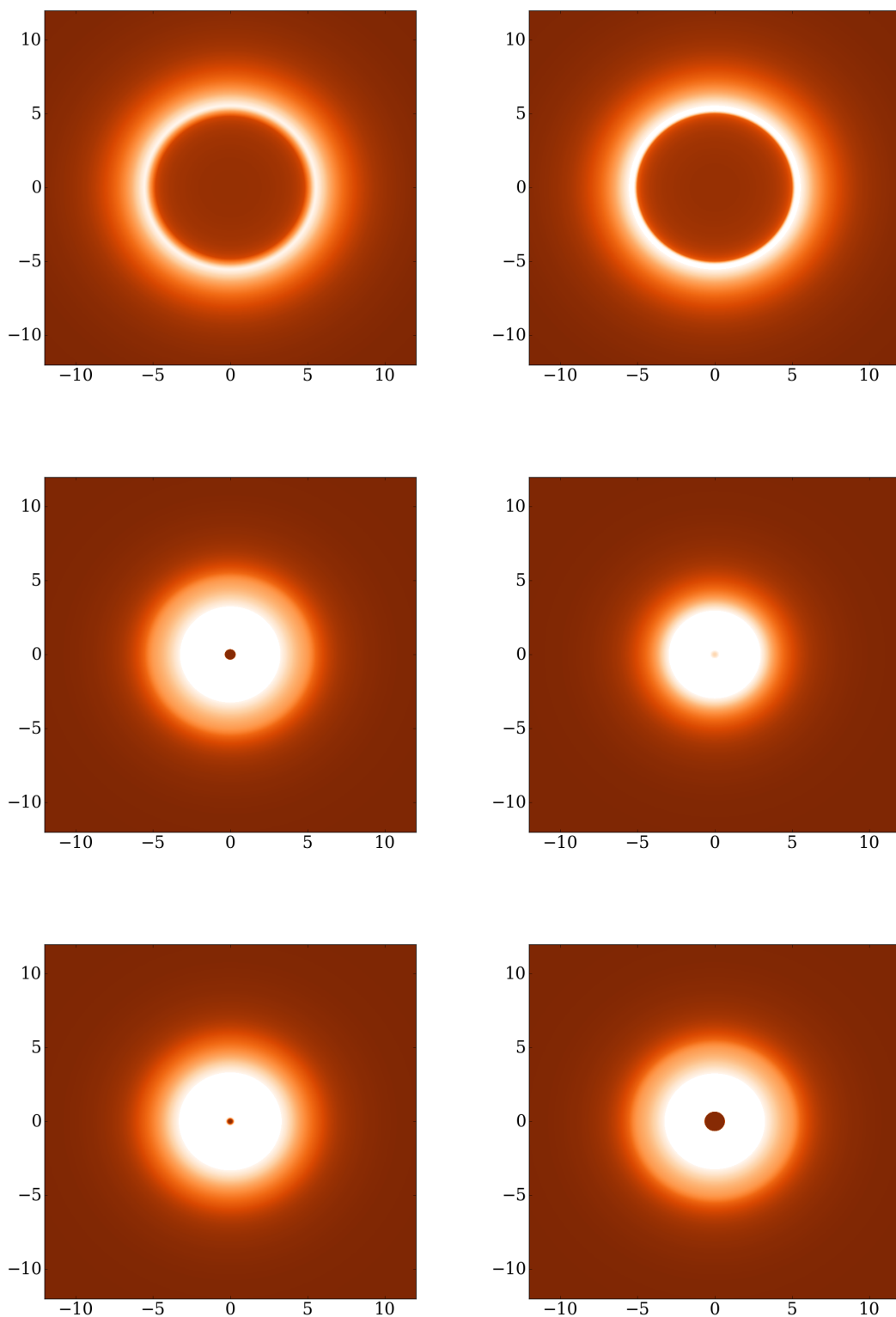
FIGURE 3.7: Shows images in the mm band (200–250 GHz) for the accretion models described in §3.6. All the panels use the same (arbitrary) color scale. Top Row: From left to right, the images correspond to the Schwarzschild black hole, JMN-1 naked singularity with $M_0 = 0.7$, and JMN-1 with $M_0 = 0.6$. The dark spot at the center of the third image is because the inner edge of the grid is at $r = 10^{-4}M$ rather than at 0. Bottom Row: The left two images correspond to the JMN-2 naked singularity with $\lambda = 0.8$ and $\lambda = 0.4$, respectively. The rightmost panel corresponds to the same model as the one above it (JMN-1, $M_0 = 0.6$), except that the inner edge of the grid in this case is at $r = 10^{-3}M$.

We emphasize that the accretion model considered here, which includes substantially more radiation physics, is significantly different from that in §3.5. Also, the images in figure 3.7 correspond to the mm-band, whereas in §3.5 we considered monochromatic emission and counted all the radiation. As a result, there are some quantitative differences between figure 3.7 and figures 3.4, 3.5. The rings around the shadows are somewhat narrower in the present models, and the full-moon images are somewhat smaller in angular size. Nevertheless, the qualitative results are very similar.

One feature that needs discussion is the dark spot at the center of the full-moon images in figure 3.7. This is an artefact. Because the metrics of the two JMN naked singularity spacetimes have power-law behaviour as $r \to 0$, it is necessary to use a logarithmic grid in r when computing numerical models. As a result, the grid has to be truncated at some finite radius. For the calculations presented here, we used an inner radius of $r_{min} = 10^{-4}M$. This is well inside the boundary radius R_b where the naked singularity interior is matched with the Schwarzschild exterior. Nevertheless, the truncation does result in a small dark spot at the center of the image, caused by the missing spacetime inside r_{min}. To illustrate better the effect of this truncation, the two panels in the rightmost column of figure 3.7 show images corresponding to the same model (JMN-1 $M_0 = 0.6$) except that the upper panel corresponds to $r_{\min} = 10^{-4}M$, while the lower panel corresponds to $r_{\min} = 10^{-3}M$. The former has a smaller dark spot than the latter, confirming that the spot will disappear in the limit $r_{\min} \to 0$.

Figure 3.8 shows radial profiles of the image intensity as a function of impact parameter for the five models. The profiles in the mm band (left panel) are quite different from those based on the bolometric radiation (right panel). The latter are more similar to the profiles shown in figures 3.4 and 3.5 (but note that those use a linear scale whereas figure 3.8 employs a logarithmic scale).

3.7   Conclusions

Here, following [121], we analyzed images produced by two spherically symmetric models of naked singularities, and compared them with the image produced by a spherically symmetric (Schwarzschild) black hole. We showed that naked singularities could, in some cases, cause shadows that are very similar to those produced by black holes, but in other cases, the two would have very different image structures and would be clearly distinguishable. It follows that a careful investigation of the shadow structure will be needed before the EHT can confirm the existence of an event horizon, and thus a black hole, in Sgr A⋆.

To expand on the above point, even if the EHT finds a shadow in Sgr A⋆, it will not conclusively establish the presence of a black hole in this object. The same shadow could be produced by certain naked singularity models. Among the two naked singularity models analyzed here, called JMN-1 and JMN-2, we find that JMN-1 will produce shadows whenever the parameter M_0 (see equation 3.2.1) lies in the range $M_0 \geq 2/3$. This is equivalent to the condition that the matching radius R_b between the naked singularity interior spacetime and the exterior Schwarzschild spacetime satisfies $R_b < 3M$, where M is the mass of the object. JMN-1 models that do not satisfy the above condition lack a shadow, and produce what we term a "full-moon" image. The JMN-2 model produces a full-moon image for all physically allowed choices of its parameters.

The fact that a shadow does not automatically imply an event horizon was already emphasized by [280], who showed that a model of Sgr A⋆ with a hard surface will also produce a shadow in mm-band images. The total
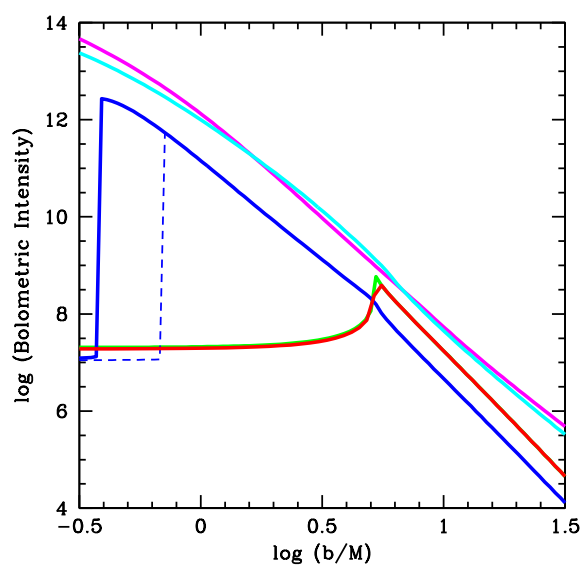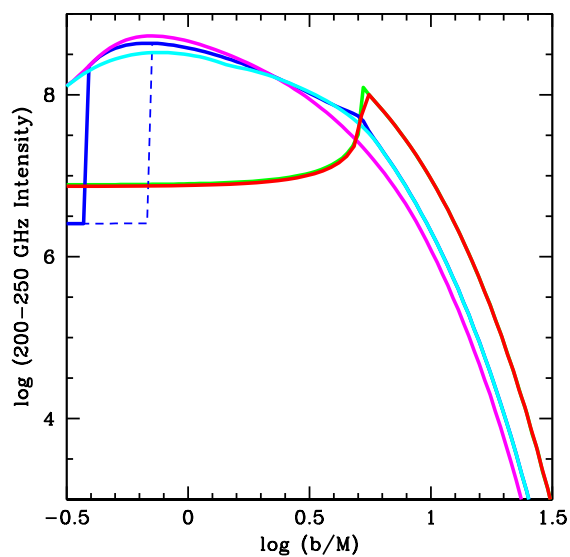
FIGURE 3.8: Left: Radial profiles of the mm band (200–250 GHz) image intensity versus the impact parameter b/M for the Schwarzschild black hole (red), JMN-1 naked singularity with $M_0 = 0.7$ (green, under red) and $M_0 = 0.6$ (blue), and JMN-2 naked singularity with $\lambda = 0.8$ (magenta) and $\lambda = 0.4$ (cyan). The solid and dashed blue lines correspond to the same model, but with $r_{\min} = 10^{-4}M$ (solid) and $r_{\min} = 10^{-3}M$ (dashed). Right: Corresponding results when the bolometric radiation ($10^8 - 10^{24}$ Hz) is considered. Note the change in the vertical scale.

spectrum would, however, be different. In particular, those authors argued that observations in the infrared would easily distinguish a hard-surface model from a true black hole, because the emission from the surface would dominate in the infrared.

The naked singularity models that produce shadows, viz., JMN-1 with $M_0 \geq 2/3$, $R_b \leq 3M$, are different in that their images and spectra at *all wavelengths* are nearly identical to those of a black hole (compare the red and green curves in figures 3.6 a, 3.8). Distinguishing these models will thus be much more difficult.

The full-moon image produced by the remaining naked singularity models we considered is also interesting. If such an image were observed, it would certainly rule out a black hole. Whether or not it would confirm the presence of a naked singularity remains to be seen since other non-black hole models might also produce such images.

Similar results to those described here are obtained when we consider the Schwarzschild solution with a scalar field, the so called JNW naked singularity spacetimes [6]. For a range of parameter values, these spacetimes admit a photon sphere, and for other parameter values they do not. In that case as well, the two kinds of models produce shadows and full-moon images, respectively. These results will be reported elsewhere.

Finally, we note that both the JMN-1 and JMN-2 models are characterized by two parameters, namely, the mass parameter M_0 and the matching radius R_b. The occurrence of a naked singularity in these models is stable with respect to variations in these two parameters, but this stability is limited since it is restricted to these specific spherically symmetric models.

More generally, the mode stability of the JMN spacetimes as well as their stability against fluid perturbations are unproven and are currently under investigation. Because of this, the astrophysical relevance of the specific models considered here is uncertain. On the other hand, the qualitative results presented here regarding the nature of images and shadows are likely common for a wide class of naked singularity models. In this sense, however, the theoretical implications of our results are indeed astrophysically relevant. It is important to keep this in mind, since the EHT is already operational and collecting data. Specifically, we emphasize that shadows are not a consequence of event horizons, but of photon spheres. Therefore, if an object casts a shadow, it does not have to necessarily possess an event horizon.

We look to working on generalizing the solutions discussed here to rotating naked singularity models. It would be physically much more realistic to compare the shadow structure of such rotating naked singularities with shadows produced by a Kerr black hole.

Chapter 4

Gravitomagnetism near Black Holes and its effect on Pulsars[1]

4.1 Overview

Here the focus will be on effect that gravitomagnetism, intrinsic to stationary black hole or naked singularity spacetimes, has on the appearance of a pulsar present near such compact objects, with the aim of extracting properties of the background spacetime.

Towards this end, we will use pulsars as a probe, and model it here via the standard lighthouse model, i.e. the pulsar spins around its own axis with a conserved intrinsic spin-angular momentum, at a constant spin angular frequency. We assume that this angular frequency doesn't change considerably even when the pulsar enters strong gravitational fields. The direction in which the beam of radiation is emitted rotates around its spin-axis at a fixed angle, at this frequency. The large mass ratio between intermediate-mass BHs (10^2–$10^4 M_\odot$; IMBHs) or super-massive BHs ($10^5 - 10^9 M_\odot$; SMBHs) and pulsars ($\sim 1.5 M_\odot$; see for example [301–303]) allows for a test spinning particle approximation for the pulsars. We will discuss this approximation in some more detail in eventual sections. Further, here we neglect spin-curvature coupling, which causes deviations in the world-lines of spinning particles from the world-lines of non-spinning particles [304, 305]. That is, we model pulsar motion by the motion of a test particle in the Kerr spacetime and simply account for the evolution of its intrinsic spin angular momentum along its world-line via the Fermi-Walker transport law. This enables us to bypass solving the full Mathisson-Papapetrou-Dixon equations [306–308] that govern the dynamics of spinning objects in general relativity, and this effect will be incorporated elsewhere.

We will not restrict our study to pulsars that only move along geodesics for two reasons: firstly, the magnitude of the spin-precession frequency is larger for accelerating pulsars and it would be astrophysically significant if one could observe such pulsars even for a short period of time, as we argue below. Next, we want to understand the effects of acceleration on their appearance since in realistic astrophysical scenarios there can be various sources of accelerations for pulsars. For example, gravitational waves emitted by a nearby compact binary could cause a pulsar to accelerate. Other causes could be due to interactions with other astrophysical objects

---

via scattering processes in dense regions like globular clusters or active galactic nuclei, or due to the supernova kicks that birth them.

Another important source of acceleration is the aforementioned coupling of the spin angular momentum to the background tidal tensor. This acceleration is proportional to the magnitude of the spin of the test object and to the rate of the fall-off of the strength of the gravitational field across it, which is captured by the tidal tensor $R^{\mu}_{\nu\rho\sigma}$. Recently, in [138] it was demonstrated that the motion of a millisecond (ms)-pulsar (which have spins of $\approx .3787 \text{m}^2$, using a spherical model for the pulsar) present close to a BH ($r \lesssim 50 M_{\text{BH}}$), with mass in the range $M_{\text{BH}} \approx 10^3 - 10^6 M_{\odot}$, exhibits deviations from geodesic motion due to the acceleration arising from spin-curvature coupling. Strikingly, it is found there that the motion of the pulsar becomes non-planar due to spin-curvature coupling, and the pulsar leaves the $x - y$ plane. They show how the complexity of the orbit increases with increase in spin and with decrease in mass of the BH. Notably, the 'z-signal' is potentially observable through variation in pulse arrival time over arrival times that would result if the pulsar stayed in a planar orbit. They argue that it is reasonable to expect the path length of the ray from the pulsar to the Earth to vary by ±5 km from the path length of a ray from a pulsar in an otherwise similar planar orbit, which translates to a timing change estimate of the order of $±10\mu s$. In a subsequent study [309], the orbit-precession of these ms-pulsars (non-zero spin-curvature coupling) was analysed and the usual de Sitter and Lense-Thirring pieces were obtained. Additional contributions arising from spin-curvature coupling and the coupling of the pulsar's spin to its orbital angular momentum (see for example equation 18 therein) were also reported, a consequence of which is that orbit-precession is enhanced. Further, spin-precession experienced by such a pulsar was also carefully analysed numerically, and it is shown that the spin-precession frequency due to spin-orbit and spin-spin coupling decays with an increase in orbit-radius of the pulsar as $\propto M_{\text{BH}}/r$. In particular, they point out that these couplings cannot be ignored for systems that qualify as intermediate-mass-ratio binaries i.e., $M_{\text{BH}}/m_{\text{p}} \sim 10^2 - 10^3$, with m_{p} being the mass of the pulsar. The upshot of their findings are that spin-precession causes the times of arrival and widths of pulses to change. For example, for a ms-pulsar present about $20 M_{\text{BH}}$ away from a Schwarzschild BH, with mass in the range $10^3 - 10^6 M_{\odot}$, shifts in the times of arrival of pulses accumulate to about 2.5 μs every $\sim$35s.

On a related note, considering the effect of spin-curvature on the dynamics of a spinning object to be negligible (as is done in the present work) is an excellent approximation for pulsars that are sufficiently slowly-spinning [310] or when they are present in regions where the background tidal tensor is very small. It is useful to remember that the tidal tensor decays with increase in distance from and mass of the BH. Therefore, our calculations apply very well for normal pulsars around massive BHs, and even for ms-pulsars when they are either about $r \gtrsim 50 M$ away from the BH or if they are near a BH with mass larger than about $10^6 M_{\odot}$ [138, 309].

To be precise, here we consider pulsars to be moving along the world-lines of equatorial Killing observers in the Kerr spacetime. The trends in the accelerations experienced by such observers, with changes in orbit-radius, BH parameters etc. is carefully discussed in appendix C. Further, the spin-precession frequencies experienced by spinning objects on these orbits do not vary with time, which greatly simplifies our calculations. Therefore, the observers we will be interested in are: (a) *static Killing observers*: observers whose spatial position remains unchanged over time, and (b) *stationary Killing observers*: observers that move on equatorial circular orbits. Although the former class of static observers form a proper subset of the latter class of stationary observers, it will be useful for our purposes to demarcate the two. Further, the class of stationary orbits contains the astrophysically important set of equatorial circular geodesics. Now, we find here, from a purely analytical calculation, that as the spin-axis of a pulsar precesses, it pulls the beam vector along with it, and this leads to

a modification in the pulse frequency as seen from the earth. Thus, due to stationary gravitational fields, this frequency is no longer simply equal to the intrinsic spin angular frequency of the pulsar about its axis. In our concluding section, we point out how this is a promising first step in this new story of pulsars and black holes involving spin-precession, and discuss more physically interesting extensions.

Apart from the few we have already mentioned, there have been other significant initiatives to advance our understanding about strong field gravity effects in recent years like the event horizon telescope, which aims to probe the physics of very strong gravity regions near the event horizon. Notably, EHT reported constructing the first event-horizon-scale image of the supermassive BH candidate thought to be present at the center of the M87 galaxy [120]. From such a perspective, we investigate here effects of gravitomagnetism on observed pulsar periods in the strong field region of the Kerr spacetime and use primarily the strong field results of [151, 311, 312] to obtain the frequency of spin-precession for pulsars located deep inside strong gravitational fields.

The outline of this chapter is as follows. In §4.2, we attempt to provide a quick primer on how the equation of motion of a test spinning object present in a gravitational field is derived in general relativity. In §4.3, we review the properties of Killing observers in the Kerr spacetime. In §4.3.1, we will discuss the adapted-Kerr spacetime, which is obtained by choosing coordinates co-moving with a particular observer moving on a circular orbit, and demonstrate that one can treat stationary observers in the Kerr spacetime as static observers in the adapted-Kerr spacetime. We will argue that this simplifies the problem of characterizing the accelerations and spin-precession frequencies for the full class of stationary observers in §4.3.2, following [151]. We then briefly discuss the features of the spin-precession frequencies experienced by arbitrary Killing observers in §4.4 and restrict to the astrophysically interesting case of equatorial Killing observers in §4.5. In §4.6, we work out the complete time evolution of the beam vector for static pulsars and obtain their observed pulse frequencies, without approximation. In §4.6.6, we extend this analysis to pulsars moving on equatorial circular orbits around the central object at constant angular speeds. In §4.7 and §4.8, we explore the astrophysical consequences of our work, reported in [125], and conclude with a quick summary and a few comments on possible future extensions.

Conventions: Greek and Latin indices (with the exception of i, j, k) run from 0–3. i, j, k take values 1–3. Hatted indices represent components projected onto a tetrad. We will also switch to the Euclidean three-vector notation in sections where all entities will be calculated relative to a spatial triad, i.e. $a^i \rightarrow \vec{a}$. Also, when b^i denotes a unit three-vector, we shall write $b^i \rightarrow \hat{b}$. This switch will be highlighted explicitly whenever made.

4.2   Interaction of Spin with Gravity in General Relativity[2]

The notion of intrinsic spin angular momenta is slightly nuanced in general relativity and so we begin with a very quick review of these ideas, and proceed to discuss the outline of the derivation of the equation of motion of a test spinning object in GR.

Before we begin, let us first remember that an extended object in non-relativistic Galilei-Newtonian mechanics, whose mass density and velocity at a general material point r_i are denoted by ρ, u_i, has total linear p_i and

---

[2]See [151, 308, 313] for this section.

angular momentum S_{ij} defined as,

$$p_i = \int \mathrm{d}V \rho u_i, \ S_{ij} = 2 \int \mathrm{d}V \rho r_{[i} u_{j]}. \tag{4.2.1}$$

Under the influence of no forces barring gravity, given by a Newtonian gravitational potential Φ, it's dynamics is completely specified via,

$$\frac{\mathrm{d}p_i}{\mathrm{d}t} = -\int \mathrm{d}V \rho \partial_i \Phi, \tag{4.2.2}$$

$$\frac{\mathrm{d}S_{ij}}{\mathrm{d}t} = 2p_{[i}v_{j]} - 2 \int \mathrm{d}V \rho r_{[i} \partial_{j]}\Phi. \tag{4.2.3}$$

In GR, the equations of motion of an arbitrary distribution of matter that moves freely in a background spacetime with metric $g_{\mu\nu}$ are obtained simply by demanding that its energy-momentum tensor $T^{\mu\nu}$ be covariantly conserved,

$$\nabla_\mu T^{\mu\nu} = 0. \tag{4.2.4}$$

In a seminal paper [308], it was pointed out that the energy-momentum tensor $T^{\mu\nu}$ of such a material object can be expanded into an infinite set of multipole moments, depending on the strength of the background Riemann tensor, enabling an expansion approach to solve the full set of equations of motion (4.2.4), similar to the non-relativistic case. Following [313], we represent the multipoles via the integrals,

$$\int_{x^0=\mathrm{const}} \sqrt{-|g|}\mathrm{d}^3x \ T^{\mu\nu} \delta x^{\alpha_1} \cdots \delta x^{\alpha_n}, \tag{4.2.5}$$

where $|g| \equiv \det(g_{\mu\nu})$, and the above integrals are calculated around a certain representative world-line $X^\alpha(\tau)$ chosen within the object. $\delta x^\alpha \equiv x^\alpha - X^\alpha$ is a deviation from the representative world-line of a material point x^α in the volume of the object and τ is the proper time of the representative world-line X^α.

In this construction, the first two moments of $T^{\mu\nu}$ over the volume of the body turn out naturally to be the energy-momentum vector p^μ and the intrinsic spin angular momentum $S^{\mu\nu}$ of the object,

$$p^\mu = \left[\int_{x^0=\mathrm{const}} \sqrt{-|g|}\mathrm{d}^3x \ T^{\mu 0}\right] + \Gamma^\mu_{\rho\sigma} \frac{u^\rho}{u^0} S^{\sigma 0},$$

$$= mu^\mu - u_\nu u^\alpha \nabla_\alpha S^{\mu\nu}, \tag{4.2.6}$$

$$S^{\mu\nu} = \int_{x^0=\mathrm{const}} \sqrt{-|g|}\mathrm{d}^3x \left(T^{\nu 0}\delta x^\mu - T^{\mu 0}\delta x^\nu\right), \tag{4.2.7}$$

where m is the kinematical or monopole rest mass of the particle, u^μ is its kinematical four-velocity (tangent to the object's representative world-line $x^\mu(\tau)$), and $S^{\mu\nu}$ is its intrinsic spin angular momentum, an antisymmetric two-tensor.

It can be seen that the Newtonian gravity analogue of this expansion technique is obtained by replacing the Riemann tensor $R^\mu_{\nu\rho\sigma}$ of general relativity with spatial derivatives of the classical Newtonian gravitational potential Φ on the one side, and the energy-momentum tensor $T^{\mu\nu}$ with the mass density ρ of the object under study on the other (see §1 of [308]).

The evolution equations (4.2.4) in terms of these moments (4.2.5) reduce to a set of equations in powers of $(R/l)^n$, where R is the size of the object and l is the background curvature length-scale and is given in terms of the Riemann tensor $R^\mu_{\nu\rho\sigma}$. Now, when the size of the material object is sufficiently small enough compared to

the background curvature length-scale, all its multipoles beyond its dipole can be neglected and the dynamical problem is greatly simplified. Such an approximation is called the pole-dipole approximation and is useful in the treatment of test spinning objects.

That is, for a pulsar of mass and radius m_p, R_p present in the vicinity of a Kerr black hole whose mass and angular momentum are M, J, and for a radial separation between their centre of masses given by r, this implies that when $m_p \ll M < r$ and $R_p \ll r$, the interaction of the pulsar's spin *quadrupole* moment with inhomogeneities of the gravitational field can be neglected, and the interaction is dominated by the two lowest moments. Under these circumstances, the pulsar can be treated as a a classical pole-dipole spinning particle and the governing equations (4.2.4) reduces to the Mathisson-Papapetrou equations [306, 307],

$$u^\alpha \nabla_\alpha p^\sigma = -\frac{1}{2} R^\sigma_{\rho\mu\nu} u^\rho S^{\mu\nu}, \tag{4.2.8}$$

$$u^\alpha \nabla_\alpha S^{\mu\nu} = p^\mu u^\nu - p^\nu u^\mu. \tag{4.2.9}$$

The term appearing on the right in equation 4.2.8 is the famed spin-curvature coupling, which was explored notably in [304, 305], and is responsible for the deviation from geodesic motion of spinning particles.

Further, the above equations of motion (4.2.8, 4.2.9) do not form a closed set of first order differential equations; there are 4+3 equations for 10 unknowns: $m, u^\mu (3)$ and $S^{\mu\nu} (6)$ (see for example [313]). Therefore one needs to specify a set of three supplementary conditions, which amount to specifying the reference point $X^\alpha(\tau)$ about which the momentum and spin of the particle were calculated in equation 4.2.5. This is usually taken to be the centre of mass of the particle which, however, is frame-dependent [314]. Here we choose the set of supplementary conditions to be given by the Pirani condition [315],

$$S^{\mu\nu} u_\nu = 0, \tag{4.2.10}$$

A condition of the sort given above is an algebraic condition on the components of the spin tensor components. Specifically, the Pirani condition above has the implication that the spin tensor will have support only in directions transverse to the four-velocity u^μ of the spinning object. We direct the reader to see [316, 317] for a detailed discussion on these supplementary conditions. Equivalently, this is the statement that the spin angular momentum vector which is defined by duality,

$$S^\mu = -\frac{1}{2m} \epsilon_{\mu\nu\alpha\beta} p^\nu S^{\alpha\beta}, \tag{4.2.11}$$

lies in the corresponding local rest space.

More generally, when a force acts on the centre of mass of the spinning object, generating an acceleration $\alpha^\mu = \nabla_u u$, the intrinsic spin angular momentum vector S^μ satisfies[3] (see for example [172]),

$$\nabla_u S = (S \cdot \alpha) u, \tag{4.2.12}$$

where $(\cdot)$ represents an inner product. When no forces or torques are applied to a spinning object with low spin angular momentum S^μ, the equation governing the world-line of the spinning particle (4.2.8) reduces to

---

[3]In favour of a cleaner representation of the mathematics, we will suppress the space-time indices for the rest of this section. We will also not use boldfaced letters to represent tensors as was the case in Chapter 2.

the geodesic equation for the orbital motion of a point-like spinless object in an background gravitational field
[310].

When using the Pirani supplementary condition (4.2.10), the evolution equation for spin angular momenta
(4.2.12) is equivalent to the statement that they are Fermi-Walker (FW) transported ([148]; also see for example
[8]),

$$\mathbb{F}_u \mathcal{S} = 0, \tag{4.2.13}$$

where in the above we have introduced the Fermi derivative of a vector field X along u as [147],

$$\mathbb{F}_u X = \nabla_u X - (X \cdot \alpha) u + (X \cdot u) \alpha, \tag{4.2.14}$$

It is clear that along a geodesic i.e. for $\alpha = 0$, Fermi-Walker transport reduces to parallel transport.

The advantage of employing the Pirani condition (4.2.10) is that we can now restrict to analysing the evolution
of the space-like spin three-vector S. This is best accomplished by constructing an orthonormal frame spanned
by three space-like vectors, which are also orthogonal to the four-velocity u, all along the world-line of the
spinning object and projecting the evolution equation (4.2.13) onto this triad. The Frenet-Serret (FS) tetrad
comprises of precisely such a set of four orthonormal vectors, three spacelike with the timelike leg being
the four-velocity of the spinning object. The FS tetrad is also one of the most natural frames associated
with a given curve because it is invariant under reparametrization and captures inherent differential geometric
properties of the curve, namely its generalized curvatures, which play a fundamental role in the analysis of the
evolution of their spin vectors, as we shall discuss below.

Furthermore, since in the present chapter we will consider only the evolution of spin vectors carried by Killing
observers of the Kerr spacetime, it is important to note that this choice of tetrad is particularly convenient: it
was pointed out by [151] that for Killing observers in arbitrary stationary spacetimes the associated FS tetrad
and generalised curvatures are all time-independent, simplifying our analysis greatly. Furthermore, after a
review of the properties of Killing observers of the Kerr spacetime, we will discuss also why our choice to
study pulse profiles of pulsar moving on Killing orbits is of fundamental physical importance.

The FS tetrad attached to an observer that moves along an arbitrary time-like world-line comprises of a set
of four orthonormal vector fields $\{e_{\hat{\alpha}}, (\hat{\alpha} = 0 - 3)\}$ and is constructed as follows. The timelike leg is simply
defined to be the four-velocity along the world-line, $e_{\hat{0}} = u$. Next, $e_{\hat{1}}$ will be defined to be the normal to the
curve and to find it, we introduce the directional derivative along the four-velocity, denoted by an overdot,
$\dot{} = \nabla_u = d/d\tau$. That is,

$$\dot{e}_{\hat{0}} = \kappa e_{\hat{1}}, \tag{4.2.15}$$

where $\kappa = (\dot{e}_{\hat{0}} \cdot e_{\hat{1}})$ measures the curvature of the world-line relative to the osculating plane spanned by $e_{\hat{0}}$ and
$e_{\hat{1}}$. Note that since $e_{\hat{0}}$ is normalised, $\dot{e}_{\hat{0}}$, and hence $e_{\hat{1}}$, is orthogonal to it. This is clear if we recognise that
$\alpha = \kappa e_{\hat{1}}$ is simply the four-acceleration of the observer, and that $\nabla_u (u \cdot u) = 0 \Rightarrow \alpha \cdot u = 0$. Now, we turn to $\dot{e}_{\hat{1}}$.
This vector will be a linear combination of $e_{\hat{0}}, e_{\hat{1}}$ and a unit vector $e_{\hat{2}}$ orthogonal to the osculating plane. Yet
again, since $e_{\hat{1}}$ has unit-norm, we can write,

$$\dot{e}_{\hat{1}} = \kappa e_{\hat{0}} + \sigma_1 e_{\hat{2}}, \tag{4.2.16}$$

where $\sigma_1 = (\dot{e}_{\hat{1}} \cdot e_{\hat{2}})$ is called the first torsion. Proceeding similarly to the above, the following picture emerges. The tetrad legs $\{e_{\hat{\alpha}}, (\hat{\alpha}=0-3)\}$ are respectively the tangent, normal, binormal and trinormal vectors along the world-line of the observer and satisfy,

$$(e_{\hat{\alpha}} \cdot e_{\hat{\beta}}) = \eta_{\hat{\alpha}\hat{\beta}}. \tag{4.2.17}$$

In terms of the generalized curvatures $(\kappa, \sigma_1, \sigma_2)$, the evolution equations of the tetrad legs along the world-line can be written out succinctly as,

$$\begin{bmatrix} \dot{e}_{\hat{0}} \\ \dot{e}_{\hat{1}} \\ \dot{e}_{\hat{2}} \\ \dot{e}_{\hat{3}} \end{bmatrix} = \begin{bmatrix} 0 & \kappa & 0 & 0 \\ \kappa & 0 & \sigma_1 & 0 \\ 0 & -\sigma_1 & 0 & \sigma_2 \\ 0 & 0 & -\sigma_2 & 0 \end{bmatrix} \begin{bmatrix} e_{\hat{0}} \\ e_{\hat{1}} \\ e_{\hat{2}} \\ e_{\hat{3}} \end{bmatrix}, \tag{4.2.18}$$

where in the above we introduced $\sigma_2 = (\dot{e}_{\hat{2}} \cdot e_{\hat{3}})$ the second torsion. σ_1, σ_2 measure the deviation of the world-line from being a planar curve restricted to the osculating plane. The curvature κ has been identified as being the particle acceleration and the two torsions are directly related to spin-precession, as we shall see below.

Since we want to analyse the evolution of the spin vector in this tetrad, and we know that it is FW-transported along its world-line (4.2.13), we now study the FW-transport of the FS tetrad. We obtain immediately that (see [172]),

$$\mathbb{F}_u e_{\hat{\alpha}} = \omega_{\hat{\alpha}}{}^{\hat{\beta}} e_{\hat{\beta}}, \tag{4.2.19}$$

where $\omega_{\hat{\alpha}}{}^{\hat{\beta}}$ is given as,

$$\omega_{\hat{\alpha}}{}^{\hat{\beta}} = \begin{bmatrix} 0 & 0 & 0 & 0 \\ 0 & 0 & \sigma_1 & 0 \\ 0 & -\sigma_1 & 0 & \sigma_2 \\ 0 & 0 & -\sigma_2 & 0 \end{bmatrix}, \tag{4.2.20}$$

The FW-transport of the FS tetrad (4.2.19) along with the equation of motion of the spin vector (4.2.13) imply that the spin three-vector $S = S^{\hat{i}} e_{\hat{i}}$ satisfies[4],

$$\dot{S}^{\hat{i}} e_{\hat{i}} + S^{\hat{j}} \mathbb{F}_u e_{\hat{j}} = 0, \tag{4.2.21}$$

and we have,

$$\dot{S}^{\hat{i}} = \omega^{\hat{i}}{}_{\hat{j}} S^{\hat{j}}. \tag{4.2.22}$$

That is, the spin of the gyroscope precesses relative to the FS spatial triad $\{e_{\hat{i}}, \hat{i} = 1, 2, 3\}$ with an angular velocity Ω_{p},

$$\omega_{\hat{i}\hat{j}} = \epsilon_{\hat{i}\hat{j}\hat{k}} \Omega_{\mathrm{p}}^{\hat{k}}, \tag{4.2.23}$$

and we can write,

$$\Omega_{\mathrm{p}} = -(\sigma_2 e_{\hat{1}} + \sigma_1 e_{\hat{3}}), \tag{4.2.24}$$

---

[4]$\mathbb{F}_u S^{\hat{i}} = \dot{S}^{\hat{i}}$. See §2.10.3 of [172] for a quick review on the properties of the Fermi derivative.

when the FS spatial triad is right-handed [151]. Then, employing standard three-dimensional vector notation, in the *Euclidean* FS triad, we can write equation 4.2.22 as,

$$\dot{\vec{S}} = \vec{S} \times \vec{\Omega}_{\mathrm{p}}.$$

(4.2.25)

In the above discussion, we have not imposed any restrictions on u barring that it be timelike. In the rest of this chapter, as mentioned above, we shall restrict u to be tangent to arbitrary Killing orbits of the Kerr spacetime and we now move to a discussion of the spin-precession properties of these observers.

4.3   Killing Observers in the Kerr Spacetime

We remind the reader of the form of the Kerr metric in the standard Boyer-Lindquist (BL) coordinates $x^{\mu} = (t, r, \theta, \phi)$,

$$ds^2 = -\left(1 - \frac{2Mr}{\rho^2}\right)dt^2 - \frac{4Mar\sin^2\theta}{\rho^2}dt\,d\phi + \frac{A\sin^2\theta}{\rho^2}d\phi^2 + \frac{\rho^2}{\Delta}dr^2 + \rho^2 d\theta^2$$

(4.3.1)

$$= g_{00}dt^2 + 2g_{03}dt\,d\phi + g_{33}d\phi^2 + g_{11}dr^2 + g_{22}d\theta^2.$$

Here J and M are the angular momentum and mass of the Kerr collapsed object respectively, and $a = J/M$ is the specific angular momentum. Also, $\Delta = r^2 - 2Mr + a^2$, $\rho^2 = r^2 + a^2 \cos^2\theta$ and $A = (r^2 + a^2)^2 - a^2 \Delta \sin^2\theta$.

The Kerr spacetime possesses a time-like Killing vector, $\xi = \partial_0$, corresponding to time-translational invariance, and a space-like Killing vector, $\psi = \partial_3$, corresponding to azimuthal rotational invariance. A constant-coefficient linear combination of these two is the most general Killing vector, $\xi' = \xi + \Omega\,\psi$. The time-translational Killing vector becomes null on the ergosurface of the Kerr spacetime, which is characterised by $g_{00} = 0$, i.e. on the ergosurface, $\xi^2 = (\xi \cdot \xi) = g_{00} = 0$. Similarly, it can be shown that $\xi'^2 = 0$ is the location of the event horizon. The ergoradii $r_{\pm}$ and the radius of the event horizon r_{H} are given respectively as,

$$r_{\pm} = M \pm \sqrt{M^2 - a^2 \cos^2\theta}, \ \ r_{\mathrm{H}} = M + \sqrt{M^2 - a^2}.$$

(4.3.2)

The black hole ergoregion is defined as being the region between the event horizon and the outer ergoradius, i.e. $r_{\mathrm{H}} \leq r \leq r_+$; the ergosurface is defined to be the hypersurface $r_{\mathrm{ergo}} = r_+$. On the other hand, for a Kerr naked singularity, the ergoregion is defined to be the region between the two ergoradii, i.e. $r_- \leq r \leq r_+$, and the ergosurface is defined to be the hypersurface $r_{\mathrm{ergo}} = r_{\pm}$. It is to be noted that r_{ergo} is in fact single-valued, as can be seen from figure 4.1 (see also [200, 311])[5].

A real value for radius of ergosurface for the naked singularity ($M < a$) can be obtained only for a certain range of θ; i.e., the ergoregion does not exist for the spacetime region $0 \leq \theta < \cos^{-1}(M/a)$. It is evident then that the ergoregion shrinks towards equator as the spin parameter of the central compact object a increases. In principle, the outer ergoregion never vanishes completely, even for $a/M \rightarrow \infty$, when it lies only in the equatorial plane, with its limiting volume being zero. Interestingly, in the BL coordinates, the outer ergoradius in the equatorial plane is always at $r_+(\theta = \pi/2) = 2M$, irrespective of whether or not a horizon exists.

Fathomably, the angular dependence of the ergoradii has interesting implications for the shape of the and *topology* of the ergosurface. We highlight in figure 4.1 the distinct difference in the topologies of the ergoregions of Kerr black holes and naked singularities, in both Boyer-Lindquist and Cartesian Kerr-Schild coordinates [4]. In panel (e) there, for $a = 2M$, the ergoregion exists for the range $\pi/3 \leq \theta_e \leq \pi/2$ and $-\pi/2 \leq \theta_e \leq -\pi/3$, whereas there is no ergoregion for $-\pi/3 < \theta_{ne} < \pi/3$. So the radii of the outer and inner ergoregions in the equatorial plane are $r_+ = 2M$ and $r_- = 0$ respectively. The boundaries of inner and outer ergoregions coincide at $\theta = \pi/3$, where the radii of both of the regions are $r_+ = r_- = M$.

It is striking to note that any increment in the spin parameter beyond the Kerr bound $M \leq a$ drastically modifies the structure of ergoregion/ergosurface. In particular, a finite angular cone opens up around the polar axis and one can get to $r = 0$ through this region, without having passed through the ergoregion. On the other hand, since the ergoregion around a black hole covers it completely, one must always pass through it when trying to reach its singularity from the outside.

In a stationary spacetime, observers that remain fixed spatially with respect to infinity are called static Killing observers [8] and their four-velocities are given as,

$$u = \frac{\xi}{\sqrt{-\xi \cdot \xi}}. \tag{4.3.3}$$

Since $g_{00} < 0$ outside the ergosurface, u is time-like only outside it. Observers that move on circular orbits around the axis of the black hole at fixed angular speeds Ω in planes parallel to the equatorial plane are called stationary Killing observers and their four-velocities are given by,

$$u' = \frac{\xi'}{\sqrt{-\xi' \cdot \xi'}}. \tag{4.3.4}$$

Since we will only be interested in timelike stationary observers, we require $(\xi' \cdot \xi') < 0$, which has the consequence that $\Omega_- < \Omega < \Omega_+$,

$$\Omega_\pm = \frac{-g_{03} \pm \sqrt{g_{03}^2 - g_{00}g_{33}}}{g_{33}} = \frac{2Mar\sin\theta \pm \rho^2\sqrt{\Delta}}{A\sin\theta}. \tag{4.3.5}$$

For $\Delta \geq 0$, we require the radial coordinate to satisfy $r \geq r_H$, i.e. stationary Killing observers exist only outside the horizon. Clearly, static observers form the subclass of stationary observers satisfying $\Omega = 0$. Also, we note that stationary observers with $\Omega = \Omega_\pm$ are stationary null observers.

The relation between the FW spin-precession frequency experienced by a static Killing observer and the vorticity of the static Killing congruence, which characterizes the local rotation of nearby world lines in the congruence, was explored in [151]; remarkably, they found that these two quantities were equal (see [172] for a nice demonstration of this statement). Moreover, since this congruence is also rigid, the FS frame associated with static Killing observers of a spacetime acquires the interpretation of being axes-at-rest relative to asymptotic static Killing observers ('fixed stars'). Basically, the projection of a connecting null vector of the static Killing congruence in the FS triad of a static Killing observer is simply a constant vector. This implies that photons shot out at different times along the same direction relative to the FS frame attached to a static Killing observer in a stationary spacetime all reach the same asymptotic observer. Therefore, the legs of such a FS triad are usually called 'optical axes.' These axes can be physically constructed by placing three telescopes pointing towards three (orthogonal) non-planar asymptotic spatially-fixed stars. Therefore,

(a) Black Hole $a = .6M$; Boyer-Lindquist coordinates

(b) Black Hole $a = .6M$; Kerr-Schild coordinates

(c) Naked Singularity $a = 1.01M$; Boyer-Lindquist coordinates

(d) Naked Singularity $a = 1.01M$; Kerr-Schild coordinates

(e) Naked Singularity $a = 2M$; Boyer-Lindquist coordinates

(f) Naked Singularity $a = 2M$; Kerr-Schild coordinates
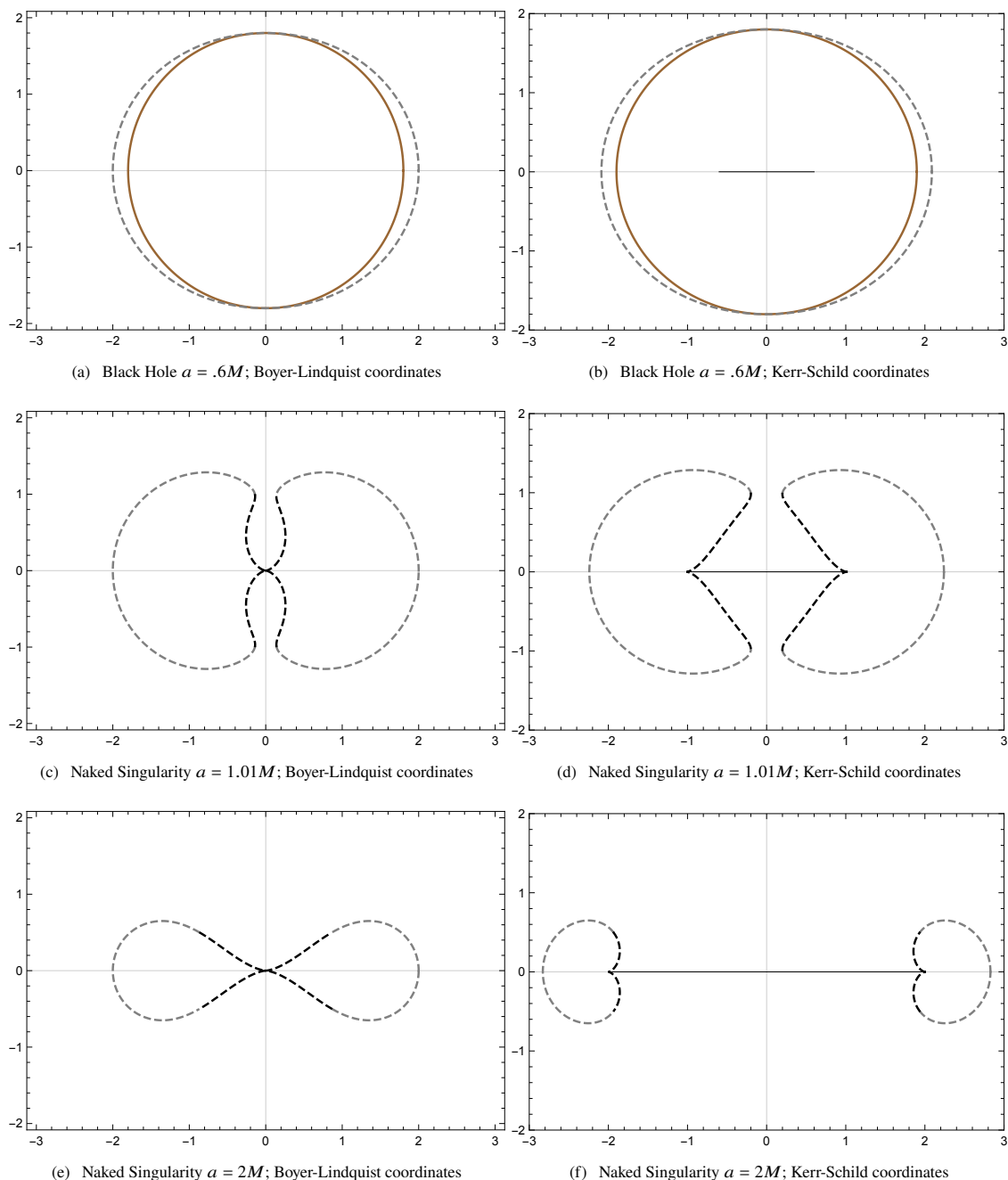
FIGURE 4.1: We show here azimuthal sections of ergoregions for a Kerr black hole and naked singularity in Boyer-Lindquist coordinates in the left panels, and in Kerr-Schild coordinates in the right panels. The color coding is as follows: in brown, dashed-gray and dashed-black, we represent the event horizon, outer ergoradius and inner ergoradius respectively. The black hole ergoregion is defined as being the region between the event horizon and the outer ergoradius, i.e. $r_H \leq r \leq r_+$; the ergosurface is defined to be the hypersurface $r_{\text{ergo}} = r_+$. On the other hand, for a Kerr naked singularity, the ergoregion is defined to be the region between the two ergoradii, i.e. $r_- \leq r \leq r_+$, and the ergosurface is defined to be the hypersurface $r_{\text{ergo}} = r_\pm$. We have also shown, in solid-black, a cross-section of the ring singularity in the Kerr-Schild coordinates, which satisfies $x^2 + y^2 = a^2 M^2$. This corresponds to $r = 0, \theta = \pi/2$ in the Boyer-Lindquist coordinates. See for example [200] for further details.

measuring the change of the spin vector relative to this triad gives us the change in the spin relative to fixed asymptotic observers (see for example §II.C of [317]). One can see §2 of [318] for a more general discussion on the relation between the FW spin-precession frequency along arbitrary time-like observers and the vorticity of their congruence.

The take-away here is that, in non-static stationary spacetimes, like the Kerr spacetime, the Frenet-Serret frames associated with the congruence of static Killing observers (4.3.3) play a fundamental role in translating physical statements made relative to a particular observer's comoving tetrad frame into the more desirous statements that are made relative to asymptotically spatially-fixed observers. This is of critical importance if, for example, one would like to study the frequency at which the magnetic-axis of a pulsar, present in the vicinity of a Kerr black hole, crosses the line of sight towards earth.

Finally, it is important to note the following. In static spacetimes the spin-precession frequency of static Killing observers identically vanishes $\Omega_p = 0$. This is evident from equation 4.3.16 for static Killing observers ($\Omega = 0$) in the Schwarzcshild spacetime ($a = 0$), or more explicitly for equatorial static Killing observers ($\theta = \pi/2$) see (4.5.6). Also, the congruence of such observers is irrotational. Therefore, if one initially arranged a set of telescopes to point along three non-planar stars and set atop them three gyroscopes that also pointed along these stars, the gyroscopes and telescopes would remain aligned at all times. This does not hold true for non-static stationary spacetimes and the gyroscopes would precess relative to the telescopes.

We have discussed why the class of static Killing observers is of fundamental importance and a study of the pulse profiles of pulsars moving along such orbits will be presented in §4.6. However, from an astrophysical standpoint, it would be even more interesting if one could extend this study to a description of the more general class of stationary Killing observers, and this is discussed in §4.6.6. This class of observers contains within it, for example, the set of observers that move on time-like equatorial circular geodesics in the Kerr spacetime, which satisfy,

$$\nabla_{u'} u' = 0. \tag{4.3.6}$$

This above condition just imposes a constraint on the allowed orbital angular frequencies, and such observers move at Kepler frequencies, $\Omega = \Omega_{K\pm}$. The $+$ and $-$ signs are associated with co-rotating and counter-rotating equatorial Kepler observers and we have,

$$\Omega_{K\pm} = \frac{M^{1/2}}{aM^{1/2} \pm r^{3/2}}. \tag{4.3.7}$$

It is important to note that stable timelike co-rotating and counter-rotating Kepler observers exist only outside the respective innermost stable circular orbits (ISCOs), and the expressions for the ISCO radii can be found in [117]. See figure 4.2 for how the ISCO radii for co-rotating ($r_{\text{ISCO}+}$) and counter-rotating ($r_{\text{ISCO}-}$) equatorial Kepler observers vary with change in the spin parameter a of the Kerr black hole. As can be seen from the figure the ISCO for the equatorial co-rotating Kepler observers lies inside the ergoregion ($r_{\text{ISCO}+} < 2M$) for $a > 0.943M$ (see for example [312]). In this chapter, whenever we consider observers moving on equatorial circular geodesics, we will exclusively consider only those that are on stable orbits i.e., those that satisfy $r \geq r_{\text{ISCO}\pm}$ for co-rotating and counter-rotating orbits respectively.

Yet another set of astrophysically important observers are the zero angular momentum observers (ZAMOs). [117] showed that the frame attached to a ZAMO is a powerful tool in the analysis of physical processes near astrophysical objects and these are observers whose world-lines are normal to the $t =$ const. hypersurfaces.
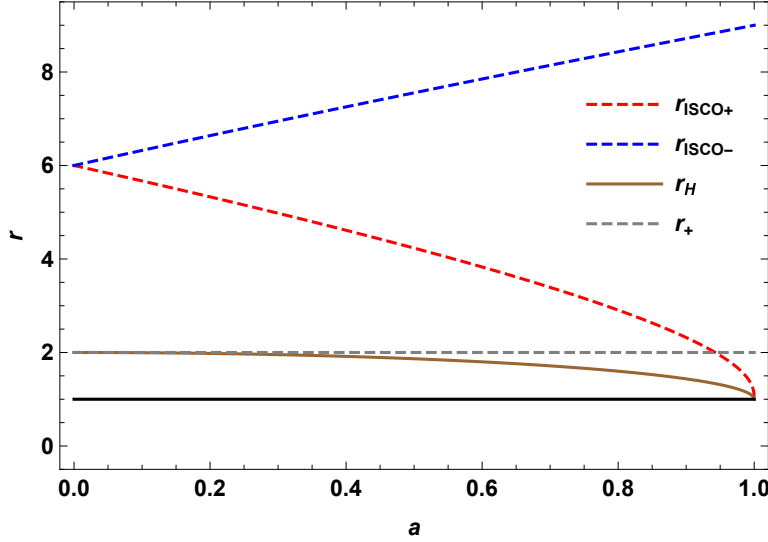
FIGURE 4.2: We plot here in dashed-red, dashed-blue, brown and dashed-gray respectively the radii of the co-rotating (+) and counter-rotating (-) innermost stable circular orbits (ISCOs) $r_{\text{ISCO}\pm}$ (outside which Kepler observers are time-like and hence allowed), the radius of the horizon r_{H} and the radius of the ergosurface r_+ in the equatorial plane as functions of the spin parameter of the black hole a, both in units of M. It should be noted that $r_{\text{ISCO}+}$ lies inside the ergoregion for $a > 0.943M$ (see for example [312]).

They fall within the class of stationary Killing observers and move at angular speeds of,

$$\Omega_{\text{Z}} = \frac{\Omega_+ + \Omega_-}{2} = -\frac{g_{03}}{g_{33}} = \frac{2Mar}{(r^2 + a^2)^2 - a^2 \Delta \sin^2 \theta}. \tag{4.3.8}$$

In following sections, we shall parametrize the orbital angular velocity Ω of the pulsar by q as [312],

$$q(\Omega) = \frac{\Omega - \Omega_-}{\Omega_+ - \Omega_-}, \tag{4.3.9}$$

with $0 < q < 1$. Let us denote the q-values of static observers, ZAMOs and of co-rotating and counter-rotating Kepler observers as q_{static}, q_{Z} and $q_{\text{K}\pm}$ respectively. Then,

$$q_{\text{static}} = -\frac{\Omega_-}{\Omega_+ - \Omega_-}, \quad q_{\text{Z}} = .5, \quad q_{\text{K}\pm} = \frac{\Omega_{\text{K}\pm} - \Omega_-}{\Omega_+ - \Omega_-}. \tag{4.3.10}$$

See figure 4.3 for how q_{static} and $q_{\text{K}\pm}$ change with radius for different black hole spin parameters $a = .1M, .5M$ and $.9M$ denoted in green, black and purple respectively.

4.3.1 The Adapted-Kerr Metric

Following [151], we demonstrate below that stationary Killing observers of the Kerr metric are equivalent to static Killing observers in the 'adapted-Kerr metric,' which is simply the Kerr metric expressed in coordinates comoving with Kerr stationary Killing observers with a particular orbital angular frequency Ω. We argue therefore that by studying the properties of the spin-precession frequency experienced by adapted-Kerr static Killing observers, one can obtain a complete description of spin-precession effects experienced by the full class of Killing observers of the Kerr spacetime. Another advantage of shifting to the adapted-Kerr spacetime

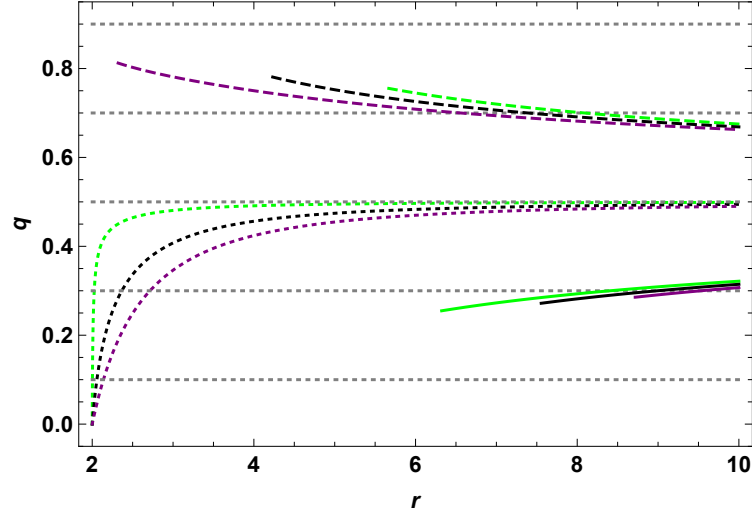FIGURE 4.3: Here we plot the values of q_{static} in dotted lines between $r = 2 - 10M$, in regions of strong gravitational fields, and $q_{\text{K}\pm}$ in dashed and solid lines respectively between $r = r_{\text{ISCO}\pm} - 10M$. The different colors represent black hole spin parameters $a = .1M, .5M$ and $.9M$ in green, black and purple respectively. The dashed-gray lines correspond to the grid-lines $q = .1, .3, .5, .7, .9$. See figure 4.2 for how the ISCO radii for co-rotating (+) and counter-rotating (-) equatorial Kepler observers $r_{\text{ISCO}\pm}$ vary with the spin parameter a.

is that one can obtain the evolution of the line-of-sight to earth in the comoving frame of a stationary Killing observer easily, as discussed in appendix D.

The relevant change of coordinates from the usual Boyer-Lindquist coordinates x^μ to those comoving with a Kerr stationary Killing observer with an orbital angular speed of Ω, which we shall call adapted-BL coordinates $x^{\bar{\mu}} = (\bar{t}, \bar{r}, \bar{\theta}, \bar{\phi})$ is given by,

$$\mathrm{d}t = \mathrm{d}\bar{t}, \ \mathrm{d}\phi = \mathrm{d}\bar{\phi} + \Omega \, \mathrm{d}\bar{t}. \tag{4.3.11}$$

r, θ are left unchanged and the Kerr metric (4.3.1) now becomes,

$$\mathrm{d}s^2 = \left[g_{00} + 2\Omega g_{03} + \Omega^2 g_{33}\right] \mathrm{d}\bar{t}^2 + 2\left[g_{03} + \Omega g_{33}\right] \mathrm{d}\bar{t}d\bar{\phi} + g_{33}\mathrm{d}\bar{\phi}^2 + g_{11}\mathrm{d}r^2 + g_{22}\mathrm{d}\theta^2,$$

$$= g_{\bar{0}\bar{0}}\mathrm{d}\bar{t}^2 + 2g_{\bar{0}\bar{3}}\mathrm{d}\bar{t}d\bar{\phi} + g_{33}\mathrm{d}\bar{\phi}^2 + g_{11}\mathrm{d}r^2 + g_{22}\mathrm{d}\theta^2. \tag{4.3.12}$$

We shall refer to this metric as the adapted-Kerr metric and the Jacobian associated with this coordinate transformation is,

$$J^{\bar{\mu}}_{\ \nu} = \frac{\mathrm{d}x^{\bar{\mu}}}{\mathrm{d}x^\nu} = \begin{bmatrix} 1 & 0 & 0 & 0 \\ 0 & 1 & 0 & 0 \\ 0 & 0 & 1 & 0 \\ -\Omega & 0 & 0 & 1 \end{bmatrix}. \tag{4.3.13}$$

Under the coordinate transformation, ξ'^μ transforms to $\xi'^{\bar{\mu}} = J^{\bar{\mu}}_{\ \nu}\xi'^\nu$ so that,

$$\xi'^{\bar{\mu}} = (1, 0, 0, 0). \tag{4.3.14}$$

That is, $\xi' = \frac{\partial}{\partial \bar{t}} = \partial_{\bar{0}}$. Therefore, Kerr stationary observers become adapted-Kerr static observers. Also, Kerr static observers become adapted-Kerr stationary observers, although with the sign of the angular speed reversed. This is of importance because earth, which will naturally be modelled to be an asymptotic static Killing observer in the Kerr spacetime, becomes a stationary Killing observer of the adapted-Kerr metric, i.e.,

its four-velocity becomes,

$$\xi^{\bar{\mu}} = (1, 0, 0, -\Omega) \,. \tag{4.3.15}$$

A corollary of the above discussion is that in the original Boyer-Lindquist coordinates, ξ' became null-like ($\xi' \cdot \xi' = 0$) on the event horizon. Now since we have also $\xi' \cdot \xi' = g_{\bar{0}\bar{0}}$, the coordinate transformation (4.3.11) maps the event horizon of the Kerr metric onto the ergosurface of the adapted-Kerr metric, as it should.

4.3.2   Accelerations and Spin-Precession Frequencies

As discussed above, the Frenet-Serret generalised curvature invariants and tetrad associated with Kerr Killing observers can be obtained by treating them as adapted-Kerr static Killing observers (4.3.14), and from [151] we have,

$$\bar{\kappa}^2 = \frac{1}{4g_{\bar{0}\bar{0}}^2} \left[\frac{g_{\bar{0}\bar{0},1}^2}{g_{11}} + \frac{g_{\bar{0}\bar{0},2}^2}{g_{22}} \right], \tag{4.3.16}$$

$$\bar{\sigma}_1^2 = -\frac{g_{\bar{0}\bar{3}}^2 g_{11} g_{22}}{4\Delta_{03}} \frac{\left[\frac{g_{\bar{0}\bar{0},1}}{g_{11}} \left(\frac{g_{\bar{0}\bar{3},1}}{g_{\bar{0}\bar{3}}} - \frac{g_{\bar{0}\bar{0},1}}{g_{\bar{0}\bar{0}}} \right) + \frac{g_{\bar{0}\bar{0},2}}{g_{22}} \left(\frac{g_{\bar{0}\bar{3},2}}{g_{\bar{0}\bar{3}}} - \frac{g_{\bar{0}\bar{0},2}}{g_{\bar{0}\bar{0}}} \right) \right]^2}{\left[g_{\bar{0}\bar{0},1}^2 g_{22} + g_{\bar{0}\bar{0},2}^2 g_{11} \right]},$$

$$\bar{\sigma}_2^2 = -\frac{1}{4\Delta_{03}} \frac{\left[g_{\bar{0}\bar{0},1} g_{\bar{0}\bar{3},2} - g_{\bar{0}\bar{0},2} g_{\bar{0}\bar{3},1} \right]^2}{\left[g_{\bar{0}\bar{0},1}^2 g_{22} + g_{\bar{0}\bar{0},2}^2 g_{11} \right]},$$

where we have introduced the determinant $\Delta_{03} = g_{\bar{0}\bar{0}} g_{33} - g_{\bar{0}\bar{3}}^2 = -\Delta \sin^2 \theta$. Note that Δ_{03} is the same in both the BL and adapted-BL coordinate systems. Also, the vectors that form the Frenet-Serret tetrad associated with adapted-Kerr static Killing observers, written out in terms of the adapted-BL coordinate basis $(\partial_{\bar{0}}, \partial_1, \partial_2, \partial_{\bar{3}})$, are given as,

$$e_{\hat{\bar{0}}}^{\bar{\nu}} = \left(\frac{1}{\sqrt{-g_{\bar{0}\bar{0}}}}, 0, 0, 0 \right), \tag{4.3.17}$$

$$e_{\hat{\bar{1}}}^{\bar{\nu}} = \frac{1}{2\bar{\kappa} g_{\bar{0}\bar{0}}} \left(0, \frac{g_{\bar{0}\bar{0},1}}{\sqrt{g_{11}}} \frac{1}{\sqrt{g_{11}}}, \frac{g_{\bar{0}\bar{0},2}}{\sqrt{g_{22}}} \frac{1}{\sqrt{g_{22}}}, 0 \right),$$

$$e_{\hat{\bar{2}}}^{\bar{\nu}} = \frac{1}{\sqrt{g_{\bar{0}\bar{0}} \Delta_{03}}} \left(-g_{\bar{0}\bar{3}}, 0, 0, g_{\bar{0}\bar{0}} \right),$$

$$e_{\hat{\bar{3}}}^{\bar{\nu}} = \frac{1}{2\bar{\kappa} g_{\bar{0}\bar{0}}} \left(0, \frac{g_{\bar{0}\bar{0},2}}{\sqrt{g_{22}}} \frac{1}{\sqrt{g_{11}}}, -\frac{g_{\bar{0}\bar{0},1}}{\sqrt{g_{11}}} \frac{1}{\sqrt{g_{22}}}, 0 \right).$$

The accent choices for the indices are as follows: $\bar{\nu}$ and $\hat{\bar{b}}$ are for objects represented in the adapted-BL coordinate basis and the FS tetrad associated with adapted-Kerr static Killing observers respectively. Therefore $e_{\hat{\bar{0}}}^{\bar{\nu}}$ represents the components of the time-like leg of the FS frame of an adapted-Kerr static Killing observer defined relative to the adapted-BL coordinate basis,

$$e_{\hat{\bar{0}}} = e_{\hat{\bar{0}}}^{\bar{\nu}} e_{\bar{\nu}}. \tag{4.3.18}$$

For conversions between the BL coordinate basis, the adapted-BL coordinate basis, the Kerr static Killing FS tetrad and the adapted-Kerr static Killing FS tetrad, see appendix A. Also, an alternative derivation of the above quantities (4.3.16, 4.3.17) via a neat differential geometric approach may be found in [172, 311, 312].

The spin-precession frequency $\vec{\Omega}_p$ can then be obtained from equations 4.3.16, 4.3.17 and 4.2.24 as,

$$\vec{\Omega}_p = \frac{\sqrt{\Delta}}{2\rho^2 g_{33}} \left[1 + \frac{2q(1-q)}{(2q-1)^2} \frac{1}{\sqrt{\Delta} \sin\theta} \right]^{-1/2} \left[-\sqrt{g_{11}} g_{33,2} \frac{\partial_1}{\sqrt{g_{11}}} + \sqrt{g_{22}} g_{33,1} \frac{\partial_2}{\sqrt{g_{22}}} \right]. \tag{4.3.19}$$

The modulus of the spin-precession frequency $\Omega_p \equiv |\vec{\Omega}_p|$ is then given as,

$$\Omega_p = \frac{\sqrt{\Delta}}{2\rho^2 g_{33}} \left[1 + \frac{2q(1-q)}{(2q-1)^2} \frac{1}{\sqrt{\Delta} \sin\theta} \right]^{-1/2} \sqrt{g_{11} g_{33,2}^2 + g_{22} g_{33,1}^2}. \tag{4.3.20}$$

Also, of the one-parameter class of coordinate transformations given in equation 4.3.11, the (identity) transformation corresponding to $\Omega = 0$ leaves the Kerr metric components unchanged and one can obtain the corresponding FS entities associated with Kerr static Killing observers simply by replacing the barred adapted-Kerr metric components $g_{\bar{\mu}\bar{\nu}}$ with the (unbarred) Kerr metric components $g_{\mu\nu}$ in the above equations (4.3.16, 4.3.17).

4.4 Features of the Spin-Precession Frequency associated with Arbitrary Killing Observers[6]

Naturally, we are interested in studying how the spin-precession frequency varies with the black hole or naked singularity parameters J and M, and with the properties of motion of the test spinning object, characterized by q, r, and θ. In fact the focus in [312] was to examine precisely these aspects in order to set up local experiments to distinguish black holes from naked singularities.

Following [312], we report the expression for the spin-precession frequency for arbitrary Killing observers in the Kerr spacetime to be given as,

$$\Omega_p = \chi \sqrt{A^2 \Delta \cos^2\theta + B^2 \sin^2\theta}, \tag{4.4.1}$$

where,

$$\chi = \frac{(r^2 + a^2)^2 - a^2 \Delta \sin^2\theta}{4q(1-q)\, \rho^7 \Delta}, \tag{4.4.2}$$

$$A = 2aMr - \frac{\Omega}{8} \left[8r^4 + 8a^2 r^2 + 16a^2 Mr + 3a^4 + 4a^2(2\Delta - a^2)\cos 2\theta + a^4 \cos 4\theta \right] + 2\Omega^2 a^3 Mr \sin^4\theta,$$

$$B = aM(r^2 - a^2 \cos^2\theta) + \Omega \left[a^4 r \cos^4\theta + r^2(r^3 - 3Mr^2 - a^2 M(1 + \sin^2\theta)) \right.$$
$$\left. + a^2 \cos^2\theta(2r^3 - Mr^2 + a^2 M(1 + \sin^2\theta)) \right] + \Omega^2 aM \sin^2\theta \left[r^2(3r^2 + a^2) + a^2 \cos^2\theta(r^2 - a^2) \right].$$

We have not re-expressed Ω in the expressions for A and B above in terms of $q, \Omega_\pm$ for brevity; see equation 4.3.9 above. Now, immediately it can be seen from these expressions that A and B are finite valued. Further χ, and therefore Ω_p, diverge at $\rho = 0$ or $\Delta = 0$. Note that $q = 0, 1$ are not allowed values since they correspond to Killing *null* observers. Remember that $\rho = 0$ corresponds to the ring singularity and $\Delta = 0$ to the event horizon. Therefore, one may expect to be able to locate the event horizon from spin-precession considerations in the case of a black hole and the naked singularity itself, when horizons are absent.

We obtain distinguishing characteristic features specifically in the radial profile of Ω_p for both BH and NS cases, which we will discuss as we proceed. Further, we also obtain features in the radial profile of Ω_p that could help distinguish near-extremal NSs from those with higher spin. We explore the details of such features and provide a criterion to separate near-extremal NS ($1 < a/M < 1.1$) from those with higher spins ($1.1 \leq a/M$) in appendix B.

For a BH with $a/M = 0.9$, we can see from the left panels of figure 4.4 that the spin-precession frequency indeed becomes arbitrarily large close to the horizon for all values of $a/M, q$ and θ, except $q = 0.5$. From panel (a), we can see that for $q < 0.5$ the radial variation of Ω_p is monotonic, with no maxima or minima. However, for $q > 0.5$, a minima starts appearing, which can be seen from panels (e) and this minima is sharp for $\theta = \pi/2$. For observers at the ZAMO frequency, $q = 0.5$, the spin-precession frequency remains smooth and finite, as can be seen from panel (c), even for gyros orbiting close to the horizon. We note that the ZAMO frequency exhibits consistently peculiar behaviour which might lead to interesting insights on exploring further. On the other hand, for a NS with $a/M = 1.1$, as can be seen from the plots on the right in figure 4.4, the spin-precession frequency does not diverge. It remains finite and regular even as one approaches $r = 0$ for all angles $0 < \theta \lesssim 90^0$. Near $r = 0, \theta = 90^0$, the spin-precession frequency becomes arbitrarily large because of the presence of the ring singularity. This is also in stark contrast to the BH case in the present chapter, for which we obtain a divergence in the spin-precession frequency close to the event horizon, 'far away' from $r = 0$. One also finds that a local minima and a local maxima appear for $q \geq 0.5$ for some angles, i.e. there are additional features that might help to ascertain the angular velocity of a stationary observer w.r.t. the ZAMO frequency. We also note here that it can be seen from the y-axis scales in the panels (a), (b) and (e), (f) of figure 4.4 relative to the scales in the other panels that Ω_p rises sharply as the angular momentum of the stationary observer Ω nears its allowed bounding values $\Omega_{\pm}$. These panels represent $q = 0.1, 0.9$ respectively for BH and NS.

In figure 4.5, we demonstrate that the features obtained for $a/M = 0.9$ are characteristic to all BHs by plotting Ω_p for other values of $a/M = 0.2, 0.4, 0.6, 0.8, 1$. We show that the spin-precession frequency is finite and smooth both inside and outside the ergoregion but it diverges near the horizon for all $a/M, q, r$ and θ, except for $q = 0.5$. Finally, in figure 4.6, we demonstrate that the features obtained for $a/M = 1.1$ are characteristic of NSs, in general, by considering other values of $a/M = 1.01, 1.05, 1.09, 2, 5$. We have picked these values at non-uniform intervals anticipating additional features in the plots for near-extremal NSs. We show that the spin-precession frequency is finite and smooth both inside and outside of the ergoregion, same as the BH case, but it diverges near the ring singularity for all $a/M, q, r$ and θ. This is different from the BH case, as we have already mentioned above. Indeed, we also note here that near-extremal NSs appear to have additional characteristic features which could be used to distinguish them from other generic higher spin NSs, as can be seen clearly from the panels of this figure, and we explore this observation in the following section.

We relegate a description of our (somewhat unrealistic) local experiments distinguish a Kerr black hole from a Kerr naked singularity to Chapter 5.

4.5   Equatorial Killing Observers

Now, if gravitomagetic spin-precession modifies the appearance of pulsars present near Kerr compact objects, and if this modification pops up in pulsar timing data, then one could potentially extract black hole parameters
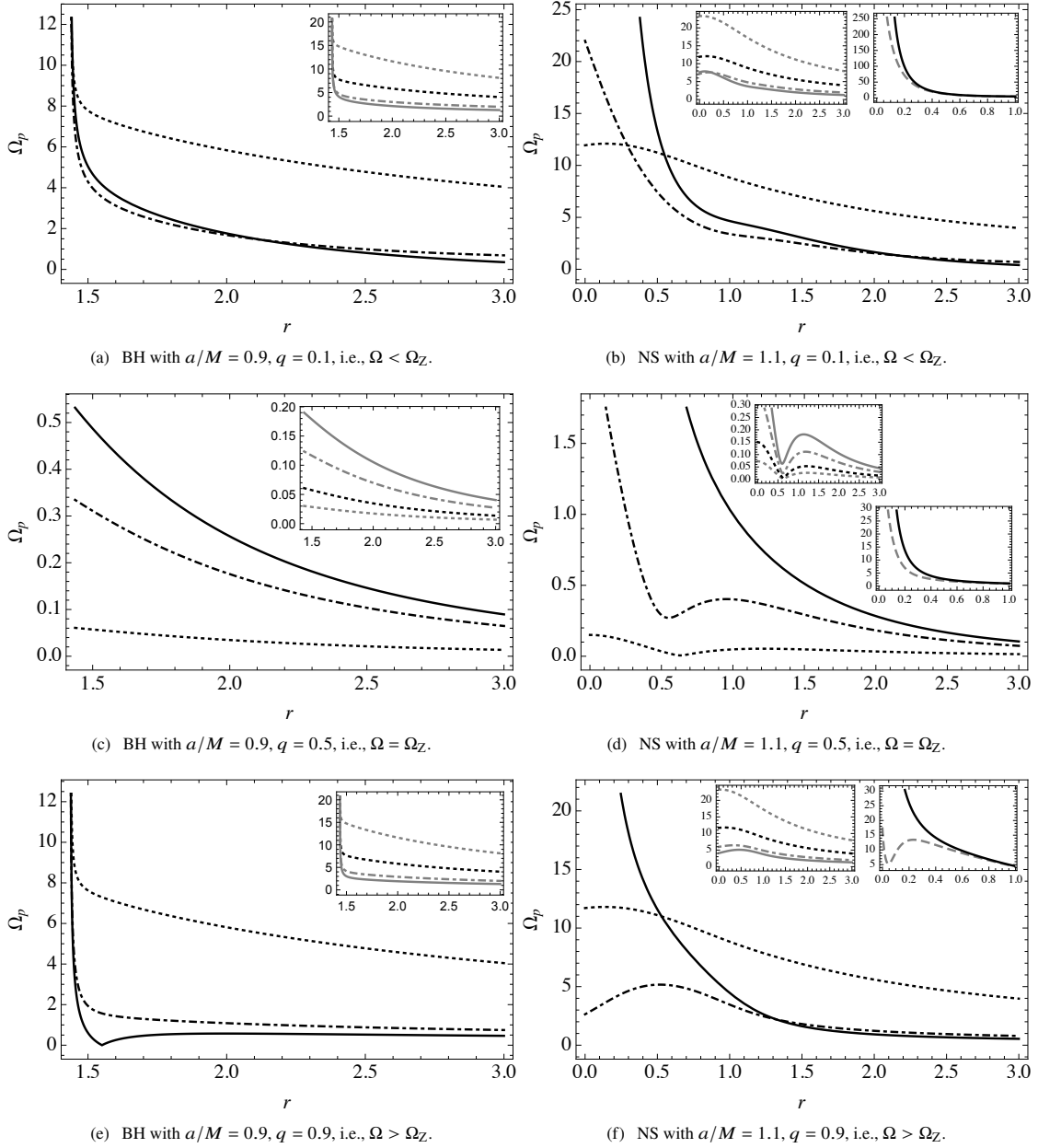
FIGURE 4.4: We have plotted in each panel the modulus of the spin-precession frequency of stationary gyroscopes $\Omega_{\rm p}$ (in M^{-1}) versus r (in M) around a black hole (left panels) with $a/M = .9$ and a naked singularity (right panels) with $a/M = 1.1$ for different q and θ. Each of the rows has a different value of q, which measures its angular velocity, and in each panel, θ takes values $10^0, 50^0, 90^0$ represented in dotted black, dot-dashed black and black respectively. For the BH, r ranges from the horizon radius (which is at ~ 1.44, in this case) to 3. For the NS, the plots begin from $r = 0$ (specifically, the singularity is at $r = 0$ *and* $\theta = 90^0$) to 3 and the ergosurface is at 2 for $= 90^0$. It can be seen that there is a much bigger drop in $\Omega_{\rm p}$ from 10^0 to 50^0 than from 50^0 to 90^0. We have therefore inset plots (left inset for NS panels) for additional θ values (close to the pole) of $5^0, 20^0$ and 30^0 in dotted gray, dot-dashed gray and gray along with 10^0 in dotted black, same as the main panel. Further, for the NS case, since the singularity is at $\theta = 90^0$ in these coordinates, as $r \to 0, \theta \to 90^0$, the frequency blows up. We have zoomed in on the range of r between 0 and 1 and inset (on the right in the NS panels) the plots for $\theta = 80^0, 90^0$ in dashed gray and black to demonstrate how quickly $\Omega_{\rm p}$ increases relative to angles much smaller than 90^0.
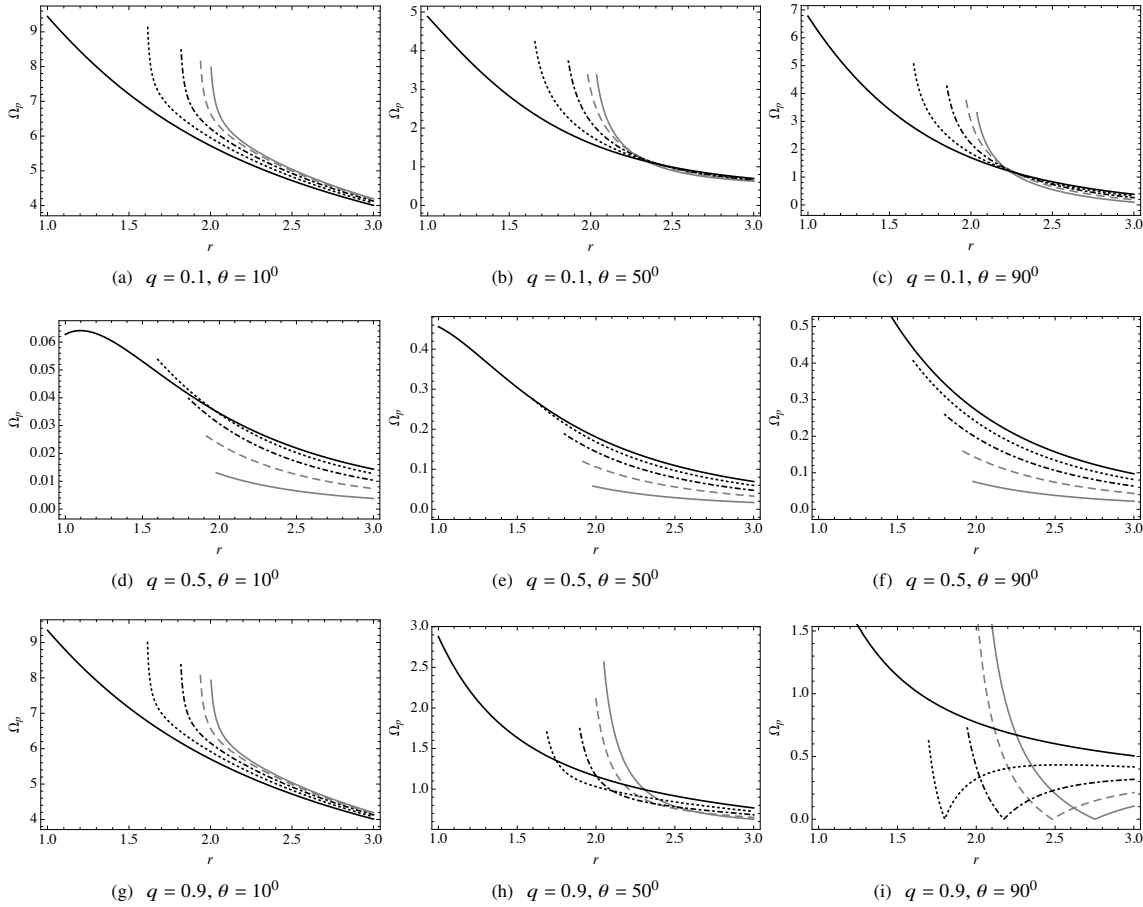
FIGURE 4.5: We have plotted here, for black holes, the modulus of the spin-precession frequency Ω_{p} (in M^{-1}) vs r (in M) for different $a/M, q$ and θ. We have $q = 0.1, 0.5, 0.9$ in the top, middle and bottom rows respectively and $\theta = 10^0, 50^0, 90^0$ in the left, centre and right columns respectively. In each panel, the line style is gray, dashed gray, dot-dashed black, dotted black and black for $a/M = .2, .4, .6, .8, 1$ respectively. We have plotted Ω_{p} for each BH (with different a/M) between its horizon radius (r_+) and $r = 3$. The ergosurface is at $r = 2$ for $\theta = 90^0$ (bottom row), for reference. This figure clearly demonstrates that for all values of $a/M, q, \theta$, the spin-precession frequency Ω_{p} becomes arbitrarily large near the event horizon, in general. As can be seen from the bottom row, for $q > 0.5$, minimas appear. Specifically, from panel (i), it can be seen that the sharpness of the minimas increases with a/M, with extremal black holes as exceptions.

from such considerations. Further, since of most astrophysical relevance due to gravitational dynamics are pulsars moving on equatorial circular orbits at constant angular speeds around a Kerr black hole ([117, 319]; also see [320] and references therein), we shall henceforth restrict our discussion to such pulsars. Note that we will not introduce a subscript to denote that we will be displaying equatorial plane quantities.

If we adopt the usual convention $\bar{\kappa} \geq 0$, then clearly $e_{\hat{1}}$ and $e_{\hat{3}}$ change signs at $\Omega_{\mathrm{K}\pm}$, outside the horizon ($r_{\mathrm{H}} \leq r$). And with the introduction of $\epsilon_{\bar{3}}$ (see §3 of [321]),

$$\epsilon_{\bar{3}} = \frac{-g_{\bar{0}\bar{3}}\partial_{\bar{0}} + g_{\bar{0}\bar{0}}\partial_{\bar{3}}}{\sqrt{g_{\bar{0}\bar{0}}\Delta_{03}}}, \tag{4.5.1}$$

(a) $q = 0.1, \theta = 10^0$

(b) $q = 0.1, \theta = 50^0$

(c) $q = 0.1, \theta = 90^0$

(d) $q = 0.5, \theta = 10^0$

(e) $q = 0.5, \theta = 50^0$

(f) $q = 0.5, \theta = 90^0$

(g) $q = 0.9, \theta = 10^0$

(h) $q = 0.9, \theta = 50^0$

(i) $q = 0.9, \theta = 90^0$
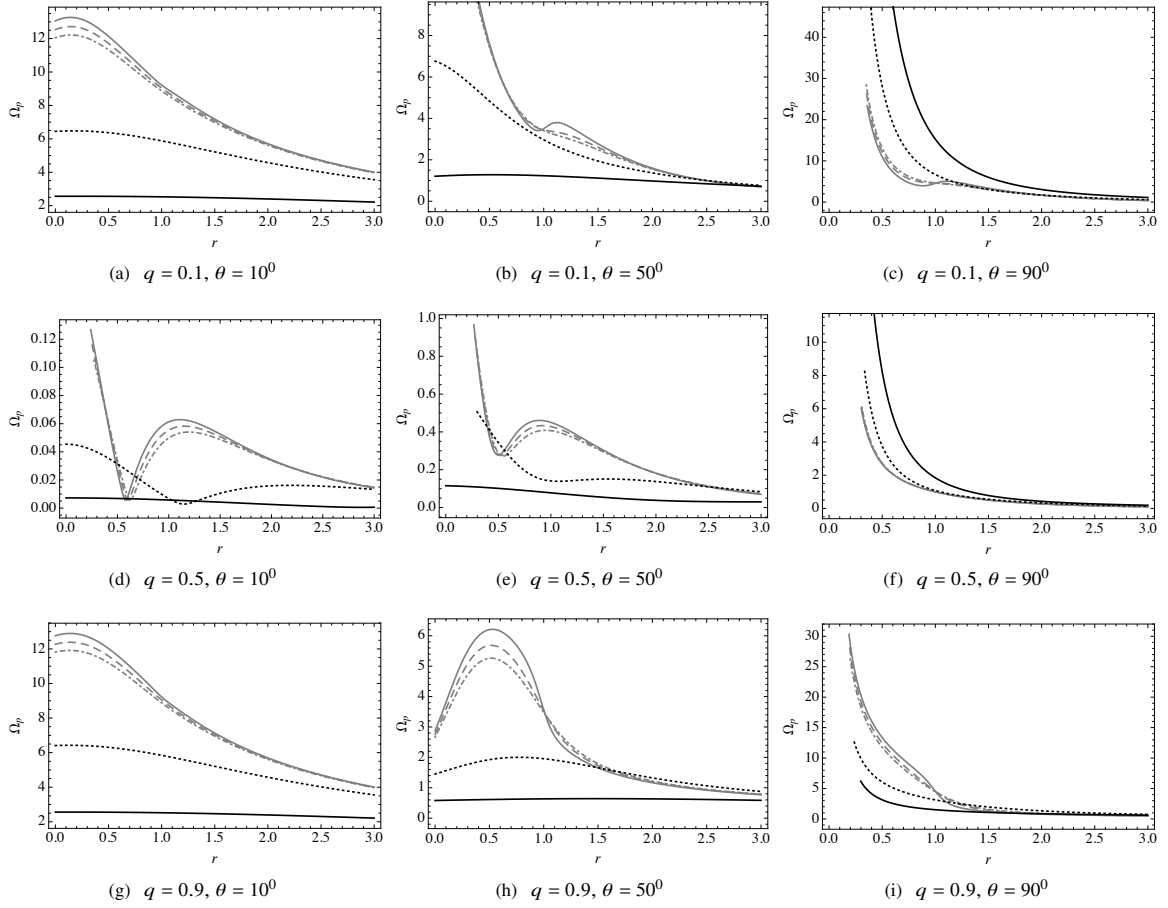
FIGURE 4.6: We have plotted here, for naked singularities, the modulus of the spin-precession frequency Ω_p (in M^{-1}) vs r (in M) for different $a/M, q$ and θ. We have $q = 0.1, 0.5, 0.9$ in the top, middle and bottom rows respectively and $\theta = 10^0, 50^0, 90^0$ in the left, centre and right columns respectively. In each panel, the line style is gray, dashed gray, dot-dashed gray, dotted black and black for $a/M = 1.01, 1.05, 1.09, 2, 5$ respectively. We have plotted Ω_p for each NS (with different a/M) between $r = 0$ and $r = 3$. The ergoregion extends upto $r = 2$ for $\theta = 90^0$ (bottom row), for reference. This figure clearly demonstrates that for all values of $a/M, q, \theta$, the spin-precession frequency Ω_p becomes arbitrarily large near the ring singularity. Further, the gray lines are all near-extremal NSs and this figure demonstrates how near-extremal NSs appear to have additional characteristic features that can be used to distinguish them from NSs with higher angular momentum. Motivated thus, we explore this distinction in greater detail in appendix B since near-extremal naked singularities are of great interest from an observational standpoint, if they exist.

we can represent the right-handed FS triad for these observers in the equatorial plane succinctly as,

$$\left\{ e_{\hat{1}}, e_{\hat{2}}, e_{\hat{3}} \right\} = \begin{cases} \left\{ -\frac{\partial_1}{\sqrt{g_{11}}}, \epsilon_{\bar{3}}, \frac{\partial_2}{g_{22}} \right\}, & \text{for } \Omega_- < \Omega \le \Omega_{K-}, \\ \left\{ \frac{\partial_1}{\sqrt{g_{11}}}, \epsilon_{\bar{3}}, -\frac{\partial_2}{g_{22}} \right\}, & \text{for } \Omega_{K-} < \Omega \le \Omega_{K+}, \\ \left\{ -\frac{\partial_1}{\sqrt{g_{11}}}, \epsilon_{\bar{3}}, \frac{\partial_2}{g_{22}} \right\}, & \text{for } \Omega_{K+} < \Omega < \Omega_+. \end{cases} \tag{4.5.2}$$

For a discussion on defining the FS tetrads appropriately in regions where Ω_{K+} are not allowed orbital angular frequencies, i.e. inside the respective ISCOs, see appendix C.

Accelerations experienced by these observers is given as,

$$\alpha' = \bar{\kappa} e_{\hat{1}} = \left| \frac{\sqrt{\Delta}(a^2 M - r^3)(\Omega - \Omega_{K+})(\Omega - \Omega_{K-})}{r^3 \left[1 - (r^2 + a^2)\Omega^2 - \frac{2M(a\Omega - 1)^2}{r} \right]} \right| e_{\hat{1}}. \tag{4.5.3}$$

Outside the horizon, the acceleration changes sign at $\Omega = \Omega_{K\pm}$. Physically, this means that the sense of the centrifugal force reverses at the locations of the Kepler orbits, for which $\alpha' = 0$ [322]. A detailed discussion on this is presented in appendix C and we partition the regions in the Kerr spacetime where accelerations (and centrifugal forces) experienced by observers moving on equatorial circular orbits are directed along $\pm\partial_1$ respectively in figure C.1.

Also, since in the equatorial plane $\bar{\sigma}_2 = 0$ and the spin-precession frequency for these observers is given as,

$$\Omega'_p = -\bar{\sigma}_1 e_{\hat{3}}, \tag{4.5.4}$$

$$\bar{\sigma}_1 = \frac{\Omega r^3 + 3M\Omega r^2(a\Omega - 1) + aM(a\Omega - 1)^2}{r^3 \left[1 - (r^2 + a^2)\Omega^2 - \frac{2M(a\Omega - 1)^2}{r} \right]},$$

it is clear that Ω'_p changes sign at the zeroes of

$$\Omega r^3 + 3M\Omega r^2(a\Omega - 1) + aM(a\Omega - 1)^2 = 0. \tag{4.5.5}$$

It must be noted that the orbits where the reversal of the spin-precession frequency occurs do not, in general, coincide with the Kepler orbits where the centrifugal force reverses. For a detailed discussion on the sense of the spin-precession frequency see appendix C. In figure C.2, we display the regions in the Kerr spacetime where observers moving on equatorial circular geodesics experience positive and negative spin-precession frequencies relative to the $e_{\hat{3}}$ leg of their respective right-handed FS tetrads.

In particular, the spin-precession frequencies experienced by equatorial Kerr static observers $\Omega_p = \Omega'_p (\Omega = 0)$ never changes sign and is given as,

$$\Omega_p = \frac{aM}{r^2(r - 2M)} \frac{\partial_2}{\sqrt{g_{22}}}. \tag{4.5.6}$$

The spin-precession frequencies experienced by the equatorial ZAMOs are given as,

$$\Omega'_p (\Omega = \Omega_Z) = \frac{aM(a^2 + 3r^2)}{r^2(r^3 + a^2(r + 2M))} \frac{\partial_2}{\sqrt{g_{22}}}. \tag{4.5.7}$$

Note that the zero angular momentum observers experience spin-precession in the same sense as static observers. Also, it is interesting that for both co-rotating and counter-rotating equatorial Kepler observers of the Kerr spacetime, the magnitude of their spin-precession frequencies are independent of the spin-parameter,

$$|\Omega'_p| (\Omega = \Omega_{K\pm}) = \frac{M^{1/2}}{r^{3/2}}. \tag{4.5.8}$$

Since this form is reminiscent of pure geodetic spin-precession [150], we think it relevant to mention here that, as can be seen from equation 4.2.14, when a pulsar moves on an equatorial circular geodesic ($\alpha = 0$), its spin vector is simply parallel transported.

The eventual analysis presented in §4.7 of this chapter will largely depend on the strength of the spin-precession frequency, and so in figure 4.7, we discuss the trends in the absolute values of the accelerations $\bar{\kappa}$ and spin-precession frequencies $|\bar{\sigma}_1|$ experienced by pulsars that move along equatorial circular orbits around Kerr black holes, which we define from equations 4.5.3 and 4.5.4 as,

$$\bar{\kappa} = \left| \frac{\sqrt{\Delta}(a^2 M - r^3)(\Omega - \Omega_{K+})(\Omega - \Omega_{K-})}{r^3 \left[1 - (r^2 + a^2)\Omega^2 - \frac{2M(a\Omega - 1)^2}{r} \right]} \right|, \tag{4.5.9}$$

$$|\bar{\sigma}_1| = \left| \frac{\Omega r^3 + 3M\Omega r^2(a\Omega - 1) + aM(a\Omega - 1)^2}{r^3 \left[1 - (r^2 + a^2)\Omega^2 - \frac{2M(a\Omega - 1)^2}{r} \right]} \right|.$$

We display these quantities for BHs of mass $M = 100 M_\odot$ with different spin-parameters $a = .1M, .5M, .9M$, at different radii r and orbital angular velocities Ω. On an orbit of any particular radius r, a pulsar can move at angular speeds $\Omega_-(r) < \Omega(r) < \Omega_+(r)$, and we parametrize Ω by its q-value (4.3.9). We consider pulsars present in the strong gravitational field regime of the Kerr spacetime, at distances of $r = r_H - 10M$ and consider $q = .1, .3, .5, .7, .9, q_{\text{static}}, q_{K\pm}$. See equation 4.3.10 for the definitions of $q_{\text{static}}, q_{K\pm}$ and figure 4.3 for how they vary with a, r. It is useful to remember that static observers with $q = q_{\text{static}}$ and *stable* Kepler observers with $q = q_{K\pm}$ are allowed only outside $r > 2M$ and $r \geq r_{\text{ISCO}\pm}$ respectively. In Geometrized units ($\mathscr{G} = c = 1$), $r, \bar{\kappa}$ and $\bar{\sigma}_1$ scale with the mass of the black hole as M, M^{-1} and M^{-1} respectively. Therefore, the larger the mass of the black hole, larger are the sizes of the orbits and smaller are the accelerations and spin-precession frequencies associated with these world-lines. The sharp changes at $\bar{\kappa} = 0$ and $|\bar{\sigma}_1| = 0$ are an artefact of the modulus and actually correspond to a smooth change in the sign of the acceleration or spin-precession frequency respectively. $\bar{\kappa} = 0$ occurs at the Kepler orbits and the zeroes of the spin-precession frequency occur at the solutions of equation 4.5.5. Note that we have displayed $\bar{\kappa}$ and $\bar{\sigma}_1$ in these plots only for co-rotating and counter-rotating Kepler observers only outside their respective ISCOs (i.e. for stable Kepler observers). For a detailed discussion on the reversals of the accelerations and the spin-precession frequencies, see appendix C. And for a more detailed analysis of the trends in the modulii of the spin-precession frequencies experienced by pulsars moving on Killing orbits around both Kerr black holes and naked singularities, we direct the reader to consult [312].

It is also important to note that the r coordinate used in all these expressions is the Boyer-Lindquist radial coordinate. The actual physical radius of the orbit would be given by the Kerr-Schild radial coordinate $\tilde{r}$. The relation between the Kerr-Schild and the BL radial coordinates, in the equatorial plane, is given as (see for example [200]),

$$\tilde{r} = \sqrt{r^2 + a^2}. \tag{4.5.10}$$

So, for example, the Kerr ergosurface in the equatorial plane is at $r_+ = 2M$ in the Boyer-Lindquist chart but at $\tilde{r}_+ = \sqrt{4M^2 + a^2}$ in Kerr-Schild coordinates. To not complicate matters, we shall exclusively use the Boyer-Lindquist radial coordinate r until §4.7.

4.6   Effect of Gravitomagnetism on Pulsar Beam Evolution

We shall treat pulsars to be test spinning objects, i.e. as small but extended 'pole-dipole' test particles (see for example [308]). For the test spinning object approximation to hold, the primary requirement is that the

(a) $a = .1M$, Magnitude of Accelerations $\bar{\kappa}$

(b) $a = .1M$, Magnitude of Precession Frequencies $|\bar{\sigma}_1|$

(c) $a = .5M$, Magnitude of Accelerations $\bar{\kappa}$

(d) $a = .5M$, Magnitude of Precession Frequencies $|\bar{\sigma}_1|$

(e) $a = .9M$, Magnitude of Accelerations $\bar{\kappa}$

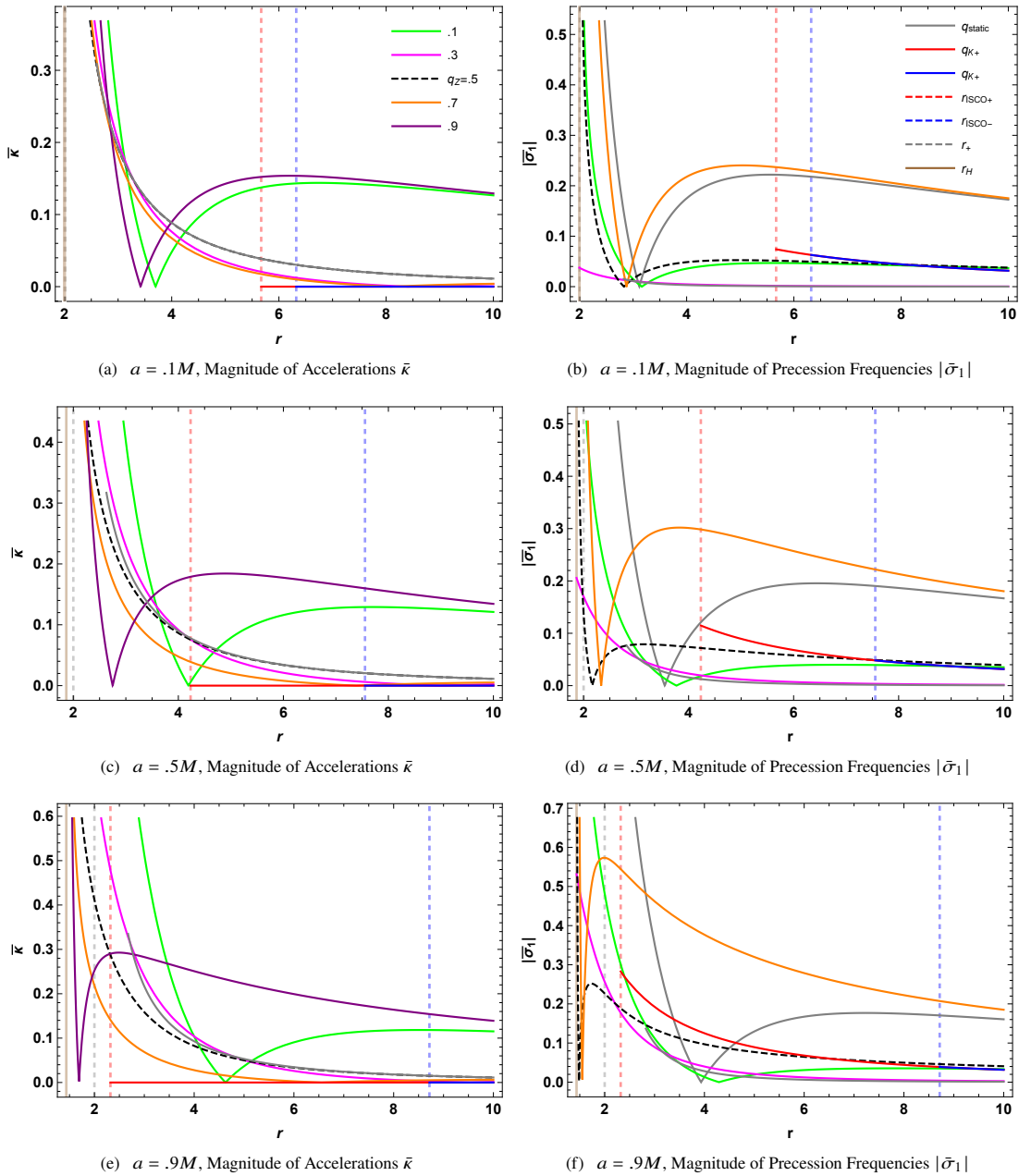(f) $a = .9M$, Magnitude of Precession Frequencies $|\bar{\sigma}_1|$

FIGURE 4.7: We show here the absolute values of the accelerations and spin-precession frequencies $\bar{\kappa}$ and $|\bar{\sigma}_1|$ experienced by observers moving on equatorial circular orbits at different Boyer-Lindquist orbital radii r, around Kerr black holes with specific angular momenta $a = .1M, .5M, .9M$. Such observers have restrictions on the values of allowed angular velocities at any given r, i.e. $\Omega_- < \Omega < \Omega_+$. We parametrize Ω using $0 < q < 1$ as $\Omega = q\Omega_+ + (1 - q)\Omega_-$, and plot here $q = .1, .3, .5, .7, .9$ in green, magenta, dashed-black, orange and purple respectively. In particular, $q = .5$ corresponds to the zero angular momentum observer (ZAMO). Gray represents Kerr static Killing observers with $\Omega = 0$ and red and blue represent non-accelerating co-rotating (+) and counter-rotating (-) Kepler observers, $\Omega = \Omega_{K\pm}$ respectively. The vertical dashed-red, dashed-blue, dashed-gray and brown lines indicate the location of the innermost stable circular orbits for co-rotating and counter-rotating observers $r_{\text{ISCO}\pm}$, the ergoradius in the equatorial plane $r_+(\theta = \pi/2)$ and the location of the horizon r_H respectively. In Geometrized units ($G = c = 1$), $r, \bar{\kappa}$ and $\bar{\sigma}_1$ scale with the mass of the black hole as M, M^{-1} and M^{-1} respectively. Therefore, the larger the mass of the black hole, larger are the sizes of the orbits and smaller are the accelerations and spin-precession frequencies associated with these world-lines. In the above plots, r runs from the location of the horizon r_H to $10M$. The conversion to physical units for r is $1M_\odot = 1.5$ km, $\bar{\kappa}$ is $1/M_\odot = 6.0 \times 10^{10}$ km/s^2 and $\bar{\sigma}_1$ is $1/M_\odot = 1.3 \times 10^5$ rad/s. Also, in panel (a) the gray line, corresponding to the Kerr static observer, lies very close to the dashed-black line, corresponding to the ZAMO. This can be cross-checked from figure 4.3 from which it is evident that $q_{\text{static}} \approx .5$ in this case.

background gravitational field due to the black hole must not vary much over the spatial size of the pulsar. That is, for a pulsar of mass and radius m_p, R_p present in the vicinity of a Kerr black hole whose mass and angular momentum are M, J, and for a radial separation between their centre of masses given by r, when $m_p \ll M < r$ and $R_p \ll r$, the interaction of the pulsar's spin *quadrupole* moment with inhomogeneities of the gravitational field can be neglected [138], it can be treated as such a test spinning object. The dynamics of the pulsar which is governed by the conservation equation,

$$\nabla_\mu T^{\mu\nu} = 0, \tag{4.6.1}$$

is then dominated by the two lowest $T^{\mu\nu}$-moments, namely its monopole p^μ and its dipole $S^{\mu\nu}$, which are its four-momentum and intrinsic spin-angular momentum tensor respectively [308]. Once one chooses the Pirani condition (4.2.10), one can associate with the dipole tensor an intrinsic spin-angular momentum four-vector $\mathcal{S}^\mu$ and subsequently an intrinsic spin angular momentum three-vector S^μ, which we introduced in §4.2. As mentioned before, we ignore the spin-curvature coupling in this work and calculations incorporating this effect will be reported elsewhere. Therefore, the equation of motion for the spin angular momentum reduces to the by Fermi-Walker transport law given in equation 4.2.13; see for example [316].

All calculations henceforth will be performed in orthonormal right-handed Euclidean Frenet-Serret spatial triads, which for a Kerr static Killing observer ($\Omega = 0$) is given as (see equation 4.5.2),

$$\left\{ \frac{\partial_1}{\sqrt{g_{11}}}, \frac{g_{00}\partial_3 - g_{03}\partial_0}{\sqrt{g_{00}\Delta_{03}}}, \frac{-\partial_2}{\sqrt{g_{22}}} \right\}. \tag{4.6.2}$$

Therefore, we can switch to the Euclidean three-vector notation and the FS frame written out above (4.6.2) will be denoted by $\{\hat{e}_1, \hat{e}_2, \hat{e}_3\}$. That is, for a vector $a = a^i e_{\hat{i}}$ defined in the FS frame, we will use $\vec{a} = (a^1, a^2, a^3)$, and for a unit vector, we will use $\hat{b}$. In §4.6.6, we will generalize our calculations to describe the full class of equatorial Kerr stationary Killing observers.

The world-line of a pulsar that remains at a fixed spatial location, or that moves at very low orbital angular velocities $\Omega \approx 0$, over the period of observation can be approximated to be a static Killing orbit with four-velocity given in equation 4.3.3. For such a pulsar, let us denote the instantaneous unit vector along which the spin-axis (or the intrinsic spin angular momentum) lies by $\hat{S}(\tau)$. In this notation, we can now rewrite the time dependence of the spin-axis $\hat{S}$ that arises from the spin-precession due to its coupling with the gravitomagnetic field of the Kerr black hole (4.2.25) as,

$$\dot{\hat{S}} = -\sigma_1 \hat{S} \times \hat{e}_3,$$

where the $\dot{}$ represents a derivative with respect to the proper time τ in the pulsar's comoving FS frame and $\sigma_1 = \bar{\sigma}_1(\Omega = 0)$ (see equation 4.5.4). Therefore, $\hat{S}$ moves on a cone of half-opening angle β around the precession-axis $\hat{e}_3$ at the spin-precession frequency $-\sigma_1$.

Now, if we represent by $\hat{B}$ and ω the instantaneous direction along which the pulsar's beam of radiation points and the (fixed) angular frequency at which the pulsar spins about its spin-axis, then the beam vector $\hat{B}$ just moves on the surface of a cone with axis $\hat{S}$ and half-opening angle α (not to be confused with the acceleration four-vector), at an angular speed of ω. See figure 4.8 for the geometry of the various vectors involved. The requisite equations of motion in the Euclidean Frenet-Serret frame are the following set of coupled first order

differential equations,

$$\dot{\hat{S}} = -\sigma_1 \hat{S} \times \hat{e}_3, \tag{4.6.3}$$

$$\dot{\hat{B}} = \omega \hat{B} \times \hat{S}, \tag{4.6.4}$$

4.6.1 Earth Line of Sight in the Frenet-Serret Triads of Kerr and adapted-Kerr Static Observers

As previously argued in §4.3, the FS triad associated with Kerr static Killing observers can be interpreted as axes-at-rest relative to asymptotic fixed observers. Hence, the projection of the tangent to the null-geodesic connecting the pulsar's spatial location to an arbitrary asymptotic fixed observer's position, like earth (when it is causally connected with the pulsar), onto this FS triad always remains a constant, and we can write,

$$n^{\hat{i}} = \left(\sin \theta_E \cos \phi_E, \sin \theta_E \sin \phi_E, \cos \theta_E \right), \tag{4.6.5}$$

For simplicity, we set $\phi_E = 0$,

$$n_E^{\hat{i}} = \left(\sin \theta_E, 0, \cos \theta_E \right). \tag{4.6.6}$$

Further, in the FS triad of an equatorial adapted-Kerr static Killing observer, we can write (see appendix D),

$$n_E^{\hat{\bar{j}}}(\tau) = \left(\cos \left(\Omega \tau \right) \sin \bar{\theta}_E, \mp \sin \left(\Omega \tau \right) \sin \bar{\theta}_E, \cos \bar{\theta}_E \right), \tag{4.6.7}$$

where the upper (-) and lower (+) signs apply to observers whose Frenet-Serret trinormal leg $e_{\hat{\bar{3}}}$ points along and opposite to the z-axis (or direction the black hole spin), denoted by $\hat{z}$ respectively. That is the signs $\mp$ correspond to the cases (see equation 4.3.17 and also the discussion in appendix D),

$$e_{\hat{\bar{3}}} = \pm \hat{z} = \mp \frac{\partial_2}{\sqrt{g_{22}}}. \tag{4.6.8}$$

Therefore, we can represent the apparent direction along which earth lies $\hat{n}_E$ as (cf. 4.6.6),

$$\hat{n}_E = \left(\sin \theta_E, 0, \cos \theta_E \right). \tag{4.6.9}$$

We are interested in finding the frequency at which $\hat{B}$ points along the apparent direction of earth, $\hat{n}_E$, first in the FS frame and eventually in earth's frame. At every time τ such that $\hat{B}(\tau) = \hat{n}_E$, a pulse is seen on earth. This corresponds to the frequency at which the deflection vector $\vec{\zeta}$ vanishes,

$$\vec{\zeta}(\tau) = \hat{B}(\tau) - \hat{n}_E. \tag{4.6.10}$$

If the frequency at which ζ goes to zero is given by ν_{FS}, then we can use the red-shift formula to find the observed pulse frequency on earth ν_E as (see for example [8]),

$$1 + z = \frac{d\tau}{dt} = \frac{\nu_E}{\nu_{FS}} = \left[-g_{00} \left(r, \frac{\pi}{2} \right) \right]^{-1/2}, \tag{4.6.11}$$

where t is the coordinate time measured by an asymptotic static observer, like an astronomer on earth.
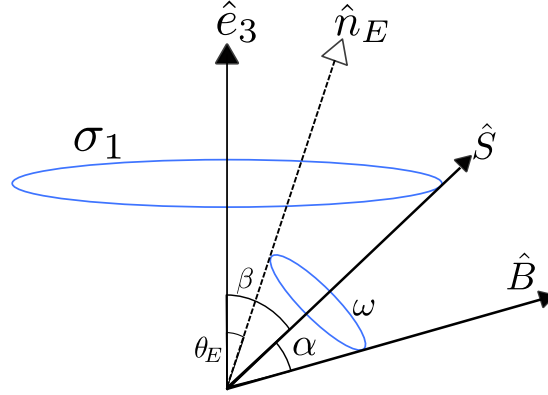
FIGURE 4.8: If a pulsar that remains spatially fixed, or moves at small orbital angular velocities $\Omega \approx 0$ in the equatorial plane of a Kerr black hole, its spin axis $\hat{S}$ precesses around a precession axis $\hat{e}_3$, at the spin-precession frequency σ_1, in the clockwise sense. Here β denotes the angle between these axes. Further, the direction in which the beam is emitted $\hat{B}$ rotates around this time-varying spin axis $\hat{S}(\tau)$ at the intrinsic spin angular frequency of the pulsar $+\omega$ (in the counter-clockwise sense: a convention), with $\alpha = \angle(\hat{B}, \hat{S})$ remaining constant. Earth lies along $\hat{n}_E$, with $\theta_E = \angle(\hat{n}_E, \hat{e}_3)$, also a constant.

4.6.2   Initial Conditions

We shall suppose that the apparent direction (direction cosines) of the Earth is given as (cf. 4.6.6),

$$\hat{n}_E = (\sin\theta_E, 0, \cos\theta_E). \tag{4.6.12}$$

Let us use the initial condition that at time $\tau = 0$, a pulse is received on earth, i.e. $\hat{B}$ points along the apparent direction of earth,

$$\hat{B}_0 = \hat{B}(\tau = 0) = (\sin\theta_E, 0, \cos\theta_E). \tag{4.6.13}$$

Since $\hat{S}$ moves on a cone of half-angle β around $\hat{e}_3$, the most general initial condition that we can write is,

$$\hat{S}_0 = (\sin\beta\cos\psi, \sin\beta\sin\psi, \cos\beta). \tag{4.6.14}$$

Now, since $\hat{B}$ moves on a cone of half-angle α around $\hat{S}(\tau)$, we require that the following be satisfied,

$$\hat{B}_0 \cdot \hat{S}_0 = \cos\alpha. \tag{4.6.15}$$

Let us note here that α, β, θ_E are fixed by the geometric configuration of the system. ψ however is simply an initial phase for $\hat{S}_0$, which we are free to choose thereby exhausting all freedom in initial conditions. The above equation imposes the following constraint,

$$\cos\alpha = \sin\theta_E \sin\beta\cos\psi + \cos\theta_E\cos\beta. \tag{4.6.16}$$

4.6.3   Solution for the Spin and Beam Vectors

One can simply obtain the solution $\hat{S}(\tau)$ to the spin-equation of motion (4.6.3) by using Rodrigues' rotation formula (see for example [323]) as,

$$\hat{S} = (\sin\beta\cos(\psi + \sigma_1\tau), \sin\beta\sin(\psi + \sigma_1\tau), \cos\beta). \tag{4.6.17}$$

It can be checked that $\hat{S}(\tau = 0)$ satisfies the initial conditions given in equation 4.6.14. The solution for the beam vector that satisfies the relevant equation of motion (4.6.4) and the initial condition (4.6.13) is then given as (see appendix E for an analytic derivation),

$$
\begin{aligned}
B_1 =& D_1 \left[\cos\left(\omega_{\text{eff}}\tau\right)\cos\left(\psi+\sigma_1\tau\right)\cos\chi + \sin\left(\omega_{\text{eff}}\tau\right)\sin\left(\psi+\sigma_1\tau\right)\right] \\
&+ D_2 \left[\sin\left(\omega_{\text{eff}}\tau\right)\cos\left(\psi+\sigma_1\tau\right)\cos\chi - \cos\left(\omega_{\text{eff}}\tau\right)\sin\left(\psi+\sigma_1\tau\right)\right] \\
&+ D_3 \cos\left(\psi+\sigma_1\tau\right)\sin\chi, \\
B_2 =& D_1 \left[\cos\left(\omega_{\text{eff}}\tau\right)\sin\left(\psi+\sigma_1\tau\right)\cos\chi - \sin\left(\omega_{\text{eff}}\tau\right)\cos\left(\psi+\sigma_1\tau\right)\right] \\
&+ D_2 \left[\sin\left(\omega_{\text{eff}}\tau\right)\sin\left(\psi+\sigma_1\tau\right)\cos\chi + \cos\left(\omega_{\text{eff}}\tau\right)\cos\left(\psi+\sigma_1\tau\right)\right], \\
&+ D_3 \sin\left(\psi+\sigma_1\tau\right)\sin\chi \\
B_3 =& -\sin\chi\left[D_1\cos\left(\omega_{\text{eff}}\tau\right) + D_2\sin\left(\omega_{\text{eff}}\tau\right)\right] + D_3\cos\chi,
\end{aligned}
\tag{4.6.18}
$$

where

$$
\begin{aligned}
D_1 &= \sin\theta_E\cos\chi\cos\psi - \cos\theta_E\sin\chi, \\
D_2 &= -\sin\theta_E\sin\psi, \\
D_3 &= \cos\theta_E\cos\chi + \sin\theta_E\sin\chi\cos\psi.
\end{aligned}
\tag{4.6.19}
$$

Also we have introduced,

$$
\omega_{\text{eff}}^2 = \omega^2 + \sigma_1^2 + 2\omega\sigma_1\cos\beta,
\tag{4.6.20}
$$

$$
\chi = \sin^{-1}\left(\frac{\omega}{\omega_{\text{eff}}}\sin\beta\right).
\tag{4.6.21}
$$

Now, let us pick the initial phase for $\hat{S}_0$, without loss of generality, to be $\psi = 0$. From equation 4.6.16, it is clear that one obtains pulses only for specific geometric configurations, $\theta_E = \pm\alpha + \beta$. Also,

$$
\begin{aligned}
D_1 &= \sin\left(\theta_E - \chi\right), \\
D_2 &= 0, \\
D_3 &= \cos\left(\theta_E - \chi\right),
\end{aligned}
\tag{4.6.22}
$$

Then the deflection vector is given by,

$$
\begin{aligned}
\zeta_1 =& \cos\left(\sigma_1\tau\right)\left[\cos\left(\omega_{\text{eff}}\tau\right)\sin\left(\theta_E - \chi\right)\cos\chi + \cos\left(\theta_E - \chi\right)\sin\chi\right] \\
&+ \sin\left(\sigma_1\tau\right)\sin\left(\omega_{\text{eff}}\tau\right)\sin\left(\theta_E - \chi\right) - \sin\theta_E, \\
\zeta_2 =& -\cos\left(\sigma_1\tau\right)\sin\left(\omega_{\text{eff}}\tau\right)\sin\left(\theta_E - \chi\right) \\
&+ \sin\left(\sigma_1\tau\right)\left[\cos\left(\omega_{\text{eff}}\tau\right)\sin\left(\theta_E - \chi\right)\cos\chi + \cos\left(\theta_E - \chi\right)\sin\chi\right], \\
\zeta_3 =& -\cos\left(\omega_{\text{eff}}\tau\right)\sin\left(\theta_E - \chi\right)\sin\chi + \cos\left(\theta_E - \chi\right)\cos\chi - \cos\theta_E.
\end{aligned}
\tag{4.6.23}
$$

The components of $\vec{\zeta}$ are, in general, *almost* periodic functions of τ [324, 325]. That is, $\vec{\zeta}$ approaches zero arbitrary closely but $\vec{\zeta}$ does not necessarily vanish periodically, or even vanish exactly at all. This is clear immediately if one remembers that σ_1 and ω (and therefore ω_{eff}) are in general incommensurate frequencies. When $\sigma_1, \omega_{\text{eff}}$ are rational multiples of each other, $\vec{\zeta}$ is exactly periodic and one obtains pulses indeed, at the

lowest common multiple (LCM) of these frequencies.

One can immediately anticipate implications for the existence of sub-millisecond pulsars. That is, ordinary garden variety pulsars could appear to pulse at faster (sub-millisecond) rates when in the vicinity of a Kerr black hole, due to gravitomagnetic spin-precession. Further, one could possibly explain quasi-periodic oscillations (QPOs) in pulsar observations, pulsar nulling and multi-peaked pulsar frequency profiles by accounting for the presence of a Kerr black hole in the vicinity of the pulsar.

Let us remember that the analysis thus far has been conducted entirely at the location of the pulsar, in its comoving FS frame. To obtain the relation between differences in times measured in the pulsar frame $\mathrm{d}\tau$ and on earth $\mathrm{d}t$, as mentioned before we assume that the earth is at asymptotic infinity, and use the gravitational redshift to write,

$$\frac{\mathrm{d}t}{\mathrm{d}\tau} = \left[-g_{tt}\left(r, \frac{\pi}{2} \right) \right]^{-1/2}. \tag{4.6.24}$$

In particular when when $\vec{\zeta}$ is periodic i.e., when the ratio of ω_{eff} and σ_1 is rational, the zeroes of $\vec{\zeta}$ will occur at the LCM of these two frequencies. If we denote this frequency as ν_{FS}, then the frequency at which pulses are observed on earth ν can be obtained as,

$$\nu_{\mathrm{E}} = \left(1 - \frac{2M}{r} \right)^{1/2} \nu_{\mathrm{FS}}. \tag{4.6.25}$$

4.6.4   Non-Zero Beam Width

Furthermore, since the beam width is not exactly of zero measure, pulses will still be recorded on earth when $\sigma_1, \omega_{\mathrm{eff}}$ are not exact rational multiples of each other. More concretely, let us suppose that the beam has some finite size and model it here as a cone of half-opening angle μ. Then if $\hat{n}_{\mathrm{E}}$ lies anywhere within this cone, i.e. when $\angle(\hat{B}, \hat{n}_{\mathrm{E}}) \leq \mu$ or equivalently whenever,

$$|\vec{\zeta}|^2 \leq 4\sin^2\left(\mu/2 \right), \tag{4.6.26}$$

one 'sees the pulsar.' This is particularly important to take into account since we now have access to a continuous pulse profile whenever the above condition is satisfied, as opposed to a far lesser amount of information corresponding to just the information of when a pulse was observed in our earlier consideration of zero beam width, $\mu = 0$.

In the case of an isolated pulsar, the Fourier spectrum of its pulse profile will effectively contain only one peak, corresponding to its intrinsic spin frequency ω. In stark contrast, Fourier spectra corresponding to observations of pulsars present in strong gravitational fields like near the ergosurface of a Kerr black hole or naked singularity will be multiply peaked and will contain information regarding the relevant frequencies in the problem, $\sigma_1, \omega_{\mathrm{eff}}$, and also regarding other geometry parameters like $\beta, \theta_{\mathrm{E}}$. And from this spectrum, one can potentially extract black hole parameters a, M.

The aim of the present work is just to point out that it is possible from measurements of pulsar spin-precession to extract information regarding black hole parameters but we do not attempt a detailed analysis of the 'inverse problem' here, namely what the shape of the pulse profile is as seen in earth's frame etc. However, it is clear

that if we define in the pulsar frame, two sets of times $\tau_{\text{on},i}, \tau_{\text{off},j}$ as follows,

$$|\zeta^2|(\tau_{\text{on},i}) = |\zeta^2|(\tau_{\text{off},j}) = 4 \sin^2 (\mu/2), \tag{4.6.27}$$

$$\frac{\mathrm{d}|\zeta^2|(\tau_{\text{on},i})}{\mathrm{d}\tau} < 0, \quad \frac{\mathrm{d}|\zeta^2|(\tau_{\text{off},j})}{\mathrm{d}\tau} > 0,$$

then one sees the pulsar for the duration $\Delta\tau_i = \tau_{\text{off},i} - \tau_{\text{on},i}$. In the above, we have used the same index i to denote that these are consecutive on and off times that satisfy equation 4.6.27. Note that $\Delta\tau_i$ are in general not of the same length. The amount of time for which the pulsar is visible is captured by the set $\Delta\tau_i$ and how frequently it is visible is indicated by the set $\tau_{\text{on},i}$, and these quantities depend on black hole parameters. Finally, one can obtain the relevant times and time differences in earth's frame via a simple redshift calculation.

4.6.5   Kerr Static Pulsars: Approach to the Ergosurface

Very slowly moving pulsars can be modelled as test spinning objects that move along Kerr static Killing orbits. In particular, when such pulsars are close to the ergosurface $r \rightarrow r_+$, the spin-precession frequency they experience becomes unboundedly large $\sigma_1 \rightarrow \infty$ and in this limit, we have $\chi \approx 0$ and $\omega_{\text{eff}} \approx \sigma_1$. In this extreme case, the deflection vector just becomes periodic and the pulse frequency of such a pulsar, measured in the FS frame, locks onto the spin-precession frequency, i.e.,

$$\lim_{r \rightarrow r_+} \nu_{\text{FS}} = \frac{\sigma_1}{2\pi}. \tag{4.6.28}$$

If we introduce a dimensionless parameter $\delta = \frac{r}{2M} - 1$, which measures the radial distance from the ergosurface in the equatorial plane, then in this limit, the redshift goes as $1 + z \approx \delta^{1/2}$, the spin-precession frequency goes as $\sigma_1 \approx \frac{a}{8M^2} \frac{1}{\delta(1+\delta)^2}$ and we find that the observed pulse frequency on earth ν_{E} behaves as,

$$\nu_{\text{E}} \approx \frac{a}{8\pi M^2} \frac{1}{\delta^{1/2}}. \tag{4.6.29}$$

If the pulsar is present in this region, one obtains pulses on the Earth far more rapidly than an isolated pulsar, i.e., $\nu_{\text{E}} \gg \omega/2\pi$. Specifically, in the limit $\delta \rightarrow 0$, we obtain $\nu \rightarrow \infty$, i.e., the pulses disappear and we see a rather continuous beam from the earth. This is somewhat reminiscent of the chirp one sees in a gravitational wave calculation [135].

Finally, we would like to note that even if for a short proper time a pulsar moves on a circular orbit with a small orbital angular velocity $\Omega \approx 0$ near the ergosurface of a Kerr black hole (or even a naked singularity), and is observed on earth, then since they experience nearly vanishing geodetic spin-precession, measurements from such pulsars could allow us to pick out pure gravitomagnetic effects in the Kerr spacetime. This could potentially lead to an independent estimate of the spin parameter of the central Kerr black hole.

4.6.6   Pulsar Spin-Precession: Kerr Stationary Observers

We had discussed the equivalence between Kerr stationary and adapted-Kerr static observers in §4.3.1 and our analysis of the evolution of the beam vector of a pulsar moving along the integral curve of a Kerr static observer

presented in this section thus far can now be immediately extended to study the case of pulsars moving on Kerr stationary Killing orbits.

In terms of the spin-precession frequency experienced by an adapted-Kerr static observer measured relative to its Frenet-Serret tetrad Ω'_p which is given as,

$$\Omega'_p = -\bar{\sigma}_1 e_{\hat{3}}, \tag{4.6.30}$$

$$\bar{\sigma}_1 = \frac{\Omega r^3 + 3M\Omega r^2 (a\Omega - 1) + aM(a\Omega - 1)^2}{r^3 \left[1 - (r^2 + a^2)\Omega^2 - \frac{2M(a\Omega-1)^2}{r}\right]},$$

we introduce,

$$\bar{\omega}_{\text{eff}} = \sqrt{\omega^2 + \bar{\sigma}_1^2 + 2\omega\bar{\sigma}_1 \cos\beta}, \quad \text{and} \tag{4.6.31}$$

$$\bar{\chi} = \sin^{-1}\left(\frac{\omega}{\bar{\omega}_{\text{eff}}} \sin\beta\right),$$

and proceed to directly write out the expressions for the deflection vector $\vec{\bar{\zeta}}$ as,

$$\bar{\zeta}_1 = \cos(\bar{\sigma}_1\tau)\left[\cos(\bar{\omega}_{\text{eff}}\tau)\sin(\bar{\theta}_E - \bar{\chi})\cos\bar{\chi} + \cos(\bar{\theta}_E - \bar{\chi})\sin\bar{\chi}\right]$$
$$+ \sin(\bar{\sigma}_1\tau)\sin(\bar{\omega}_{\text{eff}}\tau)\sin(\bar{\theta}_E - \bar{\chi}) - \cos(\Omega\tau)\sin\bar{\theta}_E, \tag{4.6.32}$$
$$\bar{\zeta}_2 = -\cos(\bar{\sigma}_1\tau)\sin(\bar{\omega}_{\text{eff}}\tau)\sin(\bar{\theta}_E - \bar{\chi}) \pm \sin(\Omega\tau)\sin\bar{\theta}_E$$
$$+ \sin(\bar{\sigma}_1\tau)\left[\cos(\bar{\omega}_{\text{eff}}\tau)\sin(\bar{\theta}_E - \bar{\chi})\cos\bar{\chi} + \cos(\bar{\theta}_E - \bar{\chi})\sin\bar{\chi}\right]$$
$$\bar{\zeta}_3 = -\cos(\bar{\omega}_{\text{eff}}\tau)\sin(\bar{\theta}_E - \bar{\chi})\sin\bar{\chi} + \cos(\bar{\theta}_E - \bar{\chi})\cos\bar{\chi} - \cos\bar{\theta}_E.$$

where we used the important fact that earth lies along $n_E^{\hat{\bar{j}}}$ in the adapted-Kerr static Killing FS spatial-triad (4.6.7) or equivalently in the Euclidean notation along,

$$\hat{\bar{n}}_E(\tau) = \left(\cos(\Omega\tau)\sin\bar{\theta}_E, \mp\sin(\Omega\tau)\sin\bar{\theta}_E, \cos\bar{\theta}_E\right). \tag{4.6.33}$$

In the above equations (4.6.32, 4.6.33), the signs correspond to the signs of $e_{\hat{3}}$ relative to the direction of the spin of the black hole $\hat{z}$ (4.6.8).

The Fourier transform of this beam signal will contain information regarding various combinations of all three frequencies in the problem now, $\Omega, \bar{\sigma}_1, \bar{\omega}_{\text{eff}}$, from which one can extract necessary data to potentially solve the inverse problem and obtain black hole parameters namely a, M, as well as the orbital frequency of the pulsar Ω. We do not attempt a detailed analysis of the trends of the Fourier transforms here but in §4.7, we argue that the spin-precession frequencies in various realistic scenarios become comparable to the intrinsic spin period of the pulsar and hence these effects must be taken into account when analysing pulsar profiles of pulsars present near rotating compact objects. The redshift relations for these observers can be found in [326], for example.

Lastly, for pulsars moving on circular orbits close to the event horizon of a Kerr black hole, i.e. for $r \rightarrow r_H$ we have, $\bar{\sigma}_1 \rightarrow \infty$ and $\Omega \rightarrow \Omega_H$, where we have defined the horizon frequency as,

$$\Omega_H \equiv \lim_{r \rightarrow r_H} \Omega_+ = \lim_{r \rightarrow r_H} \Omega_- = \frac{a}{2Mr_H}. \tag{4.6.34}$$
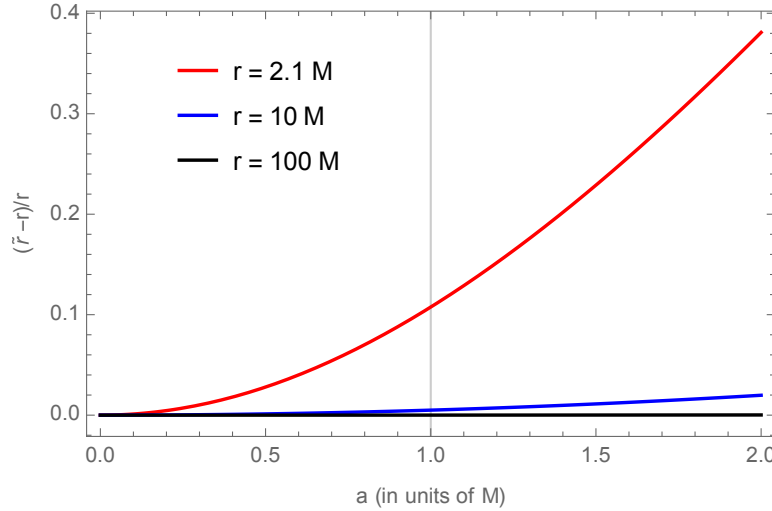
FIGURE 4.9: Here we highlight the difference in the useful Boyer-Lindquist (BL) coordinate r and the physical Kerr-Schild coordinate $\tilde{r}$ in the equatorial plane of the Kerr spacetime, by displaying the variation of $\tilde{r}/r - 1$ with change in a and r. Therefore, this roughly measures the distortion from spherical symmetry, and we show here that these coordinates agree well for larger distances r and smaller central spins a. Also, since this is a fractional quantity, evidently these qualitative features are representative of black holes ($0 \leq a \leq M$) and naked singularities ($M < a$), independently of their masses. In particular, if we consider a pulsar at $r = 2.1M$ near a BH with spin $a = .1M$ and one with $a = M$, the corresponding physical distances would be $\tilde{r} \approx M$ and $\tilde{r} \approx 1.1 \times 2.1M$ respectively. Clearly, for larger central masses, this difference in measurement of distances can be significant ($1M_\odot = 1.5$ km). Note that $r_+ = 2M$ is the location of the ergosurface (BL), and is independent of the central spin.

In this limit, $\bar{\chi} \approx 0$ and $\bar{\omega}_{\text{eff}} \approx \sigma_1$, and in this extreme case, the deflection vector just becomes,

$$\bar{\zeta}_1 \approx [1 - \cos{(\Omega_H \tau)}] \sin{\bar{\theta}_E}, \tag{4.6.35}$$
$$\bar{\zeta}_2 \approx \pm \sin{(\Omega_H \tau)} \sin{\bar{\theta}_E},$$
$$\bar{\zeta}_3 \approx 0.$$

That is, for pulsars very close to the event horizon of a Kerr black hole, one obtains pulses on earth every $\nu_{FS} \approx \Omega_H/2\pi$.

4.7 Analysis and Results

In the remainder of this article, we will switch from Geometrized units ($G = c = 1$) to physical units, and keep only two significant digits when reporting values of physical quantities. The conversions for distances, angular frequencies, and accelerations are given as: $1M_\odot = 1.5$ km, $1M_\odot^{-1} = 1.3 \times 10^6$ rad/s and $1M_\odot^{-1} = 6.0 \times 10^{10}$ km/s^2 respectively. Also, we will freely use both the convenient Boyer-Lindquist r and the more physical Cartesian Kerr-Schild $\tilde{r}$ radial coordinates (see equation 4.5.10). Therefore, we find it useful to mention here that the fractional change in the distances measured in these coordinate systems, $\tilde{r}/r - 1$, decreases with distance from and increases with spin of the central Kerr object, as is evident from figure 4.9.

Firstly, let us note that for an isolated pulsar ($\sigma_1 = 0$) at rest ($\Omega = 0$), we can write the deflection vector from (4.6.23) as,

$$
\begin{aligned}
\zeta_1 &= (\cos(\omega\tau) - 1)\sin(\theta_E - \beta)\cos\beta, \\
\zeta_2 &= -\sin(\omega\tau)\sin(\theta_E - \beta), \\
\zeta_3 &= (1 - \cos(\omega\tau))\sin(\theta_E - \beta)\sin\beta.
\end{aligned}
\tag{4.7.1}
$$

Clearly, the Fourier spectrum of the squared modulus of the deflection vector $|\zeta^2(\tau)|$ for such a pulsar has a single peak corresponding to its intrinsic spin angular frequency ω. On the other hand, the Fourier spectrum of $|\zeta^2(\tau)|$ for a pulsar near a Kerr black hole is multiply peaked, with these peaks correspond to the magnitudes of its orbital angular velocity Ω, its spin-precession frequency $\bar{\sigma}_1$ and the effective vector sum of the intrinsic spin angular frequency (ω) and the spin-precession frequency, denoted by ω_{eff}. Of course, this spectrum contains other peaks corresponding to certain sums and differences of these three frequencies. However, for qualitative insight into how gravitomagnetic spin-precession (spin-spin coupling) and orbital motion (spin-orbit coupling) affect pulsar timing, it is useful to consider the following ratios,

$$
f_{\text{p}} = \frac{|\bar{\sigma}_1|}{\omega}, \quad f_{\text{o}} = \frac{\Omega}{\omega},
\tag{4.7.2}
$$

and we can capture the role of ω_{eff} on pulsar timing measurements, using f_{p} and β, via,

$$
\frac{\omega_{\text{eff}}}{\omega} = \sqrt{1 + f_{\text{p}}^2 \pm 2f_{\text{p}}\cos\beta}.
\tag{4.7.3}
$$

Now, since the spin-precession (4.5.4) and orbital angular frequencies (4.3.5) typically decrease with an increase in size of pulsar orbit r, it makes sense to analyse pulsar-BH binaries depending on their sizes. Therefore, we can broadly divide these systems into two categories: (a) when a pulsar is present sufficiently close to the BH such that the relevant ratios $f_{\text{p}}(r)$ and $f_{\text{o}}(r)$ are comparable to, or much larger than unity, then gravitomagnetic spin-precession effects modify the pulse profile on the time-scale of the pulsar's intrinsic spin period; and (b) when a pulsar is sufficiently far away such that these ratios are much smaller than unity, one finds longer-time-scale variations in the pulse profile (for example, as secular shifts in the times of arrival of pulses). To best demonstrate these points, we will now consider figures 4.10 and 4.11, and table 4.12. In figure 4.10, we consider the all-important case of pulsars moving on stable equatorial circular geodesics around IMBHs of mass $10^2 M_\odot$ and SMBHs of mass $10^5 M_\odot$ (similar to the BHs of the Seyferts in the study of [327]), and analyse how gravitomagnetic spin-precession effects modify the times of arrival of pulses. In figure 4.11, the focus will be on the strength of the spin-precession frequency (in physical units) relative to the intrinsic spin-frequency of typical pulsars, to understand which effect dominates the beam evolution, with (a) increase in distance between the pulsar and BH, (b) change in the orbital angular velocity of the pulsar, and (c) with change in mass and spin of the BH. We conclude the present analysis with an exhaustive catalogue of the possible orbital angular velocities, accelerations and spin-precession frequencies experienced by pulsars present at varying distances near intermediate-mass Kerr BHs of varying spins $a = .1M, .5M, .9M$ but of same mass $10^2 M_\odot$.

Now, we show in figure 4.10 the time plots of the squared-modulus of the deflection vector $|\zeta^2(\tau)|$ for pulsars moving on (stable) equatorial circular Kepler orbits with $\Omega = \Omega_{\text{K+}}$ near intermediate-mass ($10^2 M_\odot$) and supermassive ($10^5 M_\odot$) Kerr BHs (in blue), contrasted against $|\zeta^2(\tau)|$ for isolated pulsars (in red), for different values of the spin for the BH a, spin-frequencies of the pulsar ω (corresponding to normal pulsars which

have $\omega = 2\pi$ rad/s, and ms-pulsars for which $\omega = 200\pi$ rad/s) moving on assorted values of orbit radii r. As discussed in §4.6.4, when $|\zeta^2(\tau)| \approx 0$, one obtains a pulse on earth. Therefore, the period at which this quantity vanishes corresponds to period of the pulsar as seen on earth, once redshift is accounted for. From this figure, it is evident that as the BH mass increases, the spin-precession frequency drops, and this is directly manifest in the $|\zeta^2|$ profile. A similar statement holds also for increase in distance between pulsar and black hole. Now, when $f_p, f_o \gtrsim 1$ - see for example panels (a) and (c) - gravitomagnetic spin-precession (significantly) modifies the observed pulse period on the dynamical time-scale itself (which is determined by the spin-period of the pulsar $2\pi/\omega$). Further, even when spin-precession effects are not as strong (panels b, d, e), we still see significant modifications in the pulse period albeit on time-scales larger than the spin-period of the pulsar. These findings indicate that when modelling pulse profiles of pulsars near BHs, one must account for gravitomagnetic spin-precession effects, even if the pulsar is not 'very close' to the BH. Finally, when spin-precession effects are very small ($f_p, f_o \ll 1$), as in panel (f), then pulses appear to arrive at $2\pi/\omega$. However, the gravitomagnetic spin-precession effects due to the companion BH are imprinted onto the shape of the pulse. What these results imply are that if one were to find pulsars moving on astrophysically relevant (equatorial stable circular Kepler) orbits in a reasonably large radial-band around a BH, one can obtain an independent estimate of BH parameters by looking for effects of gravitomagnetic spin-precession. For an idea of how far away a pulsar must be from a BH to neglect spin-precession effects, see figure 4.11 and also glance at table 4.12.

Now, in figure 4.11, we present a systematic study of how $\log f_p$ varies with changes in the mass M and spin a of the BH, the distance of the pulsar from it $\tilde{r}$, the orbital angular frequency of the pulsar Ω and the intrinsic spin frequency of the pulsar ω. The contour $\log f_p \approx 0$ divides the $a - \tilde{r}$ parameter space into the 'strong-precession effects' region ($f_p \gtrsim 1$) and the weak-precession effects region ($1 > f_p \gtrsim 10^{-4}$), as discussed above. Now, for pulsars with small spins around IMBHs (top row), the strong- and weak-precession region can be identified roughly (in Kerr-Schild coordinates) as being upto about $\approx 1.3 \times 10^3$ km and $\approx 4.9 \times 10^3$ km respectively. For pulsars with high spins around BHs of similar masses (middle row), these regions correspond to distances of $\approx 3. \times 10^3$ and $\approx 1.1 \times 10^3$ km respectively. Finally, for pulsars with small spins around SMBHs (bottom row), spin-precession effects are severely suppressed since they scale inversely with mass of the central BH; one can still expect to see weak imprints of spin-precession upto a region of about $\approx 5.0 \times 10^5$ km. The picture that emerges is when considering the interaction of spin gravitating objects like pulsars present close ($\lesssim 100M$) to intermediate-mass BHs ($10^2 - 10^5 M_\odot$), one cannot neglect the effect that gravitomagentic spin-precession has on their observed pulse profiles. Additionally, these systems would serve as excellent probes of properties of BH spacetimes.

Finally, in table 4.12, we show the magnitudes, in physical units, of the accelerations $\bar{\kappa}$ and spin-precession frequencies $\bar{\sigma}_1$ experienced by pulsars on equatorial circular time-like orbits with varying sizes $\tilde{r}$ and angular frequencies Ω. Although the calculations presented here apply generally to BHs (and naked singularities; see [312]) of masses $\gtrsim 10^2 M_\odot$, as an example, here we display the values corresponding to central masses of $10^2 M_\odot$. We choose this mass for the central objects in order to ensure that the test spinning object approximation for the pulsar $m_p \ll M < r$ holds well, as discussed in §4.6. The angular frequency values ($\Omega, \bar{\sigma}_1$), which are the relevant entities that modify observed pulse periods, can be easily compared against the intrinsic spin angular frequency of typical pulsars which lie in the range $\omega \approx 1 - 10^2$ rad/s. Clearly, gravitomagnetic spin-precession would be easily detectable from the modifications in the Fourier transform of the pulse profile when $f_p, f_o \gtrsim 10^{-4}$. For larger mass black holes, the accelerations, orbital angular frequencies and spin-precession frequencies would be suppressed by a factor of $100 M_\odot / M$. However, the

radius of the orbit also scales as $M/100M_\odot$, making pulsars on such orbits much easier to detect. Also, it can be seen from this table that pulsars that experience accelerations ($q \neq q_{K\pm}$) typically experience larger spin-precession frequencies. Therefore, observations corresponding to pulsars that experience a temporary phase of acceleration could be helpful to obtain black hole parameters from the pulsar's Fourier spectrum.

4.8   Discussion and Astrophysical Implications

It is thought that globular clusters [328, 329] and ultra-compact dwarf galaxies [330, 331] house IMBHs ($10^2 - 10^4 M_\odot$) at their centres. In fact, some large galaxies like M83 may even host two such BHs [332]. Now, globular clusters are known also to host a large population of pulsars [301]; these are mostly ms-pulsars [333–336] and so, the formation of a ms-pulsar-IMBH binary becomes quite plausible in such globular clusters [337–339]. Further, if the estimate of the frequency of occurrence of such binaries per cluster ~1–10 is accurate, then a few tens of such binaries could reside in the globular clusters in the Local Group galaxies, meaning that pulse emission from such ms-pulsars could be detected by SKA and FAST. Normal pulsars have also been found in globular clusters [340, 341]; for example, of the ~150 detected globular cluster pulsars in our galaxy[7], $\lesssim 10$ of them are of this variety. Therefore, a case can be made for the discovery of a normal-pulsar-IMBH binary in a globular cluster. Searches for pulsars in dwarf galaxies are yet to yield positive results as of [342].

On the other hand, SMBHs (10^5–$10^9 M_\odot$) are expected to be present abundantly at the centres of nearly all large galaxies [37, 343]. Of these, although the existence of SMBHs with masses below $10^6 M_\odot$ has not been firmly established [344], there is some evidence in their favour [327, 345]. The higher end of the mass-spectrum of astrophysical BHs (ultra-massive BHs) is thought to be around ~$10^{10} M_\odot$ (for example, the central BH in NGC 1277; [346]). Large populations of about ~10^5 active normal pulsars and ~10^4 ms-pulsars are estimated to reside in our galaxy [301]. Of these pulsars, about ~ 10^3 are expected to exist in the central region of our Galaxy [347–349]. Due to indications that such high number densities of pulsars near the centre of galactic nuclear SMBHs are typical, binaries are expected to form, either through sequences of stellar interactions in the case of large spheroidal galaxies or due to capture by the central BH of a small elliptical or spiral galaxy (see for example the excellent discussion in [309]), and it is not unreasonable to expect to see inspiral events [338, 350].

Astrophysical systems involving pulsars inspiralling into massive BHs are typically divided into two categories depending on the mass of the BH, as intermediate-mass-ratio inspiral (IMRI; 10^3–$10^4 M_\odot$) systems and extreme-mass-ratio-inspiral (EMRI; $10^5 - 10^6 M_\odot$) systems, and form major classes of gravitational wave sources for LISA [137]. If we consider, in particular, the scenario of a pulsar that is slowly inspiralling into a BH, then its orbit can be well approximated as being a quasi-circular orbit [351]; for example, when spin-curvature coupling is negligible and the pulsar orbit lies outside the ISCO. Also, when IMRIs/EMRIs enter the relativistic regime, pulsar orbits are greatly circularized by gravitational wave emission (see for example [309] and references therein for a discussion on this). Now, such orbits are approximately the world-lines of stationary observers (and hence our results apply to such systems), with their four-velocities given by $u^\mu_{\text{slow-infall}} \propto (1, \epsilon, 0, \Omega)$, with $\epsilon \ll \Omega$. Now, when the pulsar is within about $\approx 100M$, spin-precession effects due to gravitomagnetism would be measurable from pulsar profiles, as we have shown here, either due to change in the observed period of pulses or in the systemic change in the morphology of the pulse shape (see [301] for a discussion on

---

[7]see for example the comprehensive catalogue of Galactic globular clusters compiled by P. Freire at http://www.naic.edu/~pfreire/GCpsr.html

(a) $\omega = 2\pi$ rad/s, $a = .1M$, $r = 50M$, $f_p = 5.9$, $f_o = 5.9$

(b) $\omega = 2\pi$ rad/s, $a = .1M$, $r = 50M$, $f_p = 5.9 \times 10^{-3}$, $f_o = 5.9 \times 10^{-3}$

(c) $a = .5M$, $\omega = 2\pi$ rad/s, $r = 10^2 M$, $f_p = 2.1$, $f_o = 2.1$

(d) $a = .9M$, $\omega = 2\pi$ rad/s, $r = 100M$, $f_p = 2.1 \times 10^{-3}$, $f_o = 2.1 \times 10^{-3}$

(e) $a = .9M$, $\omega = 200\pi$ rad/s, $r = 10M$, $f_p = .65$, $f_o = .64$

(f) $a = .5M$, $\omega = 200\pi$ rad/s, $r = 10M$, $f_p = 6.5 \times 10^{-4}$, $f_o = 6.4 \times 10^{-4}$
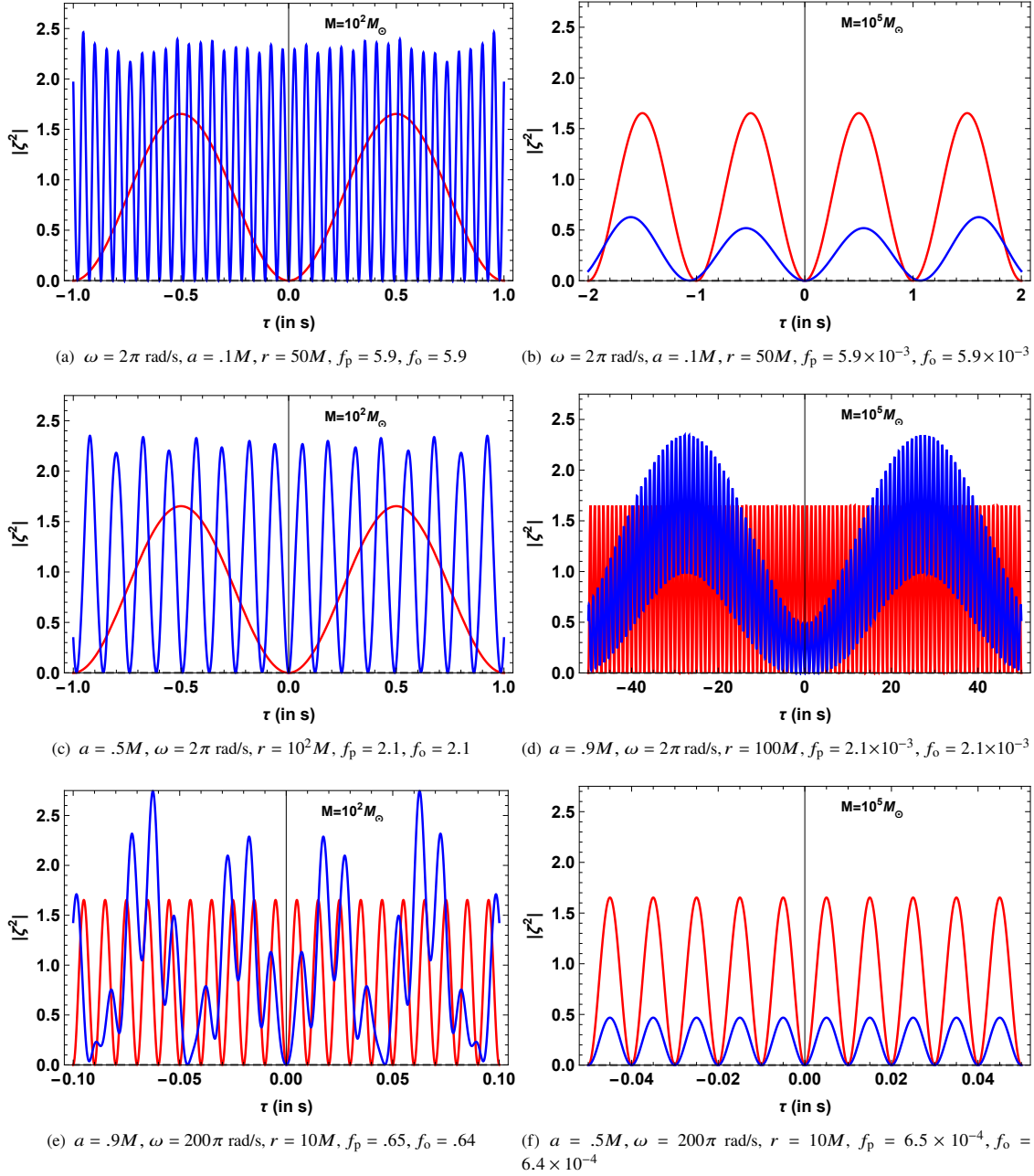
FIGURE 4.10: We demonstrate here changes in the time profile of the squared-modulus of the deflection vector $|\zeta^2|$ of a pulsar present near Kerr BHs, of masses $10^2 M_\odot$ (IMBHs) and $10^5 M_\odot$ (SMBHs), due to gravitomagnetism. In red we represent an isolated spatially-fixed pulsar ($\Omega = 0$, $\sigma_1 = 0$), and in blue we have a pulsar moving on an equatorial circular geodesic ($\Omega = \Omega_{K+}$) around a Kerr black hole. The organisation in this figure is as follows: the top and middle rows are for pulsars with spin frequencies $\omega = 2\pi$ rad/s, and the bottom row is for ms-pulsars with $\omega = 200\pi$ rad/s. We have used placeholder values of $\beta = 30°$, $\theta_E = 50°$ in all panels. We have used assorted values for the black hole spin parameter a and the orbit radius r for pulsars in the Kerr spacetime, indicated below each panel; we have also included there the values of the associated spin-precession and orbital angular velocity ratios f_p and f_o, which effectively determine the Fourier spectrum of $|\zeta^2(\tau)|$. Note that these plots are associated with the rest frame of the pulsar. Nonetheless, it is clear that even after incorporating redshift considerations gravitomagnetic spin-precession in the vicinity of a Kerr black hole can cause significant deviations in the observed time profile of such a pulsar from that of an isolated pulsar. Now, even though the spin-precession frequencies $\bar{\sigma}_1$ (see equation 4.5.8) experienced by pulsars on such Keplerian orbits are independent of the spin-parameter of the central Kerr compact object a, their orbital angular velocities Ω_{K+} (see equation 4.3.7) and the physical size of their orbits $\tilde{r}$ (Kerr-Schild radial coordinate) are not. Therefore, from observed profiles of such pulsars, one can obtain independent estimates for both BH parameters. It is useful to remember that $\tilde{r}$ can be obtained from the Boyer-Lindquist radius values given here using equation 4.5.10 as $\tilde{r} = \sqrt{r^2 + a^2} \times 1.5 \times (M/M_\odot)$ km, where r and a are in units of M. So, the size of the orbit in panel (c) is $\tilde{r} = 1.5 \times 10^4$ km.

(a) $M = 10^2 M_\odot, \Omega = 0, \omega = 2\pi$ rad/s

(b) $M = 10^2 M_\odot, \Omega = \Omega_Z, \omega = 2\pi$ rad/s

(c) $M = 10^2 M_\odot, \Omega = \Omega_{K+}, \omega = 2\pi$ rad/s

(d) $M = 10^2 M_\odot, \Omega = 0, \omega = 200\pi$ rad/s

(e) $M = 10^2 M_\odot, \Omega = \Omega_Z, \omega = 200\pi$ rad/s

(f) $M = 10^2 M_\odot, \Omega = \Omega_{K+}, \omega = 200\pi$ rad/s

(g) $M = 10^5 M_\odot, \Omega = 0, \omega = 2\pi$ rad/s

(h) $M = 10^5 M_\odot, \Omega = \Omega_Z, \omega = 2\pi$ rad/s

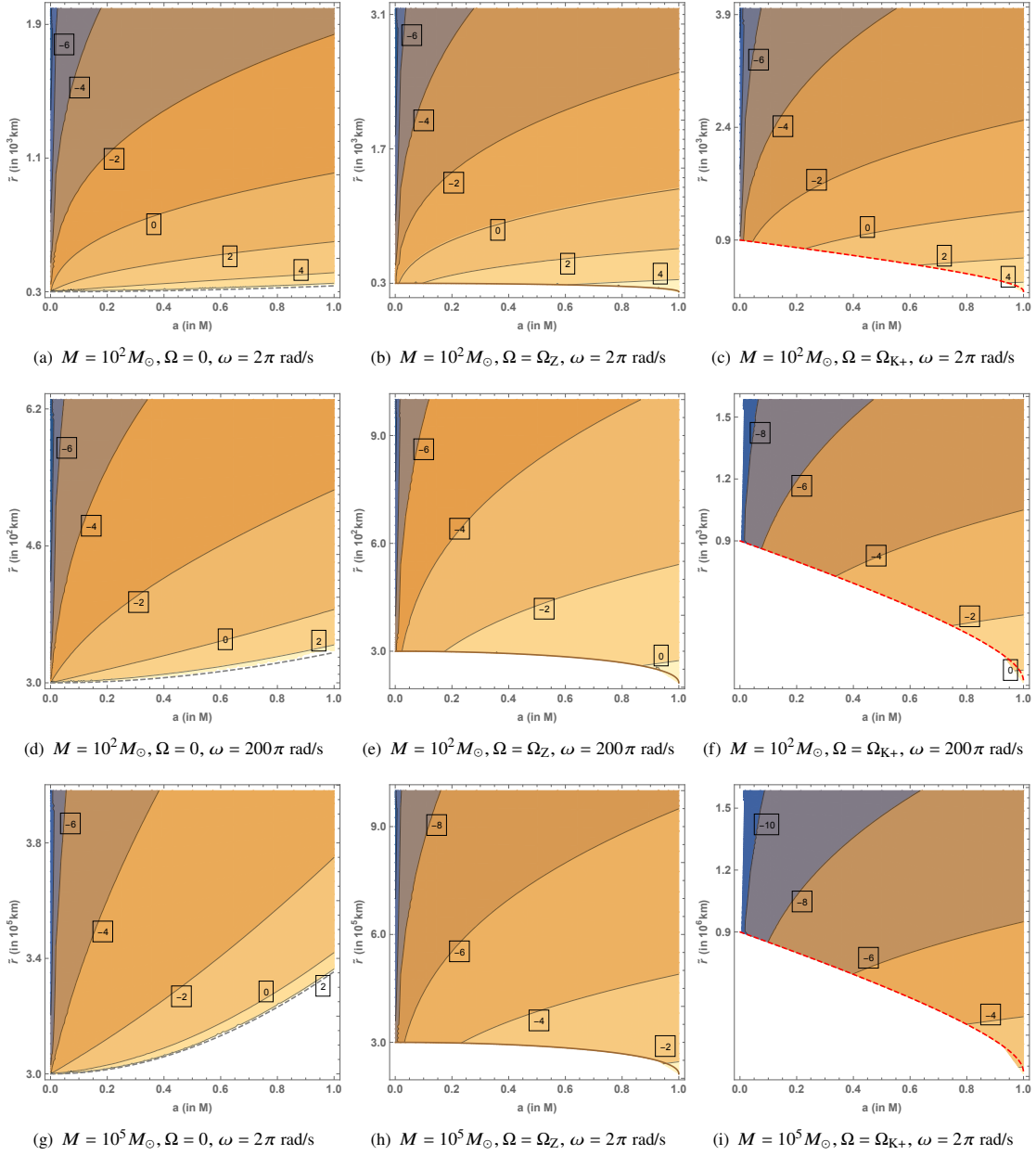(i) $M = 10^5 M_\odot, \Omega = \Omega_{K+}, \omega = 2\pi$ rad/s

FIGURE 4.11: The aim of this figure is to serve as an indicator for how the strength of the spin-precession frequency varies with BH mass and spin, and position and orbital angular velocity of the pulsar. Towards this end, we show here the contour plot of $\log f_p = \log(|\bar{\sigma}_1|/\omega)$ in the $a - \tilde{r}$ parameter space. On the x-axis, a is represented in units of M and on the y-axis, the physical Kerr-Schild size $\tilde{r}$ (see equation 4.5.10) of the pulsar orbit is given in km. The masses of the BHs and the intrinsic spin angular frequencies of the pulsars are given below panels. We consider here BHs of masses $10^2 M_\odot$ (IMBHs) and $10^5 M_\odot$ (SMBHs), the associated gravitational radii ($r_g = M$) of which are 1.5×10^2 km and 1.5×10^5 km respectively. In the left column, pulsars move at very low orbital angular frequencies $\Omega \approx 0$ (static observers). In the centre column, pulsars move at the ZAMO orbital angular frequency, $\Omega = \Omega_Z$, and in the right column, pulsars move on stable co-rotating Kepler orbits, i.e. $\Omega = \Omega_{K+}$. It is useful to remember that static observers, ZAMOs and stable co-rotating Kepler observers are allowed outside the ergoregion (dashed-gray), horizon (brown) and the co-rotating ISCO (dashed-red) respectively. Now, when $\log f_p \gtrsim 0$, effects of gravitomagnetic spin-precession appear on the dynamical time-scale of the pulsar. When this quantity is much smaller, we require long-time observations to not only extract the spin-precession frequency (and therefore BH parameters), but to even *see* the pulsar again (see for example panel (d) of figure 4.10). From the current figure, it is evident that gravitomagnetic spin-precession effects are significant, and therefore must necessarily be incorporated in pulsar timing analyses, for slowly-spinning (sub-ms) pulsars present sufficiently close to IMBHs Further, studying the spin-precession properties of such systems would yield excellent constraints on BH parameters.

	a	.1M (Black Hole)					.5M (Black Hole)				
	r	2.1	1.0 (1)	1.0 (2)	1.0 (3)	1.0 (4)	2.1	1.0 (1)	1.0 (2)	1.0 (3)	1.0 (4)
	$\tilde{r}$	3.2 (2)	1.5 (3)	1.5 (4)	1.5 (5)	1.5 (6)	3.2 (2)	1.5 (3)	1.5 (4)	1.5 (5)	1.5 (6)
$q = q_{K+}$	Ω_{K+}	-	4.1 (2)	1.3 (1)	4.1 (-1)	1.3 (-2)	-	4.0 (2)	1.3 (1)	4.1 (-1)	1.3 (-2)
	$\bar{\kappa}$	-	0	0	0	0	-	0	0	0	0
	$\lvert\bar{\sigma}_1\rvert$	-	4.1 (2)	1.3 (1)	4.1 (-1)	1.3 (-2)	-	4.1 (2)	1.3 (1)	4.1 (-1)	1.3 (-2)
$q = q_{K-}$	Ω_{K-}	-	-4.1 (2)	-1.3 (1)	-4.1 (-1)	-1.3 (-2)	-	-4.2 (2)	-1.3 (1)	-4.1 (-1)	-1.3 (-2)
	$\bar{\kappa}$	-	0	0	0	0	-	0	0	0	0
	$\lvert\bar{\sigma}_1\rvert$	-	4.1 (2)	1.3 (1)	4.1 (-1)	1.3 (-2)	-	4.1 (2)	1.3 (1)	4.1 (-1)	1.3 (-2)
$q = q_{static}$	Ω	0	0	0	0	0	0	0	0	0	0
	$\bar{\kappa}$	6.4 (8)	6.7 (6)	6.1 (4)	6.0 (2)	6.0	9.2 (8)	6.7 (6)	6.1 (4)	6.0 (2)	6.0
	$\lvert\bar{\sigma}_1\rvert$	2.9 (3)	1.6	1.3 (-3)	1.3 (-6)	1.3 (-9)	1.5 (4)	8.1	6.6 (-3)	6.5 (-6)	6.5 (-9)
$q = .1$	Ω	-8.2 (2)	-9.3 (2)	-1.0 (2)	-1.0 (1)	-1.0	-1.8 (2)	-9.2 (2)	-1.0 (2)	-1.0 (1)	-1.0
	$\bar{\kappa}$	1.7 (9)	7.6 (7)	1.0 (7)	1.1 (6)	1.1 (5)	1.3 (9)	7.3 (7)	1.0 (7)	1.1 (6)	1.1 (5)
	$\lvert\bar{\sigma}_1\rvert$	2.8 (4)	2.2 (3)	2.8 (2)	2.9 (1)	2.9	2.3 (4)	2.2 (3)	2.8 (2)	2.9 (1)	2.9
$q = .3$	Ω	-2.7 (2)	-4.6 (2)	-5.1 (1)	-5.2	-5.2 (-1)	5.4 (2)	-4.5 (2)	-5.1 (1)	-5.2	-5.2 (-1)
	$\bar{\kappa}$	7.3 (8)	2.1 (6)	1.1 (6)	1.1 (5)	1.1 (4)	5.2 (8)	1.4 (6)	1.1 (6)	1.1 (5)	1.1 (4)
	$\lvert\bar{\sigma}_1\rvert$	6.2 (3)	4.8 (2)	6.1 (1)	6.2	6.2 (-1)	5.8 (3)	4.6 (2)	6.1 (1)	6.2	6.2 (-1)
$q = .5$	Ω_Z	2.8 (2)	2.6	2.6 (-3)	2.6 (-6)	2.6 (-9)	1.3 (3)	1.3 (1)	1.3 (-2)	1.3 (-5)	1.3 (-8)
	$\bar{\kappa}$	6.1 (8)	6.7 (6)	6.1 (4)	6.0 (2)	6.0	3.8 (8)	6.7 (6)	6.1 (4)	6.0 (2)	6.0
	$\lvert\bar{\sigma}_1\rvert$	4.2 (2)	3.9	3.9 (-3)	3.9 (-6)	3.9 (-9)	1.9 (3)	1.9 (1)	1.9 (-2)	1.9 (-5)	1.9 (-8)
$q = .7$	Ω	8.3 (2)	4.7 (2)	5.1 (1)	5.2	5.2 (-1)	2.0 (3)	4.8 (2)	5.1 (1)	5.2	5.2 (-1)
	$\bar{\kappa}$	6.9 (8)	2.4 (6)	1.1 (6)	1.1 (5)	1.1 (4)	3.6 (8)	3.1 (6)	1.1 (6)	1.1 (5)	1.1 (4)
	$\lvert\bar{\sigma}_1\rvert$	5.0 (3)	4.9 (2)	6.1 (1)	6.2	6.2 (-1)	4.5 (2)	5.1 (2)	6.1 (1)	6.2	6.2 (-1)
$q = .9$	Ω	1.4 (3)	9.3 (2)	1.0 (2)	1.0 (1)	1.0	2.7 (3)	9.4 (2)	1.0 (2)	1.0 (1)	1.0
	$\bar{\kappa}$	1.5 (9)	7.8 (7)	1.0 (7)	1.1 (6)	1.1 (5)	5.2 (8)	8.1 (7)	1.0 (7)	1.1 (6)	1.1 (5)
	$\lvert\bar{\sigma}_1\rvert$	2.4 (4)	2.3 (3)	2.8 (2)	2.9 (1)	2.9	5.7 (3)	2.3 (3)	2.8 (2)	2.9 (1)	2.9

	a	.9M (Black Hole)					1.1M (Naked Singularity)				
	r	2.1	1.0 (1)	1.0 (2)	1.0 (3)	1.0 (4)	2.1	1.0 (1)	1.0 (2)	1.0 (3)	1.0 (4)
	$\tilde{r}$	3.4 (2)	1.5 (3)	1.5 (4)	1.5 (5)	1.5 (6)	3.6 (2)	1.5 (3)	1.5 (4)	1.5 (5)	1.5 (6)
$q = q_{K+}$	Ω_{K+}	-	4.0 (2)	1.3 (1)	4.1 (-1)	1.3 (-2)	3.2 (3)	4.0 (2)	1.3 (1)	4.1 (-1)	1.3 (-2)
	$\bar{\kappa}$	-	0	0	0	0	0	0	0	0	0
	$\lvert\bar{\sigma}_1\rvert$	-	4.1 (2)	1.3 (1)	4.1 (-1)	1.3 (-2)	4.3 (3)	4.1 (2)	1.3 (1)	4.1 (-1)	1.3 (-2)
$q = q_{K-}$	Ω_{K-}	-	-4.2 (2)	-1.3 (1)	-4.1 (-1)	-1.3 (-2)	-	-4.2 (2)	-1.3 (1)	-4.1 (-1)	-1.3 (-2)
	$\bar{\kappa}$	-	0	0	0	0	-	0	0	0	0
	$\lvert\bar{\sigma}_1\rvert$	-	4.1 (2)	1.3 (1)	4.1 (-1)	1.3 (-2)	-	4.1 (2)	1.3 (1)	4.1 (-1)	1.3 (-2)
$q = q_{static}$	Ω	0	0	0	0	0	0	0	0	0	0
	$\bar{\kappa}$	1.4 (9)	6.7 (6)	6.1 (4)	6.0 (2)	6.0	1.5 (9)	6.8 (6)	6.1 (4)	6.0 (2)	6.0
	$\lvert\bar{\sigma}_1\rvert$	2.7 (4)	1.5 (1)	1.2 (-2)	1.2 (-5)	1.2 (-8)	3.0 (4)	1.6 (1)	1.3 (-2)	1.3 (-5)	1.3 (-8)
$q = .1$	Ω	1.1 (2)	-9.0 (2)	-1.0 (2)	-1.0 (1)	-1.0	1.5 (2)	-9.0 (2)	-1.0 (2)	-1.0 (1)	-1.0
	$\bar{\kappa}$	1.1 (9)	6.9 (7)	1.0 (7)	1.1 (6)	1.1 (5)	1.0 (9)	6.8 (7)	1.0 (7)	1.1 (6)	1.1 (5)
	$\lvert\bar{\sigma}_1\rvert$	2.0 (4)	2.1 (3)	2.8 (2)	2.9 (1)	2.9	1.9 (4)	2.1 (3)	2.8 (2)	2.9 (1)	2.9
$q = .3$	Ω	9.8 (2)	-4.4 (2)	-5.1 (1)	-5.2	-5.2 (-1)	1.1 (3)	-4.4 (2)	-5.1 (1)	-5.2	-5.2 (-1)
	$\bar{\kappa}$	3.7 (8)	6.6 (5)	1.1 (6)	1.1 (5)	1.1 (4)	3.5 (8)	4.7 (5)	1.1 (6)	1.1 (5)	1.1 (4)
	$\lvert\bar{\sigma}_1\rvert$	5.4 (3)	4.3 (2)	6.1 (1)	6.2	6.2 (-1)	5.4 (3)	4.3 (2)	6.1 (1)	6.2	6.2 (-1)
$q = .5$	Ω_Z	1.9 (3)	2.3 (1)	2.3 (-2)	2.3 (-5)	2.3 (-8)	2.0 (3)	2.6 (1)	2.6 (-2)	2.6 (-5)	2.6 (-8)
	$\bar{\kappa}$	2.2 (8)	6.7 (6)	6.1 (4)	6.0 (2)	6.0	1.9 (8)	6.7 (6)	6.1 (4)	6.0 (2)	6.0
	$\lvert\bar{\sigma}_1\rvert$	3.0 (3)	3.5 (1)	3.5 (-2)	3.5 (-5)	3.5 (-8)	3.2 (3)	3.9 (1)	3.9 (-2)	3.9 (-5)	3.9 (-8)
$q = .7$	Ω	2.7 (3)	4.9 (2)	5.1 (1)	5.2	5.2 (-1)	2.9 (3)	4.9 (2)	5.2 (1)	5.2	5.2 (-1)
	$\bar{\kappa}$	1.1 (8)	3.7 (6)	1.1 (6)	1.1 (5)	1.1 (4)	7.1 (7)	3.9 (6)	1.1 (6)	1.1 (5)	1.1 (4)
	$\lvert\bar{\sigma}_1\rvert$	2.8 (3)	5.3 (2)	6.1 (1)	6.2	6.2 (-1)	3.3 (3)	5.3 (2)	6.1 (1)	6.2	6.2 (-1)
$q = .9$	Ω	3.6 (3)	9.5 (2)	1.0 (2)	1.0 (1)	1.0	3.8 (3)	9.5 (2)	1.0 (2)	1.0 (1)	1.0
	$\bar{\kappa}$	1.6 (8)	8.3 (7)	1.0 (7)	1.1 (6)	1.1 (5)	2.8 (8)	8.4 (7)	1.0 (7)	1.1 (6)	1.1 (5)
	$\lvert\bar{\sigma}_1\rvert$	7.4 (3)	2.4 (3)	2.8 (2)	2.9 (1)	2.9	9.6 (3)	2.4 (3)	2.8 (2)	2.9 (1)	2.9

FIGURE 4.12: We report here the absolute values of the accelerations $\bar{\kappa}$ (in km/s^2) and the spin-precession frequencies $\lvert\bar{\sigma}_1\rvert$ (in rad/) experienced by pulsars moving on equatorial circular orbits with physical (Kerr-Schild) radii $\tilde{r}$ (in km) in the equatorial plane of a Kerr spacetime with *arbitrary* orbital angular velocities Ω (in rad/s) around black holes of mass $M = 100M_\odot$ with spin parameters $a = .1M, .5M, .9M$. We also include these values for a Kerr naked singularity of the same mass and spin parameter $a = 1.01M$. To compare, the intrinsic spin frequency of a pulsar ω lies between $1 - 10^2$ rad/s. We consider pulsars with varying Boyer-Lindquist orbit radii $r = 2.1M, 10M, 10^2M, 10^3M, 10^4M$. We choose these values for r since the ergosurface in the equatorial plane is at $r_+ = 2M$. At each of these radii, we vary the angular speeds of the pulsars between their maximum and minimum allowed values $\Omega_- < \Omega < \Omega_+$ and parametrize them with q as $\Omega = q\Omega_+ + (1-q)\Omega_-$. We choose $q = q_{K+}, q_{K-}, q_{static}, .1, .3, .5, .7, .9$, where we have defined $q_{K\pm}$ and q_{static} as satisfying $\Omega(q_{K\pm}) = \Omega_{K\pm}$ and $\Omega(q_{static}) = 0$, corresponding to the equatorial non-accelerating co-rotating and counter-rotating circular Kepler observers and the Kerr static Killing observers respectively. Dashes in entries below denote that Kepler observers are disallowed for those values of $a, r,$ and q (since $r < r_{ISCO\pm}$). Note also that whenever allowed, Kepler observers have zero acceleration $\bar{\kappa} = 0$ and static observers have zero orbital angular velocity $\Omega = 0$. The number in a parenthesis (n) denotes the order of magnitude of the entry, i.e. $3.2\,(2) = 3.2 \times 10^2$, and serves as a rough indicator for the ratios $\log f_o$ and $\log f_p$, for second-period pulsars. For ms-pulsars, $n - 2$ is the appropriate estimate for these ratios naturally.

how morphology can affect timing). Therefore, with high-precision pulsar timing observations courtesy of extremely sensitive astronomy missions like SKA and FAST, these astrophysical scenarios can be investigated independently, complimentary to gravitational wave observations.

Further, we have shown that a pulsar that is moving on circular orbits near a BH, and under the influence of gravitomagnetic spin-precession, is detectable on earth if and only if the following geometric condition is satisfied,

$$\theta_E = \pm\alpha + \beta, \tag{4.8.1}$$

where in the above, θ_E is the angle between the direction of the earth and the precession-axis of the pulsar, β is the angle between the spin-axis and the precession-axis and α is the angle between the spin and radiation axes. The precession-axis in the current chapter (for pulsars moving on equatorial orbits) lies along the z-axis, i.e. it is parallel to the spin-axis of the central BH. Also, when the pulsar doesn't experience spin-precession ($\beta = 0$), the condition for pulses to be observed that must be met is,

$$\theta_E = \alpha. \tag{4.8.2}$$

Now, let us consider the evolution of a single pulsar-BH system. When the pulsar is relatively far away from the BH, if one initially obtained pulses on earth (condition 4.8.2 is met), and the orientation of the spin-axis of the pulsar w.r.t. the z-axis is not small ($\beta \not\approx 0$), then the geometric condition for when the pulsar begins to experience non-trivial spin-precession, given in equation 4.8.1, would not be met. In such cases, the pulsar would eventually vanish. On the other hand, if $\beta \approx 0$, then the pulsar would be visible for the entire duration of its inspiral, opening up wonderful possibilities. Further, pulsars in binaries with BHs that did not initially satisfy equation 4.8.2, and therefore went undetected, could be caught by our detectors close to the BH if they started to approximately satisfy equation 4.8.1. In this regard, we think it relevant to mention here that there have been numerous studies that highlight the role that pulsars could play in the discovery (and the subsequent analysis of the properties) of new IMBHs near Sgr$A^\star$ (see for example [132, 352, 353]), and our results here further strengthen the case for pulsars as probes of BH spacetimes.

Another implication of our findings here is that a normal or ms-pulsar with intrinsic spin-angular frequency in the range $\omega = 1 - 10^2$ rad/s could appear to pulsate at much faster frequencies when present near a massive BH, with the consequence that it could even masquerade as a genuine sub-millisecond pulsar (see for example panels a and c of figure 4.10). Moreover, the pulsar mass-shed or break-up spin frequency is typically around $\nu_b \simeq 1200$ Hz (see for example [354]), depending on the equation of state, and an ordinary pulsar present near a massive BH could appear to pulsate at frequencies larger than even ν_b. Therefore, neglecting gravitomagnetic spin-precession effects near BHs could possible lead to incorrect conclusions regarding the internal structure of neutron stars. Furthermore, gravitomagnetic effects present one possible explanation for pulsar nulling and for pulsar-related quasiperiodic oscillations, since spin-precession could cause pulsars to appear at frequencies smaller than the intrinsic spin-period (see panels d and e of figure 4.10). If this hypothesis renders a partial explanation for QPOs (maybe for a specific class of them), this could even lead to the discovery of black hole binary partners for some pulsars.

The Kerr spacetime, depending on the relation between the specific angular momentum a and mass M of the central object, describes either a BH or a naked singularity (NS), or possibly even more exotic hypothetical objects like superspinars [55]. Disregarding for now the latter case, when $a \leq M$, the spacetime contains a BH, and a NS otherwise. We note that all of the analysis presented in this chapter applies to Kerr NSs equally

well [312]. Further, since the spin-precession frequency (and consequently the pulse frequency) depends on the spin-parameter a, one could identify what the nature of the companion of a pulsar is, namely whether or not it possesses an event horizon. In [311] and [312], the spin-precession frequency along Killing orbits in the Kerr spacetime was revisited and various trends were outlined. It was noted there that spin-precession frequencies experienced by such observers can become quite large in regions of strong gravitational fields. First, spinning objects that remain fixed spatially (static Killing orbits) close to a Kerr ergosurface would experience drastically large spin-precession frequencies. Now, as was discussed in [200] for example, since the topology of the ergosurface is drastically different for Kerr BHs (spheroidal) and NSs (toroidal), one could potentially distinguish these objects from pulsar measurements, due to the effect that gravitomagnetic spin-precession has on them [311]. Similarly, sharp rises in the spin-precession frequencies were found to occur for observers moving on equatorial circular orbits (stationary Killing orbits) either around Kerr BHs near their event horizons or around Kerr naked singularities when near the ring singularity itself. Since the physical sizes of the horizon ($\tilde{r}_H = \sqrt{2r_H}$; see equation 4.3.2) and the ring singularity ($\tilde{r}_{sing} = a$) can be easily distinguished between, one could use pulsar timing measurements to identify the nature of the compact object. Additionally, the decay of the spin-precession frequency as one moves off of the equatorial plane ($\theta = \pi/2$) to much smaller, reasonable values is much more drastic near a naked singularity, as compared to near a BH, roughly due to the presence of the horizon for $\theta \neq \pi/2$ [312]. And so, small deviations in the pulsar's orbit from the equatorial plane could also be immensely useful in distinguishing the two compact objects. Therefore, in practice, the detection of a pulsar near a supermassive collapsed object with a frequency much higher than the maximum observed pulsar frequency (716 Hz; [355]) could strongly suggest the existence of an ergoregion, event horizon or a ring singularity depending on the state of the motion of the pulsar. Further, one could also potentially test the no hair theorem for black holes (see [8]) if, for example, spin-precession measurements of 'Killing pulsars' indicate deviations from the norm in the structure of the associated horizon or ergosphere.

While the event horizon, if present, could be detected by the above method, additional measurements, for example, the ratio of the pulsar radial distance to the central collapsed object mass, could be used to estimate the spin of this collapsed object, and hence to identify its nature (BH or NS). This can be done by comparing the measured pulsar spin-precession rate with the theoretical computation of this rate as a function of the pulsar radial distance in the unit of the collapsed object mass and the collapsed object spin. The required estimation of the distance can be obtained either from the gravitational radiation chirp characteristics or from the known mass of the supermassive collapsed object and the orbital period of the pulsar. The orbital period can be inferred from a periodic variation of the pulsar's intensity, which can be associated with its orbital motion. For example, such an intensity variation (or even a periodic disappearence of the pulses) can happen due to the light bending effect, as the pulsar moves behind the central collapsed object and comes in front of it periodically. The spectrum (or the intensities in a few radio bands) may also periodically vary due to the orbital motion related Doppler effect.

Let us consider now more modest tests involving, for simplicity, a pulsar that moves with very small orbital angular velocities ($\Omega \approx 0$) around a Kerr BH or naked singularity (static Killing orbits). For such pulsars, the overall periodicity of the deflection vector $|\zeta^2(\tau)|$, and therefore of the observed pulse profile, is determined by the play-off between the spin-precession frequency Ω_p and the intrinsic spin frequency of the pulsar ω. Roughly, if $\Omega_p > \omega$, then pulses appear at rates faster than the intrinsic spin frequency. On the other hand, if this relation is reversed, one misses out pulses. Now, from table 1, one can safely conclude that spin-precession effects grow faster as a pulsar slowly moves towards the ergoregion of a Kerr naked singularity, as opposed

to that of a Kerr BH. Similar statements can be made for pulsars moving on equatorial circular orbits, and so over the course of an inspiral of a pulsar into a BH or naked singularity, if one could extract and characterize the evolution of the spin-precession frequency ($\Omega_p(r)$), then one could distinguish the two.

4.9   Conclusions

The spin-precession of the spin-angular momenta of test objects present in the vicinity of a Schwarzchild BH, due to geoedetic effects, was studied in [150], and [151] calculated the total spin-precession around Kerr BHs by including gravitomagnetic effects. In both papers, the overall deflection of the spin-vector after an entire orbit was obtained and as far as we can tell, our work [125], reviewed here, presents a new application of *instantaneous* spin-precession effects, as opposed to the cumulative spin-precession effects that have generally been studied.

If an isolated pulsar spins around its axis at an angular frequency of ω, then one obtains pulses on earth every $\Delta t = \omega/2\pi$ and the Fourier spectrum of this pulse profile contains a single unique peak. However, we find here that if the same pulsar was actually present near a Kerr BH, then its Fourier spectra would exhibit multiple peaks corresponding to its orbital angular velocity Ω, its spin-precession frequency Ω_p, the vector sum of $\vec{\omega}$ and $\vec{\Omega}_p$ denoted by $\omega_{\text{eff}} = \sqrt{\omega^2 + \Omega_p^2 + 2\omega\Omega_p \cos\beta}$, and various combinations of the sums and differences of these three frequencies. In particular, only when Ω_p and ω_{eff} are commensurate, one obtains exactly periodic pulses on earth. Although here we worked mostly in the pulsar's frame, we indicated that it was possible to obtain the change in the rate of pulses obtained on earth (see the discussion in §4.6.4).

Our computations for the astrophysically important cases corresponding to pulsars moving around IMBHs and lower-end SMBHs on equatorial circular orbits show that gravitomagnetic spin-precession leads to significant modifications in the associated observed pulse profile, either leading to substantial modifications in either pulse-arrival times or in pulse-shape. Therefore, these effects need to be accounted for properly to interpret the timing of pulsar signals when the source closely orbits a IMBH that may exist in globular cluster cores, for example. Furthermore, models for pulsar timing observations that include these effects will therefore provide accurate tests of BH spacetimes and parameters.

Standard pulsar searches use Fourier techniques [356] to search for *a priori* unknown periodic signals. Since our analysis predicts precisely the change in the number of peaks in the Fourier profile of the power spectrum of a pulsar, as discussed in §4.6.6 above, looking for gravitomagnetic spin-precession effects via pulsar timing would likely be easily implementable. However, typically one assumes in such searches that the apparent pulse period remains constant throughout the observation [301], which when violated, as will likely be the case during inspirals, could lead to a loss in signal-to-noise ratio (SNR) of the signal power in the Fourier-domain. In such instances, one could use the so-called 'acceleration searches' [357], which have been proven to improve SNR in such instances. This technique, on the other hand, assumes that the pulsar has a constant acceleration during the observation, which works excellently well for the pulsar orbits we have considered here. In fact in table 4.12 we have even catalogued the values of the accelerations experienced by pulsars on slowly inspiralling orbits around BHs for ready reference.

We note that an analytic derivation of the evolution of the beam vector for a pulsar that experiences gravitomagnetism is detailed in appendix §E to make clear that the extension to include pulsars moving along

non-equatorial Killing orbits is straightforward. It is worth mentioning that it would be useful to extend the analysis presented here to include even more astrophysically interesting scenarios of pulsars moving on arbitrary time-like orbits, building on the results of [153], where the spin-precession frequency experienced by such observers was recently obtained. Recently, [358] obtained closed-form analytic solutions for the properties of the motion (evolution of orbit with time etc.) of test objects moving on non-equatorial eccentric bound trajectories around a Kerr black hole; this work could drastically simplify the calculational aspect of obtaining spin-precession frequencies along arbitrary trajectories, and potentially help in generating pulse profile templates for pulsars around IMBHs and SMBHs for SKA and FAST to use (one would have to assume a beam structure model, though; see for instance figure 5 of [301]).

Also, as mentioned before, here we have avoided solving the full Mathisson-Papapetrou equations by neglecting the effect of spin-curvature coupling on the motion of the pulsar, which is an excellent approximation for pulsars that either (a) spin slowly, or (b) are present near SMBHs ($M_{BH} \gtrsim 10^6 M_\odot$), or (c) are sufficiently far away ($r \gtrsim 50 M_{BH}$) from massive BHs ($M_{BH} \gtrsim 10^2 M_\odot$). Further, as was discussed in a couple of excellent papers recently [138, 309], the pulse profile of ms-pulsars present in the equatorial plane of a massive Kerr black hole (and sufficiently close to it) can be significantly altered due to this effect and so, it would be safe to conclude that our calculations work best for normal pulsars around IMBHs/SMBHs and for ms-pulsars present near SMBHs or when sufficiently far away from IMBHs.

Finally, it is worth noting that we have presented proof that radiation from Killing pulsars does in fact reach earth when a certain simple geometric condition is met (see appendix D). This is equivalent to a ray tracing analysis.

Chapter 5

Summary and Conclusions

We think it useful to present here a unified summary for brevity and perspective.

As outlined in the introductory comments in Chapter 1, when a physical theory produces highly non-intuitive predictions like the existence of black holes, one must assess whether these predictions are robust, or generic. In the current context, this would entail an analysis of the full non-linear (orbital) stability of the formation of a black hole against *arbitrary* changes in the initial conditions of the formation process. Such an analysis is typically extremely complex and one reduces the difficulty considerably by examining the linear orbital stability of the formation process against *infinitesimal* perturbations of the initial data [112].

Therefore, in Chapter 2, we set up the linearized field equations that govern metric perturbations around curved vacuum background solutions to the full non-linear Einstein field equations, and discussed how establishing linear stability of the background against arbitrary solutions to these equations is also a highly non-trivial problem. Specialising further to the study of a specific type of linear perturbations, namely those that display a harmonic time dependence, we studied the mode stability of the Schwarzschild black hole in careful detail. We hinted that Kerr BHs were stable and Kerr naked singularities were not. At this point, we turned to considerations of the mode stability of Kerr superspinars.

Here the term 'Kerr superspinar' is used to denote those (thus far, largely hypothetical in 3+1 spacetime dimensions) compact objects whose exterior geometries could be described by the overspinning Kerr metric, but are devoid of the accompanying naked singularity [55]. Recently, with the following perspective, the mode stability of such objects has been explored. Even though a nakedly singular spacetime is unstable against mode perturbations or fluid perturbations, this should not mean that a study of the properties of such spacetimes must be hastily abandoned. Singular metrics are solutions of the classical Einstein field equations and the expectation is that the deeper theory of quantum gravity would smear out these singularities, irrespective of whether or not they are covered from asymptotic observers by event horizons. That is, quantum gravity could introduce classes of legitimate compact objects such that their exterior geometries are described by metrics that were classically nakedly singular, but with their central singular regions excised and replaced by regions governed by Planckian physics. For example, string theory, a popular candidate for the quantum theory of gravity, has proven to be exceptionally good at resolving spacetime geometries with various timelike singularities and such singularities, inconsistent in general relativity, then represent new classes of legitimate

compact objects in the string-theoretic completion of general relativity (see for example the pair of papers: [198, 199]).

An interesting question then arises, how strongly do the properties of a classical nakedly singular metric (like mode stability, shadows, images etc.) depend on the central naked singularity itself? Towards answering such a question, an attempt to study the stability of these singularity-excised spacetimes was recently made [70]. The study of mode stability of any given spacetime requires one to solve the linearized Einstein field equations with appropriate boundary conditions, as was discussed earlier. Irrespective of the spacetime under consideration, one typically imposes the condition that there are no sources at asymptotic infinity, i.e. no incoming radiation from spatial-infinity. As for the boundary condition at the inner edge, in the case of black hole spacetimes, one naturally imposes perfectly absorbing boundary conditions at the horizon. However, for exotic objects like Kerr superspinars, there is no such natural boundary condition for incoming modes at the 'surface' of a superspinar and one must find quasi-normal modes and their frequencies for each boundary condition. With this in mind, we presented an extensive review of our results on the mode stability of Kerr superspinars, which were originally presented in [71]. In particular, we showed how near-extremal Kerr superspinars are mode stable against an infinite class of boundary conditions. It is to be noted that this class of boundary conditions satisfied a particular condition (2.5.28). It remains to be seen whether when this condition is relaxed (C, D take all allowed values) near-extremal superspinars are still stable against mode perturbations. Further, one should also study what happens for superspinars with higher spins ($M \ll a$).

Having thus examined aspects of linear stability analyses in general relativity, we moved to a discussion of the Cauchy problem of the Einstein field equations, and a review of the statement of non-linear stability of a particular solution, which was previously deferred. Taking advantage of the fact that the evolution of a spherically symmetric, regular cloud of pressureless matter to a Schwarzschild black hole is known to be given by the Datt-Oppenheimer-Snyder (DOS) collapse [44], that it's initial data is well characterised, and the evolutions of nearby initial data are also well understood (determined by the Lemaître-Tolman-Bondi collapse models), we sought to demonstrate how a typical non-linear stability analysis in the context of general relativity proceeds. In this process, we also discussed there the visibility of the eventual spacetime singularity that forms in these collapse evolutions, following [104] (also see references therein). In specific, the DOS collapse to a Schwarzschild black hole evolves from homogeneous initial data ($\rho(0, r) = \rho_0$) and we considered a two-parameter open subset of initial data $\rho(0, r) = \rho_0 - \rho_2 r^2 (\rho_2 \geq 0)$ around it. We showed that the initial compactness $\chi = M/r_b$ of collapsing cloud (where M is the total Arnowitt-Deser-Misner (ADM) mass [248] of the cloud and r_b is its initial radius) governed the nature of the singularity in these models, i.e. when $\chi \lesssim .44$, the cloud formed a globally visible naked singularity and a black hole otherwise.

In the same chapter, we also analysed notions of stability of dynamical systems in classical mechanics, in the framework of symplectic geometry, and attempted to draw a formal analogy to equivalent notions in the study of spacetimes in GR, based on our work [104]. From a pedagogical standpoint, this geometric approach aids in developing a clearer understanding of the formal statements of stability analysis in general relativity. Beginning with a construction of the phase space of classical mechanical systems as a symplectic manifold, we revisited the concept of a symplectic Hamiltonian vector field, which is derived from a Hamiltonian function defined over phase space, and proceeded to discuss how the governing dynamical equations of motion are simply the flow equations of this vector field. Non-linear and linear stability analyses of the equilibrium or critical points of a dynamical system then obtain the intuitive geometric interpretation of having simply to do with the divergence of the flow of the Hamiltonian vector field and its linearization respectively.

Earlier we had discussed the Cauchy problem of the vacuum Einstein field equations, and argued that whenever it is well-posed, the solutions of the EEs are necessarily globally hyperbolic spacetimes $(\mathcal{M}, g)$ [208, 210, 211], i.e. they are diffeomorphic to $\Sigma \times \mathbb{R}$, where Σ is a 3-submanifold with a Riemannian 3-metric γ and $\mathbb{R}$ denotes the time direction. Therefore, typically physically relevant solutions of the Einstein field equations admit a 3+1 foliation in the above sense. Armed now with an explicit notion of time, the Hamiltonian formulation of general relativity can be set up for such spacetimes, with $\gamma(t)$ the generalised coordinate, from which one can define also a generalised conjugate momentum $\kappa(t)$. The GR Hamiltonian function whose flow equations correspond to the vacuum Einsten equations is the well known ADM Hamiltonian [248]. Then when inquiring after the stability of a spacetime $(\mathcal{M}, g)$, simply by rewriting $g \equiv \gamma(t)$, one can immediately transport statements that were made regarding the stability of solutions in CM to equivalent statements for GR. It is of vital importance that we note that we have not discussed here the construction of the reduced phase space by forming the quotient space of the constrained phase space with the gauge orbits, and therefore work remains to be done before this nice analogy can be called fully formal. We also mention in passing how the eventual desire is to find the Kerr family of solutions to be a dynamical attractor in the phase space of general relativity. One may see §2.10 for a more detailed exposition of the conclusions and comments on these aspects.

This concluded part I of this thesis on stability analysis. As discussed previously, once stability of a solution amplifies the attractiveness, from an astrophysical standpoint, of the object it describes, a study of how it may be detected becomes importance. Subsequently, we then moved to an exploration of how one may detect compact objects in general relativity, i.e. to part II.

In Chapter 3, we compared shadows cast by Schwarzschild black holes with those produced by two classes of naked singularities that result from gravitational collapse of spherically symmetric matter. The latter models consisted of an interior naked singularity spacetime restricted to radii $r \leq R_b$, matched to Schwarzschild spacetime outside the boundary radius R_b. While a black hole always has a photon sphere and always casts a shadow, we found that the naked singularity models have photon spheres only if a certain parameter M_0 that characterizes these models satisfies $M_0 \geq 2/3$, or equivalently, if $R_b \leq 3M$, where M is the total mass of the object, and such models do in fact produce shadows. However, it was shown that models with $M_0 < 2/3$ (or $R_b > 3M$) did not possess photon spheres and therefore would not produce shadows. Instead, they produce an interesting "full-moon" image. These results imply that the presence of a shadow does not by itself prove that a compact object is necessarily a black hole. The object could be a naked singularity with $M_0 \geq 2/3$, and one would require need other observational clues to distinguish the two possibilities. On the other hand, the presence of a full-moon image would certainly rule out a black hole and might suggest a naked singularity with $M_0 < 2/3$. It would be worthwhile to generalize the present study, which is restricted to spherically symmetric models, to rotating black holes and naked singularities.

Studying properties of null geoedesics, amongst other aspects, in black hole and naked singularity spacetimes has been of central interest in astrophysics, when attempting to detect these objects. This includes characterizing how compact objects lens/bend light, and as discussed above how they form shadows and images. Other methods to detect such objects include examining the motion of stars in their vicinity etc. The motivation for Chapter 4 was to determine whether the effect of gravitomagnetic spin-precession pulsars in the vicinity of spinning massive compact objects experience could yield a fresh, independent estimate of the spin of massive black hole or naked singularity. As argued there, indeed the frequency of said precession falls nicely into the category of previously-unused 'new' *local* physical observables. We provide below a short description of why considerations of this effect are exciting, particularly in the context of upcoming missions such as the Square

Kilometre Array (SKA; [131, 132]) and the Five-hundred-meter Aperture Spherical radio Telescope (FAST; [133, 134]).

In classical Galilei-Newton mechanics, the external gravitational field of an object, spinning or otherwise, was only given by its mass. In general relativity, however, it is given by both its mass and *mass current* (angular momentum). The 'passive' part of the external gravitational field that causes test objects to accelerate is termed the gravitoelectric field and the 'active' piece that causes spinning objects to precess is called the gravitomagnetic field, in analogy with electromagnetism. See for example [155–157] and references therein for a more formal description of this connection between gravity and electromagnetism in terms of their tidal tensors. The precession of spins due to frame-dragging is a manifestation of gravitomagnetism, and is also the reason behind the precession of particle orbits. This feature is incorporated into the spacetime structure and can be thought of as a sort of spin-spin interaction.

Rotating black holes and naked singularities are therefore naturally expected to influence spinning objects in this way, and building on the results obtained by [151] on the frequency of precession of spin-vectors attached to two types of Killing observers - static and stationary - in arbitrary stationary spacetimes, we showed through an extensive discussion in [311, 312] that its properties depend both on the motion of the spinning object, and arguably more importantly, on the angular momentum of the central Kerr compact object. Therefore, spin-precession frequency as this new observable fits the bill exceptionally well. We remind the reader that static observers remain fixed to a point in space and stationary observers move on circles, with fixed angular velocity, around the black hole or naked singularity axis.

Following the discussion in §4.4, we set up the following experiment in [311], using static Killing observers. Consider an astronaut, equipped with a gyroscope, that initially remains fixed at point A_1, close to a Kerr compact object. He holds himself at A_1 for a long time t and then moves to another point A_2 and holds himself fixed thereafter. t is much larger than the dynamical time-scale in the problem defined by the dimensionless spin parameter of the Kerr object, $a/M \equiv J/M^2$. Then, we showed that for points A_1, A_2 along (or close to) the rotation axis of the Kerr object, this change in Ω_{LT} can be used to identify the nature of the compact object. In this case, Ω_{LT} is also called the Lense-Thirring precession frequency and it reduces appropriately to the standard weak-field limit result. Specifically, for a BH, he would see a sharp change in the spin-precession frequency on moving from A_1 to A_2, whereas for a NS the change would always be smooth and gradual. We argued that for such 'static observers,' Ω_{LT} is 'sensitive' to the location of the ergosurface, which is the bounding surface of the ergoregion. For such observers, in both cases, in the limit of approach to the ergosurface, Ω_{LT} becomes arbitrarily large. We pointed out that since the geometric structure of the ergosurface is dramatically different for BHs and NSs, this feature of the spin-precession frequency could be used to distinguish the two. The ergosurface exists for all angles θ for a BH whereas this is not the case for a NS and a finite opening angle, which depends on a, opens up around the pole ($\theta = 0$), for which the ergosurface is non-existent; see §4.3 above.

In [312], the above experiment was extended to included the larger class of stationary Killing observers. We considered the case of an astronaut, equipped with a gyroscope, orbiting a Kerr compact object on a circle, with fixed angular velocity. We argued that for such observers the total spin-precession frequency experienced by the gyroscope, Ω_p, is sensitive to the existence/location of the event horizon. The subscript $_p$ denotes that this is the total spin-precession frequency, including the contribution from geodetic precession, and not just the Lense-Thirring precession. For BHs, Ω_p diverges close to the horizon whereas for NSs, Ω_p diverges only at the singularity. The horizon exists for all θ whereas the Kerr ring singularity lies in the equitorial plane

$\theta = \pi/2$, thereby allowing us to setup the following distinguishing criterion in terms of Ω_p. Now, suppose the astronaut is initially in a circular orbit O_1 for a long time and then switches to an orbit O_2 and then remains there, and let us say these orbits O_1, O_2 subtend $\theta_1, \theta_2 (\theta_1 \not\approx \theta_2)$ respectively at $r = 0$. Then,

- if Ω_p becomes arbitrarily large in the limit of approach to the central object for both θ_1, θ_2 then the spacetime contains a black hole, whereas

- if Ω_p becomes arbitrarily large in the limit of approach to the central object for at most one of θ_1, θ_2 then the spacetime contains a naked singularity.

Finally, we note that these results can be extended to any black hole or naked singularity spacetime with similar Killing symmetries. We have used in [311, 312] the fact that there exist invariant characterizations of ergoregions and horizons respectively in terms of the Killing vectors. We set up observers equipped with gyroscopes along integral curves of these Killing vectors and then studied the spin-precession behaviour of these gyroscopes and interpreted any arbitrarily large growth in the modulus of the spin-precession frequency as being potential indicators of the presence of an ergosurface [311] or a horizon [312].

Recently in [125], we considered the effects of gravitomagnetic spin-precession on the observed pulse profile of a pulsar that is present in a binary with a massive Kerr black hole, as an application of our results [311, 312]. In this scenario, a pulsar can then be treated as a test spinning mass, and we show that it is possible to obtain an independent estimate of the specific angular momentum of the central compact object from pulsar timing measurements. Specifically, considering pulsars to be moving on equatorial circular orbits of the Kerr spacetime, we worked out the observed rate at which pulses appear on earth. Ths is possible since measuring the change of the spin-axis of a pulsar moving along the world-line of a static Killing observer in the Kerr spacetime, relative to its Frenet-Serret triad (see for example [125] on why this frame), gives also the change in the spin relative to fixed asymptotic observers (see for example §II.C of [317]). This precious property is particular to Killing observers, as we discussed above.

Fascinatingly, we find that for unaccelerated motion, gyroscopic spin-precession, relative to asymptotic fixed observers, stems from purely geodetic parallel-transport and has no contribution from the spin of the central Kerr compact object! From observations of pulsars moving along circular geodesics, one may be able to ascertain an independent estimate of the mass of the central black hole or naked singularity and possibly the radius of the orbit. Therefore, it appears that to be able to extract information from pulsar timing regarding the spin of the Kerr black hole or naked singularity, one must observe pulsars that are accelerating, even though the phase of acceleration might be extremely brief.

We note here the important distinction from the readings one would obtain here from those for an isolated pulsar. An isolated pulsar would appear to emit pulses at a time period $\omega/2\pi$, i.e., at its intrinsic spin angular frequency. As we see here, a pulsar in a stationary spacetime will appear to pulse at a different frequency. If one considers pulsars present in strong gravitational fields like near the ergosurface of a Kerr black hole or naked singularity, pulses on earth appear at the spin-precession frequency and the intrinsic spin angular velocity is completely washed out!

Our theoretical prediction of high pulsar spin-precession rates near an event horizon implies the following new and interesting aspects, some of which could eventually be observed. The existence of sub-millisecond pulsars: our theoretical finding provides a new mechanism to give rise to apparent sub-millisecond pulsars,

which have not been observationally found so far. Identifying Kerr black holes and naked singularities: the Kerr spacetime, depending on the relation between the angular momentum J and mass M of the central object, describes either a BH or a NS. That is, when $J \leq M^2$, the spacetime contains a BH, and a NS otherwise. Since these modifications in pulse frequency are characteristic of the nature of the collapsed object, i.e., whether or not it possesses an event horizon, one could identify what the compact object companion of an observed pulsar is. In fact, these deviations from the pulsar's intrinsic spin period could be used to locate the horizon even. Other aspects include explanations of multiple-peaked pulse profiles, pulsar nulling etc. Future directions include working out trends in pulsar profiles for more general models for its motion; recent significant advances in characterizing spin-precession generally [153, 163] would go a long way towards achieving these goals.

Bibliography

[1] K. Schwarzschild, Sitzungsber. K. Preuss. Akad. Wiss **1**, 189 (1916),
    [*English Translation*] S. Antoci and A. Loinger, arXiv:physics/9905030 [physics.hist-ph] (1999).

[2] H. Reissner, Annalen der Physik **355**, 106 (1916);
    G. Nordström, Koninkl. Ned Akad. Wetenschap. Proc. **20**, 1238 (1918).

[3] A. H. Taub, Ann. Math. **53**, 3 (1951);
    E. Newman, L. Tamburino, and T. Unti, J. Math. Phys. **4**, 915 (1963).

[4] R. P. Kerr, Phys. Rev. Lett. **11**, 237 (1963).

[5] E. T. Newman, E. Couch, K. Chinnapared, A. Exton, A. Prakash, and R. Torrence, J. Math. Phys. **6**, 918 (1965).

[6] A. I. Janis, E. T. Newman, and J. Winicour, Phys. Rev. Lett. **20**, 878 (1968).

[7] C. M. Will, Liv. Rev. Rel. **17**, 4 (2014).

[8] C. W. Misner, K. S. Thorne, and J. A. Wheeler, *Gravitation* (Freeman, San Francisco, 1973).

[9] S. W. Hawking and G. F. R. Ellis, *The Large Scale Structure of Space Time* (Cambridge University Press, Cambridge, 1973).

[10] R. Wald, *General Relativity* (The University of Chicago Press, Chicago, 1984).

[11] P. S. Joshi, *Global Aspects in Gravitation and Cosmology* (Oxford University Press, Oxford, 1993).

[12] R. Penrose, Phys. Rev. Lett. **14**, 57 (1965).

[13] R. Penrose, Riv. Nuovo Cimento **1**, 252 (1969), [*Republished*] Gen. Rel. Grav. **34**, 7 (2002).

[14] R. Penrose, *General Relativity, an Einstein Centenary Survey*, p. 581 (1979).

[15] W. Israel, Found. Phys. **14**, 1049 (1984).

[16] W. Israel, Can. J. Phys. **64**, 120 (1986).

[17] D. Christodoulou, Class. Quantum Grav. **16**, A23 (1999).

[18] S. W. Hawking, Commun. Math. Phys. **25**, 152 (1972).

[19] T. W. Baumgarte, M. L. Skoge, and S. L. Shapiro, Phys. Rev. D **70**, 064040 (2004).

[20] A. E. Broderick, T. Johannsen, A. Loeb, and D. Psaltis, Astrophys. J. **784**, 7 (2014).

[21] N. Gürlebeck, Phys. Rev. Lett. **114**, 151102 (2015).

[22] D. Psaltis, F. Özel, C.-K. Chan, and D. P. Marrone, Astrophys. J. **814**, 115 (2015).

[23] Gravity Collaboration et al., Astron. Astrophys. **618**, L10 (2018).

[24] A. Almheiri, R. Mahajan, J. Maldacena, and Y. Zhao, arXiv:1908.10996 [hep-th].

[25] I. L. Shapiro, A. M. Pelinson, and F. de O. Salles, Mod. Phys. Lett. A. **29**, 1430034 (2014).

[26] J. Maldacena, Int. J. Theor. Phys. **38**, 1113 (1999).

[27] E. Berti, V. Cardoso, and A. O. Starinets, Class. Quantum Grav. **26**, 163001 (2009).

[28] B. M. S. Hansen and J. Liebert, Ann. Rev. Astron. Astrophys. **41**, 465 (2003).

[29] D. N. Spergel, M. Bolte, and W. Freedman, Proc. Natl. Acad. Sci. **94**, 6579 (1997).

[30] J. H. Taylor and J. M Weisberg, Astrophys. J. **253**, 908 (1982).

[31] J. H. Taylor and J. M Weisberg, Astrophys. J. **345**, 434 (1989).

[32] A. Wolszczan and D. A. Frail, Nature **355**, 145 (1992).

[33] P. C. Freire, M. Kramer, A. G. Lyne, F. Camilo, R. N. Manchester and N. D'Amico, Astrophys. J. **557**, 2 (2001).

[34] M. Burgay et al., Nature **426**, 531 (2003).

[35] R. Schödel et al., Nature **419**, 694 (2002).

[36] A. M. Ghez et al., Astrophys. J. **689**, 1044 (2008).

[37] J. Kormendy and L. C. Ho, Ann. Rev. Astron. Astrophys. **51**, 511 (2013).

[38] R. Narayan and J. E. McClintock, New Astron. Rev. **51**, 733 (2008).

[39] A. E. Broderick, A. Loeb, and R. Narayan, Astrophys. J. **701**, 1357 (2009).

[40] A. E. Broderick, R. Narayan, J. Kormendy, E. S. Perlman, M. J. Rieke, and S. S. Doeleman, Astrophys. J. **805**, 179 (2015).

[41] M. A. Abramowicz, W. Kluzniak, and J.-P. Lasota, Astron. Astrophys. **396**, L31 (2002).

[42] H.-T. Janka, T. Eberl, M. Ruffert, and C. L. Fryer, Astrophys. J. **527**, L39 (1999).

[43] T. Johannsen and D. Psaltis, Astrophys. J. **718**, 446 (2010).

[44] B. Datt, Zs. f. Phys. **108**, 314 (1938),
[*English Translation*] H. Pfister, Gen. Rel. Grav. **31**, 1619 (1999);
J. R. Oppenheimer and H. Snyder, Phys. Rev. **56**, 455 (1939).

[45] G. Lemaître, Ann. Soc. Sci. Bruxelles **A53**, 51 (1933),
[*English Translation*] M. A. H. MacCallum, Gen. Rel. Grav. **29**, 641 (1997);
R. C. Tolman, Proc. Natl. Acad. Sci. **20**, 12 (1934);
H. Bondi, Mon. Not. R. Astron. Soc. **107**, 410 (1947).

[46] P. C. Vaidya, Astrophys. J. **144**, 943 (1966).

[47] D. M. Eardley and L. Smarr, Phys. Rev. D 19, 2239 (1979).

[48] B. Waugh and K. Lake, Phys. Rev. D **38**, 1315 (1988).

[49] A. Ori and T. Piran, Phys. Rev. Lett. **59**, 2137 (1987);
A. Ori and T. Piran, Phys. Rev. D **42**, 1068 (1990).

[50] P. S. Joshi and I. H. Dwivedi, Phys. Rev. D **47**, 5357 (1993).

[51] P. S. Joshi, D. Malafarina, and R. Narayan, Class. Quantum Grav. **28**, 235018 (2011).

[52] M. Volonteri, Astron. Astrophys. Rev. **18**, 279 (2010).

[53] E. W. Kolb and I. I. Tkachev, Phys. Rev. Lett. **71**, 3051 (1993).

[54] J. Hansson and F. Sandin, Phys. Lett. B. **616**, 1 (2005).

[55] E. G. Gimon and P. Hořava, Phys. Lett. B. **672**, 299 (2009).

[56] T. Regge and J. A. Wheeler, Phys. Rev. **108**, 1063 (1957).

[57] L. A. Edelstein and C. V. Vishveshwara, Phys. Rev. D **1**, 3514 (1970).

[58] M. D. Kruskal, Phys. Rev. **119**, 1743 (1960).

[59] G. Szekeres, Publ. Mat. Debrecen **7**, 285 (1960), [*Republished*] Gen. Rel. Grav. **34**, 11 (2002).

[60] C. V. Vishveshwara, Phys. Rev. D **1**, 2870 (1970).

[61] F. J. Zerilli, Phys. Rev. Lett., **24**, 737 (1970).

[62] S. Chandrasekhar, Proc. R. Soc. Lond. A **343**, 289 (1975).

[63] S. Chandrasekhar, *The Mathematical Theory of Black Holes*, (Clarendon Press, Oxford, 1983).

[64] V. Moncrief, Ann. Phys. **88**, 323 (1975).

[65] E. T. Newman and R. Penrose, J. Math. Phys. **3**, 566 (1962).

[66] J. M. Bardeen and W. H. Press, J. Math. Phys. **14**, 7 (1973).

[67] S. A. Teukolsky, Phys. Rev. Lett. **29**, 1114 (1972);
S. A. Teukolsky, Astrophys. J. **185**, 635 (1973).

[68] B. F. Whiting, J. Math. Phys. **30**, 1301 (1989).

[69] G. Dotti, R. J. Gleiser, I. F. Ranea-Sandoval, and H. Vucetich, Class. Quantum Grav. **25**, 245012 (2008).

[70] P. Pani, E. Barausse, E. Berti, and V. Cardoso, Phys. Rev. D **82**, 044009 (2010).

[71] K.-I. Nakao, P. S. Joshi, J.-Q. Guo, **P. Kocherlakota**, H. Tagoshi, T. Harada, M. Patil, and A. Królak, Phys. Lett. B **780**, 410 (2018).

[72] C. T. Cunningham, R. H. Price, and V. Moncrief, Astrophys. J. **224**, 643 (1978);
C. T. Cunningham, R. H. Price, and V. Moncrief, Astrophys. J. **230**, 870 (1979);
C. T. Cunningham, R. H. Price, and V. Moncrief, Astrophys. J. **236** 674 (1980).

[73] K. D. Kokkotas and B. G. Schmidt, Liv. Rev. Rel. **2**, 2 (1999).

[74] H.-P. Nollert, Class. Quantum Grav. **16**, 159 (1999).

[75] D. Bini, C. Cherubini, R. T. Jantzen, and B. Mashhoon, Phys. Rev. D **67**, 084013 (2003).

[76] E. Berti, V. Cardoso, and J. P. Lemos, Phys. Rev. D **70**, 124006 (2004).

[77] V. Cardoso, P. Pani, M. Cadoni, and M. Cavaglià, Class. Quantum Grav. **25**, 195010 (2008).

[78] S. Aretakis, Commun. Math. Phys. **307**, 17 (2011);
     S. Aretakis, Ann. Henri Poincare **8**, 1491 (2011).

[79] S. Aretakis, arXiv:1206.6598 [gr-qc].

[80] G. Z. Tóth, Class. Quantum Grav. **33**, 115012 (2016).

[81] G. D. Birkhoff, *Relativity and Modern Physics* (Harvard University Press, Cambridge, 1923).

[82] M. Sasaki and T. Nakamura, Gen. Rel. Grav. **22**, 12 (1990).

[83] M. Dafermos and I. Rodnianski, arXiv:1010.5132 [gr-qc].

[84] J. Lucietti and H. Reall, Phys. Rev. D **86**, 104030 (2012).

[85] K. Düztaş and I. Semiz, Phys. Rev. D **88**, 064043 (2013).

[86] M. Dafermos, I. Rodnianski, and Y. Shlapentokh-Rothman, arXiv:1402.7034 [gr-qc].

[87] K. Düztaş, Class. Quantum Grav. **32**, 075003 (2015).

[88] Y. Shlapentokh-Rothman, Ann. Henri Poincaré **16** , 289 (2015).

[89] J. Natário, L. Queimada, and R. Vicente, Class. Quantum Grav. **33**, 175002 (2016).

[90] M. Richartz, Phys. Rev. D **93**, 064062 (2016).

[91] M. Sasaki and T. Nakamura, Prog. Theor. Phys. **67**, 6 (1982).

[92] J. C. Miller and S. Motta, Class. Quantum Grav. **6**, 185 (1989).

[93] H.-J. Yo, T. W. Baumgarte, and S. L. Shapiro, Phys. Rev. D **66**, 084026 (2002).

[94] L. Baiotti, I. Hawke, P. J. Montero, F. Löffler, L. Rezzolla, N. Stergioulas, J. A. Font, and E. Seidel, Phys. Rev. D **71**, 024035 (2005).

[95] A. Nathanail, E. R. Most, and L. Rezzolla, Mon. Not. R. Aston. Soc. **469**, L31 (2017).

[96] D. Christodoulou, Commun. Math. Phys. **93**, 171 (1984).

[97] D. Christodoulou, Commun. Math. Phys. **105**, 337 (1986).

[98] S. L. Shapiro and S. A. Teukolsky, Phil. Trans. R. Soc. Lond. A **340**, 365 (1992).

[99] M. W. Choptuik, Phys. Rev. Lett. **70**, 9 (1993).

[100] D. Christodoulou, Ann. Math. **140**, 607 (1994).

[101] D. Christodoulou, Ann. Math. **149,** 183 (1999).

[102] T. Harada, H. Iguchi, and K.-I. Nakao, Prog. Theor. Phys. **107,** 449 (2002).

[103] T. Crisford and J. E. Santos, Phys. Rev. Lett. **118,** 181101 (2017).

[104] **P. Kocherlakota** and P. S. Joshi, Arab. J. Math. **8,** 315 (2019).

[105] A. D. Rendall, Living Rev. Relativ. **8,** 6 (2005).

[106] I. Rodnianski, Proc. ICM Madrid **3,** 421 (2006).

[107] H. Ringström, *The Cauchy problem in general relativity* (European Mathematical Society, Zürich, 2009).

[108] D. Christodoulou, *The formation of black holes in general relativity* (European Mathematical Society, Zürich, 2009).

[109] M. Dafermos and I. Rodnianski, Clay Math. Proc. **17,** 97 (2013).

[110] M. Dafermos, Proc. ICM Seoul **3,** 747 (2014).

[111] E. Hairer, C. Lubich, and G. Wanner, *Geometric Numerical Integration: Structure-Preserving Algorithms for Ordinary Differential Equations* (Springer, 2006)

[112] M. Dafermos, G. Holzegel, and I. Rodnianski, Acta Math. **222,** 1 (2019).

[113] P. S. Joshi, D. Malafarina, and R. Narayan, Class. Quantum Grav. **31,** 015002 (2014).

[114] D. Dey, **P. Kocherlakota**, and P. S. Joshi, arXiv:1907.12792 [gr-qc].

[115] S. S. Doeleman et al., Nature **455,** 78 (2008).

[116] S. S. Doeleman et al., Science **338,** 355 (2012).

[117] J. M. Bardeen, W. H. Press, and S. A. Teukolsky, Astrophys. J. **178,** 347 (1972).

[118] H. Falcke, F. Melia, and E. Agol, Science **338,** 355 (2000).

[119] J.-P. Luminet, Astron. Astrophys. **75,** 228 (1979).

[120] K. Akiyama et al., Astrophys. J. **875,** L1 (2019).

[121] R. Shaikh, **P. Kocherlakota**, R. Narayan, and P. S. Joshi, Mon. Not. R. Astron. Soc. **482,** 52 (2018).

[122] S. Gillessen, F. Eisenhauer, S. Trippe, T. Alexander, R. Genzel, F. Martin, and T. Ott, Astrophys. J. **692,** 1075 (2009).

[123] E. Eckart and R. Genzel, Mon. Not. R. Astron. Soc. **284,** 576 (1997).

[124] A. M. Ghez, B. L. Klein, M. Morris, and E. E. Becklin, Astrophys. J. **509,** 678 (1998).

[125] **P. Kocherlakota**, P. S. Joshi, S. Bhattacharyya, C. Chakraborty, A. Ray, and S. Biswas, Mon. Not. R. Astron. Soc. **490,** 3262 (2019).

[126] M. Kramer, D. C. Backer, J. M. Cordes, T. J. W. Lazio, B. W. Stappers, and S. Johnston, New Astron. Rev. **48,** 993 (2004).

[127] G. C. Bower et al., Astrophys. J. **798**, 2 (2015).

[128] R. P. Eatough et al., Nature **501**, 391 (2013).

[129] U.-L. Pen and A. E. Broderick, Mon. Not. R. Astron. Soc. **445**, 3370 (2014).

[130] W. B. Atwood et al., Astrophys. J. **697**, 2 (2009).

[131] R. Braun, T. L. Bourke, J. A. Green, E. F. Keane, and J. Wagg, Proc. Science **215**, 40 (2014).

[132] S. Konar et al., J. Astrophys. Astron. **37**, 36 (2016).

[133] R. Nan, Sci. China G **49**, 129 (2006).

[134] R. Nan et al., Int. J. Mod. Phys. D **20**, 989 (2011).

[135] B. P. Abbott et al., Phys. Rev. Lett. **116**, 061102 (2016).

[136] T. Accadia et al., J. Inst. **7**, P03012 (2012).

[137] P. Amaro-Seoane, J. R. Gair, M. Freitag, M. C. Miller, I. Mandel, C. J. Cutler, and S. Babak, Class. Quantum Grav. **24**, R113 (2007).

[138] D. Singh, K. Wu, and G. E. Sarty, Mon. Not. R. Astron. Soc. **441**, 800 (2014).

[139] W. de Sitter, Mon. Not. R. Astron. Soc. **77**, 155 (1916).

[140] J. Lense and H. Thirring, Phys. Z **19**, 156 (1918), [*English translation*] B. Mashhoon, F. W. Hehl, and D. S. Theiss, Gen. Rel. Grav. **16**, 711 (1984).

[141] D. R. Brill and D. Goel, Am. J. Phys. **67**, 4 (1999).

[142] J. M. Bardeen and J. A. Petterson, Astrophys. J. **195**, L65 (1975).

[143] C. Chakraborty and S. Bhattacharyya, Mon. Not. R. Astron. Soc. **469**, 3062 (2017).

[144] S. Banerjee, C. Chakraborty, and S. Bhattacharyya, Astrophys. J. **870**, 95 (2019).

[145] M. Kramer, Astrophys. J. **509**, 2 (1998).

[146] J. M. Weisberg and J. H. Taylor, Astrophys. J. **576**, 2 (2002).

[147] E. Fermi, Atti. Accad. Naz. Lincei Cl. Sci. Fis. Mat. Nat. **31**, 184 (1922).

[148] A. Walker, Proc. Edinb. Math. Soc. **4**, 170 (1935).

[149] I. Ciufolini and J. A. Wheeler, *Gravitation and Inertia* (Princeton University Press, Princeton, 1995).

[150] K. Sakina and J. Chiba, Phys. Rev. D **19**, 2280 (1979).

[151] B. R. Iyer and C. V. Vishveshwara, Phys. Rev. D **48**, 5706 (1993).

[152] E. Barausse, E. Racine, and A. Buonanno, Phys. Rev. D **80**, 104025 (2009), [*Erratum*] Phys. Rev. D **85**, 069904 (E) (2012).

[153] D. Bini, A. Geralico, and R. T. Jantzen, Phys. Rev. D **95**, 124022 (2017).

[154] T. Damour, P. Jaranowski, and G. Schaefer, Phys. Rev. D **77**, 064032 (2008).

[155] B. Mashhoon, F. Gronwald, and H. I. M. Lichtenegger, Lect. Notes Phys. **562**, 83 (2001).

[156] S. J. Clark and R. W. Tucker, Class. Quantum Grav. **17**, 4125 (2000).

[157] J. Natário, Gen. Rel. Grav. **39**, 1477 (2007).

[158] L. I. Schiff, Phys. Rev. Lett. **4**, 215 (1960);
L. I. Schiff, Proc. Nat Acad. Sci. **46**, 871 (1960).

[159] C. W. F. Everitt et al., Class. Quantum Grav. **32**, 224001 (2015).

[160] I. H. Stairs, A. G. Lyne, and S. L. Shemar, Nature **406**, 484 (2000).

[161] T. Clifton and J. M. Weisberg, Astrophys. J. **679**, 687 (2008).

[162] I. H. Stairs, S. E. Thorsett, and Z. Arzoumanian, Phys. Rev. Lett. **93**, 141101 (2004).

[163] D. Bini, A. Geralico, and R. T. Jantzen, Phys. Rev. D **94**, 124002 (2016).

Chapter 2: Stability in General Relativity

[164] M. Blau, Lecture Notes on General Relativity (unpublished).

[165] S. Deser and Y. Choquet-Bruhat, Ann. Phys. **81**, 165 (1973).

[166] D. Christodoulou and S. Klainerman, *The Global Nonlinear Stability of the Minkowski Space* (Princeton University Press, New Jersey 1993).

[167] S. M. Carroll, *Spacetime and Geometry: An Introduction to General Relativity* (Addison-Wesley, 2003).

[168] É. É. Flanagan and S. A. Hughes, New J. Phys. **7**, 204 (2005).

[169] C. M. Hirata, Lecture Notes on Linearized Gravity (unpublished).

[170] R. Penrose and W. Rindler, *Spinors and Space-Time* (Cambridge University Press, Cambridge, 1984).

[171] B. Schutz, *A First Course in General Relativity* (Cambridge University Press, Cambridge, 2009).

[172] N. Straumann, *General Relativity with Applications to Astrophysics* (Springer, Berlin, 2009).

[173] M. Fierz and W. Pauli, Proc. R. Soc. Lond. A **173**, 211 (1939).

[174] E. Atlas, arXiv:1808.04722 [hep-th].

[175] A. E. Fischer and J. E. Marsden, Bull. Amer. Math. Soc. **79**, 997 (1973).

[176] J. E. Marsden, *Lectures on geometric methods in mathematical physics* (SIAM, 1981).

[177] J. Girbau and L. Bruna, *Stability by linearization of Einstein's field equation* (Springer, New York, 2010).

[178] R. d'Inverno, *Introducing Einstein's Relativity* (Oxford University Press, 1992).

[179] F. J. Zerilli, Phys. Rev. D **2**, 2141 (1970).

[180] L. Rezzolla, ICTP Lect. Notes Ser. **14**, 255 (2003).

[181] K. S. Thorne, Rev. Mod. Phys. **52**, 299 (1980).

[182] A. Nagar and L. Rezzolla, Class. Quantum Grav. **22**, R167 (2005).

[183] N. Andersson and B. P. Jensen, arXiv:gr-qc/0011025.

[184] R. M. Wald, J. Math. Phys. **20**, 1056 (1979).

[185] B. F. Schutz and C. M. Will, Astrophys. J. **291**, L33 (1985).

[186] E. W. Leaver, Proc. R. Soc. Lond. A **402**, 384 (1986).

[187] H. T. Cho, Phys. Rev. D **68**, 024003 (2003).

[188] R. H. Boyer and R. W. Lindquist, J. Math. Phys. **8**, 265 (1967).

[189] R. C. Henry, Astrophys. J. **535**, 350 (2000).

[190] B. Carter, Commun. Math. Phys. **10**, 280 (1968).

[191] D. R. Brill, P. L. Chrzanowski, C. M. Pereira, E. D. Fackerell, and J. B. Ipser, Phys. Rev. D **5**, 1913 (1972).

[192] W. Kinnersley, J. Math. Phys. **10**, 1195 (1969).

[193] G. Dotti, R. Gleiser, and J. Pullin, Phys. Lett. B **644**, 289 (2007).

[194] G. T. Horowitz and A. Sen, Phys. Rev. D **53**, 808 (1996).

[195] E. K. Boyda, S. Ganguli, P. Hořava, and U. Varadarajan, Phys. Rev. D **67**, 106003 (2003).

[196] H. Elvang, R. Emparan, D. Mateos, and H. S. Reall, Phys. Rev. Lett. **93**, 211302 (2004).

[197] D. Rasheed, Nuc. Phys. B **454**, 379 (1995).

[198] J. C. Breckenridge, R. C. Myers, A. W. Peet, and C. Vafa, Phys. Lett. B **391**, 93 (1997).

[199] E. G. Gimon and P. Hořava, arXiv:hep-th/0405019.

[200] D. L. Wiltshire, M. Visser, and S. M. Scott, *The Kerr Spacetime: Rotating Black Holes in General Relativity* (Cambridge University Press, Cambridge, 2009).

[201] J. Abedi and N. Ashfordi, J. Cosmol. Astropart. Phys. **11**, 10 (2019).

[202] Q. Wang, N. Oshita, and N. Ashfordi, Phys. Rev. D **101**, 024031 (2020).

[203] S. Detweiler, Astrophys. J. **239**, 292 (1980).

[204] V. Cardoso, Phys. Rev. D **70**, 127502 (2004).

[205] S. A. Teukolsky and W. H. Press, Astrophys. J. **193**, 443 (1974).

[206] A. A. Starobinski and S. M. Churilov, J. Exp. Theor. Phys. **38**, 1 (1974).

[207] M. Henneaux and C. Teitelboim, *Quantization of Gauge Systems* (Princeton University Press, New Jersey, 1992).

[208] Y. Fourès-Bruhat, Acta Mathematica **88**, 141 (1952); [English Translation] G. Esposito, Preprint 480, Max Planck Institute for the History of Science (2016).

[209] Y. Bruhat, in *Gravitation: an introduction to current research, 1962* (Wiley, New York, 1962) p. 130.

[210] Y. Choquet-Bruhat and R. P. Geroch, Commun. Math. Phys. **14**, 329 (1969).

[211] R. P. Geroch, J. Math. Phys. **11**, 437 (1970).

[212] P. S. Joshi and D. Malafarina, Int. J. Mod. Phys. D **20**, 2641 (2011).

[213] P. S. Joshi and D. Malafarina, Phys. Rev. D. **83**, 024009 (2011).

[214] P. S. Joshi and D. Malafarina, Class. Quantum Grav. **32**, 145004 (2015).

[215] P. Szekeres, Commun. Math. Phys. **41**, 55 (1975).

[216] C. W. Misner and D. H. Sharp, Phys. Rev. **136**, 2B (1964).

[217] M. E. Cahill and G. C. McVittie, J. Math. Phys. **11**, 1382 (1970).

[218] E. Poisson, *A Relativist's Toolkit* (Cambridge University Press, Cambridge, 2004).

[219] P. S. Joshi and T. P. Singh, Phys. Rev. D **51**, 6778 (1995).

[220] R. Abraham and J. E. Marsden, *Foundations of Mechanics* (Benjamin, New York, 1978).

[221] V. I. Arnol'd, *Mathematical Methods of Classical Mechanics* (Springer, New York, 1980).

[222] R. Bryant, in *Geometry and Quantum Field Theory, Park City, 1991*, p. 7.

[223] J. V. Jośe and E. J. Saletan, *Classical Dynamics* (Cambridge University Press, Cambridge, 1998).

[224] J. E. Marsden and T. S. Ratiu, *Introduction to Mechanics and Symmetry* (Springer, New York, 1999).

[225] T. Frankel, *The Geometry of Physics* (Cambridge University Press, Cambridge, 2001).

[226] S. Farantos, *Nonlinear Hamiltonian Mechanics Applied to Molecular Dynamics* (Springer, London, 2014).

[227] T. M. Apostol, *Mathematical Analysis: A Modern Approach to Advanced Calculus* (Addison-Wesley, Boston, 1974).

[228] J. Struckmeier and C. Riedel, Phys. Rev. Lett. **85**, 3830 (2000).

[229] J. Struckmeier, J. Phys. A: Math. Gen. **38**, 1257 (2005).

[230] C. R. de Oliveira, Rev. Bras. Ens. Fis. **21**, 22 (1999).

[231] A. N. Kolmogorov, Dokl. Akad. Nauk. SSR **98**, 527 (1954); [English Translation] H. Dahlby, Lecture Notes in Physics **93**, 5 (1979).

[232] J. K. Moser, Nach. Akad. Wiss. Göttingen, Math. Phys. Kl. II **1**, 1 (1962).

[233] V. I. Arnol'd, Russian Math. Survey **18**, 13 (1963).

[234] V. I. Arnol'd, Russian Math. Survey **18**, 85 (1963).

[235] J. K. Moser, *Stable and random motions in dynamical systems* (Princeton University Press, New Jersey, 1974).

[236] V. E. Arnold, V. V. Kozlov, and A. I. Neishtadt, *Mathematical Aspects of Classical and Celestial Mechanics* (Springer, New York, 2006).

[237] K. J. Whiteman, Rep. Prog. Phys. **40**, 1033 (1977).

[238] M. Bruni, S. Matarrese, S. Mollerach, and S. Sonego, Class. Quantum Grav. **14**, 2585 (1997).

[239] C. Dettmann, Lecture Notes on Global dynamics (unpublished).

[240] T. M. Cherry, Phil. Trans. R. Soc. A **227**, 137 (1926).

[241] J. Milnor, Commun. Math. Phys. **99**, 177 (1985); [Erratum] Commun. Math. Phys. **102**, 517 (1985).

[242] J. Auslander, N. P. Bhatia, and P. Seibert, Bol. Soc. Mat. Mex. **9**, 55 (1964).

[243] E. Coddington and N. Levinson, *Theory of ordinary differential equations* (McGraw-Hill, New York, 1955).

[244] P. Mendelson, Bol. Soc. Mat. Mex. **5**, 270 (1960).

[245] A. Ashtekar and G. T. Horowitz, J. Math. Phys. **25**, 1473 (1984).

[246] E. Witten, arXiv:1901.03928 [hep-th].

[247] C. Crnković, Class. Quant. Grav. **5**, 1557 (1988).

[248] R. Arnowitt, S. Deser, and C. W. Misner, in *Gravitation: an introduction to current research, 1962* (Wiley, New York, 1962) p. 227; [Republished] Gen. Relativ. Gravit. **40**, 1997 (2008).

[249] J. L. Friedman, Commun. Math. Phys. **63**, 243 (1978).

[250] N. Comins and B. F. Schutz, Proc. R. Soc. Lond. A **364**, 211 (1978).

[251] S. Inglima, M.Sc. Thesis, Imperial College London (2012).

[252] G. Rosensteel and D. J. Rowe, Phys. Rev. Lett. **46**, 1119 (1981).

[253] A. Weinstein, Bulletin of the AMS **5**, 1 (1981).

[254] M. Atiyah, R. Dijkgraaf, and N. Hitchin, Phil. Trans. R. Soc. A **368**, 913 (2010).

[255] J. C. Baez, A. E. Hoffnung, and C. L. Rogers, Commun. Math. Phys. **293**, 701 (2010).

[256] M. J. Betancourt, S. Byrne, S. Livingstone, and M. Girolami, arXiv:1410.5110 [stat.ME] (2014).

[257] H.-B. Xie , T. Guo , B. Sivakumar , A. W.-C. Liew, and S. Dokos, Proc. R. Soc. A **470**, 20140409 (2014).

Chapter 3: Shadows and Images of Spherically Symmetric Black Holes and Naked Singularities

[258] W. L. Ames and K. S. Thorne, Astrophys. J. **151**, 659 (1968).

[259] C. T. Cunningham and J. M. Bardeen, Astrophys. J. **183**, 237 (1973).

[260] J. L. Synge, Mon. Not. R. Astron. Soc. **131**, 463 (1966).

[261] A. F. Zakharov, Phys. Rev. D **90**, 062007 (2014).

[262] R. Takahashi, Astrophys. J. **611**, 996 (2004).

[263] K. Hioki and K. Maeda, Phys. Rev. D **80**, 024042 (2009).

[264] R. Takahashi, Publ. Astron. Soc. Jpn. **57**, 273 (2005).

[265] A. de Vries, Class. Quantum Grav. **17**, 123 (2000).

[266] P. J. Young, Phys. Rev. D **14**, 3281 (1976).

[267] A. Yumoto, D. Nitta, T. Chiba, and N. Sugiyama, Phys. Rev. D **86**, 103001 (2012).

[268] J. O. Shipley and S. R. Dolan, Class. Quantum Grav. **33**, 175001 (2016).

[269] L. Huang, M. Cai, Z.-Q. Shen, and F. Yuan, Mon. Not. R. Astron. Soc. **379**, 833 (2007).

[270] A. B. Kamruddin and J. Dexter, Mon. Not. R. Astron. Soc. **434**, 765 (2013).

[271] T. Lacroix and J. Silk, Astron. Astrophys. **554**, A36 (2013).

[272] S. Schneider and V. Perlick, Gen. Rel. Grav. **50**, 58 (2018).

[273] K.-I. Nakao, N. Kobayashi, and H. Ishihara, Phys. Rev. D **67**, 084002 (2003).

[274] L. Kong, D. Malafarina, and C. Bambi, Eur. Phys. J. C **74**, 2983 (2014).

[275] N. Ortiz, O. Sarbach, and T. Zannias, Class. Quantum Grav. **32**, 247001 (2015).

[276] N. Ortiz, O. Sarbach, and T. Zannias, Phys. Rev. D **92**, 044035 (2015).

[277] K. S. Virbhadra and C. R. Keeton, Phys. Rev. D **77**, 124014 (2008).

[278] K. S. Virbhadra and G. F. R. Ellis, Phys. Rev. D **65**, 103004 (2002).

[279] C. Bambi and K. Freese, Phys. Rev. D **79**, 043002 (2009).

[280] A. E. Broderick and R. Narayan, Astrophys. J. **638**, L21 (2006).

[281] H. Saida, A. Fujisawa, C. Yoo, and Y. Nambu, Prog. of Theor. Exp. Phys. **2016**, 043E02 (2016).

[282] N. Sakai, H. Saida, and T. Tamaki, Phys. Rev. D **90**, 104013 (2014).

[283] M. Visser and D. L. Wiltshire, Class. Quantum Grav. **21**, 1135 (2004)

[284] C. Bambi, Phys. Rev. D **87**, 107501 (2013).

[285] T. Ohgami and N. Sakai Phys. Rev. D **91**, 124020 (2015).

[286] T. Ohgami and N. Sakai Phys. Rev. D **94**, 064071 (2016).

[287] R. Shaikh, Phys. Rev. D **98**, 024044 (2018).

[288] R. C. Tolman, *Relativity, Thermodynamics and Cosmology* (Clarendon Press, Oxford, 1934).

[289] J. R. Oppenheimer and G. M. Volkoff, Phys. Rev. **55**, 374 (1939).

[290] C. B. M. H. Chirenti and L. Rezzolla, Class. Quantum Grav. **24**, 4191 (2007).

[291] P. Pani and V. Ferrari, Class. Quantum Grav. **35**, 15LT01 (2018).

[292] S. Sahu, M. Patil, D. Narasimha, and P. S. Joshi, Phys. Rev. D **86**, 063010 (2012).

[293] H. C. Ohanian, Am. J. Phys. **55**, 428 (1987).

[294] V. Bozza, Phys. Rev. D **66**, 103001 (2002).

[295] M. Jaroszynski and A. Kurpiewski, Astron. Astrophys. **326**, 419 (1997).

[296] H. Bondi, Mon. Not. R. Astron. Soc. **112**, 195 (1952).

[297] R. Narayan, Y. Zhu, D. Psaltis, and A. Sadowski, Mon. Not. R. Astron. Soc. **457**, 608 (2016).

[298] Y. Zhu, R. Narayan, A. Sadowski, and D. Psaltis, Mon. Not. R. Astron. Soc. **451**, 1661 (2015).

[299] R. Narayan, A. Sadowski, and R. Soria, Mon. Not. R. Astron. Soc. **469**, 2997 (2017).

[300] F. Yuan and R. Narayan, Ann. Rev. Astron. Astrophys. **52**, 529 (2014).

Chapter 4: Gravitomagnetism near Black Holes and its effect on Pulsars

[301] D. R. Lorimer, Liv. Rev. Rel. **11**, 8 (2008).

[302] A. W. Steiner, J. M. Lattimer, and E. F. Brown, Astrophys. J. **722**, 33 (2010).

[303] J. M. Lattimer, Astrophys. Space Sci. **336**, 67 (2011).

[304] B. M. Barker and R. F. O'Connell, Gen. Rel. Grav. **11**, 149 (1979).

[305] R. Wald, Phys. Rev. D **6**, 406 (1972).

[306] M. Mathisson, Acta Phys. Pol. **6**, 167 (1937).

[307] A. Papapetrou, Proc. R. Soc. Lond. **209**, 248 (1951).

[308] W. G. Dixon, Phil. Trans. R. Soc. A **277**, 59 (1974).

[309] K. J. Li, K. Wu, and D. Singh, Mon. Not. R. Astron. Soc. **485**, 1053 (2019).

[310] J. Ehlers and R. Geroch, Ann. Phys. **309**, 232 (2004).

[311] C. Chakraborty, **P. Kocherlakota**, and P. S. Joshi, Phys. Rev. D **95**, 044006 (2017).

[312] C. Chakraborty, **P. Kocherlakota**, M. Patil, S. Bhattacharyya, P. S. Joshi, and A. Królak, Phys. Rev. D **95**, 084024 (2017).

[313] K. Kyrian and O. Semerák, Mon. Not. R. Astron. Soc. **382**, 1922 (2007).

[314] C. Møller, Commun. Dublin Inst. Adv. Studies A **5**, 3 (1949).

[315] F. A. E. Pirani, Acta Phys. Pol. **15**, 389 (1956), [*Republished*] Gen. Rel. Grav. **41**, 1215 (2009).

[316] O. Semerák, Mon. Not. R. Astron. Soc. **308**, 863 (1999).

[317] L. F. O. Costa, J. Natário, and M. Zilhão, Phys. Rev. D **93**, 104006 (2016).

[318] D. Bini, F. de Felice, and R. T. Jantzen, Class. Quantum Grav. **16**, 6 (1999).

[319] M. De Laurentis, Z. Younsi, O. Porth, Y.,Mizuno, and L. Rezzolla, Phys. Rev. D **97**, 104024 (2018).

[320] G. A. González and F. López-Suspes, arXiv:1104.0346 [gr-qc].

[321] D. Bini, R. T. Jantzen, and A. Merloni, Class. Quantum Grav. **16**, 4 (1999).

[322] K. R. Nayak and C. V. Vishveshwara, Class. Quantum Grav. **13**, 7 (1996).

[323] H. Goldstein, *Classical Mechanics* (Addison-Wesley, Reading, 1980).

[324] A. S. Besicovitch, *Almost periodic functions* (Cambridge University Press, Cambridge, 1932).

[325] H. Bohr, *Almost-periodic functions* (Chelsea Publishing Company, Chelsea, 1947).

[326] A. Herrera-Aguilar and U. Nucamendi, Phys. Rev. D **92**, 045024 (2015).

[327] J. E. Greene and L. C. Ho, Astrophys. J. **670**, 92 (2007).

[328] N. Lützgendorf et al., Astron. Astrophys. **555**, A26 (2013).

[329] B. B. P. Perera et al., Mon. Not. R. Astron. Soc. **468**, 2114 (2017).

[330] M. Mapelli, Mon. Not. R. Astron. Soc. **376**, 1317 (2007).

[331] S. Mieske, M. J. Frank, H. Baumgardt, N. Lützgendorf, N. Neumayer, and M. Hilker, Astron. Astrophys. **558**, A14 (2013).

[332] N. Thatte, M. Tecza, and R. Genzel, Astron. Astrophys. **364**, L47 (2000).

[333] R. N. Manchester, A. G. Lyne, C. Robinson, N. D'Amico, M. Bailes, and J. Lim, Nature **352**, 219 (1991).

[334] S. M. Ransom, J. W. T. Hessels, I. H. Stairs, P. C. C. Freire, F. Camilo, V. M. Kaspi, and D. L. Kaplan, Science **307**, 892 (2005).

[335] C. Y. Hui, K. S. Cheng, and R. E. Taam, Astrophys. J. **714**, 1149 (2010).

[336] Z. Pan, G. Hobbs, D. Li, A. Ridolfi, P. Wang, and P. C. C. Freire, Mon. Not. R. Astron. Soc. **459**, L26 (2016).

[337] B. Devecchi, M. Colpi, M. Mapelli, and A. Possenti, Mon. Not. R. Astron. Soc. **380**, 691 (2007).

[338] D. Clausen, S. Sigurdsson, and D. F. Chernoff, Mon. Not. R. Astron. Soc. **442**, 207 (2014).

[339] F. Verbunt and P. C. C. Freire, Astron. Astrophys. **561**, A11 (2014).

[340] J. D. Biggs, M. Bailes, A. G. Lyne, W. M. Goss, and A. S. Fruchter, Mon. Not. R. Astron. Soc. **267**, 125 (1994).

[341] P. C. C. Freire, S. M. Ransom, S. Bé gin, I. H. Stairs, J. W. T. Hessels, L. H. Frey, and F. Camilo, Astrophys. J. **675**, 670 (2008).

[342] E. Rubio-Herrera and T. Maccarone, Proc. IAU **8**, 111 (2012).

[343] J. Kormendy and D. Richstone, Ann. Rev. Astron. Astrophys. **33**, 581 (1995).

[344] B. M. Peterson and K. Horne, Astron. Nachr. **3**, 248 (2004).

[345] T. Xiao, A. J. Barth, J. E. Greene, L. C. Ho, M. C. Bentz, R. R. Ludwig, and Y. Jiang, Astrophys. J. **739**, 28 (2011).

[346] R. C. E. van den Bosch, K. Gebhardt, K. Gültekin, G. van den Ven, A. ven der Wel, and J. L. Walsh, Nature **491**, 729 (2012).

[347] E. Pfahl and A. Loeb, Astrophys. J. **615**, 253 (2004).

[348] R. S. Wharton, S. Chatterjee, J. M. Cordes, J. S. Deneva, and T. J. W. Lazio, Astrophys. J. **753**, 108 (2012).

[349] F. Zhang, Y. Lu, and Q. Yu, Astrophys. J. **784,** 106 (2014).

[350] D. Merritt, T. Alexander, S. Mikkola, and C. M. Will, Phys. Rev. D **84**, 044024 (2011).

[351] M. C. Miller, M. Frietag, D. P. Hamilton, and V. M. Lauburg, Astrophys. J. **631**, L117 (2005).

[352] B. Kocsis, A. Ray, and S. P. Zwart, Astrophys. J. **752**, 67 (2012)

[353] A. Ray, B. Kocsis, and S. P. Zwart, Proc. IAU **9**, 419 (2013).

[354] S. Bhattacharyya, I. Bombaci, D. Logoteta, and A. V. Thampan, Mon. Not. R. Astron. Soc. **457**, 3101 (2016).

[355] J. W. T. Hessels, S. M. Ransom, I. H. Stairs, P. C. C. Freire, V. M. Kaspi, and F. Camilo, Science **311**, 1901 (2006).

[356] D. R. Lorimer and M. Kramer, *Handbook of Pulsar Astronomy* (Cambridge University Press, Cambridge, 2005).

[357] J. Middleditch and J. Kristian, Astrophys. J. **279**, 157 (1984).

[358] P. Rana and A. Mangalam, Class. Quantum Grav. **36**, 045009 (2019).

[359] Z. Li and C. Bambi, J. Cosmol. Astropart. Phys. **2013**, 031 (2013).

[360] K. R. Nayak and C. V. Vishveshwara, Gen. Rel. Grav. **30**, 593 (1998).

Appendix A

Conversions between Frames[1]

We discuss here the conversions between the various frames that we have introduced. $e_{\hat{a}}, e_{\hat{b}}$ denote elements of the Frenet-Serret basis associated with static Killing observers in the Kerr and adapted-Kerr spacetimes respectively, and $e_{\mu}, e_{\bar{\nu}}$ are elements of the Boyer-Lindquist and adapted-Boyer-Lindquist coordinate basis respectively.

We already know the Jacobian J for the coordinate transformation that transforms elements of the BL coordinate basis to their counterparts in the adapted-BL coordinate bases, $e_{\mu} \rightarrow e_{\bar{\nu}}$ (4.3.13),

$$e_{\bar{\nu}} = \left(J^{-1}\right)^{\mu}_{\bar{\nu}} e_{\mu}. \tag{A.0.1}$$

Let us now define P_1 to be the projection matrix that projects vectors defined in the BL coordinate basis onto the FS tetrad associated with Kerr static observers and P_2 to be the projection matrix that projects vectors defined in the adapted-BL coordinate basis onto the FS tetrad associated with adapted-Kerr static observers, that is,

$$e_{\hat{a}} = (P_1)^{\mu}_{\hat{a}} e_{\mu}, \tag{A.0.2}$$
$$e_{\hat{b}} = (P_2)^{\bar{\nu}}_{\hat{b}} e_{\bar{\nu}}.$$

Then, the entries of P_2 can be read off from (4.3.17) to be,

$$(P_2)^{\bar{\nu}}_{\hat{b}} = \begin{bmatrix} \frac{1}{\sqrt{-g_{\bar{0}\bar{0}}}} & 0 & 0 & 0 \\ 0 & \frac{g_{\bar{0}\bar{0},1}}{2\bar{\kappa}g_{\bar{0}\bar{0}}g_{11}} & \frac{g_{\bar{0}\bar{0},2}}{2\bar{\kappa}g_{\bar{0}\bar{0}}g_{22}} & 0 \\ -\frac{g_{\bar{0}\bar{3}}}{\sqrt{g_{\bar{0}\bar{0}}\Delta_{03}}} & 0 & 0 & \sqrt{\frac{g_{\bar{0}\bar{0}}}{\Delta_{03}}} \\ 0 & \frac{g_{\bar{0}\bar{0},2}}{2\bar{\kappa}g_{\bar{0}\bar{0}}\sqrt{g_{11}g_{22}}} & -\frac{g_{\bar{0}\bar{0},1}}{2\bar{\kappa}g_{\bar{0}\bar{0}}\sqrt{g_{11}g_{22}}} & 0 \end{bmatrix}.$$

Similarly, P_1 is obtained simply by replacing the barred metric components in the above by the unbarred Kerr metric components. Then the conversion between the FS tetrads associated with static Killing observers in

the Kerr and adapted-Kerr metrics is given as,

$$e_{\hat{b}} = (P_2)_{\hat{b}}^{\bar{\nu}} \left(J^{-1}\right)_{\bar{\nu}}^{\mu} \left(P_1^{-1}\right)_{\mu}^{\hat{a}} e_{\hat{a}}, \tag{A.0.3}$$

Let us denote the conversion matrix in the above succinctly as Q, i.e.,

$$Q_{\hat{b}}^{\hat{a}} = (P_2)_{\hat{b}}^{\bar{\nu}} \left(J^{-1}\right)_{\bar{\nu}}^{\mu} \left(P_1^{-1}\right)_{\mu}^{\hat{a}}. \tag{A.0.4}$$

Appendix B

Distinguishing Near-Extremal Kerr Naked Singularities from other Compact Objects[1]

In §4.4, we discussed how the spin-precession frequency, in the case of a BH, becomes arbitrarily large at the horizon for all values of q barring $q \sim 0.5$. For a NS, it diverges only near the ring singularity $r = 0, \theta = \pi/2$ and remains finite even for $r = 0$ for $0 < \theta \lesssim \pi/2$. We pointed out that this can be used to distinguish a BH from a NS. Further, from figure 4.6, a general feature that emerges is that with increase in a/M, the radial profile of Ω_p becomes increasingly 'smoother.' This motivates us to use the 'sharp' features that appear for naked singularities with $1 \lesssim a/M$ to separate them from those with $1 \ll a/M$. Indeed, we find that this is possible and devote this section to highlighting these aspects.

We lay emphasis on this study because of the importance of near extremal naked singularities in general relativity. For example, in a black hole binary collision, like the one studied by LIGO recently, the angular momentum of the compact object during the collision could temporarily exceed the Kerr bound and result in a temporary near-extremal naked singularity. Further, if a thick accretion disc could spin up a near-extremal black hole, it would likely form a near-extremal naked singularity due to its proximity to the black hole geometry in the $a - M$ parameter space. We mention in relation to this point that using the Polish doughnut model (although not for Kerr spacetime in particular), it was shown in [359] that overspinning compact objects can be generated by thick accretion discs.

The radial variation of the modulus of the spin-precession frequency for all q, at $\theta \sim 0^0$ is smooth, as can be seen from figure B.1 and figure B.2. For an observer moving with an angular velocity that is not close to the ZAMO frequency ($q \nleftrightarrow 0.5$), a clear maxima-minima pair appear around $r = 1$ resulting in a sharp drop/rise in Ω_p at that radius, as can be seen from panels (a) and (e) of figure B.1. The event horizon of an extremal black hole $a/M = 1$ is located at $r = 1$ and we link this sharp feature to this observation. We will discuss this in some more detail in the following subsection. Roughly, however, the reason for these sharp features is as follows. From equation 4.4.1, we see that Δ appears in the denominator. We know that $\Delta = 0$ marks the

---

(a) $a/M = 1.0001, q = 0.3$ ($\Omega < $)

(b) $a/M = 1.01, q = 0.3$ ($\Omega < $)

(c) $a/M = 1.0001, q = 0.5$ ($\Omega = $)

(d) $a/M = 1.01, q = 0.5$ ($\Omega = $)

(e) $a/M = 1.0001, q = 0.7$ ($\Omega > $)

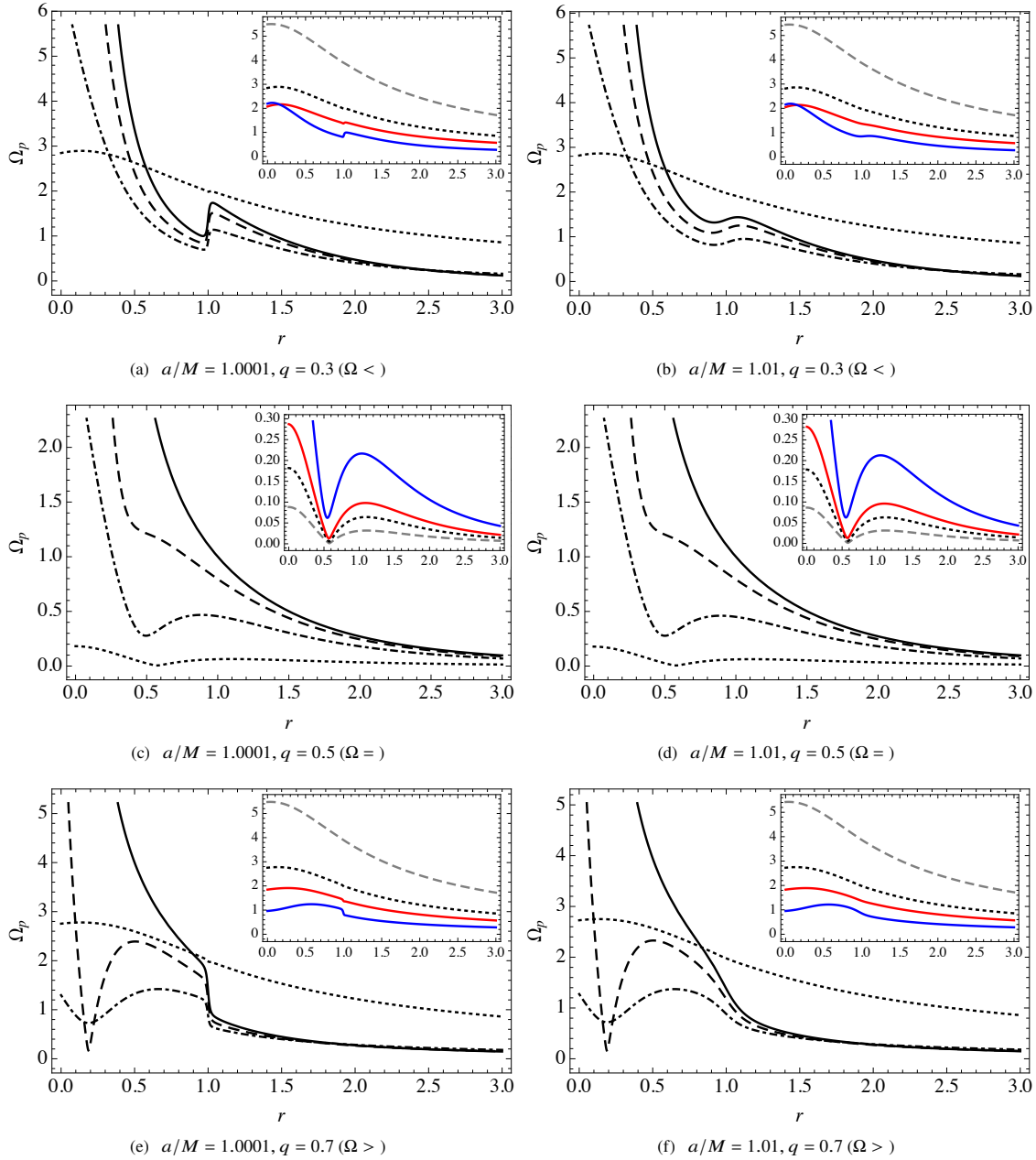(f) $a/M = 1.01, q = 0.7$ ($\Omega > $)

FIGURE B.1: The modulus of the spin-precession frequency $\Omega_{\rm p}$ (in M^{-1}) versus r (in M) has been plotted for near-extremal naked singularities with two different a/M for different q, θ. We have used $a/M = 1.0001, 1.01$ in the plots in the left and right columns and $q = 0.3, 0.5, 0.7$ in the top, middle and bottom rows, which are representative of $\Omega < \Omega_Z, \Omega = \Omega_Z$ and $\Omega > \Omega_Z$ respectively. In each panel, the black dotted, dot-dashed, dashed and regular lines represent $\theta = 10^0, 50^0, 70^0, 90^0$ respectively. This plot shows that for all q, at $\theta \sim 0^0$, the radial variation of $\Omega_{\rm p}$ is smooth. From panels (a),(e), for $\Omega \nsim$, a clear maxima-minima pair appears around $r = 1$ resulting in a sharp drop/rise in $\Omega_{\rm p}$ at that radius. The event horizon of an extremal black hole $a/M = 1$ is located at $r = 1$ and we link this sharp feature to this observation. At $\Omega = \Omega_Z$ itself $\Omega_{\rm p}$ is smooth, devoid of this particular feature. We discuss $\Omega \sim \Omega_Z$ in the next figure since these q values have richer features. As can be seen from panels (b),(f), this sharp rise/drop in $\Omega_{\rm p}$ gets smoother with increasing a/M. By $a/M \sim 1.1$, these features completely vanish and we interpret this feature as providing an important criterion based on which one can distinguish a near-extremal NS ($1 < a/M < 1.1$) from one with a higher spin. In the inset, we display approximately at what angle θ this sharp $r = 1$ feature starts to appear from and we have used $\theta = 5^0, 10^0, 15^0, 30^0$ for the gray dashed, black dotted (same as the main panel), red and blue lines respectively.

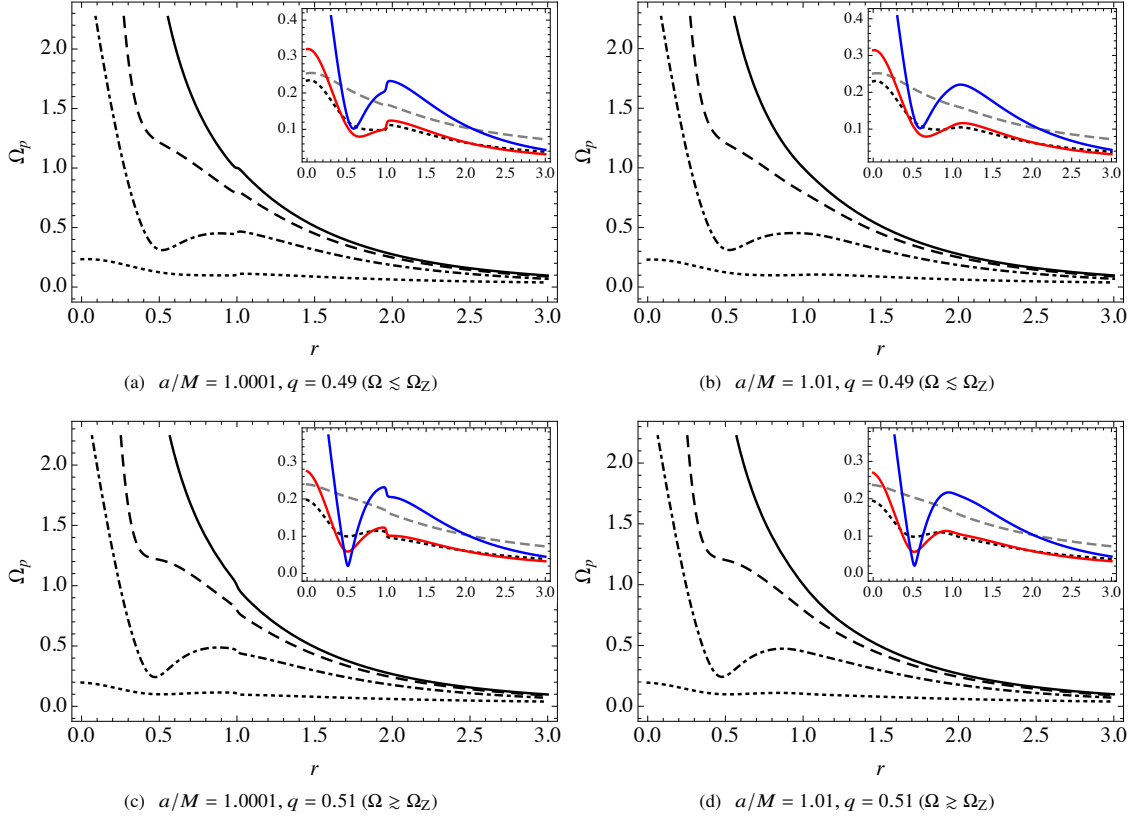(a) $a/M = 1.0001$, $q = 0.49$ ($\Omega \lesssim \Omega_Z$)

(b) $a/M = 1.01$, $q = 0.49$ ($\Omega \lesssim \Omega_Z$)

(c) $a/M = 1.0001$, $q = 0.51$ ($\Omega \gtrsim \Omega_Z$)

(d) $a/M = 1.01$, $q = 0.51$ ($\Omega \gtrsim \Omega_Z$)

FIGURE B.2: We plot now Ω_p (in M^{-1}) vs r (in M) for near-extremal naked singularities with $a/M = 1.0001$ and 1.01 at different θ, for $q \sim .5$ ($q \neq .5$). The line styles are the same as figure B.1 and the insets in this figure demonstrate that for these values of q, that is q close to .5 but not equal to, there are richer features at smaller angles θ. It can be seen from this figure, as was from figure B.1, that with increase in a/M, these features all get smoothed out.

location of the horizon for $a/M \leq 1$ and specifically, because of this, for $a/M = 1$, Ω_p exhibits a divergence at $r = 1$. This divergence is avoided for $a/M \gtrsim 1$ since $\Delta \neq 0$ but Δ changes only slightly from 0 and hence we see a sharp change at $r \sim 1$. The dependence on θ is due to the other factors in equation 4.4.1. That is, $a/M \gtrsim 1$ naked singularities feel the 'phantom effects' of the extremal event horizon. Further, we can ascertain whether an observer is rotating with an angular frequency Ω above or below the ZAMO frequency , that is we can distinguish whether $\Omega >$ or $\Omega <$, by looking at the additional maxima-minima structure in the region $r < 1$. We note here that at $\Omega =$ itself Ω_p is smooth, as can be seen from panels (c) and (d) of figure B.1 and it is devoid of the sharp features that are obtained at $r = 1$ for $q \nsim .5$. Features for $q \sim .5$ are highlighted in figure B.2.

On moving closer to the compact object, that is on decreasing r, in any direction θ, Ω_p always increases. Further, for $r \to 0$, on increasing θ, observers get closer to the ring singularity and therefore see a rapidly rising Ω_p. Specifically, as $\theta \to \pi/2$, Ω_p becomes unbounded. With increase in a/M, as is demonstrated in both figures B.1 and B.2, we see that this $r = 1$ feature becomes smoother. By $a/M \sim 1.1$, these features completely vanish and we interpret this result as providing an important criterion based on which one can distinguish a near-extremal NS ($1 < a/M < 1.1$) from one with a higher spin. In the insets of both figures, we explore approximately at what angle θ this sharp $r = 1$ feature starts to appear from and this value of θ depends on a/M, in general.

B.1 Behaviour of the Spin-Precession Frequency for Near-Extremal Naked Singularities

In this section, we will discuss the reasons for the features that are exhibited by near-extremal naked singularities that are different from those with higher spins. As before, let us define χ for convenience as,

$$\chi = \frac{(r^2 + a^2)^2 - a^2 \Delta \sin^2 \theta}{4q(1-q)\,\rho^7 \Delta}, \tag{B.1.1}$$

so that the spin-precession frequency $\vec{\Omega}_p$ becomes,

$$\vec{\Omega}_p = \chi \left[A\sqrt{\Delta} \cos \theta \, \hat{r} + B \sin \theta \, \hat{\theta} \right]. \tag{B.1.2}$$

First, we de-dimensionalise the above expression by replacing $a_* = a/M$ and introducing the dimensionless radial variable $y = r/M$. We can then write χ as,

$$\chi = \frac{(y^2 + a_*^2)^2 - a_*^2 \Delta/M \sin^2 \theta}{4q(1-q)\rho_*^7 \Delta/M} \, M^{-5}. \tag{B.1.3}$$

Therefore, χ has mass dimension -5. Similarly, A and B have mass dimensions 3 and 4 respectively, $\sqrt{\Delta}$ has mass dimension 1 and the term in the square braces of equation B.1.2 has a total mass dimension of 4. Therefore, $\vec{\Omega}_p$ has an overall mass dimension of -1. In this section, henceforth, we work exclusively with dimensionless quantities and simply drop all factors of M. We write down now the dimensionless expressions for a near-extremal NS by replacing $a/M = 1 + \epsilon$ ($\epsilon > 0$),

$$\begin{aligned}
\chi_{\mathrm{ne}} &= \frac{(y^2 + 1 + 2\epsilon)^2 - (1 + 2\epsilon)\Delta_{\mathrm{ne}} \sin^2 \theta}{4q(1-q)\rho_{\mathrm{ne}}^7 \Delta_{\mathrm{ne}}}, \\
A_{\mathrm{ne}} &= 2(1+\epsilon)y - \frac{\Omega_{\mathrm{ne}}}{8} \big\{ 8y^4 + 8(1+2\epsilon)y^2 + 16(1+2\epsilon)y + 3(1+4\epsilon) \\
&\qquad + 4(1+2\epsilon)(2\Delta_{\mathrm{ne}} - 1 - 2\epsilon)\cos 2\theta + (1+4\epsilon)\cos 4\theta \big\} + 2\Omega_{\mathrm{ne}}^2 (1+3\epsilon)y \sin^4 \theta, \\
B_{\mathrm{ne}} &= (1+\epsilon)(y^2 - (1+2\epsilon)\cos^2 \theta) + \Omega_{\mathrm{ne}} \big\{ (1+4\epsilon)y \cos^4 \theta + y^2(y^3 - 3y^2 - (1+2\epsilon)(1+\sin^2 \theta)) \\
&\qquad + (1+2\epsilon)\cos^2 \theta(2y^3 - y^2 + (1+2\epsilon)(1+\sin^2 \theta)) \big\} \\
&\qquad + \Omega_{\mathrm{ne}}^2 (1+\epsilon)\sin^2 \theta [y^2(3y^2 + 1 + 2\epsilon) + (1+2\epsilon)\cos^2 \theta(y^2 - 1 - 2\epsilon)], \\
\Omega_{\mathrm{ne}} &= \frac{2(1+\epsilon)y \sin \theta - (1-2q)\,\rho_{\mathrm{ne}}^2 \sqrt{\Delta_{\mathrm{ne}}}}{\sin \theta [\rho_{\mathrm{ne}}^2(y^2 + 1 + 2\epsilon) + 2(1+2\epsilon)y \sin^2 \theta]}, \\
\Delta_{\mathrm{ne}} &= y^2 - 2y + 1 + 2\epsilon, \\
\rho_{\mathrm{ne}}^2 &= y^2 + \cos^2 \theta + 2\epsilon \cos^2 \theta,
\end{aligned}$$

where subscript 'ne' stands for 'near-extremal.' For some constant κ, we can write,

$$\begin{aligned}
(\Delta_{\mathrm{ne}})^\kappa &\approx & (y-1)^{2\kappa}\left[1 + \epsilon\,\frac{2\kappa}{(y-1)^2}\right] &\quad, \text{ if } |y - 1| \gg \epsilon \\
&\approx & \epsilon^\kappa &\quad, \text{ otherwise,} \\
(\rho_{\mathrm{ne}}^2)^\kappa &\approx & (y^2 + \cos^2 \theta)^\kappa \left[1 + \epsilon\,\frac{2\cos^2 \theta}{y^2 + \cos^2 \theta}\right]^\kappa &\quad, \text{ if } |y^2 + \cos^2 \theta| \gg \epsilon \\
&\approx & (\epsilon \cos^2)^\kappa &\quad, \text{ otherwise.}
\end{aligned} \tag{B.1.5}$$

$y = 1$ was the location of the event horizon for an extremal black hole ($a/M = 1$), which vanished as a/M was changed slightly from 1. As can be seen from the above expressions, this is a special point for Δ_{ne}. For ρ_{ne}, the two cases correspond to being far from and near the ring singularity at $r = 0, \theta = \pi/2$ respectively.

As can be seen from equation B.1.4, Ω_{ne} is finite and smooth always (remember that at the pole i.e., for $\theta = 0$, the only allowed value of is $\Omega = 0$ and hence, $\Omega_{\mathrm{ne},\theta=0} = 0$). Therefore, A and B are also finite and smooth and we can restrict ourselves to studying χ_{ne} to find any interesting 'sharp' features in the radial profile of the modulus of the spin-precession frequency Ω_{p}, for a near-extremal NS. Indeed, we can see from χ_{ne} given in equation B.1.4 that the factor of Δ_{ne} in the denominator will drive Ω_{p} to rise sharply near $y = 1$ for near-extremal naked singularities. Specific maxima/minima structure in the radial profile of Ω_{p} can also be ascertained from equation B.1.4.

Appendix C

Reversal of the Acceleration and the Spin-Precession Frequency[1]

Kerr stationary Killing observers (or equivalently adapted-Kerr static Killing observers) have four-velocities u' (4.3.4) and four-accelerations denoted by $\alpha' = \nabla_{u'} u'$. This in the equatorial plane is given as,

$$\alpha' = \left[-\frac{\sqrt{\Delta}(a^2 M - r^3)}{r^3 g_{\bar{0}\bar{0}}} \right] (\Omega - \Omega_{K+})(\Omega - \Omega_{K-}) \frac{\partial_r}{\sqrt{g_{rr}}}. \tag{C.0.1}$$

The term in the square braces is always negative for $0 \le a \le M$ and $r_H < r$ (outside the horizon). Now, remembering that $\Omega_{K+} \ge 0, \Omega_{K-} \le 0$ and adopting the usual convention $\bar{\kappa} \ge 0$, by comparing the expression for the acceleration from the above expression with $\alpha' = \bar{\kappa} e_{\hat{1}}$, it can be verified that $e_{\hat{1}}$ should be defined as,

$$e_{\hat{1}} = \begin{cases} -\frac{\partial_1}{\sqrt{g_{11}}}, & \text{for } \Omega_- < \Omega \le \Omega_{K-}, \\ \frac{\partial_1}{\sqrt{g_{11}}}, & \text{for } \Omega_{K-} < \Omega \le \Omega_{K+}, \\ -\frac{\partial_1}{\sqrt{g_{11}}}, & \text{for } \Omega_{K+} < \Omega < \Omega_+. \end{cases} \tag{C.0.2}$$

That is, the acceleration experienced by these observers changes in direction across $\Omega = \Omega_{K\pm}$. Physically, as was discussed in [322], this is related to the change in the sense of the centrifugal forces experienced by these observers, and a more general analysis for arbitrary axially symmetric stationary spacetimes is presented in [360]. Also, for a discussion on how to define $e_{\hat{1}}$ for non-accelerating Kepler observers, see §IV.A.3 of [151].

As noted in §4.3.2, with the introduction of $\epsilon_{\bar{3}}$ as (see §3 of [321]),

$$\epsilon_{\bar{3}} = \frac{-g_{\bar{0}\bar{3}} \partial_{\bar{0}} + g_{\bar{0}\bar{0}} \partial_{\bar{3}}}{\sqrt{g_{\bar{0}\bar{0}} \Delta_{03}}}, \tag{C.0.3}$$

---

we can rewrite the right-handed FS tetrad for these observers (4.3.17) as,

$$\left\{ e_{\hat{1}}, e_{\hat{2}}, e_{\hat{3}} \right\} = \begin{cases} \left\{ -\frac{\partial_1}{\sqrt{g_{11}}}, \epsilon_{\bar{3}}, \frac{\partial_2}{g_{22}} \right\}, & \text{for } \Omega_- < \Omega \le \Omega_{K-}, \\[2mm] \left\{ \frac{\partial_1}{\sqrt{g_{11}}}, \epsilon_{\bar{3}}, -\frac{\partial_2}{g_{22}} \right\}, & \text{for } \Omega_{K-} < \Omega \le \Omega_{K+}, \\[2mm] \left\{ -\frac{\partial_1}{\sqrt{g_{11}}}, \epsilon_{\bar{3}}, \frac{\partial_2}{g_{22}} \right\}, & \text{for } \Omega_{K+} < \Omega < \Omega_+. \end{cases} \tag{C.0.4}$$

At this juncture, let us remember that both $\Omega_{K\pm}$ are allowed orbital angular frequencies only when $r_{\text{ISCO}-} \le r$. More fully,

$$\Omega_{K-}, \Omega_{K+} \in (\Omega_-, \Omega_+), \text{ for } r_{\text{ISCO}-} \le r, \tag{C.0.5}$$
$$\text{only } \Omega_{K+} \in (\Omega_-, \Omega_+), \text{ for } r_{\text{ISCO}+} \le r < r_{\text{ISCO}-},$$
$$\Omega_{K-}, \Omega_{K+} \notin (\Omega_-, \Omega_+), \text{ for } r < r_{\text{ISCO}+}.$$

Since we know that the acceleration experienced by static observers is always along $+\partial_1$, and that sign changes occur at $\Omega_{K\pm}$, we can find the direction in which the acceleration experienced by an arbitrary Killing observer in the Kerr spacetime points along.

For a pictorial representation of the above discussion, we plot in figure C.1 the variation in $\Omega_\pm, \Omega_{K\pm}$ with r, for black holes with spin parameters $a = .1M, .5M, .9M$. Orange and purple represent regions where the acceleration vector points along $\pm\partial_1$ and the appropriate definitions for the right-handed Frenet-Serret tetrads in these regions are $\left\{ \pm\frac{\partial_1}{\sqrt{g_{11}}}, \epsilon_{\bar{3}}, \mp\frac{\partial_2}{g_{22}} \right\}$ respectively.

With respect to the right-handed FS triad defined above, the spin-precession frequency is given as,

$$\Omega'_p = -\bar{\sigma}_1 e_{\hat{3}}, \tag{C.0.6}$$
$$\bar{\sigma}_1 = -\frac{\Omega r^3 + 3M\Omega r^2(a\Omega - 1) + aM(a\Omega - 1)^2}{r^3 g_{\bar{0}\bar{0}}}.$$

Clearly then the spin-precession frequency changes signs (relative to the right-handed FS triad) at the zeroes of the numerator, i.e. when,

$$\Omega r^3 + 3M\Omega r^2(a\Omega - 1) + aM(a\Omega - 1)^2 = 0, \tag{C.0.7}$$

and the orbits where the reversal of the spin-precession frequency occurs do not, in general, coincide with the Kepler orbits where the centrifugal force reverses. If we denote the roots of (C.0.7) by Ω_1, Ω_2, then

$$\Omega_1 = \frac{2aM}{2a^2M - r^2(r - 3M) + \sqrt{r^6 - 6Mr^5 + 9M^2r^4 - 4a^2Mr^3}},$$
$$\Omega_2 = \frac{1}{\Omega_1(a^2 + 3r^2)}. \tag{C.0.8}$$

Let us define the q-values corresponding to Ω_1, Ω_2 as,

$$q_1 = \frac{\Omega_1 - \Omega_-}{\Omega_+ - \Omega_-}, \quad q_2 = \frac{\Omega_2 - \Omega_-}{\Omega_+ - \Omega_-}. \tag{C.0.9}$$

It can be verified that that $q_2 < q_{\text{static}} < q_Z < q_1$. That is, the spin-precession frequencies experienced by static observers and the ZAMO always have the same sense, relative to their right-handed Frenet-Serret triads.
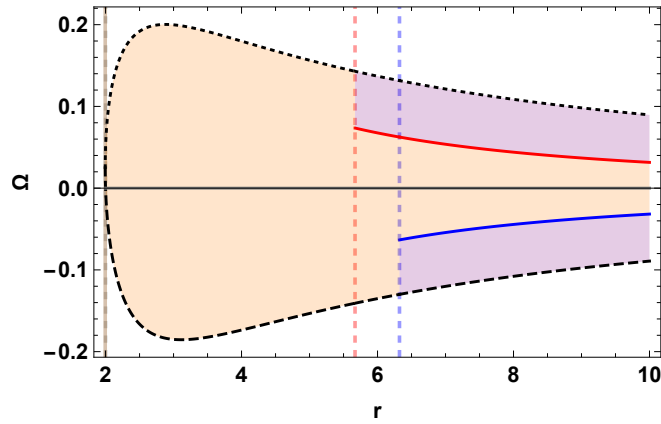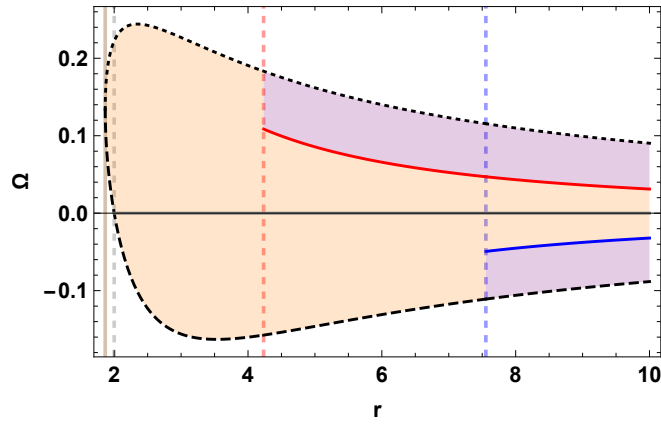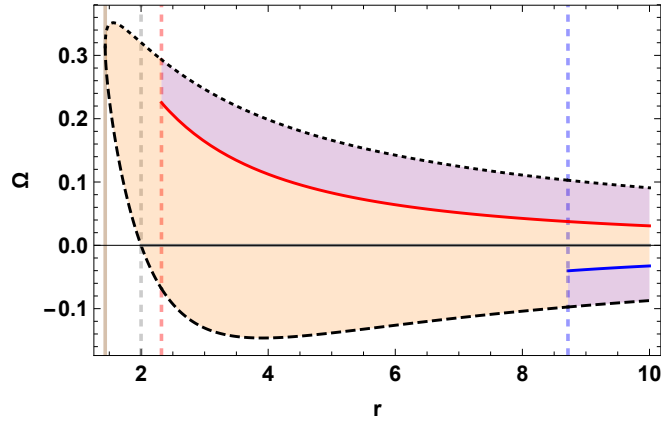
(a) $a = .1M$, Sense of the Acceleration

(b) $a = .5M$, Sense of the Acceleration

(c) $a = .9M$, Sense of the Acceleration

FIGURE C.1: We plot here the variation in $\Omega_\pm, \Omega_{K\pm}$ with r in dotted-black (topmost line), dashed-black, red and blue respectively. The vertical brown, dashed-gray, dashed-red and dashed-blue lines represent the location of the horizon r_H, the ergoradius in the equatorial plane $r_+(\pi/2)$ and the ISCOs of co-rotating and counter-rotating Kepler observers $r_{\mathrm{ISCO}\pm}$ respectively. We plot over the range $r_H < r \le 10M$ and use units of M^{-1} on the y-axis and of M on the x-axis, for black holes of mass M and spin parameters $a = .1M, .5M, .9M$ in panels (a-c) respectively. The shading represents the sign of the acceleration experienced by adapted-Kerr static Killing observers. Orange and purple represent regions where the acceleration vector points along $\pm\partial_1$ and the appropriate definitions for the right-handed Frenet-Serret tetrads in these regions are $\left\{ \pm\frac{\partial_1}{\sqrt{g_{11}}}, \epsilon_{\bar{3}}, \mp\frac{\partial_2}{\sqrt{g_{22}}} \right\}$

respectively. To compare, the direction in which the black hole spin points in is given by $\hat{z} = -\frac{\partial_2}{\sqrt{g_{22}}}$.
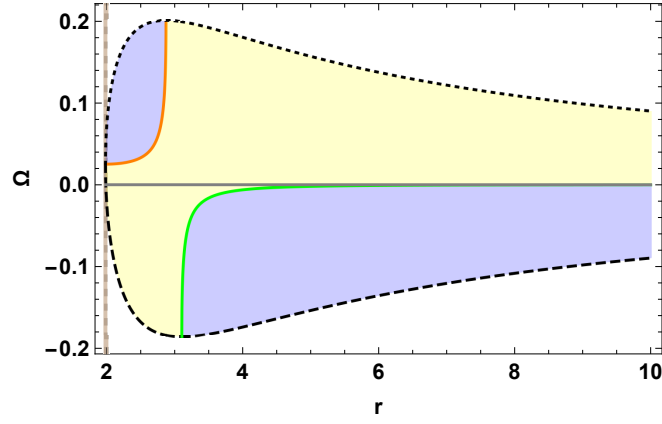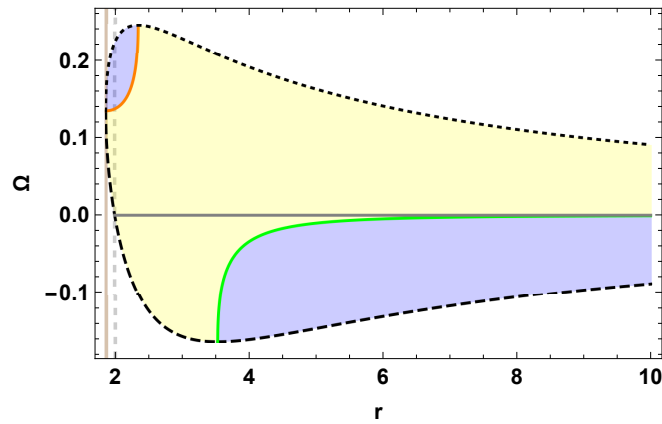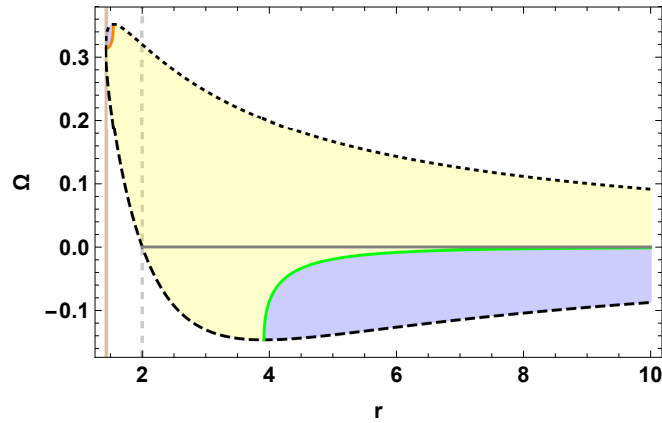
(a) $a = .1M$, Sense of the Precession Frequency

(b) $a = .5M$, Sense of the Precession Frequency

(c) $a = .9M$, Sense of the Precession Frequency

FIGURE C.2: We plot here the variation in $\Omega_{\pm}, \Omega_1, \Omega_2$ with r in dotted-black (topmost line), dashed-black, orange and green respectively. The vertical brown and dashed-gray lines represent the location of the horizon r_H and ergoradius in the equatorial plane $r_+(\pi/2)$ respectively. We display the orange and green lines only when they satisfy $\Omega_- < \Omega_1, \Omega_2 < \Omega_+$, over the range $r_H < r \leq 10M$. We plot in units of M^{-1} on the y-axis and in units of M on the x-axis, for black holes with spin parameters $a = .1M, .5M, .9M$ in panels (a-c) respectively. We display the regions in the Kerr spacetime where observers moving on equatorial circular geodesics experience positive and negative spin-precession frequencies relative to the $e_{\hat{3}}$ leg of their respective right-handed FS tetrads, in blue and yellow respectively. That is, the spin-precession frequencies in these regions are given as $\Omega' = \pm|\bar{\sigma}_1|e_{\hat{3}}$ respectively. Further, these plots imply that the spin-precession frequency associated with stationary observers of fixed orbital radius radius r changes in sense at most only once with change in Ω, i.e. either when $\Omega = \Omega_1$ or $\Omega = \Omega_2$. It is also interesting to note that there exist regions (in r) where the spin-precession frequency does not change in sense.

Moreover, as can be seen from figure 4.3, $q_{K-} < q_{static} < q_Z < q_{K+}$ and so the $e_{\hat{3}}$ legs of the static observers and the ZAMOs also point along the same direction $\hat{z} \equiv -\partial_2/\sqrt{g_{22}}$, where we have introduced $\hat{z}$ to denote the unit vector that points along the z-axis in the Boyer-Lindquist (and also adapted-Boyer-Lindquist) chart and is the direction in which the black hole spin points. Therefore, the spin-precession experienced by static observers and the ZAMOs has the same sense relative to the BH spin orientation as well.

In figure C.2, we show the variation of Ω_1, Ω_2 with r, when $\Omega_- < \Omega_1, \Omega_2 < \Omega_+$, for black holes with mass M and spin parameters $a = .1M, .5M, .9M$. Since the spin-precession frequency changes sense at $\Omega = \Omega_1, \Omega_2$, this figure implies that the spin-precession frequency associated with stationary observers at a fixed orbital radius radius r changes at most only once, either when $\Omega = \Omega_1$ or $\Omega = \Omega_2$. Furthermore, there also exists a region where the spin-precession frequency does not change in sense. In this figure, we display the regions in the Kerr spacetime where observers moving on equatorial circular geodesics experience positive and negative spin-precession frequencies relative to the $e_{\hat{3}}$ leg of their respective right-handed FS tetrads, in blue and yellow respectively. That is, the spin-precession frequencies in these regions are given as $\Omega' = \pm|\bar{\sigma}_1|e_{\hat{3}}$ respectively.

Appendix D

The Connecting Vector for Earth and Stationary Killing Observers[1]

The motion of earth in the Kerr spacetime can naturally be modelled by that of an asymptotic static observer. As discussed in §4.3, the direction to earth (when causally connected) in the Frenet-Serret spatial triad of an equatorial Kerr static observer is a constant vector. This is associated with the notion of the (null) connecting vector of the Kerr static Killing congruence. Now, if we denote the direction to earth in the Kerr static observer's FS spatial triad as $n^{\hat{i}}$, then we can write it most generally as,

$$n^{\hat{i}} = \left(\sin\theta_E \cos\phi_E, \sin\theta_E \sin\phi_E, \cos\theta_E\right). \tag{D.0.1}$$

Now, we will discuss here how to find the direction towards earth in the frame of a pulsar that moves on a circular orbit in the equatorial plane of a Kerr black hole. Such an observer can be treated as a static Killing observer in the adapted-Kerr metric. In this metric however, earth becomes a stationary Killing observer, and the aim here then is to find the connecting vector between a static and a stationary Killing observer.

Let the tangent to the null geodesic connecting a pulsar (that can be treated as moving on an adapted-Kerr static Killing orbit) and an asymptotic adapted-Kerr static Killing observer be given as $n^{\hat{\bar{j}}}$, in the associated spatial FS triad. Then, in analogy with (D.0.1), we can write,

$$n^{\hat{\bar{j}}}(\bar{\phi}_E) = \left(\sin\bar{\theta}_E \cos\bar{\phi}_E, \sin\bar{\theta}_E \sin\bar{\phi}_E, \cos\bar{\theta}_E\right). \tag{D.0.2}$$

Since a Kerr static Killing observer becomes an adapted-Kerr stationary Killing observer, in a coordinate time dt, in the adapted-Boyer Lindquist coordinates, it moves by an amount $-\Omega\,dt$ along in the $\bar{\phi}$ direction. The components of the connecting vector to an asymptotic adapted-Kerr static Killing observer that is present at an infinitesimal adapted-Boyer-Lindquist $\bar{\phi}$-coordinate shift of $-\Omega\,dt$ can be found by a rotation about the z-axis in the adapted-Kerr metric by $-\Omega\,dt$. Instead, we can simply rotate the above vector (D.0.2) in the FS frame of the adapted-Kerr static Killing observer by the appropriate rotation matrix $R[\pm e_{\hat{3}}, -\Omega\,d\tau]$. The signs turn

up because,

$$
\hat{z} = -\frac{\partial_2}{\sqrt{g_{22}}} = \begin{cases} -e_{\hat{3}}, & \text{for } \Omega_- < \Omega \le \Omega_{K-}, \\ e_{\hat{3}}, & \text{for } \Omega_{K-} < \Omega \le \Omega_{K+}, \\ -e_{\hat{3}}, & \text{for } \Omega_{K+} < \Omega < \Omega_+. \end{cases} \tag{D.0.3}
$$

Here we have assumed that the pulsar orbit radius r lies outside the counter-rotating ISCO, i.e. $r_{\text{ISCO}-} \le r$ so that both Kepler frequencies $\Omega_{K\pm}$ are allowed, $\Omega_- < \Omega_{K\pm} < \Omega_+$. The analysis can be extended to accommodate observers present on orbital radii r in the range $r_{\text{H}} < r < r_{\text{ISCO}-}$ by following the discussion in appendix C. Now, we can write

$$
n^{\hat{j}}(\bar{\phi}_{\text{E}} - \Omega d\tau) = R[\pm e_{\hat{3}}, -\Omega d\tau] n^{\hat{j}}(\bar{\phi}_{\text{E}}) = \tag{D.0.4}
$$
$$
\left(\sin \bar{\theta}_{\text{E}} \cos\left(\bar{\phi}_{\text{E}} \mp \Omega d\tau\right), \sin \bar{\theta}_{\text{E}} \sin\left(\bar{\phi}_{\text{E}} \mp \Omega d\tau\right), \cos \bar{\theta}_{\text{E}} \right),
$$

where in the above, one can use the appropriate redshift formulae to relate time differences dt and $d\tau$. Furthermore, since all infinitesimal rotations are around the same constant axis, we can write the direction to earth in FS spatial triad associated with the adapted-Kerr static Killing observer as being given by,

$$
n_{\text{E}}^{\hat{j}}(\tau) = \left(\cos\left(\Omega\tau\right) \sin \bar{\theta}_{\text{E}}, \mp \sin\left(\Omega\tau\right) \sin \bar{\theta}_E, \cos \bar{\theta}_{\text{E}} \right), \tag{D.0.5}
$$

where for convenience we have set $\bar{\phi}_{\text{E}} = 0$ and the signs correspond to the signs of $e_{\hat{3}}$ in (D.0.3). This expression is consistent with relevant statements in §3 of [321]. It is useful to note that at $\tau = 0$,

$$
n_{\text{E}}^{\hat{j}}(\tau = 0) = \left(\sin \bar{\theta}_{\text{E}}, 0, \cos \bar{\theta}_{\text{E}} \right), \tag{D.0.6}
$$

and so, the initial condition for the beam vector remains identical to the case when the pulsar is modelled as a Kerr static Killing observer.

Appendix E

Solution for the Beam Vector[1]

We show here the analytical solution to solve the beam evolution equation,

$$\dot{\hat{B}} = \omega \hat{B} \times \hat{S}, \tag{E.0.1}$$

where $\hat{S}$ in the above is obtained from (4.6.17). It is useful to include this simple calculation to indicate that the extension to pulsars moving on non-equatorial Killing orbits in the Kerr spacetime is straightforward, and involves just additional (constant) rotation matrices. Also, this can serve as a starting point for a more general analysis for pulsar's moving on arbitrary time-like orbits.

We use the Euclidean notation that was employed in §4.6. We first move to a rotating frame $\{\hat{e}'_i, i = 1, 2, 3\}$ in which $\hat{S}(\tau)$ becomes time-independent i.e., $\hat{S}'(\tau) = (\sin\beta, 0, \cos\beta)$. This achieved by a rotation around $\hat{e}_3$ by $-(\psi + \sigma_1 \tau)$, for which we use the rotation matrix $U_1 = R[\hat{e}_3, -(\psi + \sigma_1 \tau)]$ to write,

$$U_1 \hat{S}(t) = (\sin\beta, 0, \cos\beta). \tag{E.0.2}$$

Remembering that if $\vec{A} = \vec{B} \times \vec{C}$, then under rotations we have also, $U_1 \vec{A} = U_1 \vec{B} \times U_1 \vec{C}$. We now define $\hat{B}' = U_1 \hat{B}, \hat{S}' = U_1 \hat{S}$, and write in the rotating frame,

$$U_1 \dot{\hat{B}} = \omega \hat{B}' \times \hat{S}'. \tag{E.0.3}$$

To rewrite the above equation completely in terms of the rotating frame, we write out $\dot{U}_1$ as,

$$\dot{U}_1 = -\sigma_1 \begin{bmatrix} 0 & -1 & 0 \\ 1 & 0 & 0 \\ 0 & 0 & 0 \end{bmatrix} U_1, \tag{E.0.4}$$

---

to obtain the following,

$$
\begin{aligned}
\dot{\hat{B}}' &= \dot{U}_1 \hat{B} + \omega \hat{B}' \times \hat{S}' \\
&= \dot{U}_1 U_1^T U_1 \hat{B} + \omega \hat{B}' \times \hat{S}' \\
&= -\sigma_1 \begin{bmatrix} 0 & -1 & 0 \\ 1 & 0 & 0 \\ 0 & 0 & 0 \end{bmatrix} \hat{B}' + \omega \hat{B}' \times \hat{S}' \\
&= \hat{B}' \times (\sigma_1 \hat{e}_3') + \omega \hat{B}' \times \hat{S}' \\
&= \hat{B}' \times (\sigma_1 \hat{e}_3' + \omega(\sin\beta \hat{e}_1' + \cos\beta \hat{e}_3')) \\
&= \omega_{\text{eff}} \hat{B}' \times \hat{S}'_{\text{eff}},
\end{aligned}
\tag{E.0.5}
$$

where we have introduced ω_{eff} so $\hat{S}'_{\text{eff}}$ has unit norm, i.e.,

$$
\omega_{\text{eff}}^2 = \omega^2 + \sigma_1^2 + 2\omega\sigma_1 \cos\beta,
\tag{E.0.6}
$$

$$
\hat{S}'_{\text{eff}} = \left(\frac{\omega \sin\beta}{\omega_{\text{eff}}}, 0, \frac{\sigma_1 + \omega \cos\beta}{\omega_{\text{eff}}} \right).
\tag{E.0.7}
$$

And we recognize that ω_{eff} is simply the norm of the vector difference of the intrinsic spin angular frequency and the spin-precession frequency vectors, $\omega \hat{S}$ and $-\sigma_1 \hat{e}_3$.

Now that $\hat{S}'_{\text{eff}}$ is already a time-independent vector, we can immediately apply Rodrigues' rotation formula to obtain the beam vector in this frame. However, we make a second coordinate transformation and simply read off the beam vector in the new frame. We define χ from writing $\hat{S}'_{\text{eff}} = (\sin\chi, 0, \cos\chi)$, that is,

$$
\chi = \sin^{-1} \left(\frac{\omega}{\omega_{\text{eff}}} \sin\beta \right).
\tag{E.0.8}
$$

We can then send $\hat{S}'_{\text{eff}}$ to $\hat{e}_3''$ via $\hat{e}_3'' = R\left[\hat{e}_2', -\chi \right] \hat{S}'_{\text{eff}} = U_2 \hat{S}'_{\text{eff}}$. Then if we introduce $\hat{B}'' = U_2 \hat{B}'$, we can write

$$
U_2 \dot{\hat{B}}' = U_2 \left(\omega_{\text{eff}} \hat{B}' \times \hat{S}'_{\text{eff}} \right),
\tag{E.0.9}
$$

and since we are simply performing a time-independent rotation transformation, $\frac{dU_2}{d\tau} = 0$ and ,

$$
\dot{\hat{B}}'' = \omega_{\text{eff}} \hat{B}'' \times \hat{e}_3''.
\tag{E.0.10}
$$

By an application of Rodrigues' rotation formula, it can be seen immediately that the solution is simply given as,

$$
B_1'' = D_1 \cos(\omega_{\text{eff}}\tau) + D_2 \sin(\omega_{\text{eff}}\tau),
\tag{E.0.11}
$$
$$
B_2'' = D_2 \cos(\omega_{\text{eff}}\tau) - D_1 \sin(\omega_{\text{eff}}\tau),
$$
$$
B_3'' = D_3.
$$

Note that the integration constants D_1, D_2, D_3 are not free since we want to consider a specific initial condition for $\hat{B}$ given in (4.6.13). We will first obtain $\hat{B}$ by performing in series the inverse transformations on $\hat{B}''$ and

then proceed to set the initial conditions. The requisite transformations to obtain $\hat{B}$ are given as,

$$\hat{B} = U_1^T U_2^T \hat{B}'', \tag{E.0.12}$$

to obtain in the Frenet-Serret frame,

$$
\begin{aligned}
B_1 =& D_1 \left[\cos(\omega_{\text{eff}}\tau)\cos(\psi+\sigma_1\tau)\cos\chi+\sin(\omega_{\text{eff}}\tau)\sin(\psi+\sigma_1\tau)\right] \\
&+ D_2 \left[\sin(\omega_{\text{eff}}\tau)\cos(\psi+\sigma_1\tau)\cos\chi-\cos(\omega_{\text{eff}}\tau)\sin(\psi+\sigma_1\tau)\right] \\
&+ D_3 \cos(\psi+\sigma_1\tau)\sin\chi, \\
B_2 =& D_1 \left[\cos(\omega_{\text{eff}}\tau)\sin(\psi+\sigma_1\tau)\cos\chi-\sin(\omega_{\text{eff}}\tau)\cos(\psi+\sigma_1\tau)\right] \\
&+ D_2 \left[\sin(\omega_{\text{eff}}\tau)\sin(\psi+\sigma_1\tau)\cos\chi+\cos(\omega_{\text{eff}}\tau)\cos(\psi+\sigma_1\tau)\right], \\
&+ D_3 \sin(\psi+\sigma_1\tau)\sin\chi \\
B_3 =& -\sin\chi\left[D_1\cos(\omega_{\text{eff}}\tau)+D_2\sin(\omega_{\text{eff}}\tau)\right]+D_3\cos\chi.
\end{aligned}
\tag{E.0.13}
$$

From the condition that the beam vector above (E.0.13) satisfy the initial condition (4.6.13), we obtain

$$
\begin{aligned}
D_1 &= \sin\theta_E\cos\chi\cos\psi - \cos\theta_E\sin\chi, \\
D_2 &= -\sin\theta_E\sin\psi, \\
D_3 &= \cos\theta_E\cos\chi + \sin\theta_E\sin\chi\cos\psi.
\end{aligned}
\tag{E.0.14}
$$

Note that the initial phase of the spin-vector $\hat{S}$ denoted here by ψ is still free to choose. Once this is chosen, we obtain the full solution for the evolution of the beam vector of a pulsar that remains fixed in space near a Kerr black hole or naked singularity.

Without loss of generality, let us pick the initial phase for $\hat{S}_0$ to be $\psi = 0$. From equation (4.6.16), it is clear that one obtains pulses only for specific geometric configurations, $\theta_E = \pm\alpha + \beta$. Also,

$$
\begin{aligned}
D_1 &= \sin(\theta_E - \chi), \\
D_2 &= 0, \\
D_3 &= \cos(\theta_E - \chi).
\end{aligned}
\tag{E.0.15}
$$

And the beam vector is given by,

$$
\begin{aligned}
B_1 =& \cos(\sigma_1\tau)\left[\cos(\omega_{\text{eff}}\tau)\sin(\theta_E-\chi)\cos\chi+\cos(\theta_E-\chi)\sin\chi\right] \\
&+ \sin(\sigma_1\tau)\sin(\omega_{\text{eff}}\tau)\sin(\theta_E-\chi), \\
B_2 =& -\cos(\sigma_1\tau)\sin(\omega_{\text{eff}}\tau)\sin(\theta_E-\chi) \\
&+ \sin(\sigma_1\tau)\left[\cos(\omega_{\text{eff}}\tau)\sin(\theta_E-\chi)\cos\chi+\cos(\theta_E-\chi)\sin\chi\right], \\
B_3 =& -\cos(\omega_{\text{eff}}\tau)\sin(\theta_E-\chi)\sin\chi+\cos(\theta_E-\chi)\cos\chi.
\end{aligned}
\tag{E.0.16}
$$

For pulsars moving along the world-lines of arbitrary static Killing observers, not restricted to the equatorial plane, the spin-precession frequency vector $\hat{\Omega}_p$, in the FS frame, does not lie along the $\hat{e}_3$ leg of their respective spatial FS tetrads. It is still a constant vector that can be expressed as a linear combination of their FS tetrad's $\hat{e}_1$ and $\hat{e}_3$ legs, as can be seen from (4.2.24). To obtain the equivalent expression for $\hat{B}$, one starts off with a coordinate transformation (denoted by U_0, say) that corresponds to a rotation change of axes which sets

$\hat{\Omega}_p$ to $(0, 0, 1)$. One can then follow through the entire routine from (E.0.2), finally ending with the inverse coordinate transformation U_0^T to obtain the beam vector $\hat{B}(\tau)$. Heuristically, it is clear that the same divergence manifests itself for pulsars held fixed spatially off the equatorial plane and close to the ergosurface of a Kerr BH or NS, for Kerr static Killing observers.